University of Thessaly
School of Engineering
Department of Civil Engineering

Mechanical behavior of buried steel pipelines crossing active strike slip faults

Polynikis Vazouras
Civil Engineer, M.Sc.

Doctoral Dissertation

Submitted to
the Department of Civil Engineering
in Fulfillment of the Requirements
for the Doctoral Degree

Supervisor: Professor Panos Dakoulas

Volos 2013

UNIVERSITY OF THESSALY

SCHOOL OF ENGINEERING

DEPARTMENT OF CIVIL ENGINEERING

Doctor of Philosophy Dissertation

Mechanical behavior of buried steel pipelines crossing active strike slip faults

by

POLYNIKIS VAZOURAS

Diploma of Civil Engineering, U.Th.

Master of Science (M.Sc.), Department of Civil Engineering, U.Th.

Supervisor: Dr. Panos Dakoulas, Professor

Co-supervisor: Dr. Spyros A. Karamanos, Assosiate Professor

Submitted in fulfillment
of the requirements for the degree
of Doctor of Philosophy

Volos, 2013

ΠΑΝΕΠΙΣΤΗΜΙΟ ΘΕΣΣΑΛΙΑΣ

ΠΟΛΥΤΕΧΝΙΚΗ ΣΧΟΛΗ

ΤΜΗΜΑ ΠΟΛΙΤΙΚΩΝ ΜΗΧΑΝΙΚΩΝ

Διδακτορική Διατριβή

ΜΗΧΑΝΙΚΗ ΣΥΜΠΕΡΙΦΟΡΑ ΥΠΟΓΕΙΩΝ ΧΑΛΥΒΔΙΝΩΝ ΑΓΩΓΩΝ ΔΙΕΡΧΟΜΕΝΩΝ ΔΙΑΜΕΣΟΥ ΕΝΕΡΓΩΝ ΡΗΓΜΑΤΩΝ ΟΡΙΖΟΝΤΙΑΣ ΟΛΙΣΘΗΣΗΣ

Πολυνίκης Βαζούρας

Διπλωματούχος Πολιτικός Μηχανικός, Π.Θ.
Μεταπτυχιακό Δίπλωμα, Τμήμα Πολιτικών Μηχανικών, Π.Θ

Επιβλέπων: Δρ. Πάνος Ντακούλας, Καθηγητής
Συν-επιβλέπων: Δρ. Σπύρος Α. Καραμάνος, Αναπληρωτής Καθηγητής

Υπεβλήθη για την εκπλήρωση των
απαιτήσεων για την απόκτηση του
Διδακτορικού Διπλώματος

Βόλος, 2013

Examination Committee:

Dr. Panos Dakoulas (Supervisor), Professor, Dept. of Civil Eng., University of Thessaly

Dr Spyros A. Karamanos, (Co-supervisor) Associate Professor, Department of Mechanical Engineering, University of Thessaly

Dr. George Gazetas, (Advisor) Professor, Dept. of Civil Eng., National University of Athens

Dr. Pitilakis Kyriazis, Professor, Dept. of Civil. Eng., Aristotle University of Thessaloniki

Dr. Emilios Comodromos, Professor, Dept. of Civil Eng., University of Thessaly

Dr. Euripidis S. Mistakidis, Professor, Dept. of Civil Eng., University of Thessaly

Dr. Achilleas Papadimitriou, Assistant Professor, Dept. of Civil Eng., University of Thessaly

Εξεταστική Επιτροπή:

Δρ. Πάνος Ντακούλας (Επιβλέπων)
Καθηγητής, Τμήμα Πολιτικών Μηχανικών, Πανεπιστήμιο Θεσσαλίας

Δρ. Σπύρος Α Καραμάνος (Συν-επιβλέπων)
Αναπληρωτής Καθηγητής, Τμήμα Μηχανολόγων Μηχανικών, Πανεπιστήμιο Θεσσαλίας

Δρ. Γεώργιος Γκαζέτας (Μέλος Τριμελούς)
Καθηγητής, Σχολή Πολιτικών Μηχανικών, Εθνικό Μετσόβιο Πολυτεχνείο

Δρ. Κυριαζής Πιτιλάκης
Καθηγητής, Τμήμα Πολιτικών Μηχανικών, Αριστοτέλειο Πανεπιστήμιο Θεσσαλονίκης

Δρ. Αιμίλιος Κωμοδρόμος
Καθηγητής, Τμήμα Πολιτικών Μηχανικών, Πανεπιστήμιο Θεσσαλίας

Δρ. Ευριπίδης Σ. Μυστακίδης
Καθηγητής, Τμήμα Πολιτικών Μηχανικών, Πανεπιστήμιο Θεσσαλίας

Δρ. Αχιλλέας Παπαδημητρίου, Επίκουρος Καθηγητής, Τμήμα Πολιτικών Μηχανικών Πανεπιστήμιο Θεσσαλίας

This dissertation is dedicated
to my parents

Acknowledgements

The research conducted in this thesis was carried out under the supervision of Professor Panos Dakoulas and Associate Professor Spyros A. Karamanos. To both of them, I am extremely grateful for introducing me in this field of scientific research and inspiring me to continue working on my research in the future. They provided me with invaluable guidance related to my scientific research, numerical modeling procedures, scientific writing, as well as support and encourage during the years of my PhD. I am also grateful to associate professor Spyros A. Karamanos for giving me, the chance to work on several research projects in the area of computational mechanics and structural analysis, through which I had the opportunity to gain further experience and knowledge and also partially fund my postgraduate studies.

Furthermore, I am grateful to Professor George Gazetas, Professor Kyriazis Pitilakis, Professor Emilios Comodromos, Professor Euripidis Mistakidis and Assistant Professor Achilleas Papadimitriou for their remarks and suggestions that improved the study. Finally, I would like to thank the Professors and the PhD students from both the Civil Engineering and Mechanical Engineering department, with whom I have collaborated, for their help and collaboration during those years.

Last, but not least, I owe many thanks to my friends and my family for their support and their unconditional love.

Polynikis Vazouras

Mechanical behavior of buried steel pipelines crossing active strike slip faults

POLYNIKIS VAZOURAS

University of Thessaly, Department of Civil Engineering, 2013

Supervisor: Dr. Panos Dakoulas, Professor
Co-supervisor: Dr. Spyros A. Karamanos, Assosiate Professor

Abstract

Motivated by the growing demand for new major oil and gas pipeline projects worldwide, the present study investigates the performance of buried pipelines in geohazard areas subjected to permanent strike-slip fault movement. The study is based on an efficient combination of detailed numerical simulations and closed-form analytical solutions. An extensive literature review is conducted for the evaluation and assessment of available analytical and numerical models, experimental data and available commercial software. In addition standards that incorporate the strain-based design approach for pipeline design are considered. The interacting soil–pipeline system is modeled rigorously through finite elements, employing a general purpose finite element program. A closed-form solution for the force-displacement relationship of a buried pipeline subjected to tension is presented for pipelines of finite and infinite lengths. This solution is used in the form of nonlinear springs at the two ends of the pipeline in refined finite-element models, allowing an efficient nonlinear analysis of the pipe-soil system at large strike-slip fault movements. The analysis accounts for large strains, inelastic material behaviour of the pipeline and the surrounding soil, as well as contact and friction conditions on the soil-pipe interface. The effects of various soil and pipe parameters on the mechanical response of the pipeline are examined. Steel pipes with D/t ratio and material grade typical for oil and gas pipelines are considered. The effects of internal pressure on pipeline

performance are also investigated. The analysis is conducted through an incremental application of fault displacement. Appropriate performance criteria of the steel pipeline are defined and monitored throughout the analysis. The numerical results determine the fault displacement at which the specified performance criteria are reached, and are presented in diagram form, with respect to the fault crossing angle. The results of the parametric analyses demonstrate that for a strike-slip fault that is normal to the pipeline axis, local buckling occurs at relatively small fault displacements. As the angle between the fault normal and the pipeline axis increases, local buckling can be avoided due to longitudinal stretching, but the pipeline may fail due to excessive axial tensile strains or cross-sectional flattening. The numerical models consider both infinite and finite length of the pipeline corresponding to various angles between the pipeline axis and the normal to the fault plane. It is shown that the end conditions of the pipeline have a significant influence on pipeline performance. Finally, in an attempt to explain the structural behaviour of the pipeline with respect to the occurrence local buckling, a simplified analytical model is also developed that illustrates the counteracting effects of pipeline bending and axial stretching and provides reasonable closed-form estimates for the formation of local buckling for relative small values of crossing angle accounting also for end effects.

Table of contents

1   Introduction

The present dissertation deals with the mechanical behavior of pipelines crossing active faults. Permanent ground-induced actions due to earthquakes, such as fault movements, landslides, liquefaction-induced lateral spreading are responsible for the majority of seismic damages in oil and gas buried steel pipelines. These types of deformation are applied on the pipeline in a quasi-static manner, and are not necessarily associated with severe seismic shaking. Under such conditions, the pipeline may be seriously deformed in the plastic range and may experience pipe wall fracture and loss of containment, imposing obvious risks to the population and the environment. In the above cases, conventional stress-based design is no longer applicable and strain-based design is necessary. Figure 1.1 shows the EGIG (Western Europe) incidents by cause and size of leak. Ground movement induced damage attributes approximately 7% to the total amount of incidents. However, ground movement is the second leading cause for (the failure mode of) rupture of the pipeline, after third party damage.

The US Department of Transportation (US DOT) natural gas transmission data for the period 1984 to 2001 show that ground movement induced damage accounted for 8.5% of the total amount of incident, as shown in Figure 1.2. The property damage cost caused by ground movement induced damage, however, was only exceeded by the cost caused by third party damage.
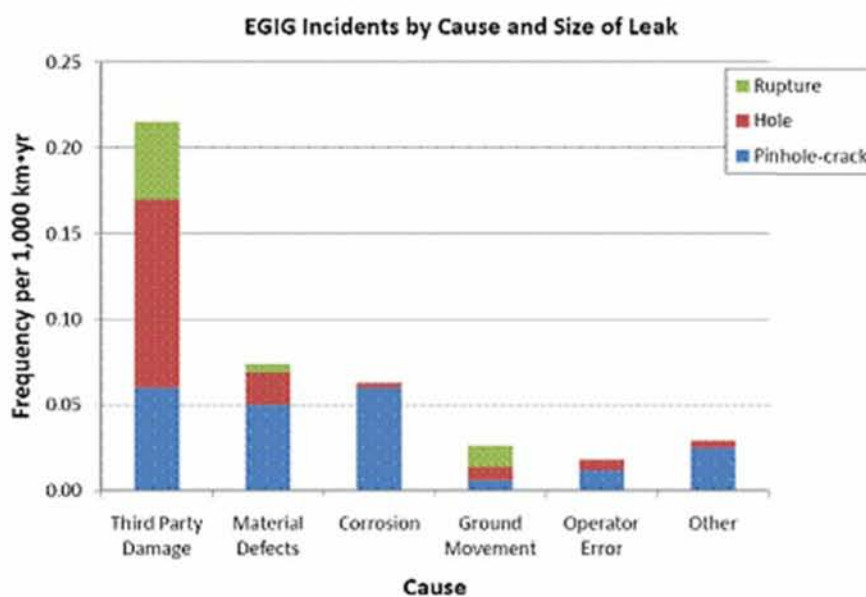
Figure 1.1: EGIG Pipeline Incident Data [1]

Incidents by Cause and Total Property Damage
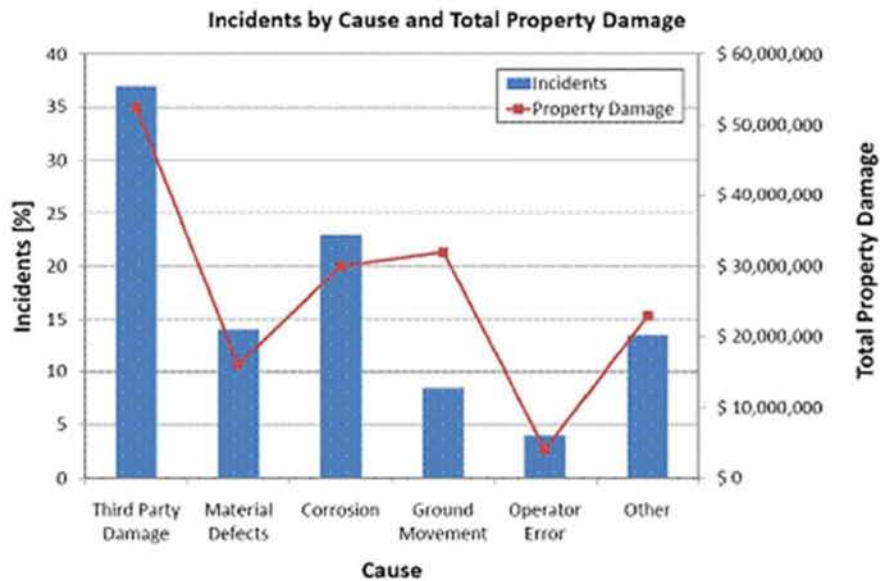
Figure 1.2: US DOT Incident Data for Gas Transmission Pipelines [2]

Incidents by Cause per 1,000 km·yr
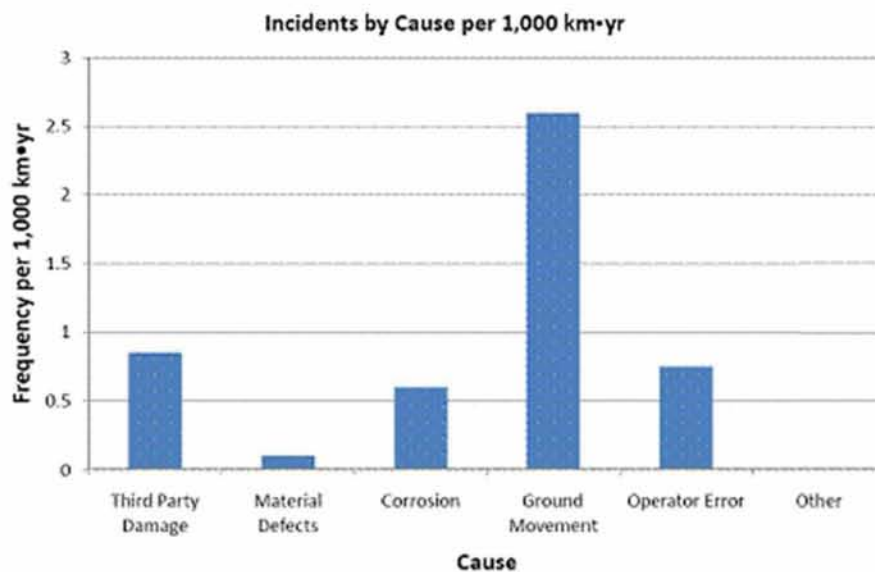
Figure 1.3: Incident Data for a Typical Andean Pipeline [2]

The relative significance of geohazards is more pronounced in areas where pipelines are constructed in difficult terrain, without a full appreciation for potential geohazards. Data for a typical pipeline indicates that ground movement may be responsible for as many as 50% of the incidents in the South American Andes, leading to an average failure frequency exceeding 2.5 per 1,000 km·yr, as shown in Figure 1.3. This frequency is about two orders of magnitude greater than that experienced in Western Europe.

This dissertation focuses on the structural response of continuous (welded) buried steel pipelines crossing active strike-slip seismic faults. Those pipelines are subjected to an imposed deformation pattern, associated with the development of high stresses and strains in critical locations, which are well beyond the elastic range of pipe material and may cause pipeline failure. In particular, high tensile stresses may cause fracture of the pipeline wall, especially at defected locations or welds, whereas high compression stresses may cause buckling, either in the form of beam-type (global) instability or in the form of pipe wall wrinkling, a shell-type instability, sometimes referred to as "local buckling" or "kinking". In the last 30 years, significant research has been conducted for establishing deformation (strain) capacity limits for steel pipelines including both the strain behaviour of the base material and the welded joints towards determining strain criteria. The performance of continuous buried steel pipelines subjected to permanent fault movement must be evaluated during engineering design against different types of permanent deformation or failure such as:

(a) *Buckling.* Compression stresses may cause buckling, either in the form of local buckling (pipe wall wrinkling) or beam-type (global) instability;

(b) *Tensile rupture.* Tensile stresses may cause fracture of the pipeline wall at defected locations, welds or areas of high-stress concentration; and

(c) *Cross-section ovalization.* Tensile stresses may cause flattening or ovalization of the pipe cross-section, thereby degrading the overall performance of the pipeline system.

The study in the present dissertation is separated into seven Chapters. Initially, in Chapter 2, a literature review regarding the methodologies and techniques, which have been developed for the treatment of this problem, and the main findings of previous research are presented. This includes analytical, numerical and experimental research that has been conducted until now. Existing guidelines for buried pipelines are briefly outlined pointing out the approach of each standard. Finally, commercial software that is used for the analysis of pipelines is presented, highlighting the advantages and disadvantages of each program.

In the sequel, Chapter 3 covers the issue of numerical modeling that is proposed and used for pipelines buried in soil medium. More particular the effect of model length for each of the three directions is parametrically investigated in order to achieve the optimum model length for each direction. For the special case of a pipeline subjected to tension along the direction of its axis, a closed-form exact mathematical solution is proposed, which can be used to model the pipe-soil interaction as a nonlinear spring. This allows an extension of the basic finite element model to a model of larger length,

which can be either finite or infinite, without increasing the total number of finite elements. Finally, the effects of fault width and discetization of the model for both soil and pipe are investigated.

In Chapter 4, buried pipelines perpendicular to fault plane are analyzed. Considering steel pipelines of various diameter-to-thickness ratios, and typical steel material for pipeline applications (API 5L grades X65 and X80), this chapter focuses on the effects of various soil and pipeline parameters on the structural response of the pipe, with particular emphasis on identifying pipeline failure (pipe wall wrinkling/local buckling or rupture). More specifically, the effects of shear soil strength, soil stiffness, horizontal fault displacement, width of the fault slip zone, are investigated. Furthermore, the influence of internal pressure on the structural response and the effect of the (finite or infinite) model length in the longitudinal direction are examined. The results from the present investigation aim at determining the fault displacement at which the pipeline fails and can be used for pipeline design purposes.

In Chapter 5, the mechanical response of buried pipelines is extended for different crossing angles, formed between the pipeline axis and the fault-plane normal direction. The pipeline is assumed to cross the vertical fault plane at various angles ranging between zero and 45 degrees. Similar parameters as those investigated in Chapter 4 are analyzed in order to find their influence on the mechanical response of pipelines. In addition to local buckling, the failure modes are now extended to account for tensile rupture and cross-section ovalization.

Chapter 6 presents a simplified model for buckling prediction, by taking into account the crossing angle (for non-positive or small positive angles), the pipe-soil interaction length and the pipe properties. The results are compared to those in Chapter 4 and Chapter 5 in order to identify whether or not buckle occurs. Finally, this simple form of the proposed model can be used to derive some useful conclusions about the influence of each factor on the mechanical behavior of the pipe-soil model.

The main conclusions and the innovative points of the present research are summarized in the last chapter of the dissertation (Chapter 7).

2 Mechanical behavior of buried pipelines - Bibliography survey

2.1 Introduction

This chapter examines available research findings and field evidence regarding the performance of buried pipelines subjected to ground induced action. Considering the fact that ground induced actions are responsible for a significant number of failures at buried pipes, many researchers have worked in this scientific area.

Research on the performance of buried pipelines usually requires the development of numerical techniques due to their highly nonlinear response and their interaction with the ground. In past decades, due to lack of efficient computational tools, research focused mostly on theoretical studies for this problem. More recently, most of the relevant publications are associated with numerical models. Both analytical and numerical previous research findings are presented in Section 2.2. As far as experimental work is concerned, only few experiments have been performed for buried pipelines subjected to strike-slip and normal faulting. These experiments are presented below in Section 2.3. Section 2.4 overviews available commercial software, pointing out their advantages and disadvantages. Section 2.5 refers to the stain-based design analysis which is employed during recent years showing its difference from the stress-based design. Section 2.6 provides a brief overview of the existing guidelines for buried pipelines. Finally, at the end of the chapter, a brief discussion regarding the contribution of the present dissertation to the treatment of this problem is presented.

2.2 Analytical and numerical models

In order to assess pipeline strength against an imposed tectonic fault displacement, the state of stress within the pipeline should be calculated for the imposed deformation. In their early publications, Newmark and Hall [3] analyzed the effects of fault movement on the pipeline considering that the pipe behaves as a cable, using small deflection theory and relating the friction of the soil-pipe system with the static earth pressure. Because of lack of flexural rigidity, the equilibrium condition cannot be satisfied and faults that cause compression in the pipeline could not be analyzed.

Continuing the pioneering paper of Newmark and Hall [3], Kennedy et al. [4] [5] developed an analytical model, considering a non-uniform friction interface between the pipe and the soil, which was assumed to be cohesionless. At this work, only values of fault angle that result in pipe tension were examined, due to the methodology limitations. These values were from fifteen to sixty degrees from the pipeline axis. The pipe was divided in two zones in order to properly account for the friction. In the first zone consisting of a straight section of the pipeline, the frictional force f is given from the following equation

$$f = \pi D p_r \tan \phi_p \qquad (2.1)$$

in which ϕ_p is the angle of friction between the pipe and the surrounding soil, p_r is the normal pressure and D is the diameter of the pipeline.

The other zone consists of a curved pipeline section. In this part, friction was difficult to accurately define. A series of analyses were performed to estimate the friction of this curved zone. Values of curved zone to straight zone friction ratio ranging from 2.4 to 3.3 were considered. Lateral and vertical soil pressures on pipe were taken into consideration in contrast with the work by previous authors, were no passive soil resistance was considered. From lateral force-displacement curves (see Figure 2.1), the force for each curve reaches a maximum value and remains almost constant for all subsequent displacements.

This assumption leads to slightly conservative results. Large deflection theory was also taken into account, by modelling the pipe as a cable. Results concerning the influence of crossing angle, depth of cover, wall thickness and pipe diameter, pipe material strength and the effect of internal pressure were presented and relevant conclusions were given. Wang and Yeh [6] improved this methodology accounting for the pipeline bending stiffness. This allowed authors to examine cases where the pipe was subjected to compression. The adopted methodology considers a division of the pipe into four segments. The two outer segments behave as beams on elastic foundation, whereas the two inner segments have a constant curvature, as shown in Figure 2.2.
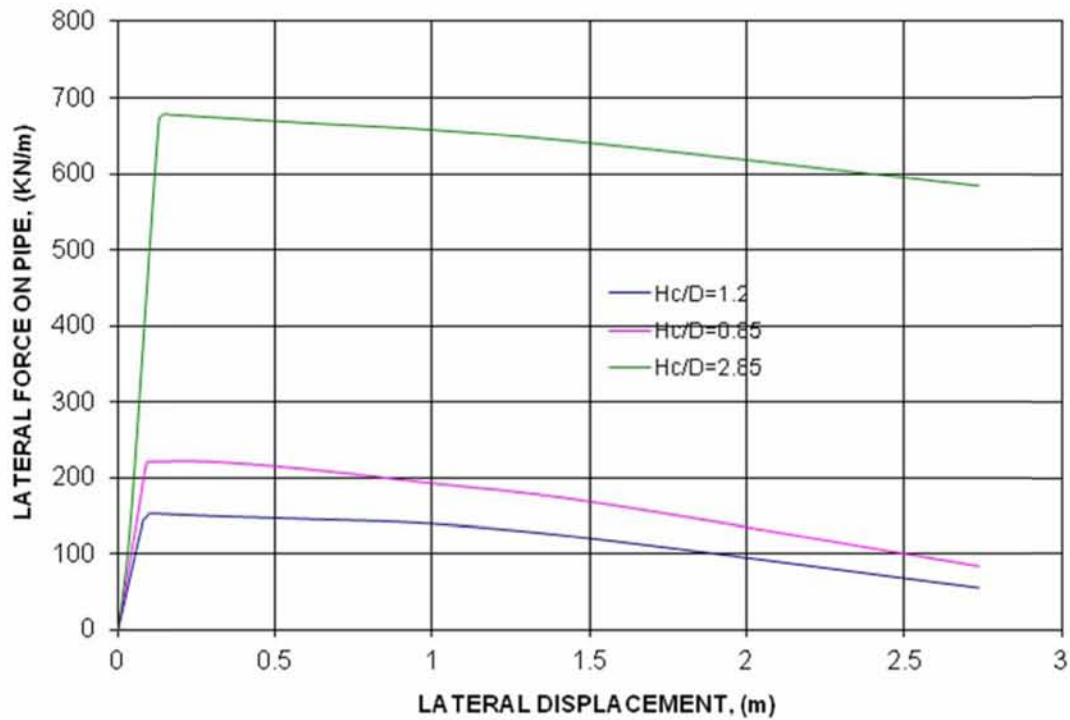
Figure 2.1: Lateral soil force versus lateral displacement for pipe buried in loose to moderately dense sand [4]
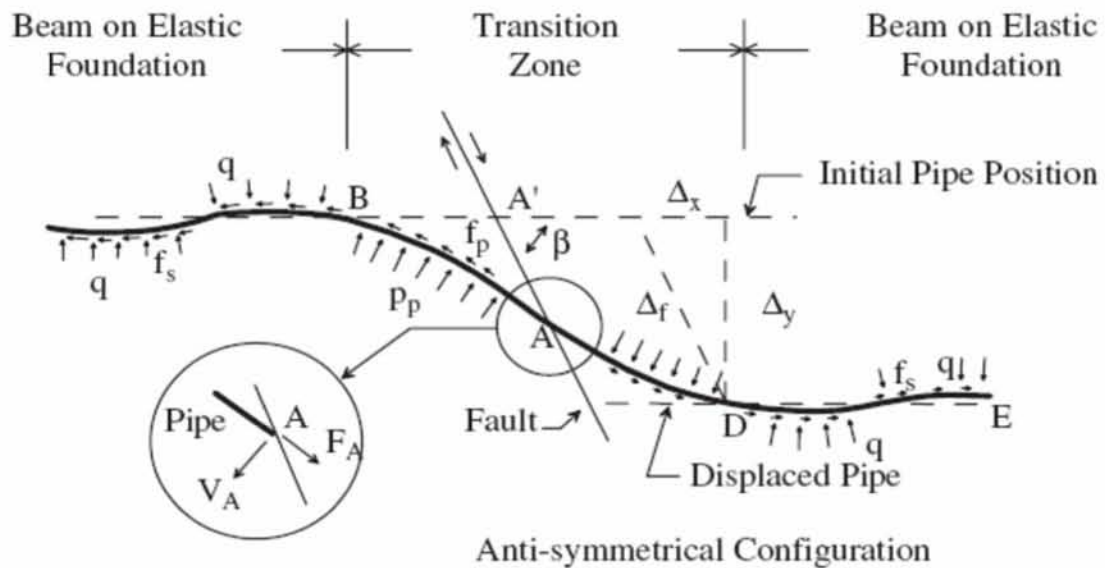

Figure 2.2: Pipeline analysis model proposed by Wang and Yeh [6]

7

An iterative procedure was developed for obtaining the axial force and bending moment at point B (Figure 2.2). These values were compared with a calculated bending moment using the expression

$$M_{pc} / M_p = \cos\frac{\pi}{2}\left(\frac{P}{P_u}\right) \qquad (2.2)$$

where M_{pc} and M_p are the resisting moment capacities of steel pipe with and without axial load P, respectively, and P_u is the ultimate axial force capacity of the pipe without any bending effects.

The design of the steel pipe was considered safe if the calculated bending moment capacity was greater than the resulting bending moment. A series of parametric studies were conducted investigating the effect of some important parameters, such as the fault movement, crossing angle, soil-pipe friction angle, buried depth and diameter of pipe. Similar conclusions were found compared to those obtained from previous methodologies, although some quantitative differences, as well as some differences in the mechanism of failure do exist because of the different approaches. Vougioukas et al. [7] considered both horizontal and vertical movement of faults and analysed numerically buried pipes considering them as elastic beams.

In later publications, McCaffrey and O'Rourke [8] and Desmod et al. [9] studied the development of strains in buried pipes crossing faults based on field observations of the performance of gas and water pipes during the San Fernando earthquake.

Wang and Wang [10] studied the problem considering the pipe as a beam on elastic foundation, whereas Takada et al. [11] presented a new simplified method for evaluating the critical strain of the fault crossing steel pipes using the relation between pipe longitudinal deformation and cross-sectional deformation. The location of bending point is first found using Kennedy's formulation and, subsequently, the bending angle is calculated. The location of point B (Figure 2.2) is found after an iterative trial and error method, in which the pipe axial force satisfies the compatibility condition between the geometrical (required) and physical (available) elongation. The geometrical elongation is defined as the elongation imposed to the pipeline due to fault movement, whereas the physical elongation is defined as the elongation resulting from axial strains along the unanchored length. A beam-shell analysis is conducted for determining the maximum strain in the pipeline. Combining the two previous findings, a relation between the pipe bending angle and the maximum strain was found. Finally this relation was enhanced with parameters such us pipe material, pipe diameter, pipe thickness, soil pressure, fault

displacement, fault crossing angle and soil-pipe friction, which form their proposed methodology for simplified design of buried steel pipes crossing active faults.

The behaviour of buried steel pipelines subjected to excessive ground-induced deformations has received significant attention in the pipeline community in recent years. It has been recognized that, apart from the geometric and the mechanical properties of the steel pipeline, site conditions (i.e. the properties of the surrounding soil) may have a strong influence on pipeline response, and that soil-pipe interaction should be taken into account [12]. Kokavessis and Anagnostidis [13], using a finite element methodology and contact elements to describe soil-pipe interaction, analyzed buried pipes under permanent ground-induced actions. More specifically, they studied the effects of consolidation settlements that were observed in the area where a pipeline was installed after the design of a new railway. The finite element program ANSYS was employed, modelling the pipe with shell elements and the soil with solid elements. All materials used were linear elastic. Karamitros et al. [14], presented an analytical methodology, refining existing methodologies proposed in [3]-[6], using a combination of beam-on-elastic-foundation and beam theory. More specifically segments AA' and CC' (Figure 2.3) were analyzed as beams-on-elastic foundation in order to obtain the relation between bending moment, shear force and rotation angle at points A and C. The differential equilibrium equation for the elastic line was:

$$EI\frac{d^4w}{dx^4} + kw = 0 \qquad (2.3)$$

where EI is the flexural stiffness, w is the deflection of the beam and k is the elastic foundation spring constant

Segments AB and BC were analyzed as elastic beams in order to obtain the maximum bending moment. At point B, where is the intersection with the fault trace, the axial force on the pipeline is calculated by equalizing the required and the available pipeline elongation. The required elongation is defined as the elongation imposed due to fault movement, whereas the available elongation was defined as the elongation resulting from the integration of axial strains along the unanchored length (the length over which slippage occurs between the pipeline and the surrounding soil). Taking into account geometric second-order effects, bending strains were computed. Maximum pipeline axial strain was calculated from the equilibrium between the externally applied axial force and the internal stresses developed in the pipeline cross-section. Finally all

9

previous values were recalculated until convergence was achieved, indicated by monitoring an updated secant Young's modulus. The above methodology was aiming at considering the contribution of axial force to bending stiffness and finding the location where the most unfavourable combination of axial and bending strain develops.
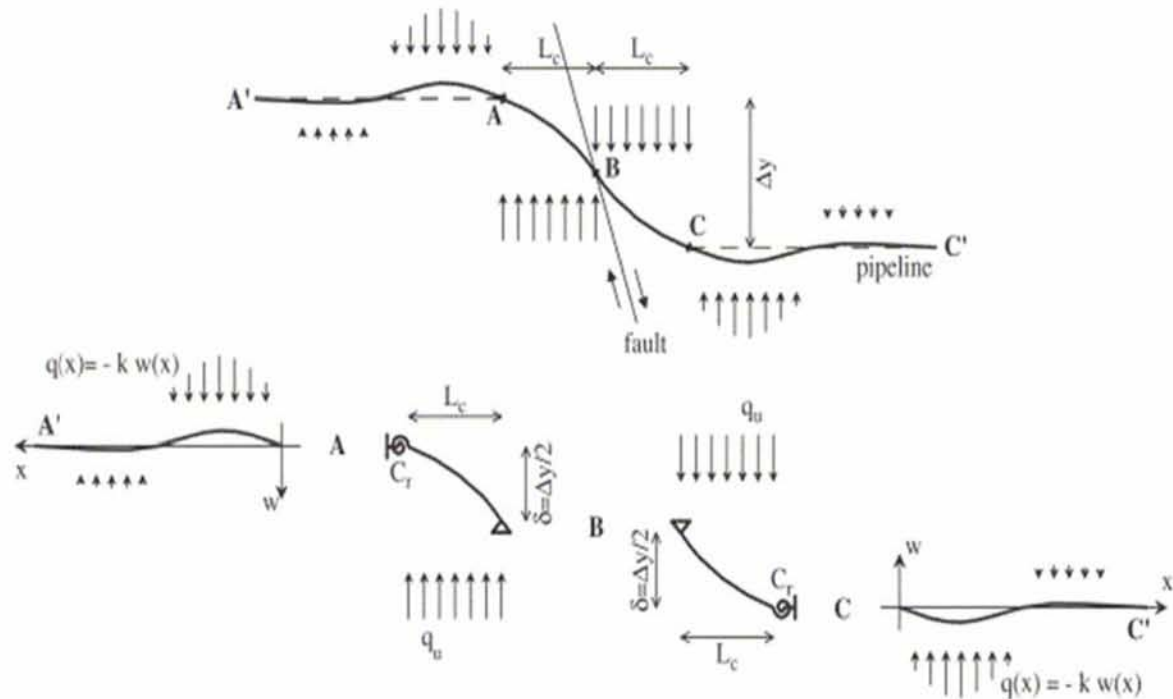
Figure 2.3: Partitioning of the pipeline into four segments [14]

Karamitros et al. [14] also compared their analytical predictions with results from a three-dimensional finite element model, which employed nonlinear springs to simulate the soil, along with shell and beam elements to model the pipe (Figure 2.4). The total model length was 1000 meters, of which 900 meters of the pipe were modelled as a beam and the rest using shell elements. A pipeline having a diameter of 36-inch, wall thickness of 0.469 inches and buried in sand, was considered. Three different fault cases were examined with fault angles equal to 30°, 45° and 60°. The final fault displacement was taken equal to two pipe diameters. Comparisons of results were made for the axial strain at the intersection of the pipeline with the fault trace, the maximum axial strain, the bending strain and the total maximum strain. The comparisons showed a very good agreement between analytical and numerical results with minor deviations resulting to less than 10% error.
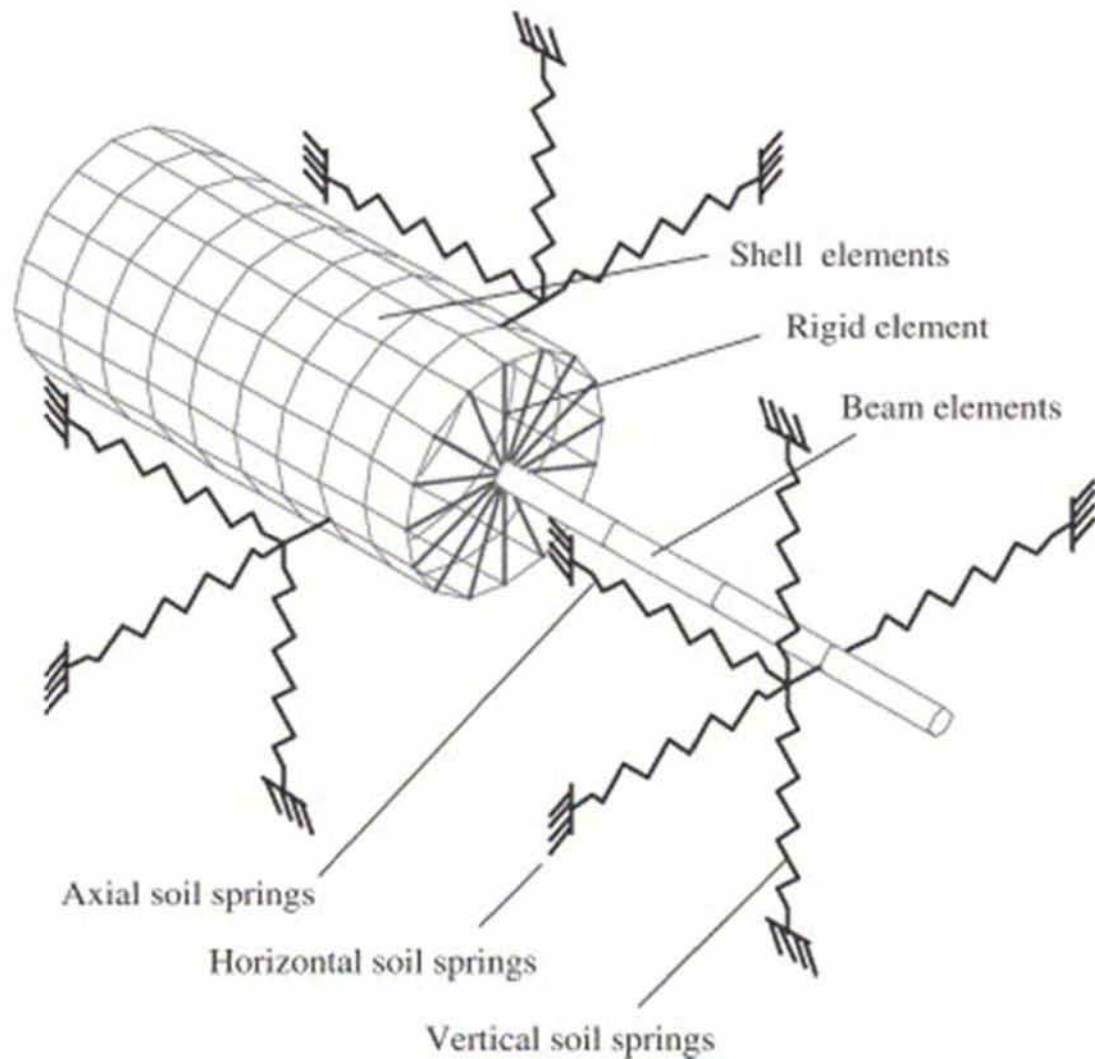
Figure 2.4: 3D model used for analyses with the Finite Element Method [14]

Liu et al. [15] presented a shell finite element simulation, similar to the numerical model in Karamitros et al. [14], and reported axial strain predictions along the pipeline. More specifically, using a 4100 meters model so that the relative movements between the pipe and the soil at the far ends of the model are very small, the authors examined the effect of internal pressure, the intersection fault angle and the influence of Lüder's extension (Lüder's extension is the state where the material yields forming a plateau in the stress-strain curve for a small range of strains). They found that the location where the strain is localized depends on the loading mode induced by the fault. At low intersection angles, the fault movement creates a large tension force in the pipe's axial direction and leads to a tension mode. Under such mode, the strain is localized near the fault trace. As the intersection angle increases, the loading mode gradually switches to bending and the strain localization moves away from the fault trace. For a 3D fault movement, an optimum intersection angle exists when the maximum tensile strain of the axial direction can be minimized.

The maximum compressive strain is reached at a 90° intersection angle. The internal pressure increases the maximum compressive strain, while it can either increase or decrease the maximum tensile strain, depending on the intersection angle and fault displacement. Finally, the effect of Lüder's extension is negligible in the above results.

Shitamoto et al. [16] focused on the development of compressive strain limit of X80 pipelines to resist ground-induced actions. They used an eight-node solid-element model of a pipe segment, modelling a quarter of the pipe, computed the strain corresponding to the maximum moment, and compared this strain capacity to strain demands dictated from soil liquefaction requirements. In order to evaluate the strain demands due to liquefied soil, finite element analysis was used. The pipe was modelled with shell elements, whereas for the soil-pipe interaction, nonlinear springs were used placed at the bottom and top of the pipe. The effect of ground displacement was given to the buried pipeline as enforced displacement. Thus, in order to estimate the maximum strain demand of pipelines, the maximum soil displacement was assumed to be equal to 3 m due to liquefaction-induced lateral spreading in a area with 400m width and 500m length, as shown in the Japan Gas Association (2001) guideline (Figure 2.5), which is based on historical experiences.
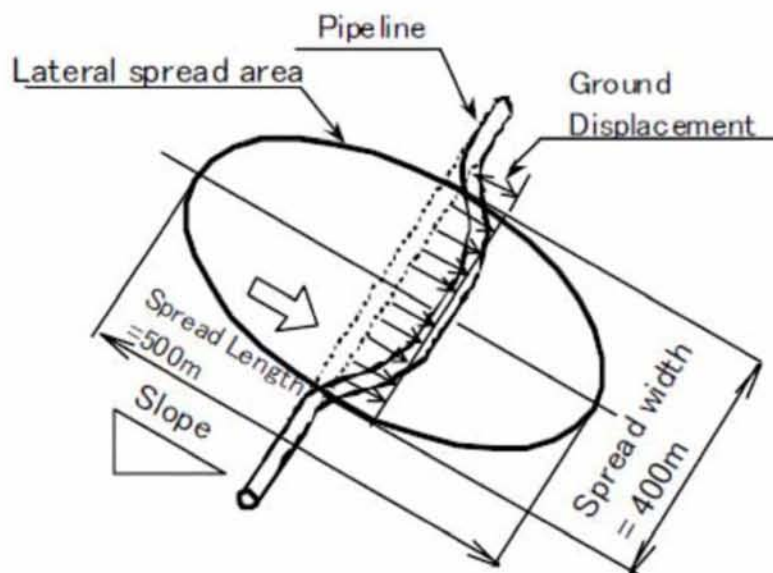

Figure 2.5: Schematic view of the horizontal soil movement on the slant ground [16]

The seismic analysis of buried and unburied pipelines, under both transient and permanent ground movements have been examined by Arifin et al. [17]. They used beam finite elements for the pipeline, nonlinear springs to model the effects of the surrounding soil for buried pipelines and rigid surface with soil contact friction when modelling the unburied pipelines. Parametric analyses consisting of three different pipelines with two wall thicknesses for each pipeline and different percentages of metal loss (loss of material that leads to a smaller thickness) resulted in some useful recommendations for mitigating seismic effects. For the buried pipe section, the direct effect of seismic wave loads on the pipeline system have been proven to be insignificant and all stresses were less than 80% of the SMYS. (The Specified Minimum Yield Strength is the allowable stress based on the Lloyd's register for construction and classification of submarine pipeline). Permanent ground deformation due to soil failure, caused failure to buried pipelines. For unburied pipelines, whether the seismic ground wave or permanent ground deformation were considered, no severe damages were caused for the specific geometric properties, seabed conditions, etc.

Odina and Tan [18] investigated buried pipeline response under seismic fault displacement, using a beam-type finite element model with elastic-plastic springs for the soil effects. In a subsequent publication, Odina and Conder [19], extended the work in [18] examining the effects of Lüder's plateau of the stress-strain material curve on the pipeline response crossing active faults. The study considered a 24-inch pipeline with wall thickness equal to 17.1mm. The pipe had a 6mm FBE anti-corrosion coat and a 40mm concrete coat. API X65 material was used. High density rockfill cover having thickness equal to 0.75m was considered. The finite element model employed for the pipe simulation used 3D elastic-plastic beam elements (2-node linear pipe element with a circular cross section and 6 degrees of freedom at each node). The soil surrounding the pipe was modelled with elasto-plastic springs in the axial lateral and vertical direction. The model length was 1.4km long and the fault angle β was equal to 22°. The rock cover was modelled as an applied pressure and additional operating pressure equal to 200bar and ambient temperature were taken into account. Three case studies have been analyzed. The first assumed Ramberg-Osgood stress-strain curve for the pipe material expressed from the following equation,

$$\varepsilon = \frac{\sigma}{E} + \frac{\sigma}{E}\frac{\alpha_r \sigma_o}{E}\left(\frac{\sigma}{\sigma_o}\right)^N \qquad (2.4)$$

where ε is the total strain, σ_o is a nominal yield stress, and α_r, N are parameters of the Ramberg-Osgood model.

The second case used the stress-strain curve with Lüder's plateau and the third case assessed the effect of strain localisation (as a weakened joint with a plastic moment capacity 10% below the nominal value occuring in the region of highest longitudinal stains) using Ramberg-Osgood stress-strain relationship. Comparing materials that exhibit a Lüder's type stress-strain behavior to those obtained from a Ramberg-Osgood model, they found that the shape of the curve plays a significant role in the magnitude of the axial strains developed. It was also observed that the 10% of difference in material properties for the weak joint has a significant effect on the peak longitudinal strains in the pipeline when compared with results from the nominal pipe properties.

A similar methodology for buried pipelines crossing reverse faults, has been presented by Gu & Zhang [20]. In this paper the soil pipe interaction is still simulated by soil-spring model where the characteristics of the axial soil spring stiffness can be determined by ASCE guidelines. By contrast, the horizontal and vertical soil springs can be obtained by a plane-strain finite element analysis for the actual cross section taking into the account the existence of a trench. The pipeline is modelled with a combination of pipe and elbow elements using elbows near the fault plane discretised with a denser mesh, whereas pipe elements are used further away from fault discretised with a more coarse mesh. The problem examined is an X80 steel pipe with diameter equal to 1.219m, wall thickness 22mm with internal pressure equal to 12MPa, embedded in sand soil conditions, with a crossing angle between the pipeline and the fault equal to 40°. The fault dip is 45°, with a vertical displacement equal to 1.414m. From the analysis, quantitative results are obtained aiming at determining the optimum crossing angle for the pipeline, embedment depth, size and shape of the trench and wall thickness. The numerical results present maximum axial strains and were compared with values derived from provisions. More specifically the allowable tensile strain was calculated according to the following formula,

$$\varepsilon_t = \frac{1}{F_t} \varepsilon_t^{crit} \qquad (2.5)$$

where ε_t^{crit} is the ultimate tensile strain of the pipeline and F_t is the stretching safety coefficient. The stretching safety coefficient is 1.25, if hoop stress is lower than $0.4\sigma_s$, and 1.5, otherwise.

The allowable compressive strain was calculated according to the following expression

$$\varepsilon_c = 0.3 \frac{\delta}{D} \qquad (2.6)$$

when no internal pressure was taken into consideration. If internal pressure was considered the following formula was used

$$\varepsilon_C = \frac{1}{F_C} \varepsilon_C{}^{crit} \qquad (2.7)$$

where $\varepsilon_C{}^{crit}$ is derived from a formula according to the level of internal pressure

A parametric investigation showed that the optimum crossing angle that restricts the axial strains within the limits derived from provisions was from 0° to 10° between the pipeline and fault. Keeping the crossing angle fixed to 10°, it was calculated that the optimum depth was 1.8 m, the bottom width of the trench was 1.9 m and a safe wall thickness was 26.4mm. For the above set of conditions, a reduction for maximum axial compressive strain of the pipeline was achieved.

An analytical investigation of buried pipeline behaviour under seismic faults has been presented by Trifonov & Cherniy [21], extending the analytical methodology proposed in Karamitros et al. [14]. In this work three modifications were made concerning (a) the lack of symmetry condition in the intersection point (wide range of fault types), (b) the incorporation of axial force in the equations of motion of the pipe in high curvature segments, in order to have a direct effect on bending stiffness and (c) the contribution of the transverse displacement to the axial elongation. The pipeline is partitioned in four segments according to Wang and Yeh [6] and Karamitros et al. [14] (Figure 2.3). The segments AA', CC' are analysed as beams–on-elastic foundation, as before, allowing computation of φ, M and V for points A and C. For segments AB and BC, the solution considers a beam in bending and tension. The equilibrium equation is

$$EI \frac{d^4 w}{dx^4} - F \frac{d^2 w}{dx^2} = q \qquad (2.8)$$

Both segments are solved independently, as no symmetry conditions are used. By solving eq. (2.8) and applying the appropriate boundary conditions, a nonlinear system of two equations yields the lengths L_1 and L_2. This system is solved with the help of Nelder-Mead [22-24] method which is found to be more robust than the Newton-Raphson method. For the special case of relatively small fault displacements, where the

maximum downward pipe displacement on segment AB does not exceed the yield displacement, a different procedure is followed. Segment AB is merged with segment AA' and analyzed as beam on elastic foundation. The axial force is calculated as in Karamitros et al [14], by taking into account also the elongation due to transverse displacement. As far as bending strains are concerned, the main difference is that the effect of axial force is taken directly from eq. (2.8) and there is no need of approximate expressions such as $\dfrac{1}{\varepsilon_b} = \dfrac{1}{\varepsilon_b{}^I} + \dfrac{1}{\varepsilon_b{}^{II}}$ used in the approach by Karamitros et al. [14].

Finally, an iterative solution is performed using the secant Young's modulus, as introduced in Karamitros et al. [14] in order to satisfy the moment equilibrium. The work in [21] has been extended by Trifonov & Cherniy [25] in an attempt to refine the analytical model for inelastic material behaviour of the steel pipeline. They considered a two-dimensional stress state with constant hoop stress and derived an analytical solution for stresses and strains. Additional results such as elastic and plastic strain in longitudinal, hoop, radial direction, and the assessment of internal pressure and thermal stresses on the maximal total and plastic strain can be derived from this elasto-plastic model. The effect of temperature and internal pressure was studied. The analytical model was verified using finite elements for the case of strike-slip fault crossing at different crossing angles. Comparison between analytical and numerical results for various loading cases showed good agreement. The analytical works outlined above [13]-[21] have been used to model the effects of the surrounding soil following a spring-type approach. A more rigorous approach has been followed by Daiyan et al. [26], who simulated the soil around a non-deformable pipe with elastic-plastic three-dimensional solid finite elements, in an attempt to understand complex soil failure processes and load transfer mechanisms during relative soil-pipeline displacements.

Abdelfettah Fredj and Aaron Dinovitzer [27] simulated the response of buried pipelines to slope movements. LS-DYNA 971 [28] was used for a 3D continuum modeling using the Smoothed-Particle Hydrodynamics (SPH) method. SPH method is a computational method used for simulating fluid flows. The pipe was modeled using shell elements and the soil was modeled using a double-hardening plasticity model, where the deviatoric and volumetric yield surfaces were independent. The model was validated using pipelines embedded in sand and clay subjected to axial ground movement. Karimian et al. [29] had performed four large scale axial tests in sand soil conditions to a 18-inch pipeline. Comparison of those results with the results obtained from finite-element analysis using the above model, provided a quite reasonable agreement regarding the soil force-displacement relationship. The numerical results

were also compared with results from pull-out tests in clay conditions for a 24-inch polyethylene wrapped pipe conducted by Scarpelli et al. [30], showing good agreement with regard to the measured forces.

Finite element analyses were also performed on a pipeline buried in 18° slope, consisting of silty clay. The active (unstable) soil mass had a slip length of 80 m, and 5 to 6 m depth parallel to the slope. The pipeline had an outside diameter of 457 mm (18 inch) and was made of APL Grade X52. The pipeline was subjected to internal pressure and differential temperature. Results concerning different interface friction angles (20°, 35°, 38°) between the pipe and soil, and the effect of the pipe-wall thickness and diameter to wall-thickness ratio (D/t=64, 76) were presented. The results indicated that the force-displacement relationship is extremely sensitive to interface friction between the pipe material and soil. Higher friction can cause an increase in the pipe strain. Also the friction coefficient is dependent on the pipe coating material and the soil properties. For the analyzed cases of different wall thicknesses, the predicted axial strains were higher for the pipe with a higher D/t ratio. Finally, the strain demands determined from the analyses were compared with the calculated CSA-Z662 compressive-strain design limit, showing that the critical compressive strain was reached only for the case of friction angle equal to 38° by imposing a fault displacement of 1.5m for D/t = 64, and of 1 m for D/t = 76.

A more recent paper of Bartolini et al. [31] presents a strain-based design approach for underground pipelines crossing active faults. Failure types such as rupture, critical tensile deformation, compressive failure and weld fracture are considered in two case scenarios: one adopting a two-hundred year return period event where minimal or no damage can occur in the pipeline and can operate with minimal interruption and another of a thousand-year return period event, where extensive damage could occur in the pipeline without rupturing. The design concept includes optimum routing to minimize compression loads, selection of steel material and wall thickness to improve pipeline deformation capacity and definition of minimum requirements of a trench. The pipeline route at the fault crossing can be subdivided in sections where different trench configurations and different steel material and wall thicknesses are selected (Figure 2.6).
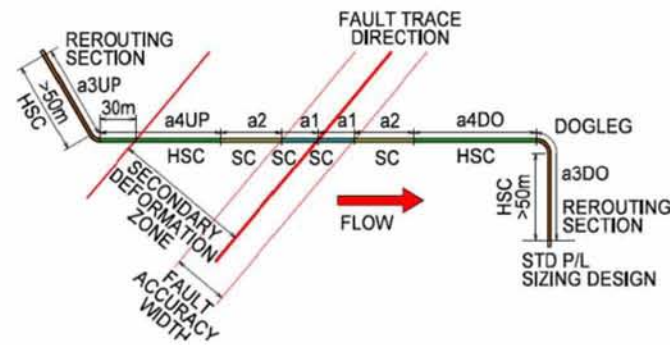
Figure 2.6: Crossing concept at fault crossings [31]

The angle between the pipeline route and the fault trace was selected as close as possible to 75° aiming to avoid compressive axial loads. For trench design two detailed analyses are conducted. A thermal analysis of the pipeline in the trench using ANSYS FEM was performed in order to define insulation requirements to avoid sub-zero temperature. Also, detailed calculations of the non-linear pipe-soil interaction were performed for determining the force versus displacement relationship during fault movement. Laboratory tests were carried out to assess the robustness of the numerical pipe-soil interaction.

For assessing the deformation capacity of pipes having girth welds, subjected to internal pressure, axial force and bending moment, a finite element model was analyzed using the program ABAQUS and validated through full-scale and laboratory tests [32]. The results showed that the deformation capacity of pipelines with different diameters was not affected significantly from the presence of Luders plateau. Under tensile failure, the integrity of the pipeline may be threatened by cracks. For the case of fault crossing, a design approach able to quantify the deformation capacity of defective girth welds was presented. Finally, for assessing the pipeline strain demand during fault movement, a 3D finite element model was employed using pipe and connector elements and a displacement controlled scheme for applying deformation.

Gantes and Boukovalas [33] presented a study for the evaluation of the effects of seismically-induced fault movement on the high-pressure natural gas pipeline system of Komotini-Alexandroupolis-Kipi. The model consisted of shell and beam elements regarding the pipeline, and spring elements accounting for the surrounding soil. The coupling between shell and beam elements was made via rigid elements. The NASTRAN Finite Element code was employed for the analysis. The pipeline diameter was equal to 0.9144m with a wall thickness that varied from 11.9mm to 17.5mm. The steel was an X65 steel with internal operating pressure equal to 7.5 MPa. The stress-strain curve was based on the Ramberg-Osgood model. The pipeline was placed within a trench of mainly

rectangular shape. The backfill material of the trench had a friction angle equal to 36° and the pipe-soil interface a friction angle equal to 24°. The fault considered was oblique normal with a maximum fault displacement equal to 0.8m. The model length of 1700m proved to be adequate for the purpose of analysis. Maximum differential temperature resulted in relatively small strains and thus it was not taken into account. Both compressive and tensile strains in the pipe were compared with respective values of Eurocode 8 and engineering practice, taking girth welds in account (ε_t=0.5%). The tensile strain criterion was not fulfilled. Based on the results, the study proposed measures such as enlargement of the trench, greater wall thickness of the pipe, use of low-friction geotextile and avoidance of sharp bends of the pipeline in the vicinity of the fault.

2.3 Experimental work

In addition to the above numerical studies, notable experimental works on the effects of strike-slip and normal faults on buried high-density polyethylene (HDPE) pipelines have been reported in a series of recent papers by Ha et al. [34] [35]. In this experimental work, four tests were conducted in a centrifuge device. In the first paper, comparison was made between a pipe crossing (a) a strike slip fault at 85° (β=5°) and (b) a normal fault (Figure 2.7), whereas in the second paper, two strike-slip faults with different crossing angles were compared (Figure 2.8). All tests utilize two types of instrumentation, using strain gages and tactile pressure sensors. The pipe was pinned at both ends to the wall of the container (Figures 2.7 and 2.8). One block of the container was subjected to the fault displacment, whereas the other one remained fixed.
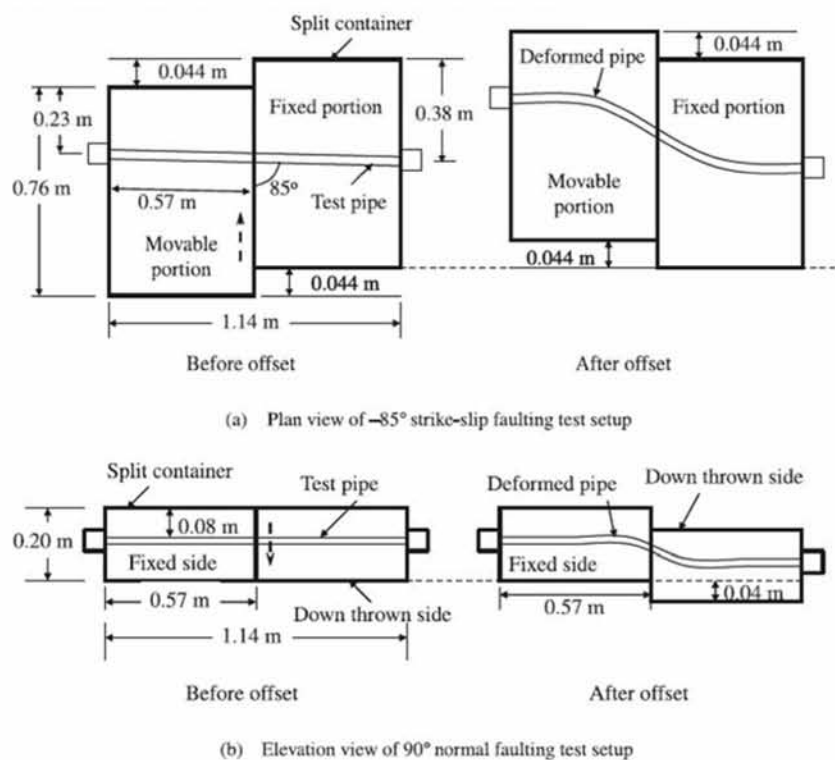

(a) Plan view of –85° strike-slip faulting test setup

(b) Elevation view of 90° normal faulting test setup

Figure 2.7: Centrifuge modelling of a pipeline crossing (a) a strike-slip at an angle β=5° and (b) a normal fault [34]

a) Plan view of -85° strike-slip faulting test setup

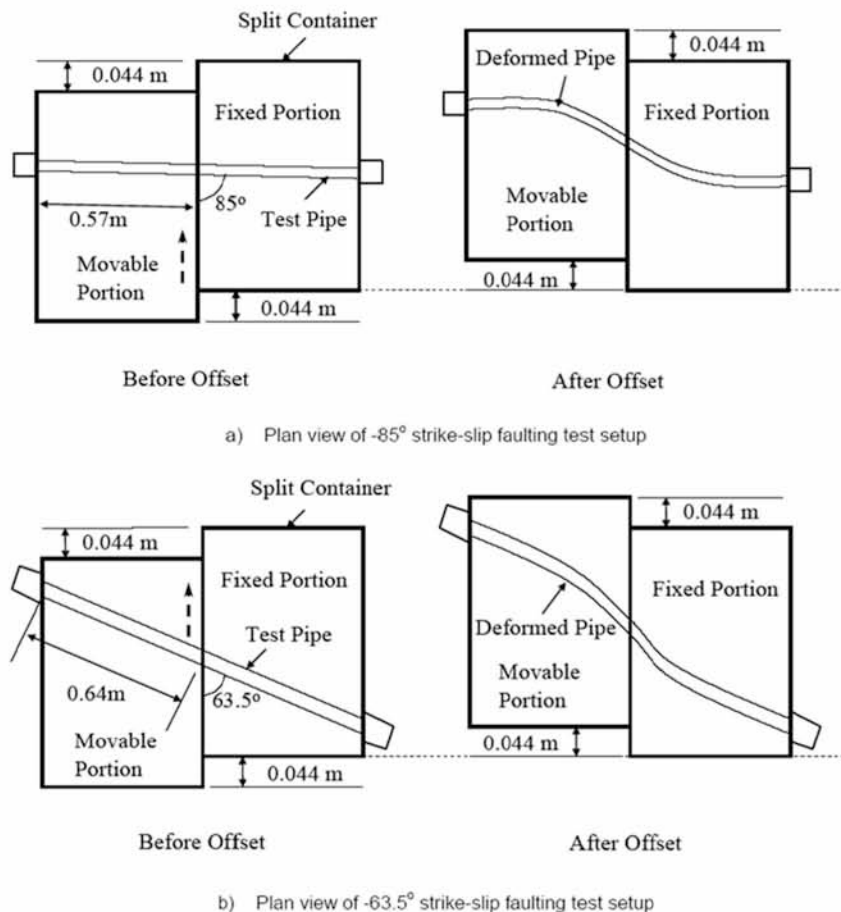b) Plan view of -63.5° strike-slip faulting test setup

Figure 2.8: Centrifuge modelling of pipeline crossing a strike-slip fault at two different angles. [35]

The experimentally measured transverse pressure and bending strain were used for both cases to develop a relationship for the interaction between soil and pipe. The relationships obtained from the experiments were compared for all cases in both papers with the ones suggested by the ASCE guidelines (ASCE 1984). For strike slip faulting the experimental p-y relation was softer than the ASCE relation, whereas the ultimate soil resistance was in agreement with the ASCE values, as indicated in the [36]. Also, the p-y relationship became "softer" away from fault and "stiffer" closer to fault [35]. For normal faulting the experimental values of peak force were found to be much smaller than those suggested by the ASCE guidelines. Having the same experimental set up for centrifuge modelling of a pipeline crossing a strike-slip fault, Abdoun et al. [37] examined the influence of several parameters using also HDPE pipes. The fault was considered to be strike-slip with a fault angle equal to 63.5° (β=26.5°). More particularly, ten centrifuge tests were carried out, in which the effects of embedment depth, fault offset rate, pipeline diameter and soil moisture content were examined. It has been

found that the fault offset rate and soil moisture plays no significant role, whereas the embedment depth (H/D) and diameter to thickness ratio (D/t) significantly influence the location and the magnitude of the peak strains along the pipe.

The experimental work of Yoshizaki et al. [38] was based on large scale tests in which permanent ground deformation effects were taken into account on steel pipelines with elbows (see Figure 2.9). A 100mm-diameter steel pipeline (Japanese steel) with 4.1mm wall thickness was used in the tests. The pipe was embedded in soil at a 0.9m depth. Four experiments were conducted at different soil water contents. These tests allowed the calibration of a sophisticated soil-pipeline interaction analytical program, which was developed in conjunction with the experimental work. The model consisted of shell and beam elements. Shell elements were used at the center point of the elbow and near it. Soil-pipe interaction was characterized by p-y and t-z curves from experiments performed at Cornell [66] and duplicated at Tokyo Gas experimental facilities [38]. Very good agreement was achieved between the analytical and experimental results for all levels of plastic deformation. Finally, significant differences were observed in the response between pipelines embedded in dry and partially saturated sand.
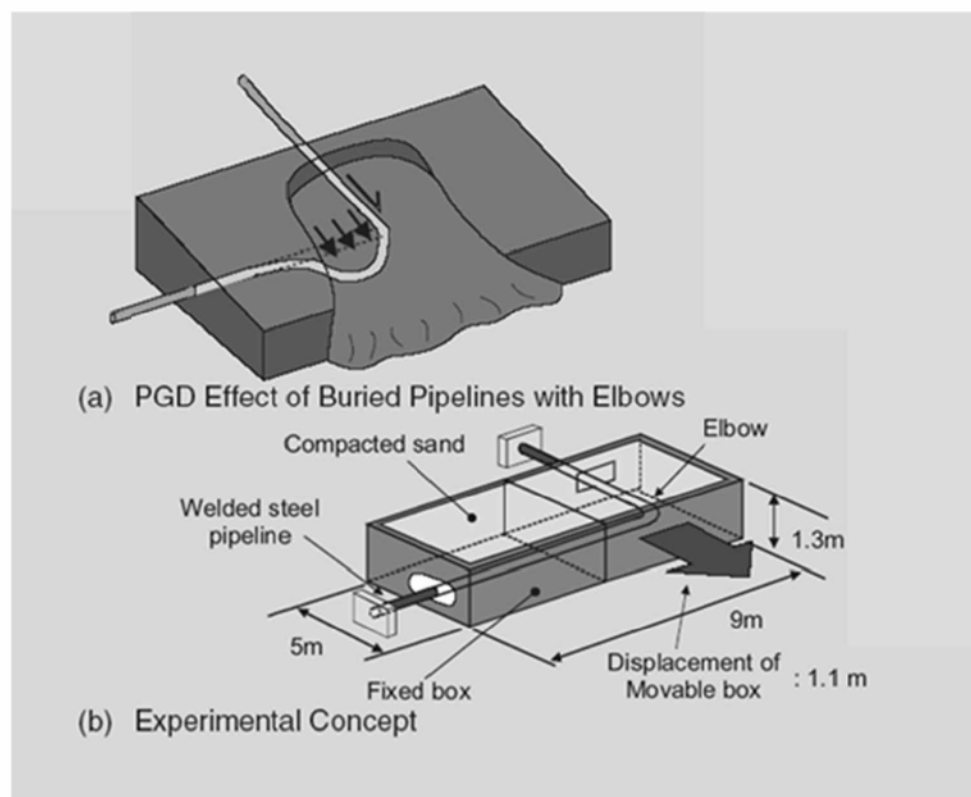

Figure 2.9: Experimental concept for permanent ground displacement (PGD) effects on buried pipelines with elbows[38]

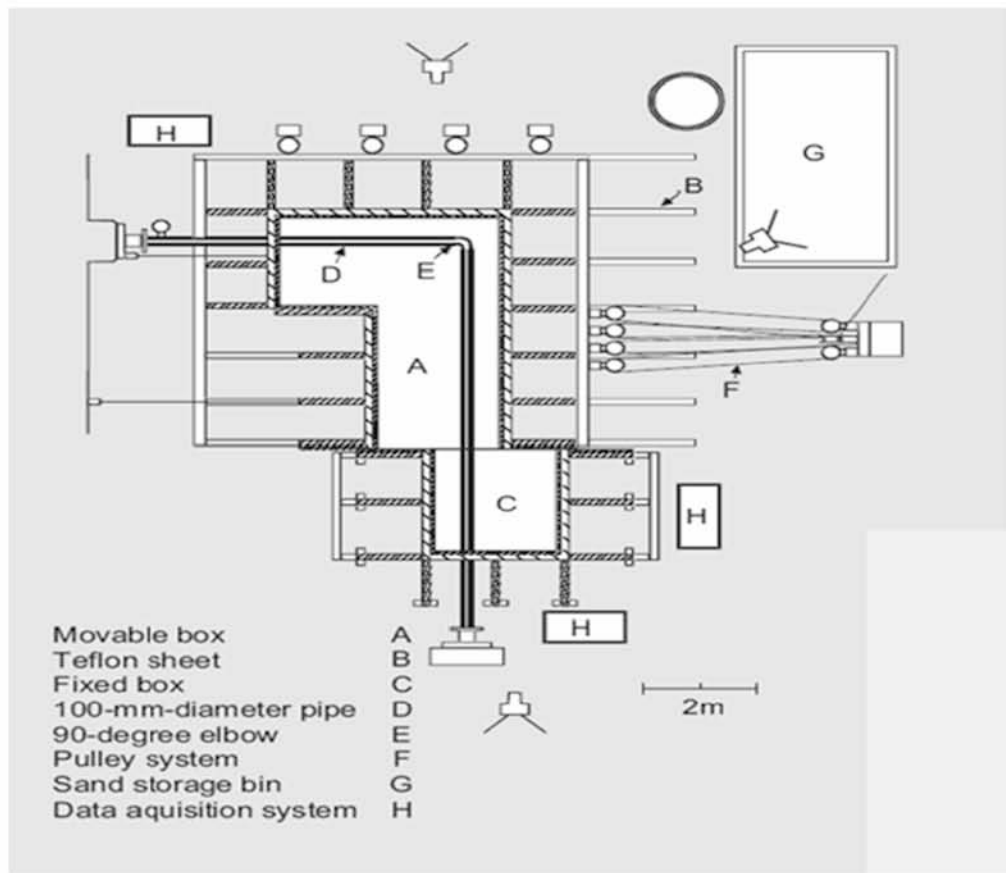|	
Movable box	A
Teflon sheet	B
Fixed box	C
100-mm-diameter pipe	D
90-degree elbow	E
Pulley system	F
Sand storage bin	G
Data aquisition system	H

Figure 2.10: Plan view of experimental set up used in [38]

It is worth noticing that apart from centrifuge tests, nine full-scale strike-slip tests were conducted in Cornell University for HDPE and steel pipelines in the course of NEES-SG project. All pipes were 12.2 meters long and embedded in sand, except of one, which was tested to validate the loading and measurement system and the pipeline response without soil. In these tests, HDPE pipes of 400mm and 250mm diameter and steel pipes of 150mm-diameter were used. The tests were performed in a basin that was 10.7 m long and 3.3 m wide and containing over 90 tons of sand. Strain gages and robotic laser measurements were used for instrumentation. Due to the smaller diameter of the steel pipe, it was possible to wrap the pipe with tactile force sensors across the pipe area in contact with adjacent soil. The HDPE pipelines were 24mm thick, whereas the steel pipe had a wall thickness of 3mm (D/t=50). The pipelines were fixed at the two ends of the test basin by electrofusion couplings that were thermally welded to the pipe and are typically used to join pipe sections. The maximum strike-slip displacement was equal to 1.2m. The angle between the fault trace and pipeline axes was set to 65° for all experiments. Eight specimens were tested in tension strike-slip conditions (including the steel pipe) with one of them pressurized at 500kPa and one in compression conditions. Data produced included strain gage readings, load cell readings, actuator

load data, soil pressuremeter readings, tactile force sensor readings, pipe temperature, test basin deformation, soils density and moisture content, and pipe displacement and deformation. A good agreement between centrifuge and large scale tests results for HDPE pipes was reported.
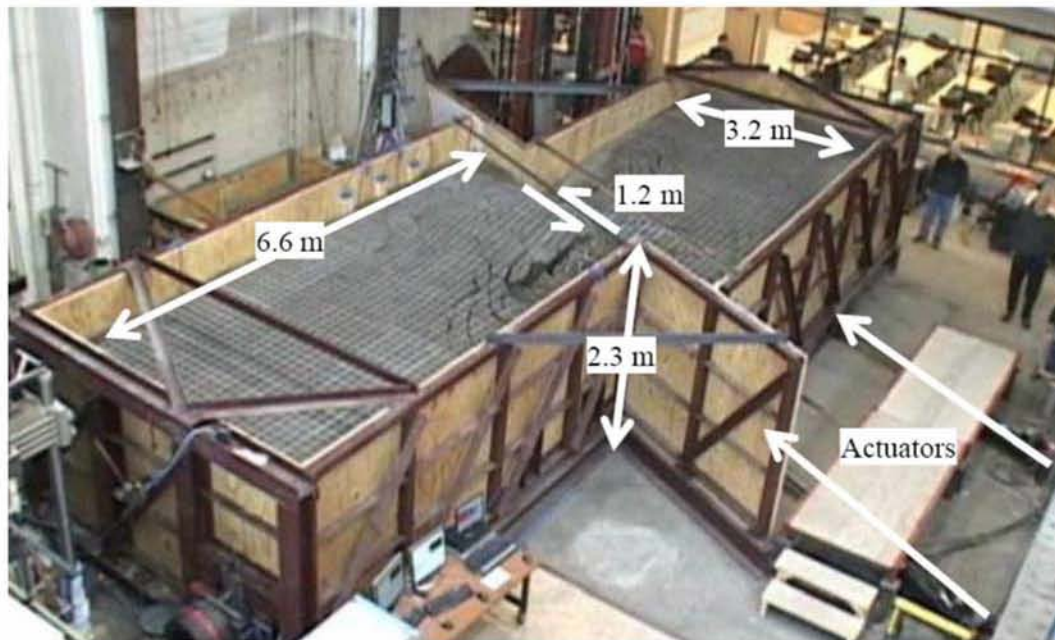

Figure 2.11: Cornell split-box test basin. [39]

Based on the project performed for the San Francisco Public Utilities Commission (SFPUC) for the seismic upgrade of Bay Division Pipelines (BDPLs) 3 and 4, five tests at 1:10 scale were performed to support the design of BDPL 3X by focusing on the behavior of the protective, segmental concrete vault (see Figure 2.12). The prototype length of concrete vault tested was 79.25 and 85.35 m, depending on whether a joint or segment center was centered on the fault. The prototype width, height, and length of the reinforced concrete segments were 6.1m. The fault angle crossing the concrete vault was equal to 50°. Partially saturated sand was used as the soil medium in which the protective vault was embedded. Secant pile walls were simulated in all tests. Sand backfill was placed between the protective enclosure and the secant pile walls for the first two tests, and expanded polystyrene (EPS) pellets were placed between the protective enclosure and the secant pile walls for the last three tests. The joints between segments were fabricated with steel cover plates with a 0.15m gap (prototype scale) between each segment in the first four tests and no cover plates with a 0.30 m gap between segments in the last test. Results indicated that the use of EPS increased the

maximum segment rotation slightly and broadened the distribution. Also, the widest distribution of segment rotation occurred when the segment was centered on the fault, whereas the maximum rotation was measured when no steel cover plates were used.
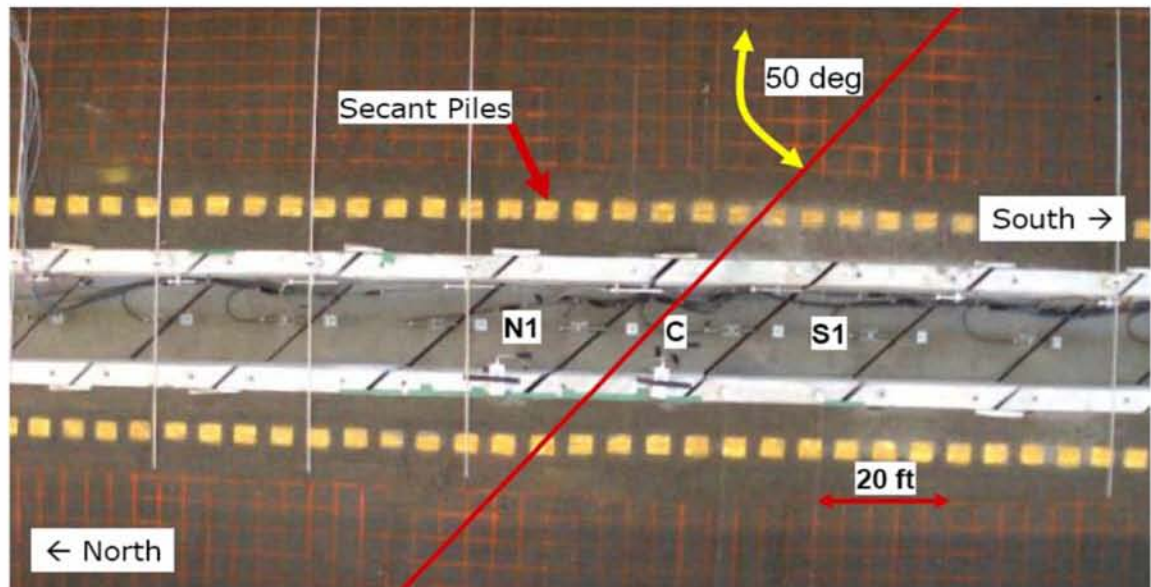

Figure 2.12: Pretest configuration of one of the five tests performed in Cornell, in which the concrete segment is centered at the fault plane. [40]

2.4 Computer programs for numerical analysis

This section provides a short overview of the commercially available soil-pipeline interaction programmes. A description of the different programmes is given, including some advantages and disadvantages.

PLE

Description

PLE is a Computer Aided Design tool for the pipeline design engineer, who has to design and evaluate the strength and stability of buried or partly buried transport pipelines in order to meet safety requirements as they are specified in Pipeline Codes and Regulations. It can be used for either high or low-pressure transmission pipelines for both onshore and offshore applications.

The computer program PLE is a (quasi-1D) finite element program for buried pipelines. The programme uses a pipeline model consisting of a series of loaded beam elements supported by a system of springs. These spring supports represent the soil behaviour surrounding the pipeline, as shown in Figure 2.13. A finite element analysis is performed resulting in the calculation of the overall pipeline behaviour, including displacements, internal forces and soil reactions. The results are given for the centre line of the actual pipeline.

Figure 2.13: Beam model with spring support system. [41]

Based on the results of this beam calculation, the individual cross-sections are analysed to give results for the actual pipeline wall behaviour, including stresses, strains and ovalisations. This is an iterative procedure required to fit the ring behaviour to the calculated beam behaviour (see Figure 2.14).
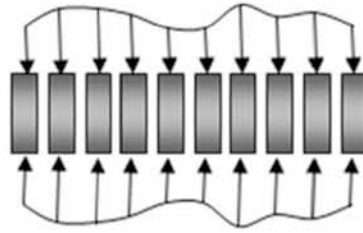
Figure 2.14: Ring model, calculation of actual pipeline behaviour. [41]

Apart from the standard stress-based elastic calculations, PLE can also perform strain-based plastic calculations on the pipelines, based on the theory given in reference [42].

Advantages

+ Specifically developed for buried pipeline assessment;

+ Realistic soil mode, validated by tests;

+ Both elastic (stress-based) and elastic-plastic (strain-based) calculations possible;

+ Built-in check according to several pipeline international standards.

Disadvantages

- Only macro description of pipeline behaviour possible. This means it is not suitable, for example, for pipe behaviour beyond the limit state of local buckling.

- No addition of user defined material models possible.

- No dynamic (time dependent) analyses possible.

CAESAR II

Description

Intergraph Caesar II is a Computer Aided Design tool to evaluate the structural response and stresses of a piping system according to international codes and standards. It is a user friendly software tool, and widely used in the calculation of industrial piping systems. Due to the focus on above ground piping systems the options for buried pipelines are limited.

The program makes use of a pipeline model consisting of a series of loaded beam elements supported by a spring support system. This is comparable to the first step in the calculation method used in PLE.

Advantages

+ User friendly interface.

+ Dynamic (time dependent) analyses possible.

+ Built-in check according to several pipeline international standards.

Disadvantages

- Simplified soil model, not validated by testing.

- Developed for above ground calculations. Limited possibilities only for buried pipeline analyses.

- No check on minimum required element length for accurate simulation of soil – pipeline behaviour.

- No analyses of ring behaviour. Only macro description of pipeline behaviour possible (i.e., local buckling cannot be considered).

- No elastic/plastic calculations possible.

ABAQUS

Description

ABAQUS is a general purpose finite element package which contains an extensive library of elements that can model virtually any geometry. It is equipped with various different material models to simulate the behavior of most typical engineering materials including metals, rubber, polymers, composites, reinforced concrete, and geotechnical materials such as soils and rock. Designed as a general-purpose simulation tool, Abaqus can be used to study structural (stress/displacement) problems, and perform simulations of heat transfer, mass diffusion, soil mechanics (coupled pore fluid - stress analyses), etc. Abaqus offers a wide range of capabilities for simulation of linear and nonlinear applications. Problems with multiple components are modeled by associating the geometry defining each component with the appropriate material models and specifying component interactions. In a nonlinear analysis it chooses automatically appropriate load increments and convergence tolerances and continually adjusts them during the analysis to ensure that an accurate solution is obtained efficiently. Static as well as dynamic analysis can be performed using either implicit or explicit analysis.

Advantages

+ Full 3D soil-structure interaction analyses possible;

+ User defined material models possible;

+ Dynamic (time dependent) analyses possible.

Disadvantages

- *Pipeline specific* standards are not included but may be added as user subroutines.

FLAC3D

Description

FLAC3D is a numerical modeling code for advanced geotechnical analysis of soil, rock, and structural support in three dimensions. It is used in analysis, testing, and design by geotechnical, civil, and mining engineers. FLAC3D is designed to accommodate any kind of geotechnical engineering project where continuum analysis is necessary. FLAC3D utilizes an explicit finite difference formulation that can model complex behaviors not readily suited to FEM codes, such as: problems that consist of several stages, large displacements and strains, non-linear material behavior and unstable systems, including cases of yield/failure over large areas, or total collapse.

Advantages

+ Full 3D soil-structure interaction analyses possible;
+ User defined material models possible;
+ Dynamic (time dependent) analyses possible.

Disadvantages

- *Pipeline specific* standards are not included but may be added as user subroutines.

PLAXIS 3D

Description

PLAXIS 3D is a finite element package intended for three-dimensional analysis of deformation and stability in geotechnical engineering. It is equipped with features to deal with various aspects of complex geotechnical structures and construction processes.

In addition, since soil is a multi-phase material, special procedures are required to deal with hydrostatic and non-hydrostatic pore pressures. Although PLAXIS 3D uses a Mohr-

Coulomb elastoplastic soil model, in its present form is not capable of giving realistic results for large soil displacements associated with plastic soil behaviour and failure.

Although the modelling of the soil itself is an important issue, many projects involve the modelling of structures and the interaction between structures and soil. An example of the possibilities of Plaxis 3D is shown in Figure 2.15.
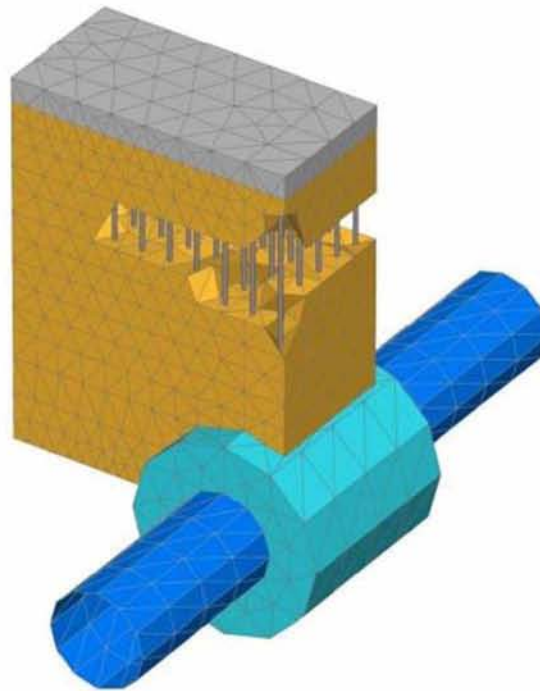

Figure 2.15: Example of the possibilities of Plaxis 3D [www.plaxis.nl].

Advantages

+ Full 3D soil-structure interaction analyses possible;
+ User defined material models possible;
+ Dynamic (time dependent) analyses possible.

Disadvantages

- Not suitable for large displacements / pipeline deformations (only elastic pipe deformations).

2.5 Strain based design

In steel pipelines several limit states have to be considered. The most important ones for onshore buried steel pipelines are the following:

- Burst caused by too high internal pressure.
- Cracking due to applied strains exceeding the ductility of the tube wall, including weld zones with possible areas of low ductility in combination with weld discontinuities (caused by bending and/or tensile strain).
- Local buckling caused by too large imposed curvature (caused by bending and/or compressive strain).
- Flattening due to combinations of external soil loads and bending.

Pipeline design for internal pressure is quite straightforward: the hoop stress must not exceed the limit stress as given in the applicable standard. Other loads do not influence the burst pressure provided that the steel behaves in a ductile manner and the imposed deformations are within certain limits (Gresnigt, 1986) [42].

Similarly to buried pipelines in settlement areas, pipelines subjected to seismic loads are mainly deformation-controlled and their deformation capacity is the governing criterion for safety. The deformation capacity may be limited by the occurrence of the limit-state cracking or local buckling.

Design for these limit states requires appropriate models for describing the moment-curvature behaviour till (cracking or local buckling) failure. Figure 2.16 shows both the behaviour under pure bending and under bending combined other loads causing extra ovalisation (thereby reducing the compressive strain at which local buckling occurs). The critical curvature ΔC_{cr} is also indicated in the figure.
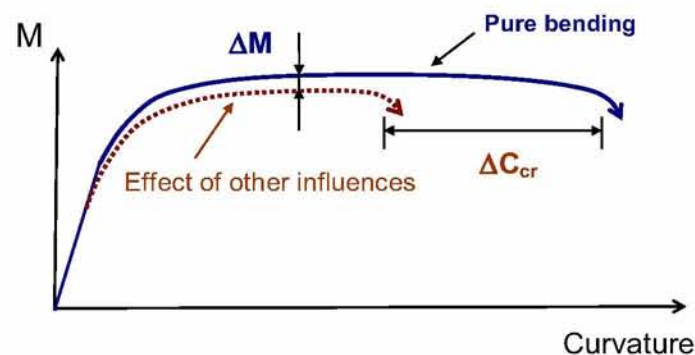

Figure 2.16: Moment-curvature diagrams for relatively thick-walled pipes (e.g. D/t=50).

Strain-based design focuses on the pipe deformation. Once the maximum curvature is determined, the forces in the cross-section can be calculated on the basis of the calculated strain distribution in the cross-section and the calculated ovalisation due to bending and soil loads. This enables the best description of the pipeline behaviour up to failure.

Looking only at the forces (stress-based design) enables accurate description only up to the maximum load, but it does not provide satisfactory information for the deformation-controlled situations as in seismic design and design for landslides. Furthermore, in case of thick-walled pipes, the maximum bending moment can be restrained over a rather long segment of the moment-curvature curve (see Figure 2.16). A small deviation in bending moment can then result in a very large increase in deformation.

2.6 Standards

There is a wide range of standards available which can be used for the design of pipelines. Some of the standards are applicable to all steel pipelines, while others refer to a specific use such as gas, hydrocarbon or water transportation. Most of the following documents incorporate the strain-based design approach:

- EN 1594 Gas supply systems – Pipelines for maximum operating pressure over 16 bar – Functional requirements[68]
- NEN 3650 Requirements for pipelines systems [51]
- ASME B31.8 Gas Transmission and Distribution Piping Systems [56]
- ASME B31.4 Pipeline Transportation Systems for Liquid Hydrocarbons and Other Liquids [55]
- AWWA M11 Steel Water Pipe: A Guide for Design and Installation[69]
- ALA 2005 Guidelines for the Design of Buried Steel Pipe[70]
- EN805 Water supply – Requirements for systems and components outside buildings[71]
- EN13480 Metallic industrial piping – Part 3: Design and calculation[72]
- EN14161 Petroleum and natural gas industries – Pipeline transportation systems[73]
- EN1993-4-3 Design of steel structures – Part 4-3: Pipelines[74]
- EN1998-4 Design of structures for earthquake resistance – Part 4: Silos, tanks and pipelines [46]
- DNV-OS-F101 Offshore Standard OS-F101, Submarine Pipeline Systems[75]

- CSA Z662-07 Oil and gas pipeline systems [44]

EN 1594: Gas supply systems – Pipelines for maximum operating pressure over 16 bar – Functional requirements

The structural analysis of the pipeline is primarily based on stress design: *"The calculation method is based on determination of stresses caused by loads during the construction and operation phases. The stresses are combined to resultant stresses (σ_v). No resultant stress shall exceed the relevant allowable stress"* (EN1594).

In the annexes, some extra information is given on the design in case of designing a pipeline in settlement areas, areas of mining subsidence, frost heave, landslide areas and areas of high seismic risk. These annexes give some notion of the use of strain-based design by suggesting the use of *"large displacement theory"* since *"conventional small-displacement beam bending theory is generally inappropriate"* for some of these cases. Further guidance is only given by referring to a number of limit states, which must not be exceeded, with respect to stress, strain and deformation.

It can thus be concluded that EN 1594 in principle does not include strain-based design, but does not forbid the use of it for pipes subjected to ground-induced actions. Generally the new EN 1594:2008 Standard is the main reference for the design of high-pressure (e.g. gas) supply systems, complementing codes of practice and operating manuals in the member countries. It describes general functional requirements (design, construction, operation and related aspects of safety, environment and public health) for gas supply through steel pipe systems for maximum operating pressure greater than 16 bar. It provides indications (in informative form) for pipeline design against "geohazards" (e.g. settlement and landslide areas, high seismic risk, etc.) and qualitative provisions, and refers to rather old research publications.

NEN 3650: Requirements for pipelines systems

The recently (2012) updated NEN 3650 includes an annex on the application of plasticity in structural design of pipelines, which is based on earlier publication in Heron (Gresnigt, 1986, [42]). The model includes the full moment curvature behaviour of a pipeline, including the effects of ovalisation and external earth pressure on two sides of the pipeline. Various limit states are given, which are also quantified with design formulas. For the axial tensile and compressive strains, limits have been stated that are independent of the accompanying stresses.

The use of strain-based design is encouraged in NEN 3650. Part 1 (General), and Part 2 (Steel Pipes) contain useful information for the consideration of the ground conditions in buried pipeline analysis and design. Nevertheless, those provisions focus mainly on differential settlements and refer to normal design practice and not extreme ground-induced actions.

ASME B31.8: Gas Transmission and Distribution Piping Systems

The ASME code is in principle stress-based, but also includes an alternate strain-based design in cases in which the pipeline experiences a predictable non-cyclic displacement of its support, e.g. in case of fault movement along the pipeline route, pipe sag before support contact or differential subsidence along the pipeline. The permissible maximum longitudinal strain should be determined based on ductility, eccentricity, out-of-roundness, etc. Local buckling and ovalisation are specifically mentioned to be incorporated in design, however the analysis of these effects is left to the designer.

ASME B31.4: Pipeline Transportation Systems for Liquid Hydrocarbons and Other Liquids

With regard to strain-based design approach, this code is similar to the ASME B31.8. In principle a stress-based design is used, but for non-cyclic deformation-controlled loads a strain-based design is allowed. Actual limit values for the strain (tensile or compressive) are not specified.

AWWA M11: Steel Water Pipe: A Guide for Design and Installation

This code specifically mentions the advantages of strain-based over stress-based design, and specifies maximum strains in the pipe wall that have been found in practice. Applications such as earth loading are specifically mentioned in this context. The code recognises the advantages a strain-based design can offer, but is lacking in-depth design information. It should be noted that AWWA (2004) M11 provisions do not cover the issue of ground-induced actions on buried steel pipelines.

ALA 2005: Guidelines for the Design of Buried Steel Pipe

The occurrence of a fault displacement, landslide displacement or earthquake displacement is specifically mentioned, and possible evaluation techniques are discussed. The use of strain limits instead of stress limits is encouraged. Simple design formulas are not specified, but reference is made to the use of 3D finite element programs, such as ANSYS or ABAQUS, or the use of specialized 2D software. For

permanent ground-induced deformations, numerical analysis is proposed, assuming nonlinear Winkler-type elements to model the effects of soil on the pipe, which is modelled as a beam. The use of strain-based design in case of large ground induced is encouraged.

EN805: Water supply – Requirements for systems and components outside buildings

EN805 prescribes the inclusion of *"the effects of potential hazards such as ground movements and/or earthquakes"* in the design and mentions the definition of a *"flexible pipe"* in which case the load carrying capacity is limited by deformation (e.g. strain). It should be noted that clear rules for design of pipelines are not provided. Although strain-based design is not excluded, the provided information is insufficient for its direct application.

EN13480: Metallic industrial piping – Part 3: Design and calculation

EN13480 considers a stress-based design approach, since: *"Elastic calculation methods shall be used in this Part, although some components might exhibit plastic behaviour"*. Even under displacement-controlled actions, elastic behaviour is assumed and plastic behaviour of pipelines is to be avoided. Strain-based design is not incorporated in this code.

EN14161: Petroleum and natural gas industries – Pipeline transportation systems

EN14161 both allows stress- and strain-based design, but does not specify calculation methods for the latter. The strain-based design is only to be used for deformation controlled situations such as earthquakes and landslides. Reference to BS7910 is made for determining the level of permissible strain. This code is primarily based on assessing the acceptability of flaws in metallic structures. The use of a real stress-strain curve is mentioned, but it is applied only to the analysis of flaws in the structure. The code does not exclude strain-based design methods, but its use is not encouraged. Any reference to strain-based design seems to be aimed at a maximum tensile strain in relation to metallic flaws, without any consideration of compressive-strain limits associated to local buckling.

EN1993-4-3: Design of steel structures – Part 4-3: Pipelines

EN1993-4-3 includes design rules to determine the bending moment curvature behaviour up to failure, including values for the various limit states. Analysis of the moment-curvature relationship and local buckling is very similar to NEN3650.

EN1998-4: Design of structures for earthquake resistance – Part 4: Silos, tanks and pipelines

EN1998-4 considers that *"welded steel pipelines exhibit significant deformation and dissipation capacity, provided that their thickness is sufficient"* for above ground pipelines. A limit-strain for underground pipelines subjected to a seismic fault movement is stated as 3% for tensile strain and the lower value of 1% and 20t/R, where t = thickness and R=radius, for compressive strain. Some general measures for mitigating seismic fault movement effects are also stated. This standard allows the use of strain-based design, but includes far less information than EN1993-4-3 and NEN3650.

DNV-OS-F101: Offshore Standard - Submarine Pipeline Systems

In this standard, strain-based design rules are adopted. An important observation is that DNV has two sets of design rules: one for load-controlled and another for deformation-controlled situations.

CSA Z662-07: Oil and gas pipeline systems

Z662-07 includes design rules to determine values for the various limit states. Generally is a stress-based design, but a strain-based approach can be used for pipeline operations, provided that pipeline deformations arise from non-cyclic displacement-controlled events such as permanent ground deformation or support movement due to environmental load events. The strain-based approach may also be used when pipeline displacements are bounded by fixed geometric constraints.

In summary, a part of the current pipeline standards acknowledge the benefits of strain-based design, and in some cases even clear design rules are stated (e.g. NEN 3650, EN1993-4-3). The effects of ground induced deformations in case of fault movements and landslides are not specifically discussed in most aforementioned standards. In the case of ALA (2005) in which they are discussed, the designer is referred to 3D FE analysis, which will be most likely too complex for daily design practice.

2.7   Performance criteria for buried steel pipelines

The main design requirement of a gas pipeline is safety against loss of containment. Under strong permanent ground-induced actions, buried steel pipelines exhibit severe deformation beyond the elastic limit. Steel material is ductile and capable of sustaining significant amount of inelastic deformation, but at locations where large tensile strains develop, rupture of the pipeline wall may occur. Wrinkling (local buckling) of pipeline

wall may also occur due to excessive compression at the pipeline wall, followed by pipe wall folding and development of significant local strains. Furthermore, severe distortions of the pipeline cross-section may render the pipeline non-operational.

To quantify the amount of damage in a buried pipeline under severe ground-induced action, appropriate performance criteria (quite often referred to as "limit states"), should be adopted. One should note that pipeline design has been traditionally based on the "allowable stress" concept. However, in the case of extreme ground-induced loading conditions, which act on the pipeline under deformation-controlled conditions, the pipeline exhibits significant inelastic deformation. Therefore, pipeline performance should be addressed in terms of limit states based on strain or deformation, rather than stress. Based on the above discussion, the following performance limit states are described and quantified below: (a) tensile strain in the longitudinal direction of the pipeline that causes pipe wall rupture, (b) local buckling (wrinkling) formation, and (c) excessive distortion of the pipeline cross-section.

(a) Maximum tensile strain

Determination of tensile strain capacity of a pipeline is of primary importance for establishing an efficient strain-based pipeline design procedure. In the absence of serious defects and damage of the pipeline, the tensile capacity is controlled mainly by the strength of the girth welds, which are usually the weakest locations due to weld defects and stress/strain concentrations. Tensile strain limits are experimentally determined through appropriate tension tests on strip specimens and in wide plates [43]. For design purposes, a simple and straightforward approach for determining tensile strain limit of girth welds in pipeline is provided by CSA Z662 pipeline design standard, Annex C [44], through the following equation that considers surface-breaking defects:

$$\varepsilon_{Tu} = \delta^{(2.36-1.583\lambda-0.101\xi\eta)} \left(1+16.1\lambda^{-4.45}\right)\left(-0.157+0.239\xi^{-0.241}\eta^{-0.315}\right) \quad (2.9)$$

where, ε_{Tu} is the ultimate tensile strain capacity in %, δ is the CTOD toughness of the weld ($0.1 \leq \delta \leq 1$), λ is the yield-to-tensile strength ratio ($0.7 \leq \lambda \leq 0.95$), ξ is the ratio of defect length over the pipe-wall thickness ($2c/t$) with $1 \leq \xi \leq 10$, and η is the ratio of defect height over the pipe-wall thickness (a/t) with $\eta \leq 0.5$. Background information for equation (2.9) can be found in the paper by Wang et al. [45]. Considering a slightly defected pipe, with $\xi = 1.0$, $\eta = 0.1$, $\delta = 0.7$ and $\lambda = 0.775$, one obtains a

value of ε_{Tu} = 4.5%. In the following, two values for the ultimate tensile strain ε_{Tu} are considered, namely 3% and 5%. It is noted that the first value is also adopted by the EN 1998-4 provisions for seismic-fault-induced action on buried steel pipelines [46] and by the seismic provisions of ASCE MOP 119 for buried water steel pipelines [47].

<u>(b) Local buckling</u>

Under ground-induced actions, along with the development of tensile strains on the pipeline wall, compressive strains (due to pipe bending deformation) may also occur. When compressive strains exceed a certain limit, the pipeline wall exhibits structural instability in the form of local buckling or wrinkling. In the presence of those "wrinkles" or "buckles", the pipeline may still fulfill its transportation function, provided that the steel material is adequately ductile [47]. However, the buckled area is associated with significant strain concentrations and, in the case of repeated loading (e.g. due to variations of internal pressure or temperature), fatigue cracks may develop, imposing a serious threat for the structural integrity of the pipeline [48],[49]. Therefore, the formation of a local buckle or wrinkle can be considered as a limit state. Extensive research on axial compression and bending of steel pipe segments has demonstrated that compressive strain limits for steel pipes depend on the diameter-to-thickness ratio (D/t), the yield stress of steel material σ_y, the presence of internal or external pressure, as well as the initial imperfections and the residual stresses (caused by the manufacturing process). A brief overview of this research is presented in a recent paper of Gresnigt and Karamanos [50]. Some typical formulations for the prediction of critical compressive strains are reported in the following equations (2.10) to (2.15) in which the various terms are:

- D, t: Outer diameter and wall thickness;
- UF: usage factor which is the ratio between the hoop stress and the SMYS (Specified Minimum Yield Strength);
- Y: yield strength;
- E: Young modulus.

DNV-OS-F101 (DNV-2000):

$$\varepsilon_C\left(\frac{D}{t}, p_{min} - p_e\right) = 0.78 \cdot \left(\frac{t}{D} - 0.01\right) \cdot \left(1 + 5.75 \cdot \frac{p_{min} - p_e}{p_b(t)}\right) \cdot \alpha_h^{-1.5} \qquad \left(\frac{D}{t} \le 45\right) \qquad (2.10)$$

ZIMMERMAN 1995:

$$\varepsilon_C\left(\frac{D}{t}, UF, Y\right) = 8.5 \cdot \left(\frac{t}{D}\right)^2 + 34 \cdot \left(120 - \frac{D}{t}\right) \cdot \left(\frac{UF \cdot Y}{E}\right)^2 + 0.0021 \qquad \left(30 \le \frac{D}{t} \le 100\right) \qquad (2.11)$$

GRESNIGT 1986:

For $t/r' < 60$: $\qquad \varepsilon_{cr} = 0.25\frac{t}{r'} - 0.0025 + 3000\left(\frac{Pr}{Et}\right)^2 \cdot \frac{|P|}{P}$ $\qquad (2.12)$

For $t/r' \ge 60$: $\qquad \varepsilon_{cr} = 0.10\frac{t}{r'} + 3000\left(\frac{Pr}{Et}\right)^2 \cdot \frac{|P|}{P}$ $\qquad (2.13)$

with: $\qquad r' = \dfrac{r}{1 - \dfrac{3a}{r}}$

where a is the ovalisation due to bending and other loads such as earth pressure, as indicated in Figure 2.17.

or

$$\varepsilon_C\left(\frac{D}{t}, UF, Y\right) = 0.5 \cdot \left(\frac{t}{D}\right) - 0.0025 + 3000 \cdot \left(\frac{UF \cdot Y}{E}\right)^2 \qquad (2.14)$$

or

$$\varepsilon_{Cu} = 0.5\left(\frac{t}{D}\right) - 0.0025 + 3000\left(\frac{\sigma_h}{E}\right)^2 \qquad (2.15)$$

where the hoop stress σ_h depends on the level of internal pressure p:

$$\sigma_h = \begin{cases} \dfrac{pD}{2t}, & if\ \dfrac{pD}{2t\sigma_y} \le 0.4 \\[4mm] 0.4\sigma_y, & if\ \dfrac{pD}{2t\sigma_y} > 0.4 \end{cases} \qquad (2.16)$$

Equation (2.15) has been initially proposed in [42] and has been adopted by the recent CSA Z662 specification [44].
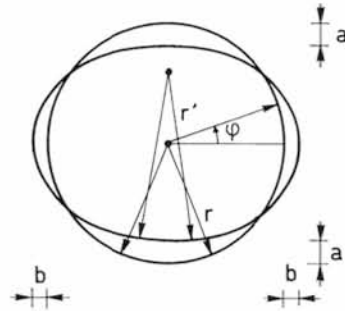
Figure 2.17: Ovalisation of pipe cross-section and radius r′ to be used in the design rules.

The predictions of the various formulations are compared with experimental results in Figure 2.18 for the unpressurized tests. Dashed lines represent the field where the formulation is out its validity. More complex is the comparison of pressurized experimental tests with critical-strain prediction formulae due to a large variety of different pressure levels and a low number of available test data. Figure 2.19 compares critical compressive-strain results from tests that have a usage factor UF > 0.5 to those derived from formulations adopting a usage factor equal to 0.74, i.e. an average value obtained from the experimental tests. In the formulations, when internal pressure is present, the yield strength has also some effect. For example, the DNV (Det Norske Veritas) formulation takes into account the Y/T (yield to tensile) ratio effect on the buckling strain through a coefficient $\alpha_h^{-1.5}$, where α_h is the maximum allowable Y/T ratio, set equal to 0.92.

(c) Distortion of pipeline cross-section

In order to maintain the pipeline operational, it is necessary to avoid significant distortions of the pipeline cross-section. A simple and efficient measure of cross-sectional distortion is ovalization, quantified through the so-called non-dimensional "flattening parameter" f defined as follows:

$$f = \frac{\Delta D}{D}$$

(2.17)

Following the suggestion in [42], a cross-sectional flattening limit state is reached when the value of the above parameter f becomes equal to 0.15, a value also adopted by the Dutch specification NEN 3650 [51].

40
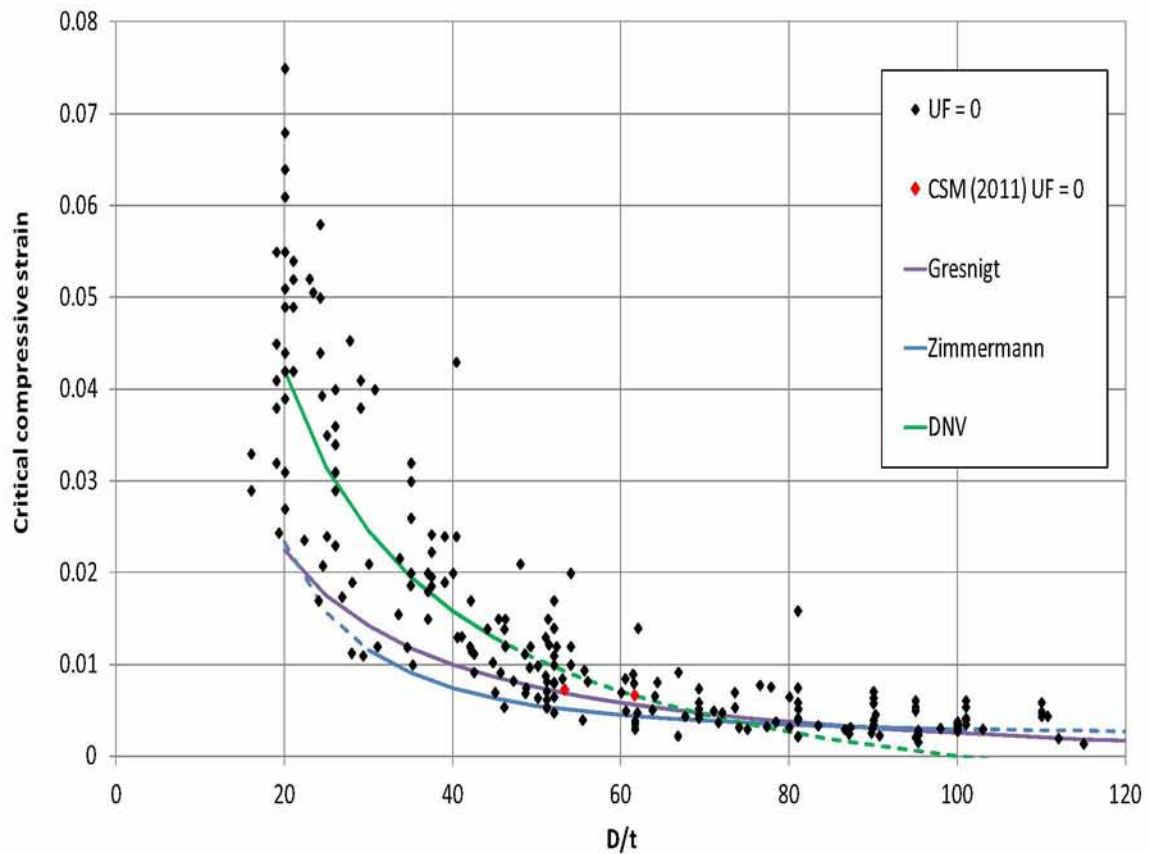
Figure 2.18: Unpressurized tests results and formulae predictions
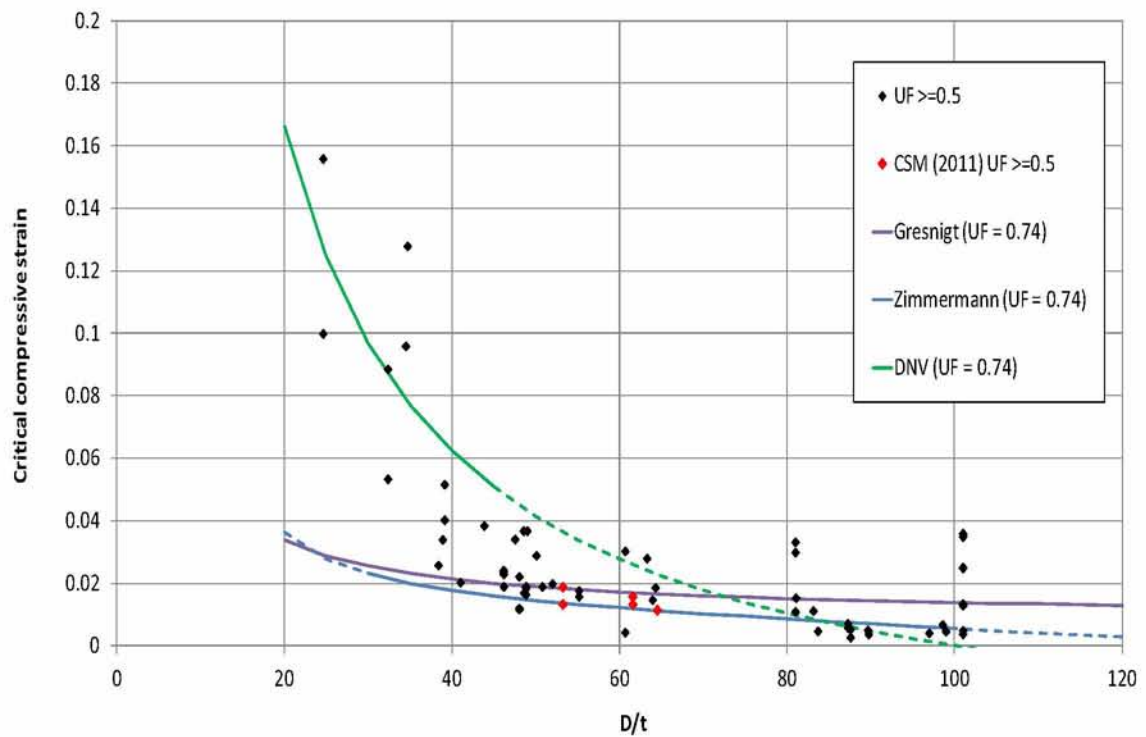
Figure 2.19: Pressurized tests results and formulae prediction

2.8   Scope of the present dissertation

The above overview indicates that current tools for stress analysis of buried steel pipelines are mainly based on rather simplified models. These tools refer to normal design practice and do not consider significant plastic deformations due to exceptional ground-induced actions. It is evident that there is a lack of well-defined methodologies for pipeline analysis and design under extreme ground-induced actions. It is further noted that limited research has been devoted so far in the determination of strain demand in complex soil environments. This need has been recognized by the pipeline industry [67], [12], and requires further research with the collaboration of various engineering disciplines (geotechnical, structural, mechanical, manufacturing, etc.), so that efficient design tools are developed within a strain-based pipeline design framework, amending existing design standards.

An integrated approach for buried steel pipelines crossing strike-slip faults (crossing the vertical fault plane at various angles) is presented here through a finite element modelling of the soil-pipeline system, which accounts rigorously for the inelastic behaviour of the surrounding soil, the interaction and the contact between the soil and the pipe (including frictional contact and the development of gap), the development of large inelastic strains in the steel pipeline, the distortion of the pipeline cross-section, the presence of internal pressure and the possibility of local buckling.

A new closed-form mathematical solution of equivalent nonlinear springs representing finite or infinitely long pipeline segments is combined with a rigorous numerical methodology, as presented before, allowing an efficient and accurate numerical methodology. Although the developed mathematical solution is applied to investigate the behaviour of pipelines crossing strike-slip faults, it is directly applicable also to normal and transverse faults, as well as to buried pipelines subjected to landslides, settlement, etc.

The mechanical behaviour of buried steel pipelines with respect to appropriate performance criteria, expressed in terms of local strain or cross sectional deformation are also examined. The fault displacements corresponding to those performance criteria are identified, in the framework of a performance-based pipeline design employing an infinite or a finite model length via the non-linear springs. Pipes from two steel grades (X65 and X80), widely used in buried pipeline applications, are considered for typical values of diameter-to-thickness ratio D/t (ranging from 57.6 to 144), in both cohesive and non-cohesive soils. The angle β between the fault plane and the perpendicular plane to the pipeline axis considers both positive and negative values (pipe in tension and

compression, respectively) from 45° to -10°. The behaviour of pressurized pipes with respect to non-pressurized pipes is also examined in terms of each of the performance criteria.

3 Numerical Modeling

3.1 Introduction

This chapter presents a description of the finite element model employed for the investigation to the problem of a typical buried pipeline, subjected to a strike-slip fault movement. A schematic representation of the buried pipeline subjected to oblique strike-slip fault movement is illustrated in Figure 3.1. The directions of the pipeline axis and the normal vector to the fault plane form an angle β, which may take either positive or negative values depending on the relative movement of the two soil blocks. In particular positive values of the angle β impose tension on the pipeline, whereas negative values impose compression. Two typical numerical (finite element) models for the pipeline-soil system are portrayed in Figure 3.2: (a) for a pipeline perpendicular to the fault corresponding to β equal to zero and (b) for an oblique strike-slip fault forming an angle $\beta = 25°$.
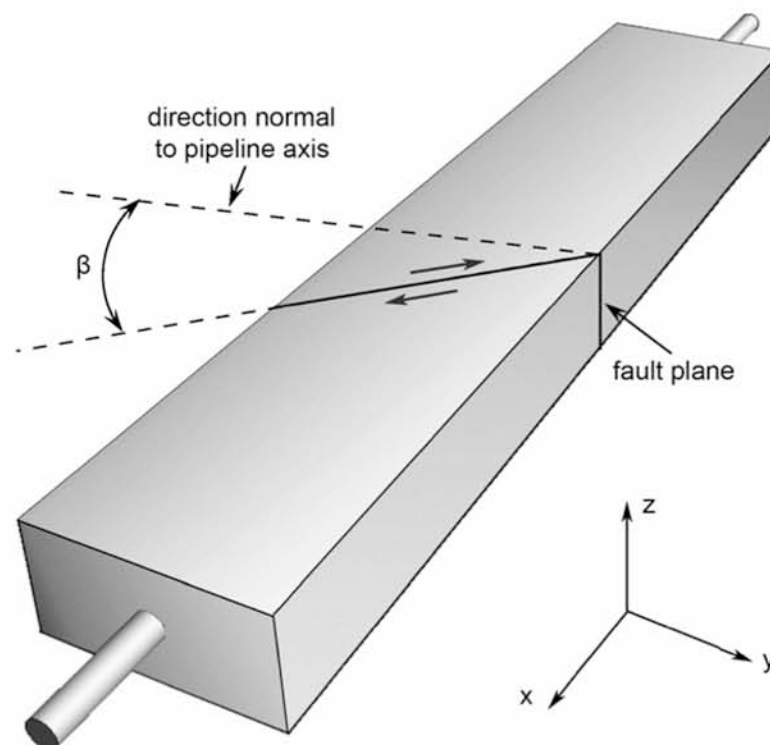
Figure 3.1: Schematic representation of a buried pipeline subjected to oblique strike-slip fault movement. The angle β is defined between the direction of the pipeline axis and the normal to the fault plane.
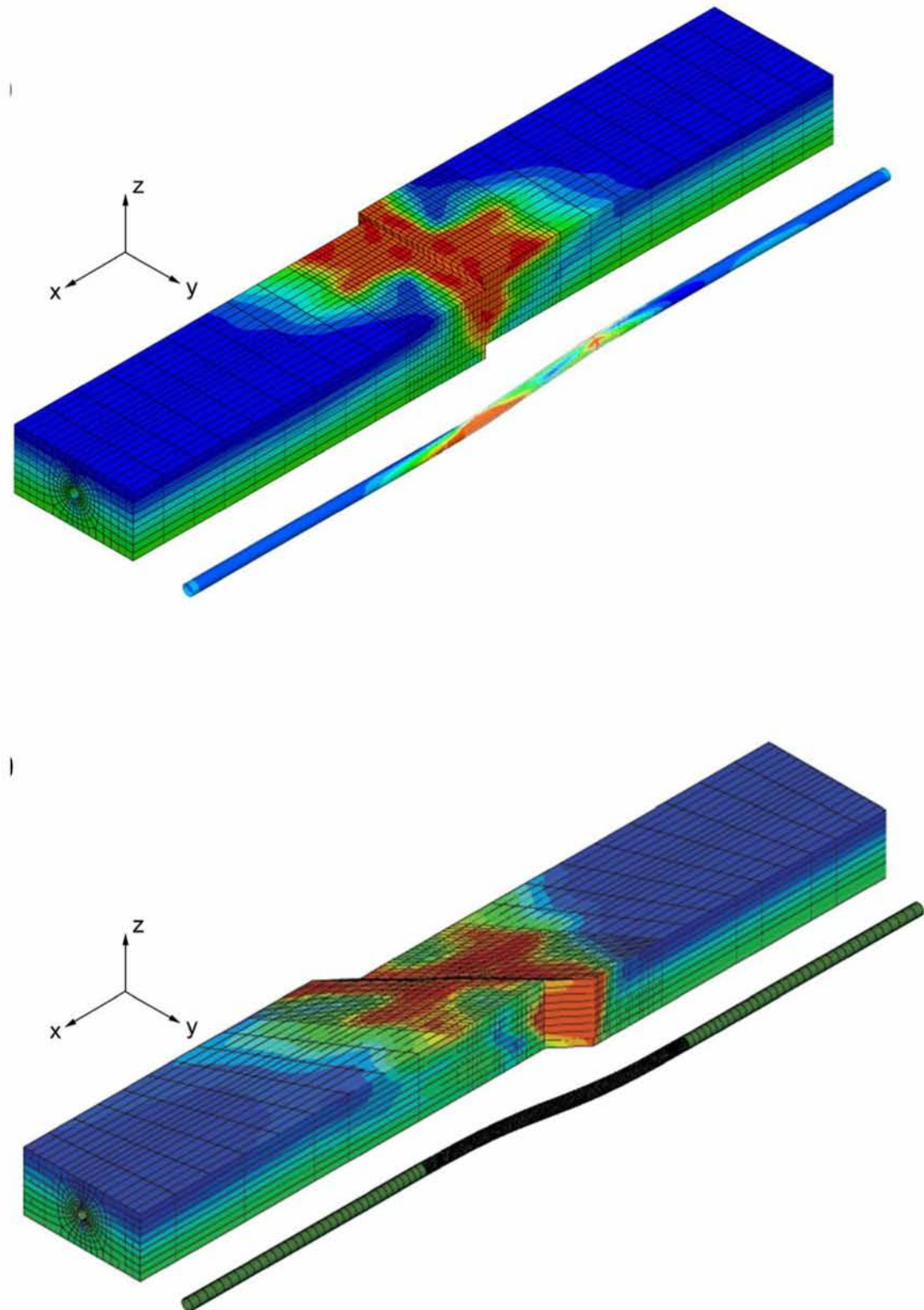
Figure 3.2: Finite element discretization of the soil prism with tectonic strike-slip fault crossing pipeline at an angle (a) $\beta = 0°$ and (b) $\beta = 45°$

For all cases investigated in the present research the soil, pipe and fault behavior are modeled using finite elements. As stated above, the fault movement may occur in a direction that induces tension to the pipeline for $\beta>0$ (Figure 3.2b) or compression for $\beta<0$, as shown in Figure 3.3.

The interaction between the soil and the pipe is considered through a contact algorithm. Several parametric studies have been conducted concerning the dimensions of the finite element model, the width of the fault and the appropriate interface friction coefficient μ between the outer surface of the steel pipe and the surrounding soil, and are presented in the following sections. The numerical model has a basic length in the longitudinal x-direction (Figure 3.1), which is discretised using solid brick and shell finite elements in order to simulate correctly the complex soil-pipeline interaction phenomena during fault movement. Apart from this basic length represented with finite elements, the rest of the model length can be simulated with nonlinear springs that can simulate the effect of a finite or infinite-length soil-pipeline system, which may be subjected to tension during fault movement.

In summary, the model consists of (a) the pipeline segment represented through finite elements surrounded by the soil (also modelled with finite elements) and (b) two nonlinear springs at the two pipeline ends representing the continuity of the pipeline outside the pipeline segment under consideration. This length of the pipeline outside the analysed segment can be finite or infinite depending on the specific characteristics of the problem. In case where a discontinuity or constraint exists, such as the presence of a service station along the pipeline, a finite length can be considered assuming no displacement at the service station.

The performance of pipelines subjected to permanent strike-slip fault movement depends on the aforementioned end-conditions of the pipeline. To optimize the efficiency of the finite element model, a closed-form solution is developed to represent the pipe-soil behaviour at the two ends of the basic finite element model. This analytical solution takes into account in an accurate manner the interaction between the pipe and soil, considering the elastic-inelastic behaviour of the interface of a pipeline segment subjected to pure tension (pipeline pull-out test). This solution is used to determine the force-displacement curve of nonlinear springs at the two ends of the pipeline. Using a series of refined finite-element models corresponding to different soil-pipe systems and different strike-slip fault conditions, allows for an efficient nonlinear analysis and improved understanding of the behaviour of the pipe-soil system under large fault movements.
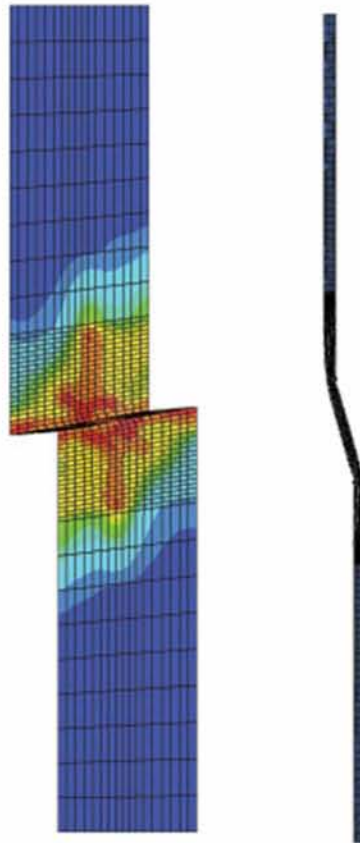
Figure 3.3: Finite element discretization of the soil prism with tectonic strike-slip fault crossing pipeline at a negative value of angle $\beta = -10°$ (plan view)

In Section 3.2, a description of the model used for simulating the soil-pipe behaviour subjected to strike-slip faulting is given. In Sections 3.3 and 3.4, the nonlinear spring force-displacement expressions for infinitely-long and finite-length pipelines, respectively, subjected to pure tension are derived. These closed-form analytical expressions are used in Section 3.5 to present results for axially-loaded pipes embedded into the soil. In Section 3.6, the efficiency and accuracy of the proposed nonlinear springs for the strike-slip fault problem is examined by comparing the results with those from beam-elements supported by distributed springs. The sensitivity of the numerical results with regard to mesh refinement is examined in Section 3.7. Finally, the effects on the size of the soil prism that surrounds the embedded pipeline are investigated in Sections 3.8 and 3.9.

3.2 Finite element model description

The response of the pipeline under strike-slip fault movement is examined numerically using the finite element program ABAQUS [53]. The pipeline is embedded in an elongated soil prism along the x axis shown in Figure 3.4a. Figure 3.4b shows the soil mesh in the y-z plane and Figure 3.4c depicts the mesh for the steel pipe. Similar finite models are used when the pipe is crossing a fault at an angle β different than zero degrees. A typical configuration of such a model is depicted in Figure 3.5.

Four-node reduced-integration shell elements (S4R) are employed for modelling the cylindrical pipeline segment and eight-node reduced-integration "brick" elements (C3D8R) are used to simulate the surrounding soil. The finite-strain elements S4R used are capable of accounting for finite membrane strains and arbitrarily large rotations. Therefore, they are suitable for large strain analysis. The C3D8R solid elements are suitable for stress/displacement analyses and provide accurate results.
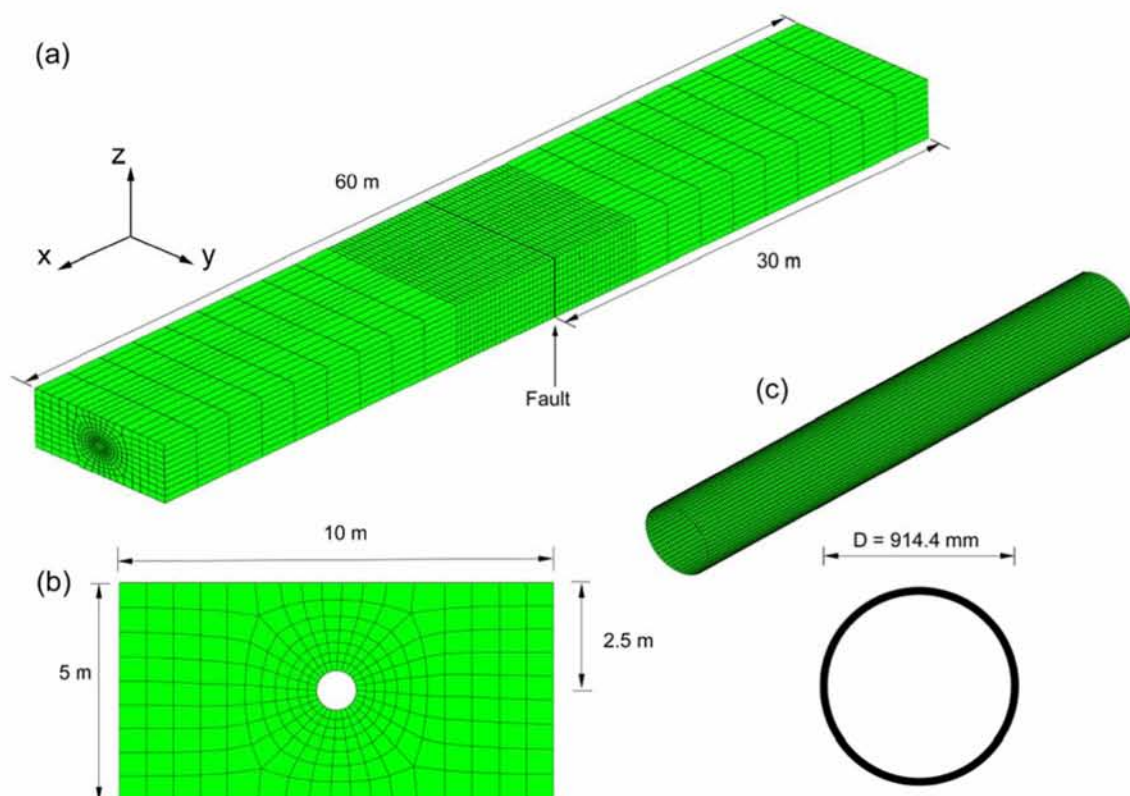
Figure 3.4: Finite element model of the (a) soil prism with tectonic strike-slip fault, (b) finite element mesh of soil prism cross-section and (c) refined finite element mesh of steel pipeline. Fault angle β=0°.
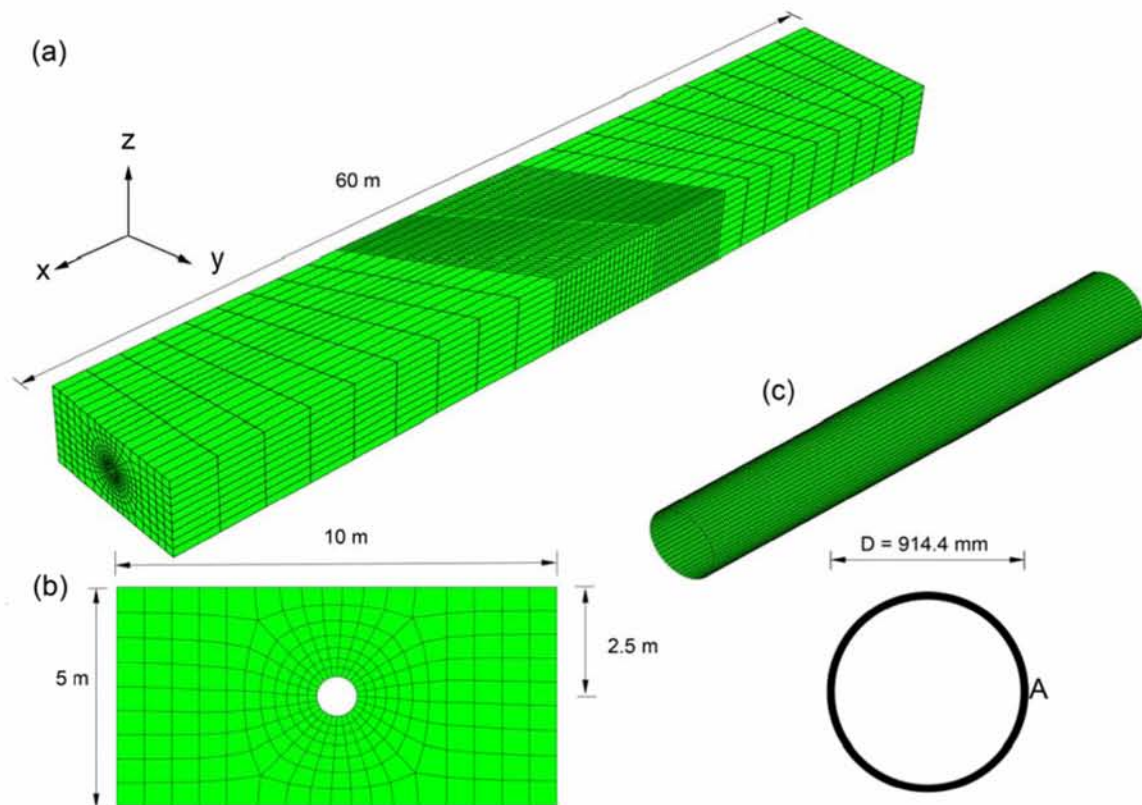
Figure 3.5: Finite element model for a 36-inch buried pipeline (a) soil prism with tectonic strike-slip fault, (b) finite-element mesh of soil prism cross-section and (c) finite-element mesh of steel pipeline. Fault angle $\beta > 0°$.

The top surface of the prism represents the soil surface, and the embedment depth is chosen equal to about 2 pipe diameters, which is in accordance with pipeline engineering practice. The soil prism length in the x direction is equal to at least 65 pipe diameters, whereas its dimensions in directions y and z are equal to 11 and 5 times the pipe diameter, respectively. These are the minimum dimensions that can be used in directions x, y, z, in order to have an effective numerical model, with no significant effect on the accuracy of the results. The above values were determined after an extensive parametric study which showed that for model dimensions larger than those, no influence is shown in the results. For the x direction, the value of 65 diameters is considered as a safe value regarding the length of the finite-element model in order to analyse accurately the pipe-soil interaction in the near-fault region. However, the pipeline length outside this basic model should be taken into consideration to account properly for the effect of the actual boundary conditions of the physical problem. An efficient way of doing this is by using equivalent nonlinear springs, derived in the next sections. So, for the case of finite model length, the appropriate (finite model) spring is employed, setting the total model length equal to the length of the actual soil-pipeline

system. If the desired actual length is the same with finite element model length (60m) the nonlinear spring are not needed and direct boundary conditions in the pipe boundary plane can be used. When an infinite length pipeline is to be modelled, the equivalent nonlinear spring, derived in the Section 3.3, is attached at the two ends of the pipeline. For either finite or infinite length the basic finite-element model configuration remains the same, as described later in this chapter. The only difference between the two cases is the mathematical expression for the nonlinear spring used.

The central part of the pipeline, where maximum stresses and strains are expected, has a fine mesh of elements. A total number of 54 shell elements around the pipe circumference in this central part have been found to be adequate to achieve convergence of solution. The size of the shell elements in the longitudinal direction has been chosen equal to $1/26^{th}$ of the pipeline outer diameter, D. This mesh has been shown capable of describing the formation of short-wave wrinkling (local buckling) on the pipeline wall. The mesh chosen for the pipe parts far from the fault location is significantly coarser. Between the dense mesh area and the coarse mesh area of the pipeline, a transition zone is created, as illustrated in Figure 3.6.
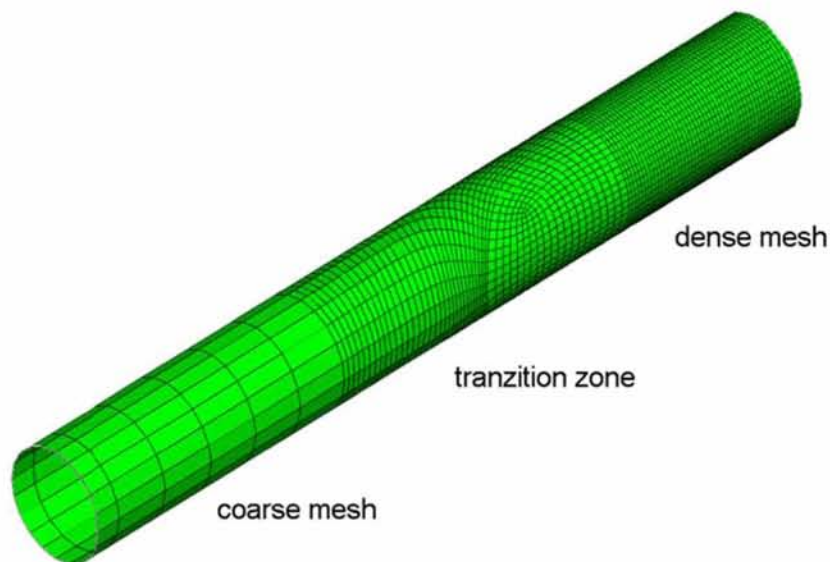
Figure 3.6: Mesh density variation of the pipeline finite-element model near the transition zone

Similarly, the finite-element mesh for the soil is more refined in the region near the fault and coarser elsewhere. The soil mesh size in the longitudinal direction is 0.33m near fault and 2.5m away from the fault. A number of 28 solid elements accounting for soil behaviour around the circumference of the pipeline is found to be adequate for the purposes of our analysis. Moreover, a larger number of 54 solid elements was also utilized for soil modelling along the pipeline circumference in subsequent, more refined numerical analyses.

The strike-slip fault plane divides the soil mass in two blocks of equal size (Figure 3.7). The analysis is conducted in two steps as follows: gravity loading is applied first and, subsequently, the fault movement is imposed, using a displacement-controlled scheme, which increases gradually the fault displacement d. For the case of pressurized pipelines, after imposing gravity, the internal pressure is also simulated.

The external soil nodes at the base and vertical boundaries of the first block remain fixed in the horizontal directions. A uniform horizontal displacement due to fault movement is imposed on the soil nodes at the base and vertical boundaries of the moving block along the horizontal n direction, which is parallel to the fault plane, whereas the motion in the vertical (z) direction is restrained only at the bases of the two blocks. The pipe nodes at the two boundary planes are connected with nonlinear springs to be described in subsequent paragraphs in order to account for the finite or infinite total length of the model, respectively. The far ends of the springs at the fixed block remain fixed, whereas those at the moving block are following the movement of the block in a direction parallel to fault plane.
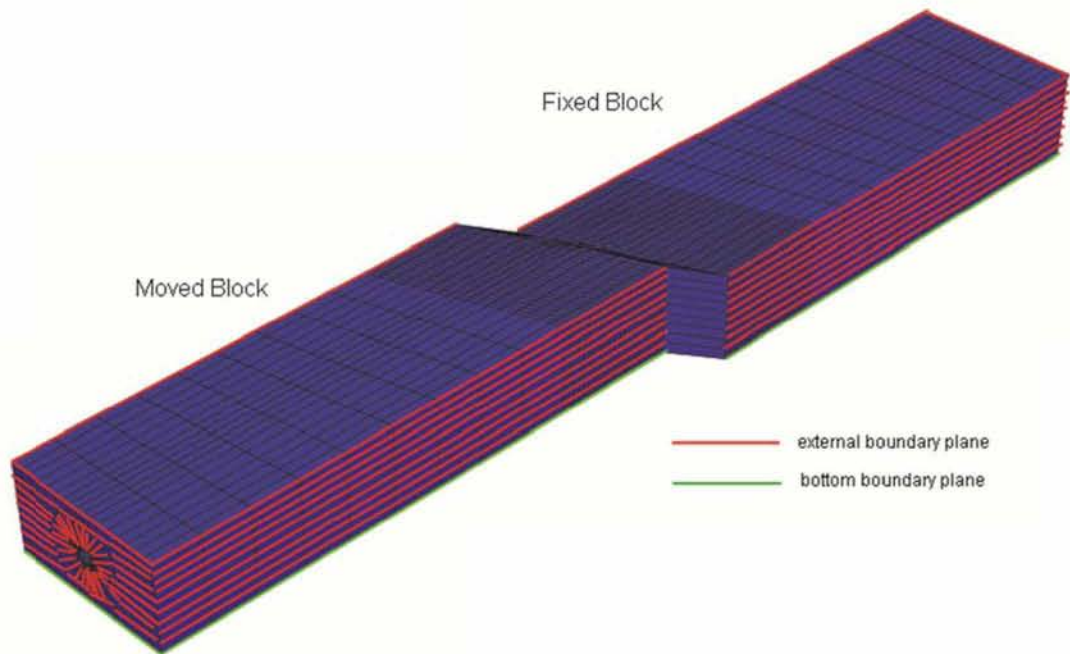
Figure 3.7: Numerical model consisting of a fixed and a moving block. The boundary planes are used for imposing the fault movement.
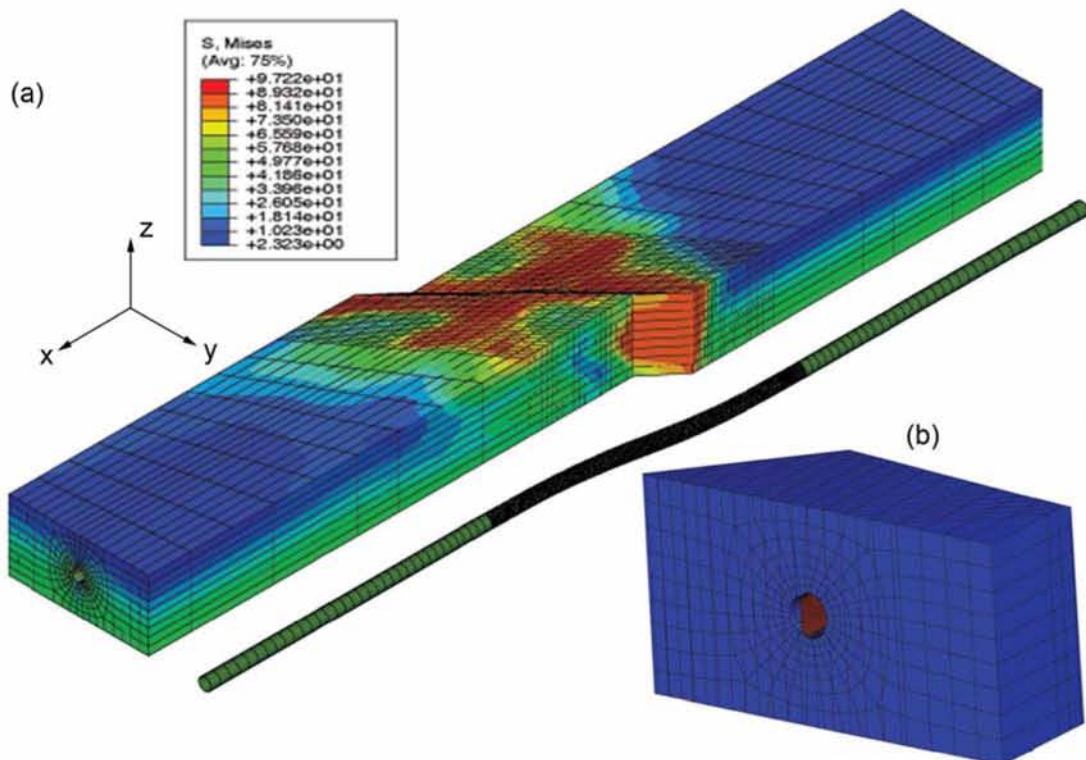
Figure 3.8: (a) Deformation of the pipeline-soil system after application of fault displacement; finite element results depict the von Mises stress. (b) Detailed view of fault displacement with detachment of pipeline from the soil.

52

Figure 3.8a plots the soil – pipeline system after a seismic fault movement in the horizontal direction. The angle β between the fault direction n and the direction y (defined in Figure 3.9) is a key parameter of the numerical study presented in the following chapters. Positive values of β indicate that the fault movement induces tension to the pipeline, whereas negative values of β refer to fault movements that result in pipeline compression. In order to induce tension to the pipeline, the block movement has to be in a direction similar of that shown in Figure 3.8a.
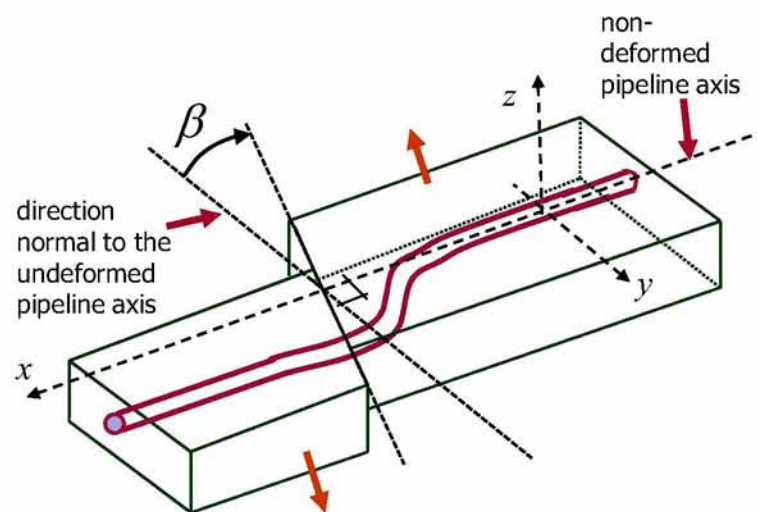
Figure 3.9: Schematic representation of a pipeline crossing a strike-slip fault at a crossing angle β.

To overcome numerical difficulties due to the discontinuity at the vicinity of the fault, the fault movement is considered to occur within a narrow zone of width w, a common practice in several recent numerical studies of fault-foundation interaction [62, 63, 64]. In addition, this assumption of a narrow band of concentrated deformation corresponds to a more realistic representation of the fault displacement mechanism. The effects of the size of fault zone, w, on the mechanical response of the pipeline are also examined. Finite element analyses have been conducted for several values of w ranging from 0.33 m to 1.0 m. The numerical results indicated that the width of the fault zone w has a minor effect on the response of the pipeline. Table 3.1 shows the critical value of fault displacement for two values of fault width, w, when the pipeline is perpendicular to fault plane. The table shows that a value of w equal to 0.33m is adequate for the purposes of the present analysis.
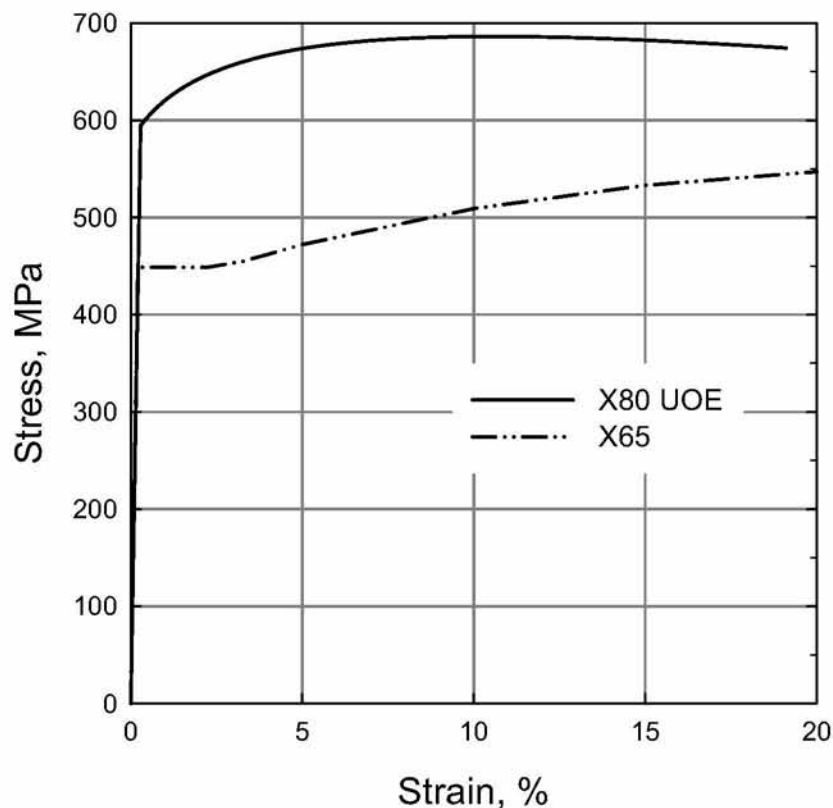
Figure 3.10: Uniaxial nominal stress-engineering strain curve for X65 and X80 steel.

Table 3.1. Critical fault displacement for local buckling ($\beta = 0^\circ$)

Fault width, m	Critical fault displacement for Local buckling, m
0.33	0.67
1	0.67

A large-strain von Mises plasticity model with isotropic hardening is used for the steel pipe material. Its calibration is performed through an appropriate uniaxial stress-strain curve derived from a tensile test on a coupon specimen from the pipeline material (see Figure 3.10) for two typical grades, namely X65 steel and X80 steel.

The mechanical behaviour of soil material is described through an elastic-perfectly plastic Mohr-Coulomb constitutive model (see Figure 3.11), characterized by the cohesion c, the friction angle ϕ, the elastic modulus E, and Poisson's ratio ν. The dilation angle ψ is assumed equal to zero for all cases considered in this dissertation.
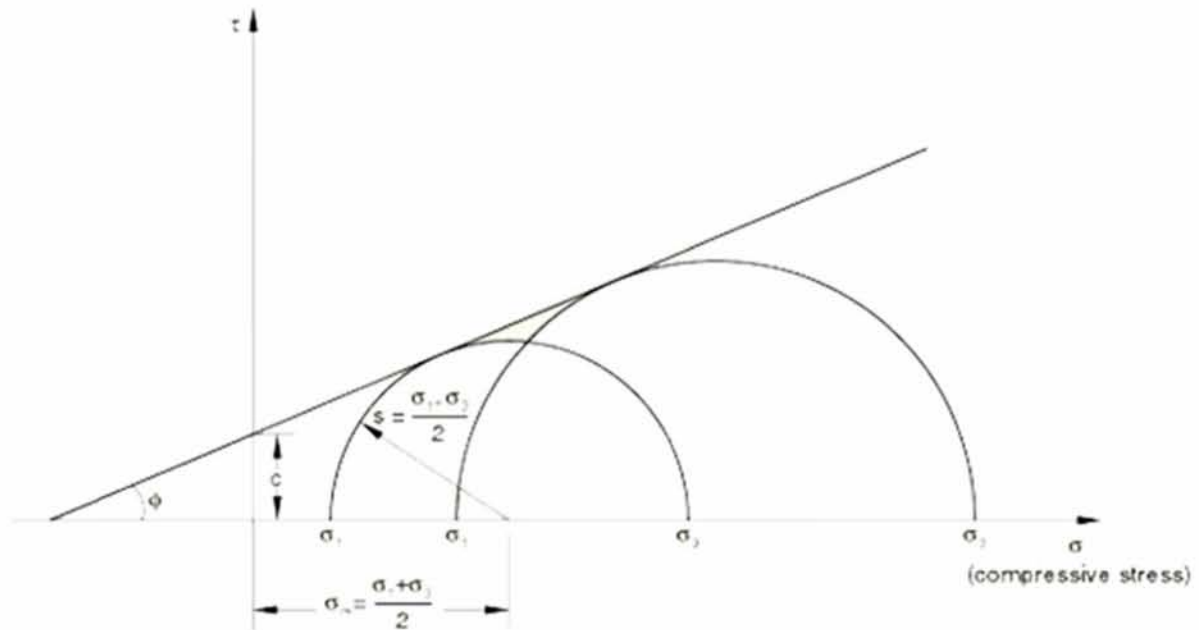
Figure 3.11: Schematic representation of Mohr-Coulomb failure envelope

The interface between the outer surface of the steel pipe and the surrounding soil is simulated with a contact algorithm, which allows separation of the pipe and surrounding soil surfaces, as shown in Figure 3.12, and accounts for interface friction, through an appropriate friction coefficient μ. In the majority of results reported in the present study, the value of μ is considered to be equal to 0.3. A small sensitivity study has been conducted for values of μ between 0.15 and 0.45. No significant differences occurred in the results of the analysis when considering the above range of μ values (for a fault angle $\beta = 0°$). In the following, the value of friction coefficient μ is assumed to be equal to 0.3.
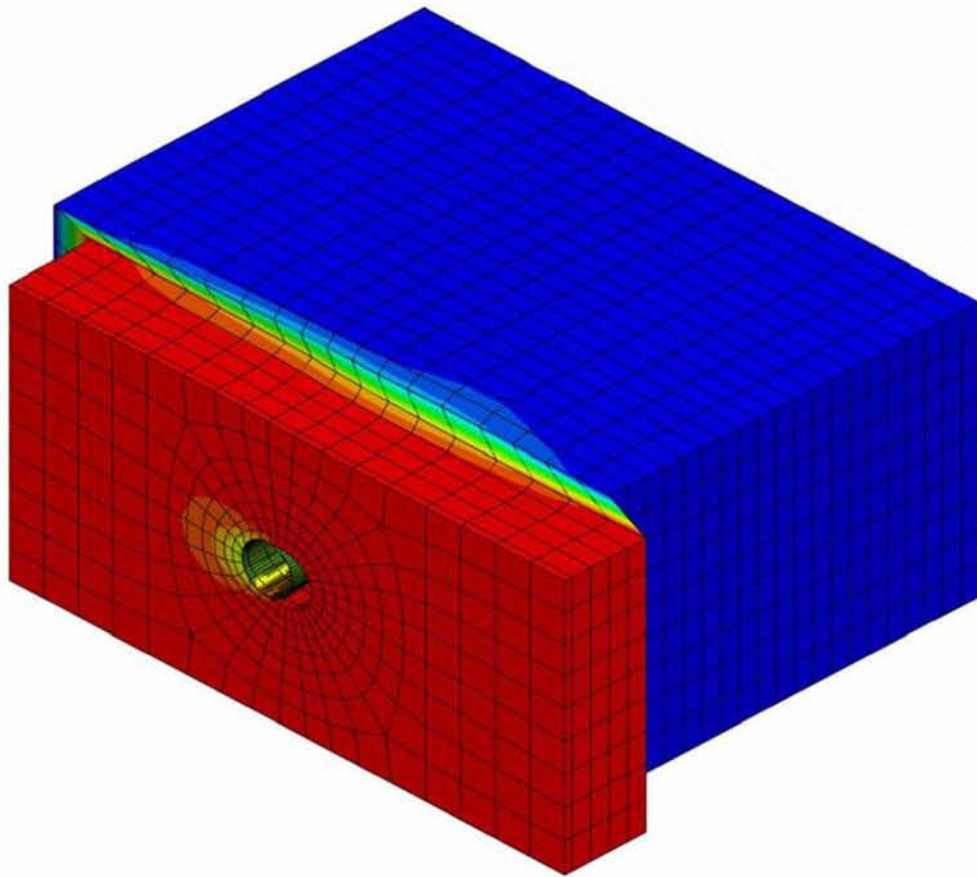
Figure 3.12: Separation of the pipe and soil surfaces during significant fault movement.

As the imposed fault displacement increases, the performance criteria are evaluated, monitoring (a) the maximum values of longitudinal and hoop strain along the pipeline, (b) the cross-sectional distortion (flattening) at critical locations and (c) the formation of pipeline wall wrinkling (local buckling).

3.3 Nonlinear spring for infinitely long pipeline in tension

A pipeline segment is considered with diameter D, thickness t, length L_a, made of a material having Young's Modulus E and Poisson's ratio v. The pipeline is buried in a soil with density ρ_s, cohesion c, friction angle ϕ, Young's Modulus E_s and Poisson's ratio v_s (Fig. 3.13a). The pipeline is subjected to a pull-out force at the near end, while keeping fixed the far end (Fig. 3.13b). The fixed far end of the pipeline may be either at an infinite distance ($L_a = \infty$) which is practically the most common case in real applications or at a finite distance ($L_a < \infty$), considering the presence of a local constraint on the pipeline, such as for example a pumping station. The former case is examined in the present section, whereas the latter case is examined in Section 3.4.
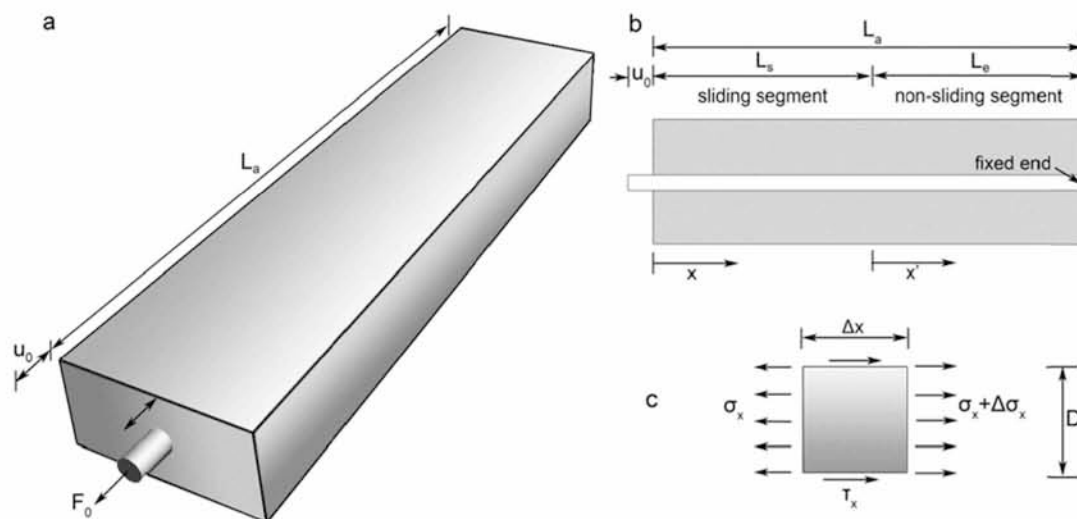
Figure 3.13: Buried pipeline subjected to tension (a) perspective view (b) vertical section and (c) free body diagram of pipeline segment. The total length L_a may be either infinite or finite.

The force–displacement relation at the pipeline head during the pull-out test depends on the stiffness and maximum shear resistance developing along the pipe-soil interface. In the case of a cohesive soil under undrained conditions ($c, \phi = 0^\circ$), the

interface shear resistance is equal to the adhesion c_a, which is a function of the undrained shear strength c. For example, the adhesion of a clay having $c = 50$ kPa may be taken approximately equal to $c_a \approx 0.35c = 17.5$ kPa, utilizing adhesion data from piles in clay [52]. In the case of a cohesionless soil, having a friction coefficient μ at the soil-pipe interface, the shear resistance τ_{max} varies along the perimeter of the pipe due to the normal stress variation. In such a case, the average value of τ_{max} may be conveniently computed through a detailed numerical analysis of the pipe-soil system, as explained below. Figure 3.14 plots schematically the stress-displacement relationship at the pipe-soil interface.
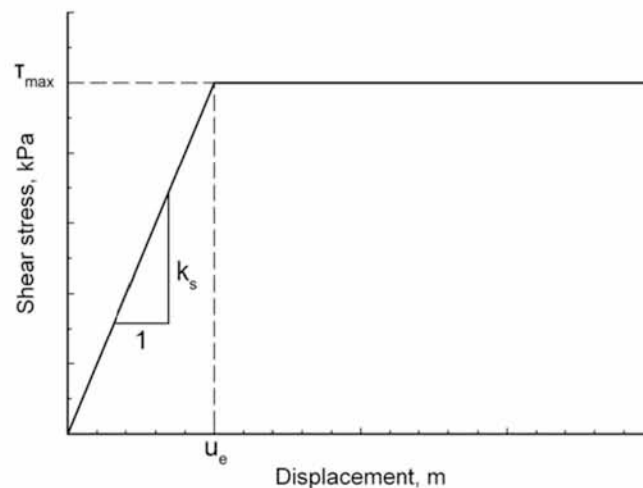
Figure 3.14: Shear stress-displacement relationship at the pipe-soil interface.

It should be noted that in a pull-out test, nonlinearity will occur first at the pipe-soil interface at which the value of shear strength is quite lower than the yield stress of soil. Thus, the soil will behave elastically, even at very high pull-out forces, at which the pipeline material may yield. This is not an actual limitation, as the near end of the pipe segment (x=0) can be assumed to be at a distance far enough from the tectonic fault so that the corresponding axial strains in that part of the pipeline remain below the yield strain of steel material.

As shown in Figure 3.13b, when the applied displacement u_0 at the near end exceeds a critical value, part of the pipeline along a distance L_s experiences sliding at its interface, whereas the rest of the infinitely long pipeline remains "bonded" to the soil that behaves elastically. In the following, pipeline response in the non-sliding and sliding parts is analysed.

58

3.3.1 Elastic behavior (non-sliding interface)

Figure 3.13c illustrates a segment of the pipeline subjected to tensile and shear stresses. For shear stress at the pipe interface $\tau \leq \tau_{\max}$, the mobilized value of τ is equal to

$$\tau = k_s u \tag{3.1}$$

Considering the axial force change dF along the pipeline of length dx

$$dF = -\pi D \tau dx = -\pi D k_s u dx \tag{3.2}$$

and using the stress-strain relationship,

$$\frac{dF}{dx} = \frac{d}{dx}(EA\varepsilon) = \frac{d}{dx}(-EA\frac{du}{dx}) = -EA\frac{d^2u}{dx^2} \tag{3.3}$$

the equilibrium equation for the pipe segment becomes

$$EA\frac{d^2u}{dx^2} - \pi D k_s u = 0 \tag{3.4}$$

Equation (3.4) may be written as

$$\frac{d^2u}{dx^2} - \lambda^2 u = 0 \tag{3.5}$$

where

$$\lambda = \sqrt{\frac{\pi D k_s}{EA}} \tag{3.6}$$

The solution of equation (3.5) is given by

$$u = C_1 e^{-\lambda x} + C_2 e^{\lambda x} \tag{3.7}$$

For $x \to \infty$, $u = 0$ and therefore $C_2 = 0$, whereas for $x = 0$, $u(0) = u_0 = C_1$. The axial force along the pipe is equal to

$$F(x) = -EA\frac{du}{dx} = \lambda EA u = \lambda EA u_0 \ e^{-\lambda x} \tag{3.8}$$

For the limit case in which sliding initiates at $x = 0$, the displacement $u(0) = u_0$ becomes equal to the elastic limit displacement $u_e = \tau_{\max} / k_s$ (Figure 3.14). Thus, the axial force at x=0 can be written as

$$F_0 = \lambda EA \frac{\tau_{\max}}{k_s} \tag{3.9}$$

Hence, for linear elastic response, the *equivalent linear spring* constant for an infinitely long pipeline subjected to tension is given by

$$K_t = \lambda EA \tag{3.10}$$

3.3.2 Inelastic behavior (sliding interface)

When the pipeline is subjected to a pull-out displacement $u_0 > u_e = \tau_{\max} / k_s$, a segment of the pipeline slides along a distance L_s, whereas the rest of the pipeline interface behaves elastically. For the sliding segment, taking the equilibrium of a pipe element (Figure 3.13c) leads to

$$EA \frac{d^2 u}{dx^2} - \pi D \tau_{\max} = 0 \tag{3.11}$$

or

$$\frac{d^2 u}{dx^2} = m \tag{3.12}$$

where

$$m = \frac{\pi D \tau_{\max}}{EA} \tag{3.13}$$

The axial strain along the pipeline, which decreases linearly with the distance x, may be written as

$$\varepsilon(x) = -\frac{du}{dx} = -mx + C_3 \tag{3.14}$$

For $x = 0$, the axial strain is equal to $\varepsilon(0) = \varepsilon_0 = -\dfrac{du}{dx}\bigg|_{x=0} = C_3$ \hfill (3.15)

whereas for $x = L_s$, it becomes equal to the elastic limit strain

$$\varepsilon(L_s) = \varepsilon_e = -\frac{du}{dx}\bigg|_{x=L_s} = -mL_s + \varepsilon_0 \tag{3.16}$$

By integrating $\varepsilon(x)$ from $x = 0$ to L_s, the displacement difference $u_0 - u_e$ is found equal to

---

$$u_0 - u_e = \frac{1}{2}(\varepsilon_0 - \varepsilon_e)L_s + \varepsilon_e L_s = \frac{1}{2}mL_s^2 + \varepsilon_e L_s \tag{3.18}$$

From (3.18), the length L_s is equal to

$$L_s = \frac{1}{m}\left(\sqrt{\varepsilon_e^2 + 2m(u_0 - u_e)} - \varepsilon_e\right) \tag{3.19}$$

Substituting the maximum elastic strain obtained from the non-sliding side of the pipeline

$$\varepsilon_e = \lambda u_e = \lambda \frac{\tau_{\max}}{k_s} \tag{3.20}$$

equation (3.19) becomes

$$L_s = \frac{1}{m}\left(\sqrt{\left(\lambda \frac{\tau_{\max}}{k_s}\right)^2 + 2m\left(u_0 - \frac{\tau_{\max}}{k_s}\right)} - \lambda \frac{\tau_{\max}}{k_s}\right) \tag{3.21}$$

The force at the pipe end is given by

$$F_0 = \pi D \tau_{\max} L_s + \lambda E A u_e \tag{3.22}$$

Finally, from equations (3.9), (3.21) and (3.22), the force–displacement relation for an infinitely long pipe becomes

$$F_0 = \begin{cases} \lambda E A u_0 & \text{for} \quad u_0 \leq \dfrac{\tau_{\max}}{k_s} \\[3mm] \lambda E A \dfrac{\tau_{\max}}{k_s} + \dfrac{\pi D \tau_{\max}}{m}\left(\sqrt{\left(\lambda \dfrac{\tau_{\max}}{k_s}\right)^2 + 2m\left(u_0 - \dfrac{\tau_{\max}}{k_s}\right)} - \lambda \dfrac{\tau_{\max}}{k_s}\right) & \text{for} \quad u_0 > \dfrac{\tau_{\max}}{k_s} \end{cases} \tag{3.23}$$

The expressions for the distributions of the displacement $u(x)$, force $F(x)$ and axial strain $\varepsilon(x)$ along the pipeline are given below.

Distribution of displacement $u(x)$

$$u(x) = \begin{cases} u_0 e^{-\lambda x} & u \leq \dfrac{\tau_{\max}}{k_s} \\[2ex] u_0 + \dfrac{m}{2}x^2 - \dfrac{F_0(u_0)}{EA}x & x \leq L_s, \quad u > \dfrac{\tau_{\max}}{k_s} \\[2ex] \dfrac{\tau_{\max}}{k_s} e^{-\lambda(x-L_s)} & x > L_s, \quad u > \dfrac{\tau_{\max}}{k_s} \end{cases} \qquad (3.24)$$

where L_s and $F_0(u_0)$ are given by equations (3.19) and (3.23), respectively.

Distribution of axial force $F(x)$

$$F(x) = \begin{cases} \lambda EA u_0 e^{-\lambda x} & u \leq \dfrac{\tau_{\max}}{k_s} \\[2ex] F_0(u_0) - \pi D \tau_{\max} x & x \leq L_s, \quad u > \dfrac{\tau_{\max}}{k_s} \\[2ex] \lambda EA \dfrac{\tau_{\max}}{k_s} e^{-\lambda(x-L_s)} & x > L_s, \quad u > \dfrac{\tau_{\max}}{k_s} \end{cases} \qquad (3.25)$$

Distribution of axial strain $\varepsilon(x)$

$$\varepsilon(x) = \begin{cases} \lambda u_0 e^{-\lambda x} & u \leq \dfrac{\tau_{\max}}{k_s} \\[2ex] \dfrac{F_0(u_0)}{EA} - mx & x \leq L_s, \quad u > \dfrac{\tau_{\max}}{k_s} \\[2ex] \lambda \dfrac{\tau_{\max}}{k_s} e^{-\lambda(x-L_s)} & x > L_s, \quad u > \dfrac{\tau_{\max}}{k_s} \end{cases} \qquad (3.26)$$

In the following section, the case of a finite-length pipeline subjected to tension is considered.

3.4 Nonlinear spring for a finite-length pipeline in tension

In this case, a pipeline segment is considered with the fixed far end located at a finite distance L_a. As shown in Figure 3.13b, the pipeline segment that experiences no sliding has a length equal to L_e, whereas the segment in which sliding occurs has a length equal to L_s so that $L_a = L_s + L_e$. For values of pull-out displacement $u_0 < \tau_{max}/k_s$, the interface behaves in a linear elastic way, i.e. $L_e = L_a$, whereas for $u_0 > \tau_{max}/k_s$, the linear elastic behaviour is confined to a length $L_e(u_0) = L_a - L_s$, which decreases with increasing values of u_0.

3.4.1 Elastic behavior (non-sliding interface)

For the non-sliding pipeline, the general solution (3.7) is

$$u = C_1 e^{-\lambda x} + C_2 e^{\lambda x}$$

For $x = L_e$, $u = 0$ and therefore

$$u = C_1 e^{-\lambda L_e} + C_2 e^{\lambda L_e} = 0 \tag{3.27}$$

For $x = 0$, $u(0) = u_0$, so that

$$u = C_1 + C_2 = u_0 \tag{3.28}$$

From equations (3.7), (3.27) and (3.28), the displacement at $x = 0$ becomes

$$u_0 = C_1(1 - e^{-2\lambda L_e}) \tag{3.29}$$

The axial force in the pipeline is given by

$$F(x) = -EA\frac{du}{dx} = \lambda EA\, C_1(e^{-\lambda x} + e^{-2\lambda L_e}e^{\lambda x}) \tag{3.30}$$

At $x = 0$,

$$F_0 = \lambda EA\, C_1(1 + e^{-2\lambda L_e}) = \lambda EA\, u_0 \frac{1 + e^{-2\lambda L_e}}{1 - e^{-2\lambda L_e}} = \frac{\lambda EA\, u_0}{\tanh(\lambda L_e)} \tag{3.31}$$

For the case of $u_0 \le \tau_{\max} / k_s$, $L_e = L_a$ and therefore the *equivalent linear spring* constant may be written as

$$K_t = \frac{F_0}{u_0} = \frac{\lambda EA}{\tanh(\lambda L_a)} \qquad (3.32)$$

which is similar to the expression in eq. (3.10), except that it contains the term $\tanh(\lambda L_a)$ in the denominator. It is noted that as $L_a \to \infty$, the nonlinear spring constant in equation (3.32) reduces to $K_t = \lambda EA$.

At the limit of the elastic behaviour, the displacement at $x = 0$ becomes

$$u_0 = u_e = \tau_{\max} / k_s \qquad (3.33)$$

and the force becomes

$$F_0 = \frac{\tau_{\max}}{k_s} \frac{\lambda EA}{\tanh(\lambda L_a)} \qquad (3.34)$$

3.4.2 Inelastic behavior (sliding interface)

Following the steps of paragraph 3.3, it can be easily shown that the force at the pipe end is given by

$$F_0 = \pi D \tau_{\max} L_s + EA\varepsilon_e \qquad (3.35)$$

where ε_e is the axial strain at the location which separates the sliding and the non-sliding pipe segments, given by

$$\varepsilon_e = \frac{\lambda \tau_{\max}}{k_s \tanh(\lambda L_e)} \qquad (3.36)$$

From equations (3.18) and (3.36), the length of sliding L_s is obtained as follows

$$L_s = \frac{1}{m} \left(\sqrt{\left(\frac{\lambda \tau_{\max}}{k_s \tanh(\lambda L_e)} \right)^2 + 2m\left(u_0 - \frac{\tau_{\max}}{k_s} \right)} - \frac{\lambda \tau_{\max}}{k_s \tanh(\lambda L_e)} \right) \qquad (3.37)$$

From (3.37) and the relationship $L_a = L_s + L_e$ (see Figure 3.13b), the following nonlinear equation is obtained

$$L_a = \frac{1}{m}\left(\sqrt{\left(\frac{\lambda\tau_{max}}{k_s \tanh(\lambda L_e)}\right)^2 + 2m\left(u_0 - \frac{\tau_{max}}{k_s}\right)} - \frac{\lambda\tau_{max}}{k_s \tanh(\lambda L_e)} \right) + L_e \qquad (3.38)$$

which is solved numerically for $L_e = L_e(u_0)$.

Finally, from equations (3.34), (3.35) and (3.38), for a pipe having a length $L_a = L_s + L_e$ and fixed at the far end the force–displacement relation is given by

$$F_0 = \begin{cases} \dfrac{\lambda EA u_0}{\tanh(\lambda L_a)} & \text{for } u_0 \leq \dfrac{\tau_{max}}{k_s} \\[4mm] \dfrac{\lambda EA}{\tanh(\lambda L_e)}\dfrac{\tau_{max}}{k_s} + \dfrac{\pi D\tau_{max}}{m}\left(\sqrt{\left(\dfrac{\lambda\tau_{max}}{k_s \tanh(\lambda L_e)}\right)^2 + 2m\left(u_0 - \dfrac{\tau_{max}}{k_s}\right)} - \dfrac{\lambda\tau_{max}}{k_s \tanh(\lambda L_e)} \right) & \text{for } u_0 > \dfrac{\tau_{max}}{k_s} \end{cases} \qquad (3.39)$$

As $L_a \to \infty$, the force-displacement relation in eq. (3.39) reduces to that in equation (3.23). The expressions for the distributions of the displacement $u(x)$, axial force $F(x)$ and axial strain $\varepsilon(x)$ along the pipeline are given below.

Distribution of displacement $u(x)$

$$u(x) = \begin{cases} u_0 \dfrac{e^{-\lambda x} - e^{-2\lambda L_e} e^{\lambda x}}{1 - e^{-2\lambda L_e}} & u \leq \dfrac{\tau_{max}}{k_s} \\[4mm] u_0 + \dfrac{m}{2}x^2 - \dfrac{F_0(u_0)}{EA}x & x \leq L_s, \quad u > \dfrac{\tau_{max}}{k_s} \\[4mm] \dfrac{\tau_{max}}{k_s}\dfrac{e^{-\lambda(x-L_s)} - e^{-2\lambda L_e} e^{\lambda(x-L_s)}}{1 - e^{-2\lambda L_e}} & x > L_s, \quad u > \dfrac{\tau_{max}}{k_s} \end{cases} \qquad (3.40)$$

where L_s and $F_0(u_0)$ are given by equations (3.37) and (3.39), respectively.

Distribution of axial force $F(x)$

$$F(x) = \begin{cases} \lambda EA u_0 \dfrac{e^{-\lambda x} + e^{-2\lambda L_e} e^{\lambda x}}{1 - e^{-2\lambda L_e}} & u \leq \dfrac{\tau_{max}}{k_s} \\[4mm] F_0(u_0) - \pi D \tau_{max} x & x \leq L_s, \quad u > \dfrac{\tau_{max}}{k_s} \\[4mm] \lambda EA \dfrac{\tau_{max}}{k_s} \dfrac{e^{-\lambda(x-L_s)} + e^{-2\lambda L_e} e^{\lambda(x-L_s)}}{1 - e^{-2\lambda L_e}} & x > L_s, \quad u > \dfrac{\tau_{max}}{k_s} \end{cases} \qquad (3.41)$$

Distribution of axial strain $\varepsilon(x)$

$$\varepsilon(x) = \begin{cases} \lambda u_0 \dfrac{e^{-\lambda x} + e^{-2\lambda L_e} e^{\lambda x}}{1 - e^{-2\lambda L_e}} & u \leq \dfrac{\tau_{max}}{k_s} \\[4mm] \dfrac{F_0(u_0)}{EA} - mx & x \leq L_s, \quad u > \dfrac{\tau_{max}}{k_s} \\[4mm] \lambda \dfrac{\tau_{max}}{k_s} \dfrac{e^{-\lambda(x-L_s)} + e^{-2\lambda L_e} e^{\lambda(x-L_s)}}{1 - e^{-2\lambda L_e}} & x > L_s, \quad u > \dfrac{\tau_{max}}{k_s} \end{cases} \qquad (3.42)$$

It can be easily shown from equations (3.31) and (3.42) that, at the constrained far end, the force and axial strain are

$$F(L_a) = \frac{\lambda EA \tau_{max}}{\sinh(\lambda L_e) k_s} \qquad (3.43)$$

and

$$\varepsilon(L_a) = \frac{\lambda \tau_{max}}{\sinh(\lambda L_e) k_s} \qquad (3.44)$$

3.5   Response of buried pipelines in pure tension

In the present section, using the analytical model described in the previous sections, a parametric study is conducted for buried pipelines (of both infinite and finite length) subjected to axial tension. The results of this study are helpful in evaluating the response of buried pipelines subjected to fault movement to be discussed later in the dissertation. The results are obtained for an X65 steel 36-inch pipeline with outer diameter D =0.914 m, thickness t =9.5 mm (3/8 inch), Young's Modulus E = 210 GPa and Poisson's ratio v =0.3. The pipeline is buried in a cohesive soil under "undrained"

conditions, having a density ρ_s =2000 kg/m³, cohesion c =50 kPa, friction angle ϕ =0°, Young's Modulus E_s =25 MPa and Poisson's ratio v_s =0.5. The above values of geometric and material properties are also considered in the following section of this Chapter.

Before proceeding with the parametric study, the stiffness, k_s, and the shear strength, τ_{max}, at the pipe-soil interface are determined through a simple numerical simulation, which is conducted using the general-purpose finite element program ABAQUS [53]. Figure 3.15a illustrates a refined FE discretization of a soil block having dimensions 20m × 10m × 5m and the aforementioned properties, in which non-deformable (rigid) 36-inch (D =0.914m) pipe is buried, considering pipe Young's modulus 100 larger than the modulus of steel, E , so that the developed shear resistance is identical along its length. The mechanical behavior of soil material is described through an elastic-perfectly plastic Mohr-Coulomb constitutive model. Four-node reduced-integration shell elements (type S4R) are employed for modeling the cylindrical pipeline segment, and eight-node reduced-integration "brick" elements (C3D8R) are used to simulate the surrounding soil. A total of 54 shell elements around the cylinder circumference have been found to be adequate to achieve convergence of solution, whereas the size of the shell elements in the longitudinal direction has been chosen equal to 1/26th of the pipeline outer diameter D. The same number of solid elements (54) has been chosen to model the soil around the cylinder circumference whereas the size of solid elements in the longitudinal direction has been equal to 0.25m.

The pipeline axis in the numerical model of Figure 3.15a is centered within the soil block at a depth equal to 2.5m. The pipeline is pulled outwards at the near end, whereas the far end remains free. Figure 3.15b plots the stress-displacement relationship for μ =0.3, resulting to an interface shear strength τ_{max} of 15 kPa and interface stiffness k_s equal to 4.138 MPa/m. Similarly, for μ =0.1 and 0.2, the values of shear strength are τ_{max} =5 kPa and 10 kPa, respectively (Figure 3.15b). A short parametric investigation showed that further refinement of the discretization of the finite element model in Figure 3.15a does not improve the computed values τ_{max} and k_s along the pipe-soil interface.
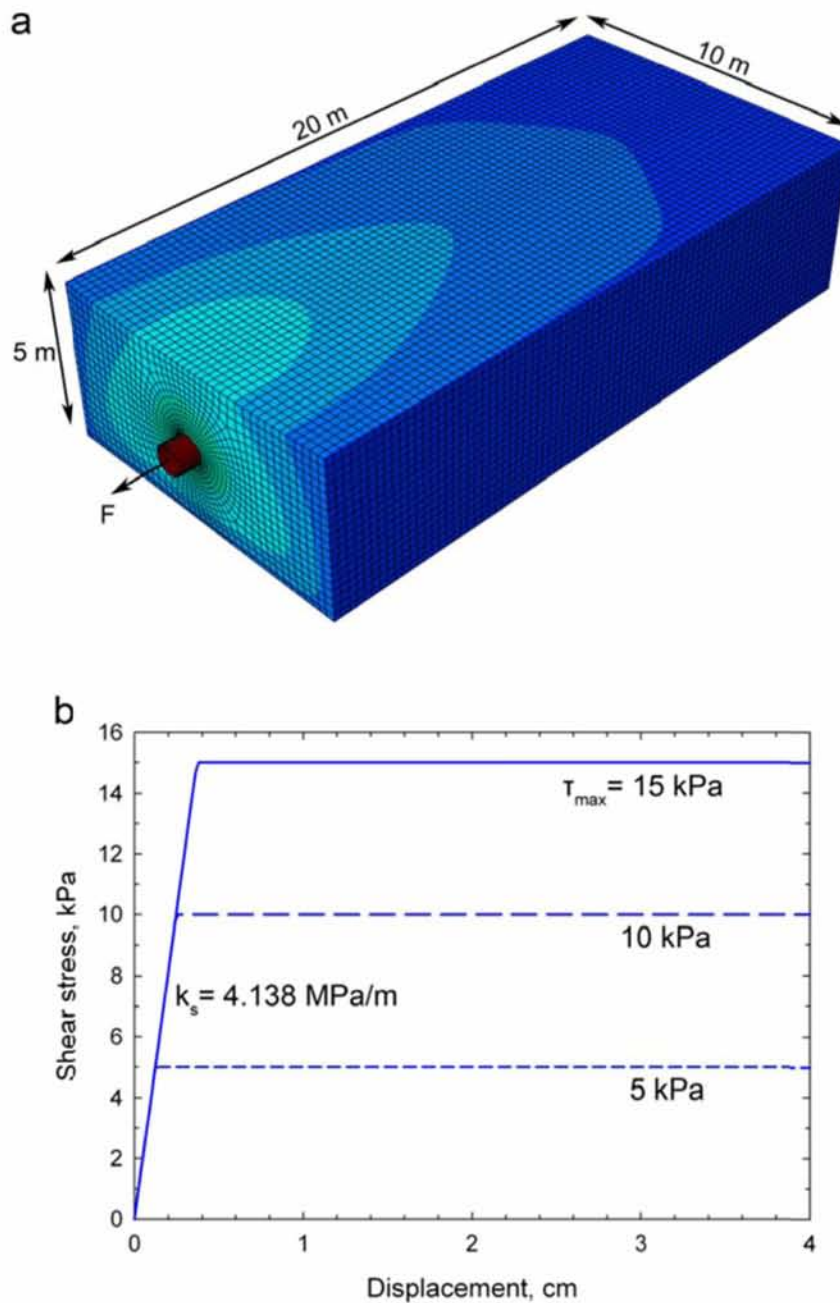
Figure 3.15: Evaluation of the soil stiffness and shear strength parameters at the pipe-soil interface using a numerical simulation of a pull-out test: (a) finite element model (b) stress-displacement relationship at the pipe-soil interface for friction coefficients μ =0.1, 0.2 and 0.3.

3.5.1 Infinitely long pipeline subjected to tension

An infinitely long pipeline ($L_a = \infty$) is considered first, having the aforementioned characteristics with. The pipeline is subjected to a pull-out force at the near end, while keeping fixed the far end (Figure 3.13b).

Figure 3.16a plots the force-displacement relationship (F_0-u_0) at the pulled end of the pipeline for various values of the interface shear strength, τ_{max}, ranging from 5 kPa to 30 kPa, based on eq. (3.23) for k_s = 4.138 MPa/m. Moreover, Figure 3.16b plots the variation of the axial force $F(x)$ along the pipeline for the same values of τ_{max} and a pull-out displacement u_0 =0.25 m, using eq. (3.25).

It is evident from Figure 3.16 that, as the value of the interface shear strength increases, the magnitude of the near end (x=0) pull-out force F_0 increases substantially, and the length of the pipeline, along which this force is distributed, is significantly reduced. For the values of u_0 and τ_{max} considered, the pipeline length strained by the pull-out test ranges between 200 m to 450 m.

Figures 3.17a and 3.17b plot the distribution of axial force along the long pipeline for shear strengths τ_{max} = 5 kPa and 15 kPa, respectively, at various values of pull-out displacement.

Also, Figures 3.18 and 3.19 plot the distribution of displacement $u(x)$ and axial strain $\varepsilon(x)$, respectively, along the pipeline length for various values of pull-out displacement. It is noted that the pipeline length along which the strain distribution is linear, experiences sliding at the interface, whereas the "bonded" segment of the pipeline is not strained significantly. In all cases considered, the maximum axial strains remain smaller than the yield strain of the steel material (0.21%).
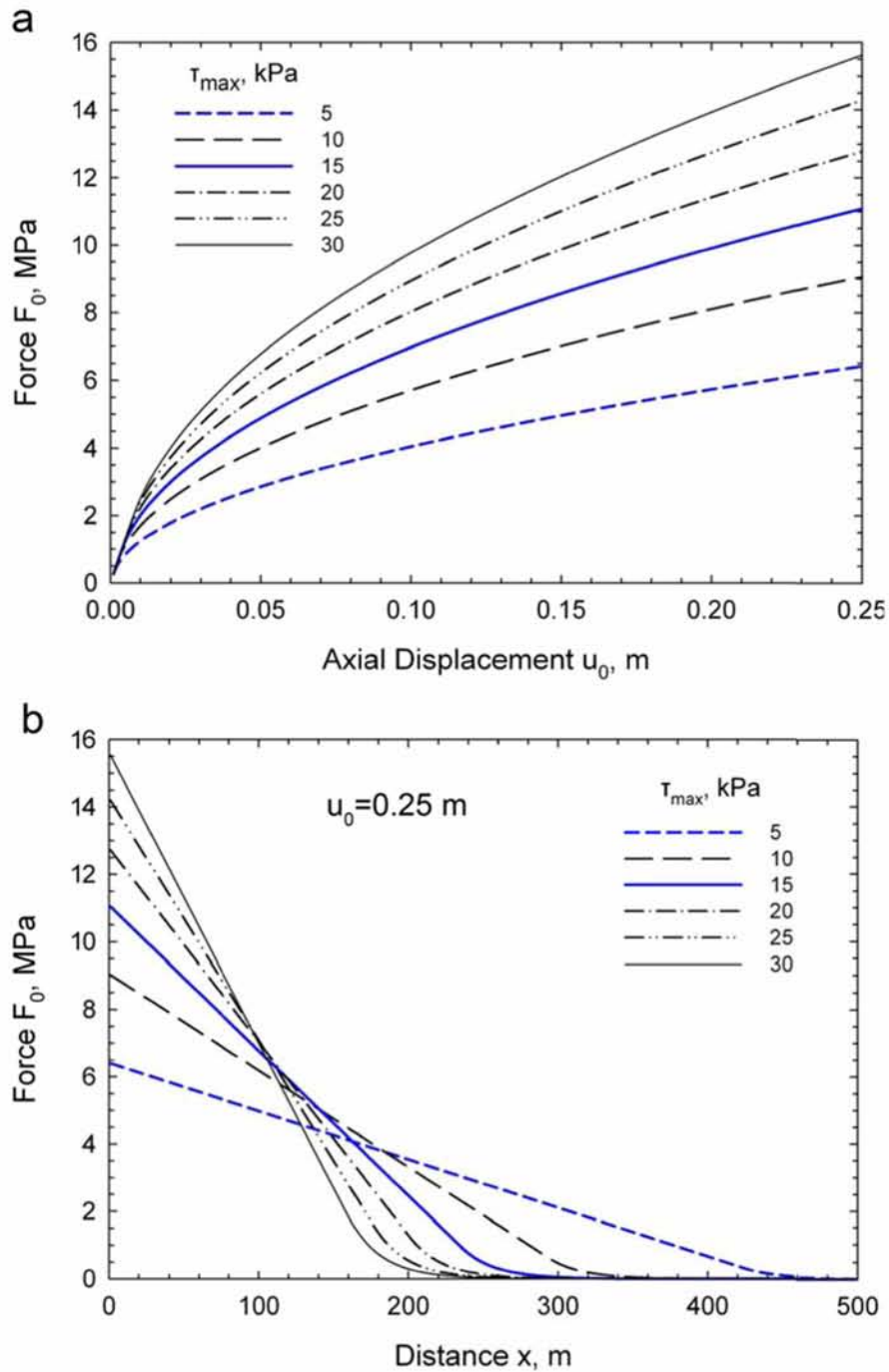
Figure 3.16: Infinitely long pipeline subjected to tension for different values of interface shear strength: (a) Force versus axial displacement at pipeline end (b) distribution of force along the pipeline for pullout displacement equal to u_x =0.25 m.
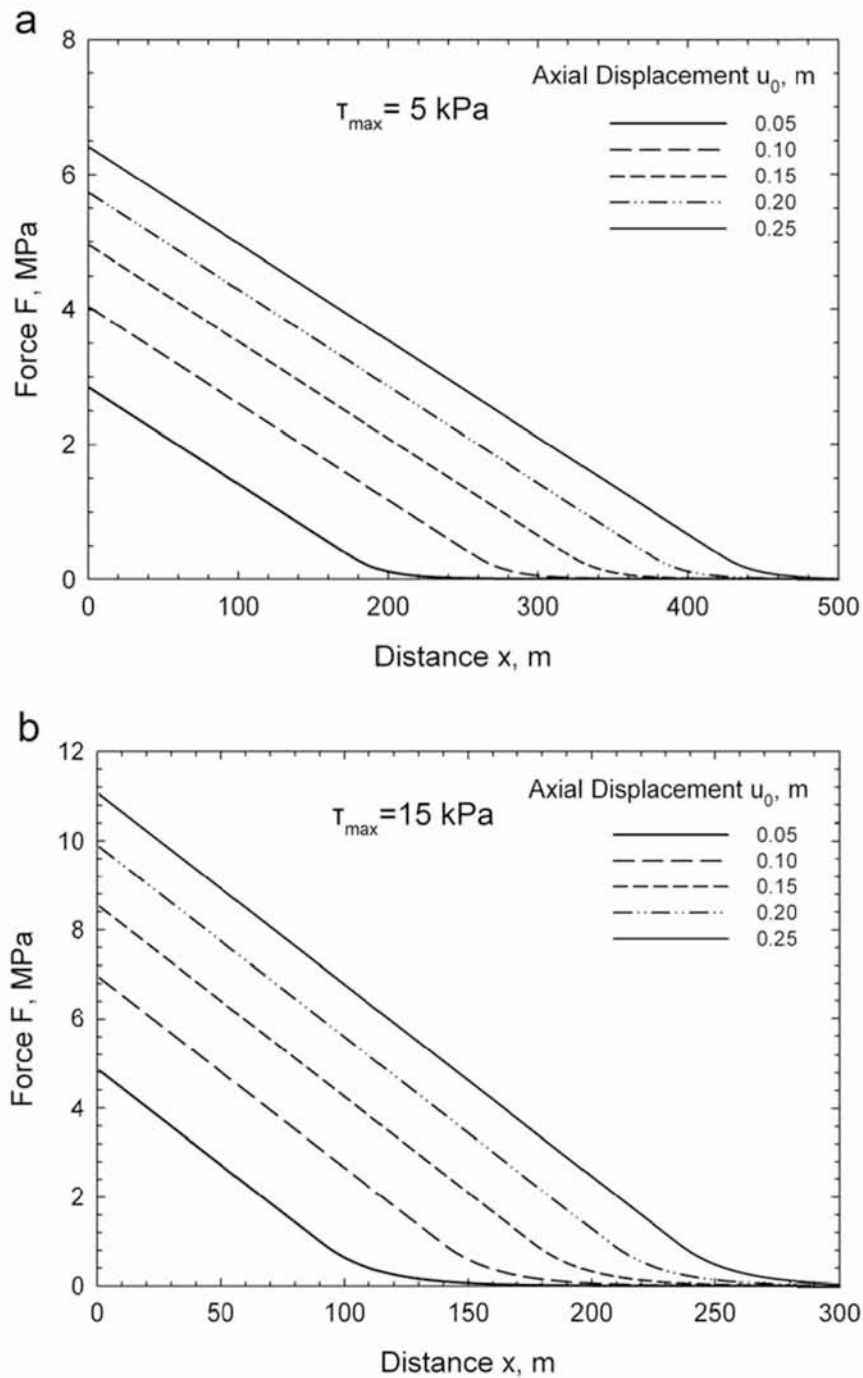
Figure 3.17: Distribution of axial force along an infinitely long pipeline subjected to tension for various values of pullout axial displacement and interface shear strength equal to: (a) τ_{max} = 5 kPa and (b) τ_{max} = 15 kPa.
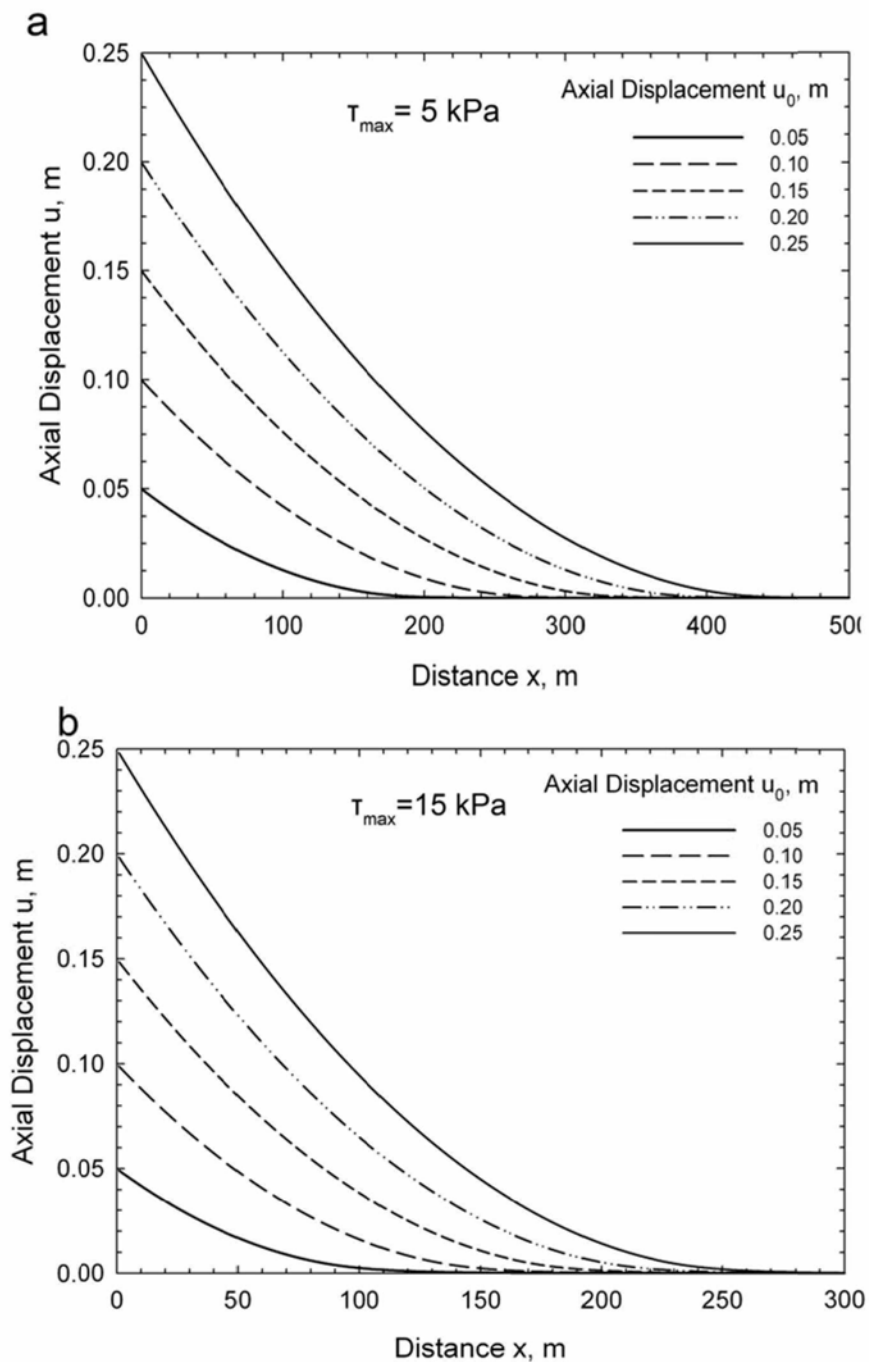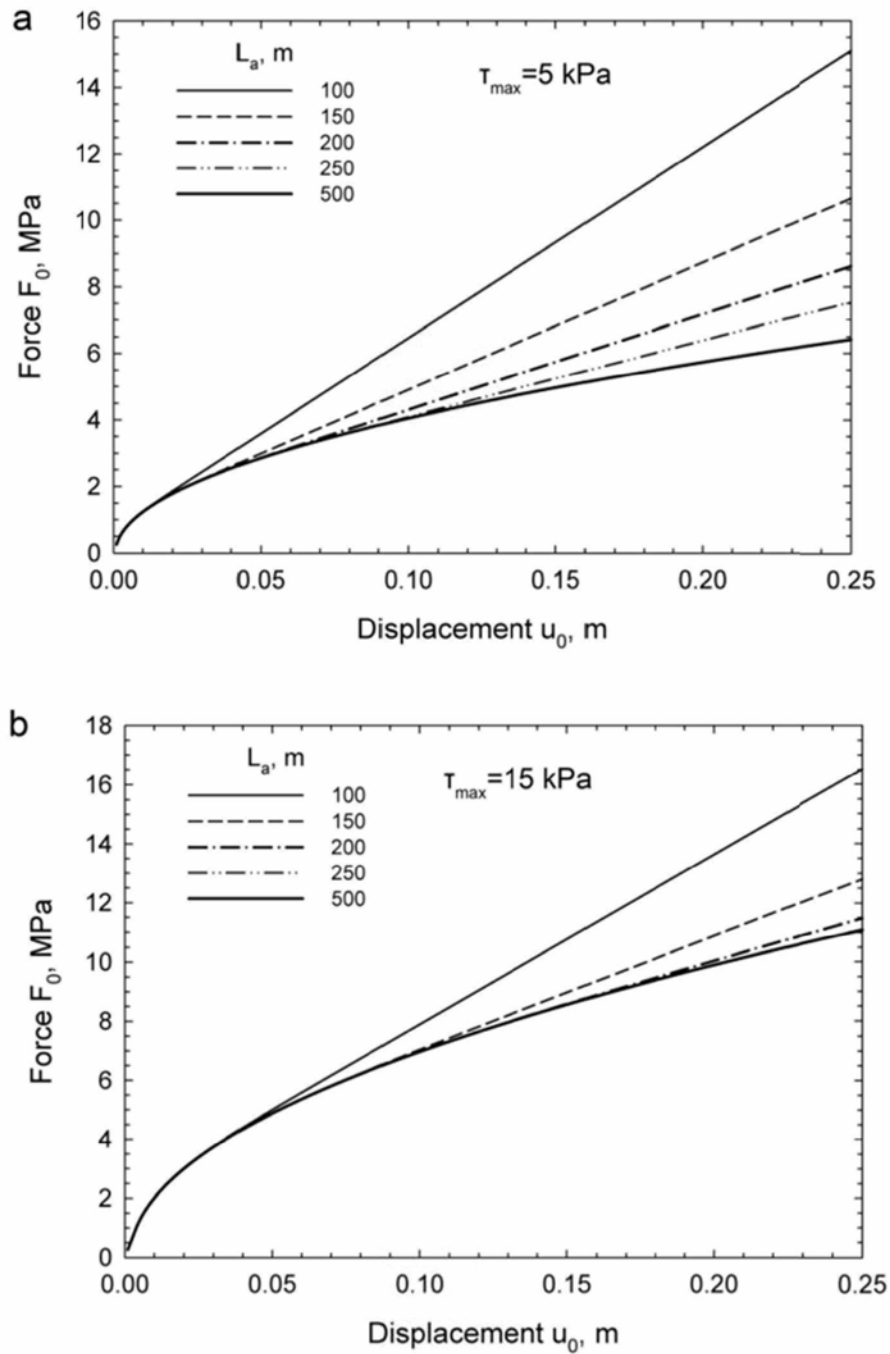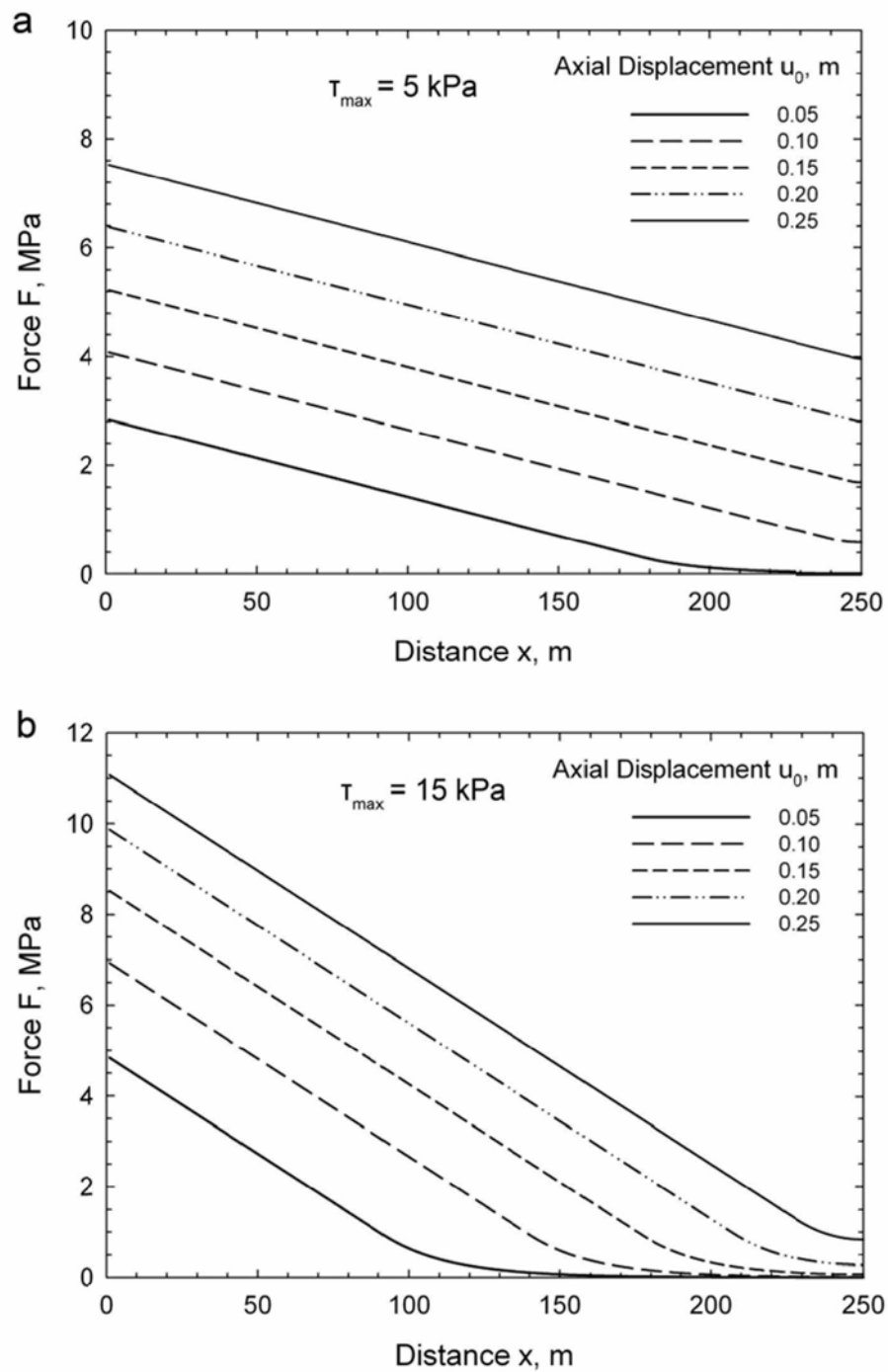
Figure 3.18: Distribution of axial displacement along an infinitely long pipeline subjected to tension for various values of pullout displacement and interface shear strength equal to: (a) τ_{max} = 5 kPa and (b) τ_{max} = 15 kPa.

a

b
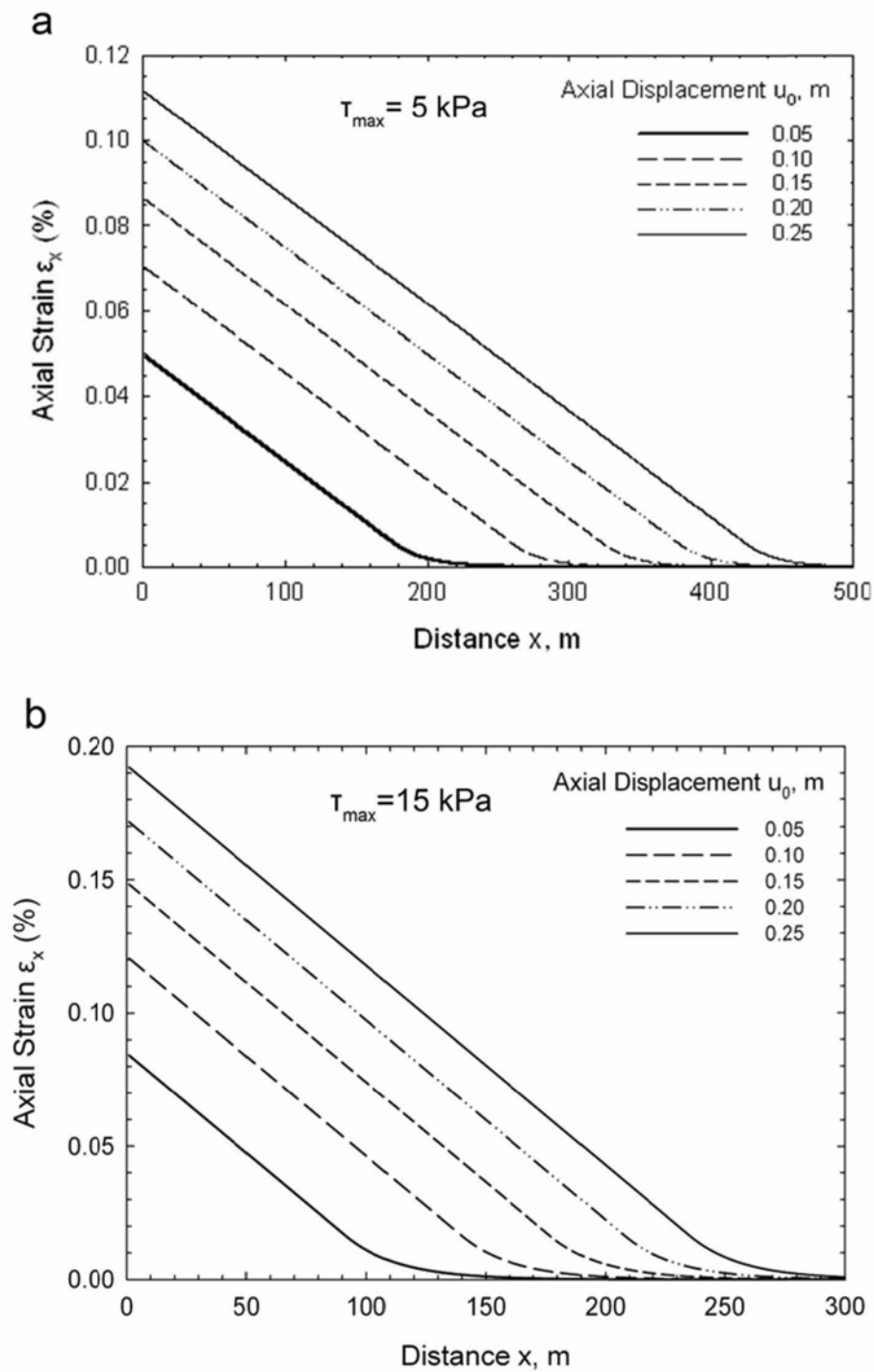
Figure 3.19: Distribution of axial normal strain along an infinitely long pipeline subjected to tension for various values of pullout displacement and interface shear strength equal to: (a) τ_{max} = 5 kPa and (b) τ_{max} = 15 kPa.

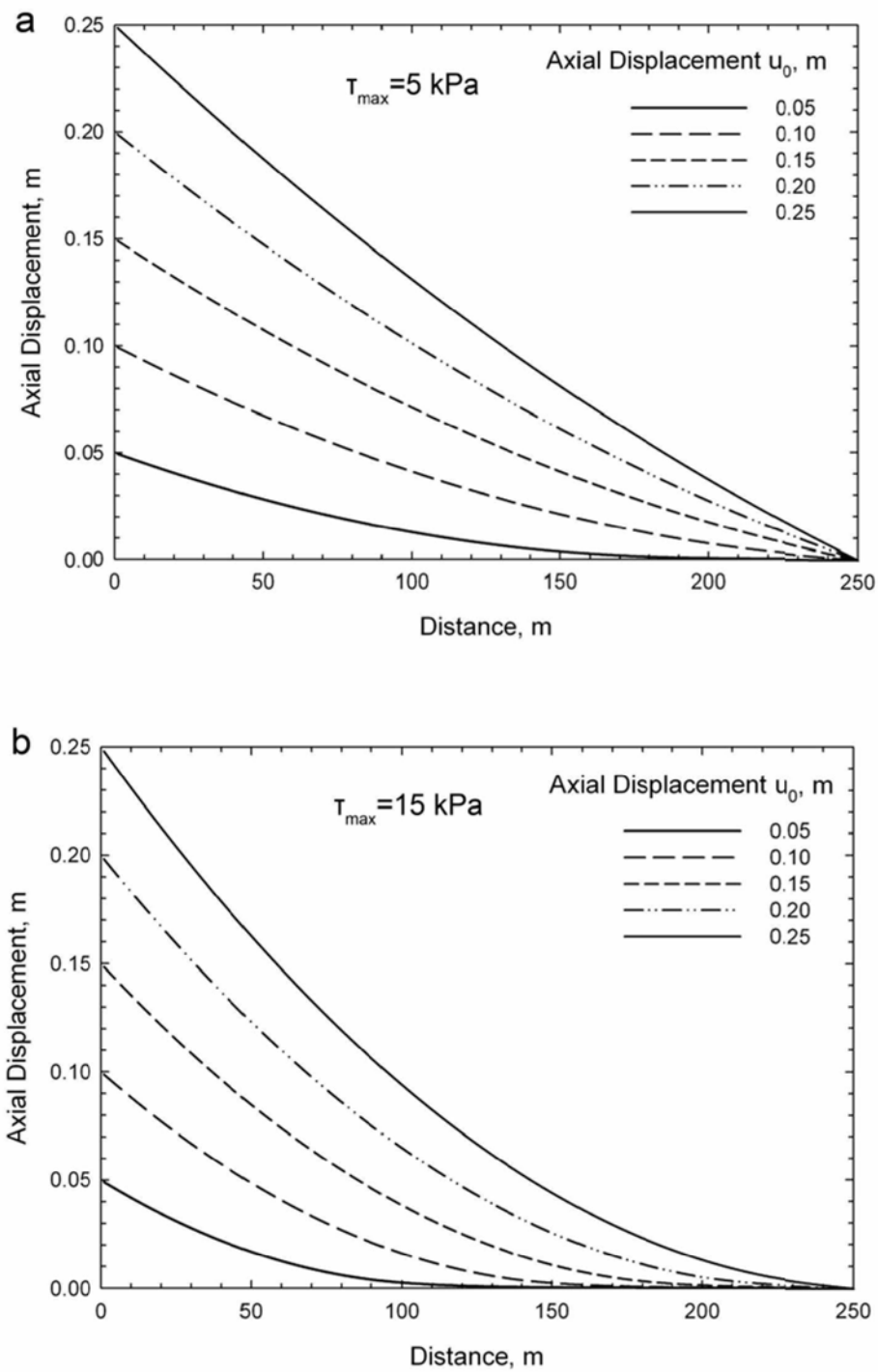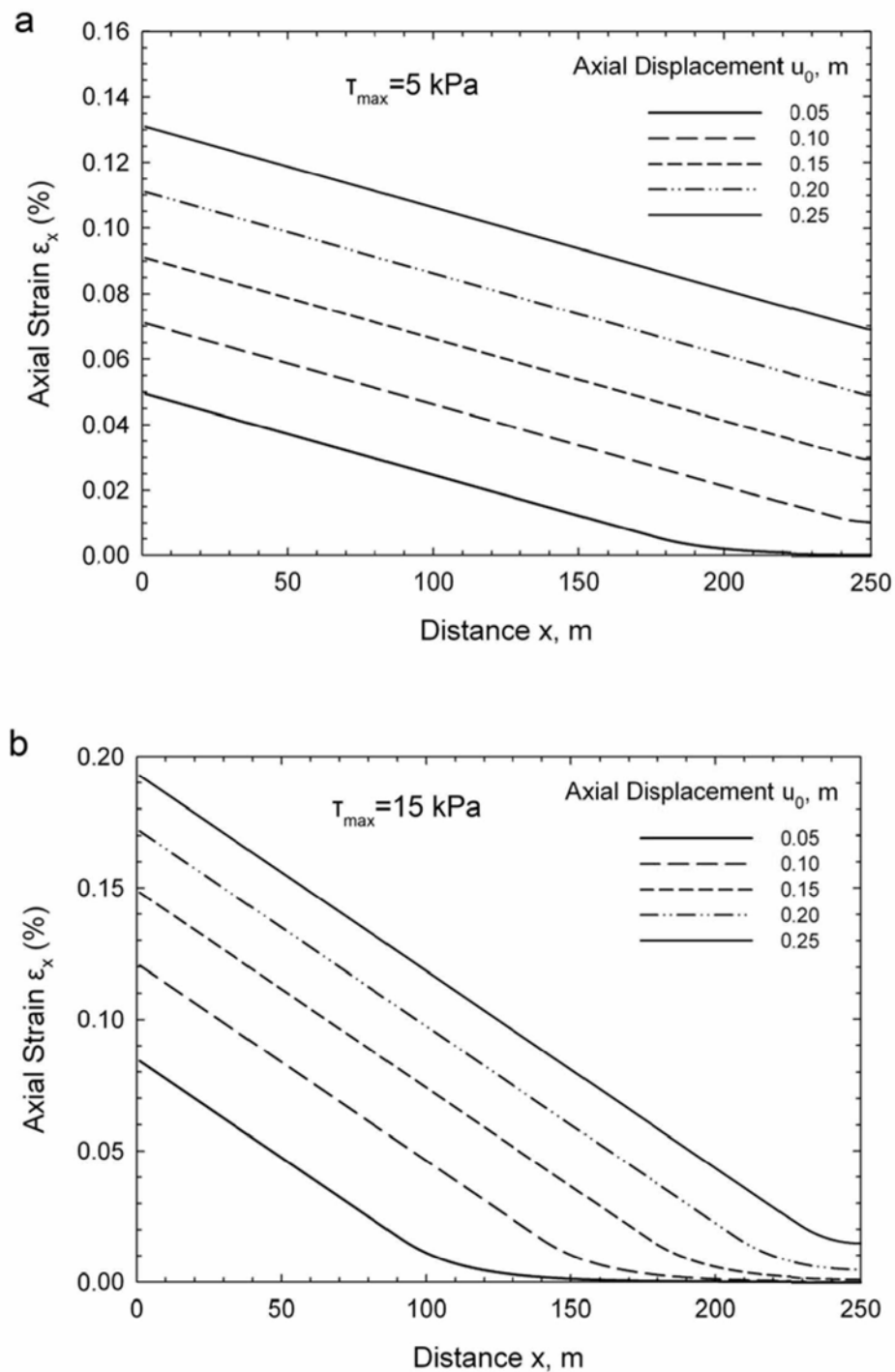### 3.5.2 Finite-length pipeline subjected to tension

For the case of a finite-length pipeline segment, which is restrained at the far end and subjected to a pull-out displacement at the near end, five different values of pipeline length L_a are considered, namely 100, 150, 200, 250 and 500 m.

Figures 3.20a and 3.20b plot the pipeline length L_s along which sliding takes place during application of the pull-out displacement for interface shear strength τ_{max} equal to 5 kPa and 15 kPa, respectively. It is evident from Figure 3.20 that for $L_a \leq 250$ m, the value of L_s is only slightly lower than the value of L_a; thus, sliding occurs along most of the length L_a of the pipeline.

Figure 3.21 plots the force-displacement relationship for different values of L_a and τ_{max}. As expected, for small values of L_a (≤ 250 m), the effect of soil resistance is significantly reduced and the magnitude of the force depends on the proximity of the fixed-end of the pipeline.

This is also shown in Figure 3.22 that plots the distribution of the force along the pipeline length for $L_a = 250$ m and for different values of pull-out displacement and τ_{max}. A comparison between the results of Figures 3.17a and 3.22a, corresponding to a low value of $\tau_{max} = 5$ kPa, demonstrates that the pipeline length has a significant effect. If the length is insufficient, as for example in Figure 3.22a, a significant portion of the force is transferred at the fixed end. By contrast, comparison of the results in Figures 3.17b and 3.22b for a soil having an interface strength of $\tau_{max} = 15$ kPa, suggests that for relatively high values of interface strength, the pipeline length has small influence on the force magnitude and distribution.

Finally, Figures 3.23 and 3.24 plot the distribution of axial displacement and axial strain, respectively, along a pipeline having a length of $L_a = 250$ m and subjected to tension. The results are given for various values of pull-out displacement and for interface shear strengths equal to $\tau_{max} = 5$ kPa and 15 kPa. Comparison with the results in Figures 3.18 and 3.20, for an infinite pipeline length, leads to similar to the above conclusions.
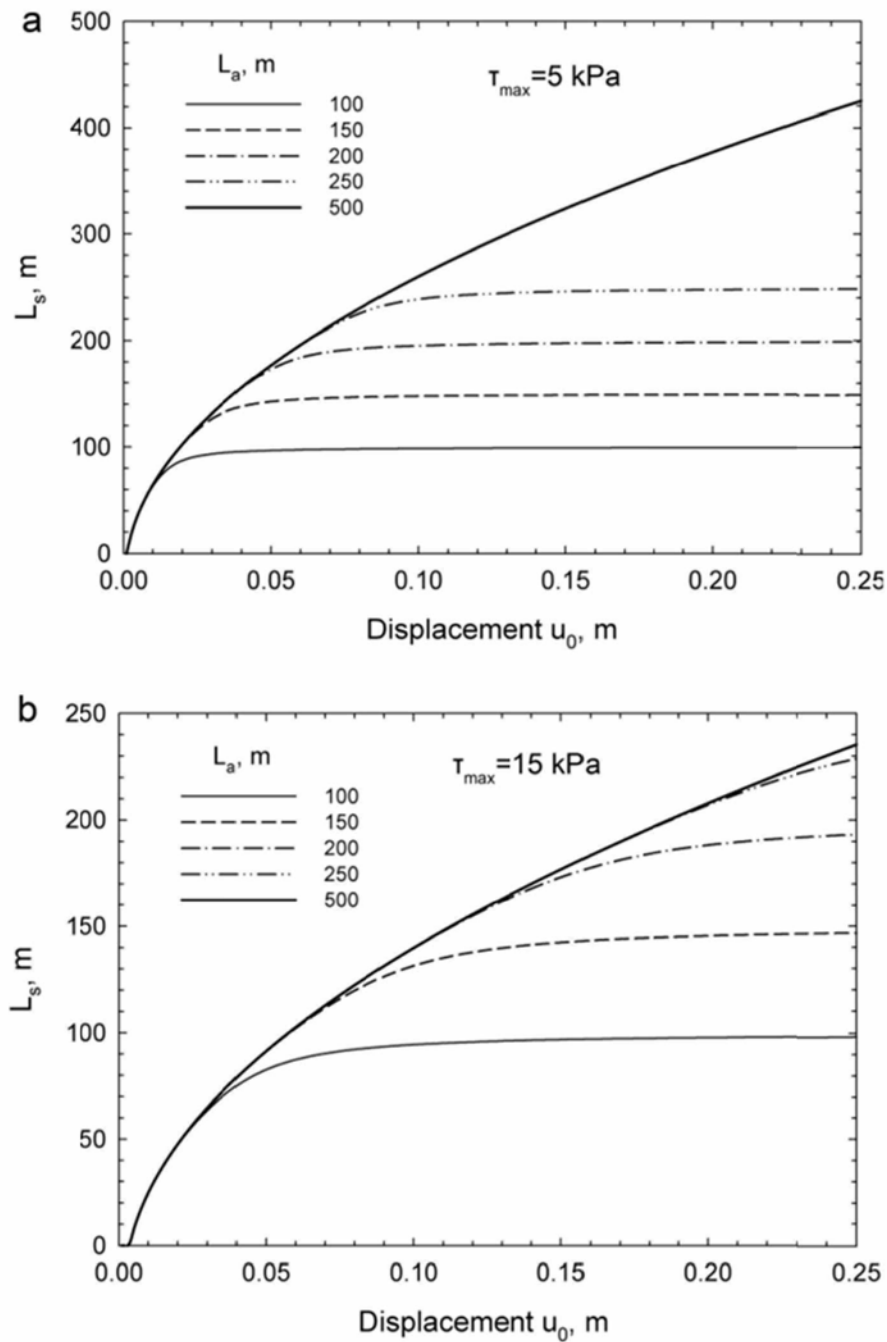
Figure 3.20: Sliding length versus pull-out displacement of a pipeline subjected to tension for various values of pipeline length and interface shear strength equal to: (a) τ_{max} = 5 kPa and (b) τ_{max} = 15 kPa.

Figure 3.21: Force versus pull-out displacement of a pipeline subjected to tension for various values of pipeline length and interface shear strength equal to: (a) τ_{max} = 5 kPa and (b) τ_{max} = 15 kPa.

Figure 3.22: Distribution of axial force along a finite-length pipeline ($L_a = 250$ m) subjected to tension for various values of pull-out displacement and interface shear strength equal to: (a) $\tau_{max} = 5$ kPa and (b) $\tau_{max} = 15$ kPa.

Figure 3.23: Distribution of axial displacement along a finite-length pipeline ($L_a = 250$ m) subjected to tension for various values of pull-out displacement and interface shear strength equal to: (a) τ_{max} = 5 kPa and (b) τ_{max} = 15 kPa.

Figure 3.24: Distribution of axial strain along a finite-length pipeline ($L_a = 250$ m) subjected to tension for various values of pull-out displacement and interface shear strength equal to: (a) $\tau_{max} = 5$ kPa and (b) $\tau_{max} = 15$ kPa.

3.6 Nonlinear spring versus beam elements for pipeline extension

It is of interest to evaluate the performance of the previously proposed hybrid finite-element soil-pipe system enhanced with the analytically-derived non-linear springs representing the pipeline end conditions. To this end, two different models of the soil-pipe system are considered, having the same basic finite-element model of length equal to 60 m, referred to in the following as Model M60. This basic model is enhanced to form two new models:

(a) Model M60-NS is formed by incorporating the force-displacement equations in the form of nonlinear springs at each end of the model M60 pipeline. For a pipeline extension length equal to L_a, the total length of the simulated pipeline-soil model in M60-NS is $L = 60 + 2L_a$.

(b) Model M60-B is formed by adding structural beam elements, having stiffness characteristics identical to those of the pipeline section and supported by distributed nonlinear springs representing the stress-displacement relationship at the pipe-soil interface, shown graphically in Figure 3.15b. The total length of the simulated pipeline-soil model in M60-B is $L = 60 + 2L_a$.

Figure 3.25a compares the displacement of the pipeline in the x direction versus the distance from the fault, obtained from the M60 model extended by beam elements (M60-B) and the proposed nonlinear-spring model (M60-NS). The results are compared for two values of total length L of the system equal to 200 m and 2000 m, respectively, and fault displacement $d = 2$ m. As shown in Figure 3.25a, the results from the two approaches are identical. Similarly identical results were obtained for all of values of model length L examined, namely, 100, 200, 400, 500, 600, 700 and 2000 m.

Fig. 3.25b plots the axial normal strain in terms of the distance from the fault, showing also an excellent agreement between the two approaches.
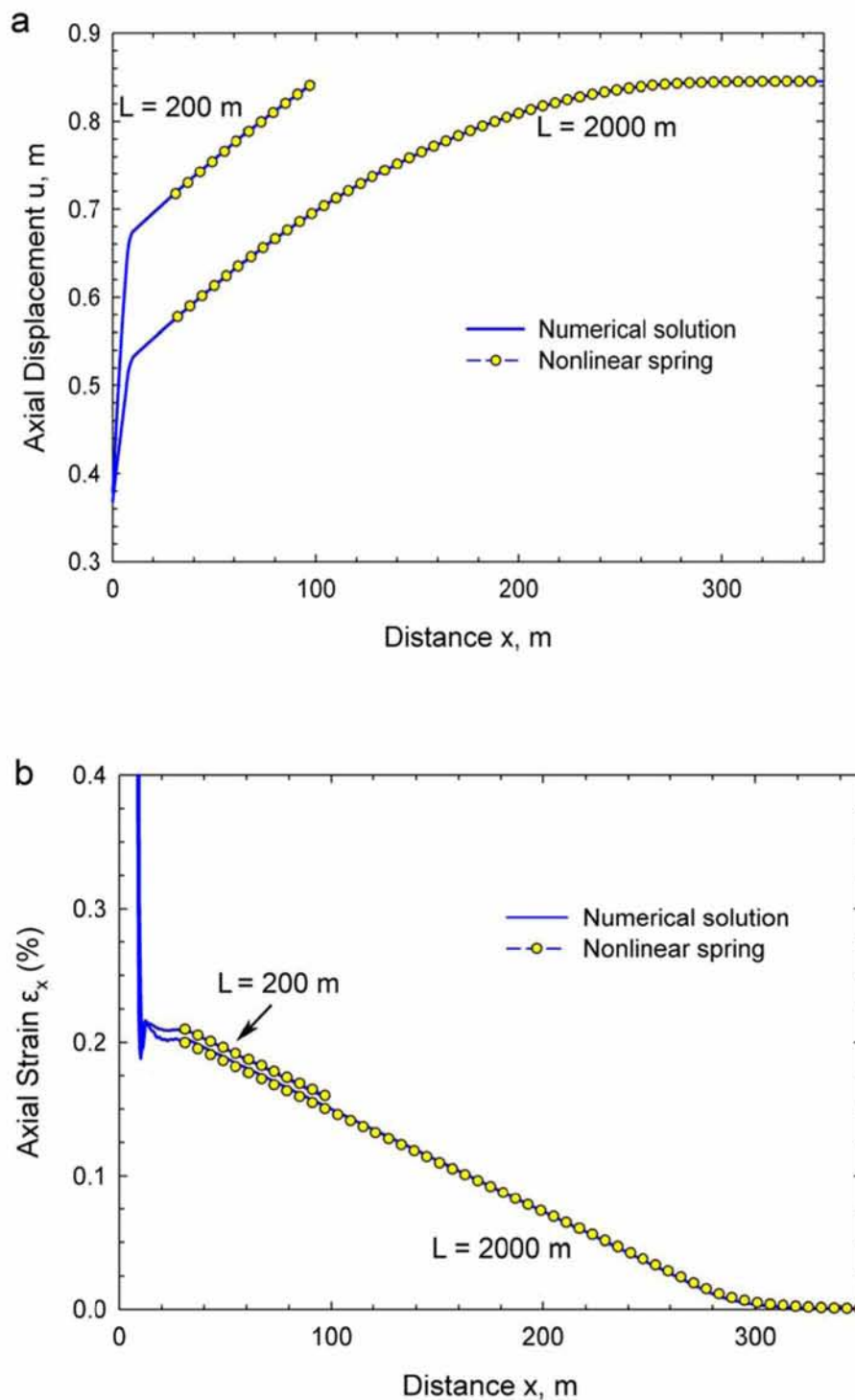
Figure 3.25: Comparison of numerical results using the 60 m long FE model extended by beam elements with distributed nonlinear springs (M60-B, solid blue line) and the proposed nonlinear spring solution (M60-NS, circles with dashed blue line): (a) axial displacement and (b) axial strain versus distance from the fault plane. (Fault movement d = 2 m, interface friction coefficient μ = 0.3).

3.7   Sensitivity on finite-element mesh refinement

Given the fact that the majority of pipeline deformation occurs near the fault, due to bending, the finite-element mesh of model M60 is relatively dense in the central region near the fault ("fault bending zone"), whereas it is much coarser in the more distant regions. However, in the case of softer soil conditions or stiffer pipe sections, the pipe-soil interaction region may extend beyond the limits of the refined, highly-strained central region of model M60 and, therefore, it might not be simulated accurately by the coarse mesh assumed in this region. In order to investigate the effect of mesh refinement away from central "fault bending zone" on the pipeline performance, a significantly more refined finite-element model is also considered, as shown in Figure 3.26. The fault angle β in this model is equal to 25°.
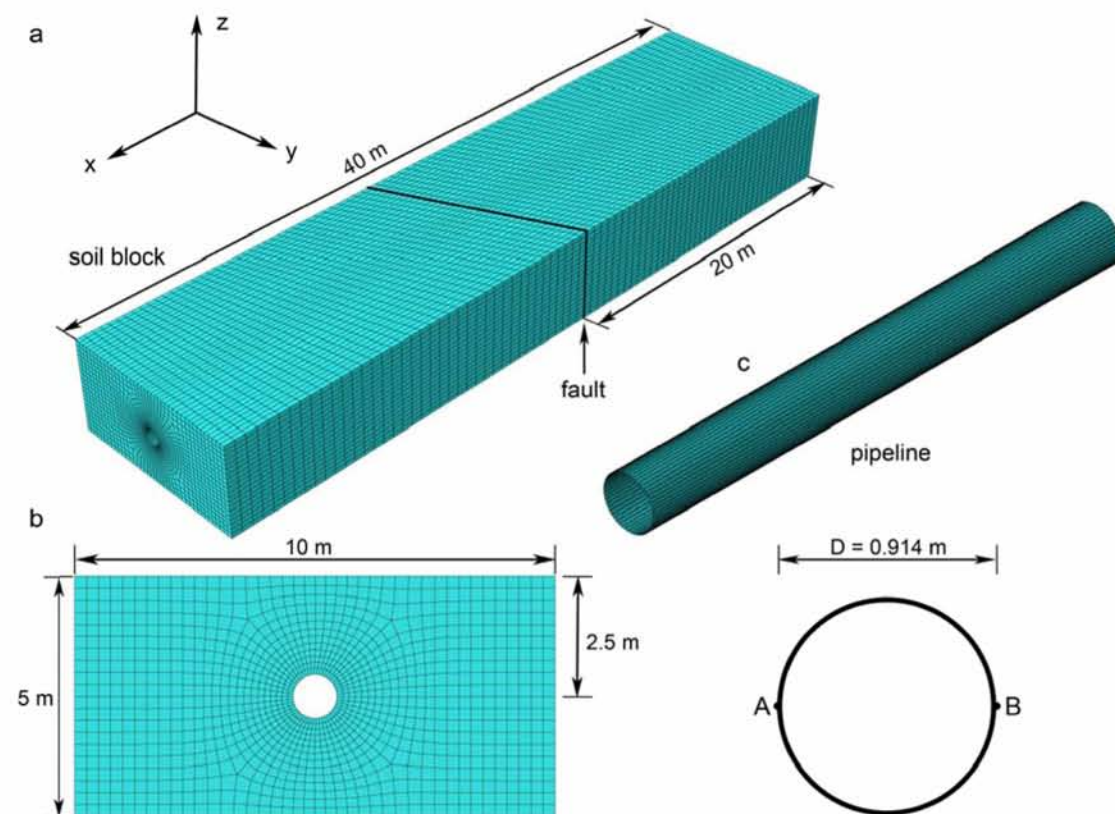
Figure 3.26: Model M40 for a fault angle β equal to 25°: Finite element discretization of the (a) soil prism with tectonic strike-slip fault (b) soil prism cross-section and (c) the steel pipeline.

This model has a soil prism length equal to 40 m and is referred to as M40 in the following. It consists of a total of about 140,000 elements and 145,300 nodes, whereas at the two ends of the pipeline it is extended by the proposed nonlinear springs given by equation (3.23) corresponding to an infinitely long pipeline. In addition to the model M40 shown in Figure 3.26 forming an angle β equal to 25°, two similarly refined models have been developed in the course of the present study for β equal to 0° and $45°$.

Figure 3.27a plots the displacement in the x direction versus the distance from the fault, evaluated at the left side being under tension and at the right side being under compression (points A and B, respectively, in Figure 3.26c) for fault displacement $d = 1$ m. The results are compared to those from model M60, in which the pipeline is extended also with the same nonlinear spring.

Similarly, Figure 3.27b plots the axial normal strain at generators A and B versus the distance from the fault. The different values of displacement and strain along the two generators A and B in Figure 3.27 is due to the significant effect of bending of the pipeline; for $d = 1$ m the maximum axial strains occur at about 4 m from the fault location (x=0). In any case, the comparison between the two models shows that the results are in good agreement. Also from Table 3.2 similar conclusions can be obtained.

Comparison of models M60-NS and M40-NS is also conducted for two other fault angles. In the case of $\beta = 0°$, the pipeline axis is normal to the fault plane that moves laterally. Thus, at relatively small fault displacements, the pipe is subjected mainly to bending, resulting to local buckling formation. Numerical results are obtained from both models, assuming infinite pipeline length. As shown in the second column of Table 3.3, the critical fault displacement predicted by the two models is identical. In this case, the flattening and the 3% or 5% tensile-strain performance criteria have little meaning because of the rapid localization of deformation, which is associated with significant cross-sectional distortion and wrinkling of pipe wall. In any case, the analysis has been continued to reach these limit states as well. The corresponding values of fault displacements computed by the two models are also in reasonable agreement despite the fact that the critical cross-section is already significantly distorted due to buckling.

Furthermore, in the case of $\beta = 45°$, in addition to the imposed lateral movement equal to $d \cos \beta$, the pipeline is subjected to overall extension by $d \sin \beta$, simulated by the M60-NS and M40-NS models, having nonlinear springs at the pipeline ends.
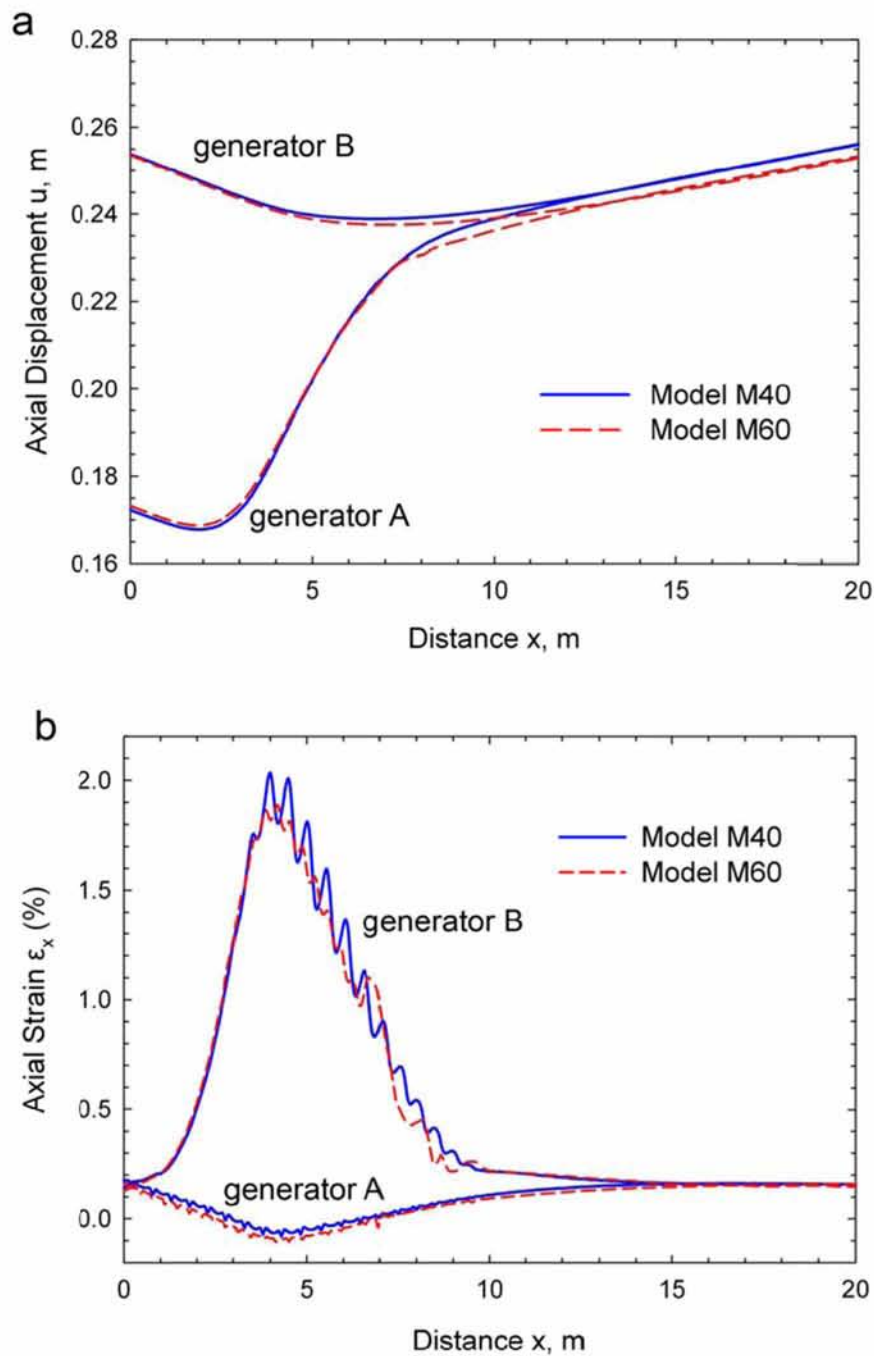
Figure 3.27: Comparison of results using Models M40-NS and M60-NS, having equivalent nonlinear springs extensions at the pipeline ends: (a) displacement and (b) axial strain versus distance from the fault plane (fault movement d=1m, friction coefficient μ=0.3, β=25°).

The comparison between the two models is summarized in Table 3.4, and shows that the results are again in reasonable agreement. Based in all previous comparisons, it can be concluded that model M60-NS can be employed for an efficient simulation of pipeline behavior.

Table 3.2. Critical fault displacement for various performance criteria ($\beta = 25°$)

Model (length L, m)	Critical fault displacement, m		
	Local buckling	Strain 3%	Strain 5%
M60-NS, (∞)	None	1.73	2.17
M40-NS, (∞)	None	1.70	2.31

Table 3.3. Critical fault displacement for various performance criteria ($\beta = 0°$)

Model (length L, m)	Critical fault displacement, m		
	Local buckling	Strain 3%	Strain 5%
M60-NS, (∞)	0.43	1.13	>4.00*
M40-NS, (∞)	0.43	1.14	>4.00*

* Not reached within a maximum fault movement of d=4 m

Table 3.4. Critical fault displacement for various performance criteria ($\beta = 45°$)

Model (length L, m)	Critical fault displacement, m		
	Local buckling	Strain 3%	Strain 5%
M60-NS, (∞)	None	1.08	1.40
M40-NS, (∞)	None	1.04	1.50

3.8 Effect of the width of the finite-element soil prism

Considering a soil prism length in the x direction equal to 65 pipe diameters, and in z direction equal to 5 times the pipe diameter, the effect of the width in y direction of the soil prism is parametrically investigated considering the following values of 10m, 30m, 50m, and 70m (Figure 3.28). Two values of the fault angle β are considered, namely, $\beta = 0°$ and $\beta = 25°$. Nonlinear springs are used at the ends of the pipe to account for an infinitely long pipeline (M60-NS). The top surface of the prism represents the soil surface, and the burial depth is chosen equal to about 2 pipe diameters, which is in

accordance with pipeline engineering practice. The central part of the pipeline, where maximum stresses and strains are expected, has a fine mesh of elements. A total of 54 shell elements around the cylinder circumference in this central part have been found to be adequate to achieve convergence of solution, whereas the size of the shell elements in the longitudinal direction has been chosen equal to $1/26^{th}$ of the pipeline outer diameter D. This mesh has been shown capable of describing the formation of short-wave wrinkling (local buckling) on the pipeline wall. The mesh chosen for the pipe parts far from the fault location is significantly coarser.

Similarly, the finite element mesh for the soil is more refined in the region near the fault and coarser elsewhere. The soil mesh distance at the longitudinal direction near fault is 0.33m, and 2.5m away from the fault. A number of 28 solid elements accounting for soil behavior around the circumference of the pipeline is found to be adequate for the purposes of our analysis. In Figure 3.29 the deformed mesh of a pipe-soil system corresponding to a 30m width is shown.

The critical fault displacement results from the models having four different width sizes is summarized in Tables 3.5 and 3.6, for $\beta = 0°$ and 25°, respectively. By comparison of the results for each performance criterion, it is evident that the four models are in reasonable agreement.
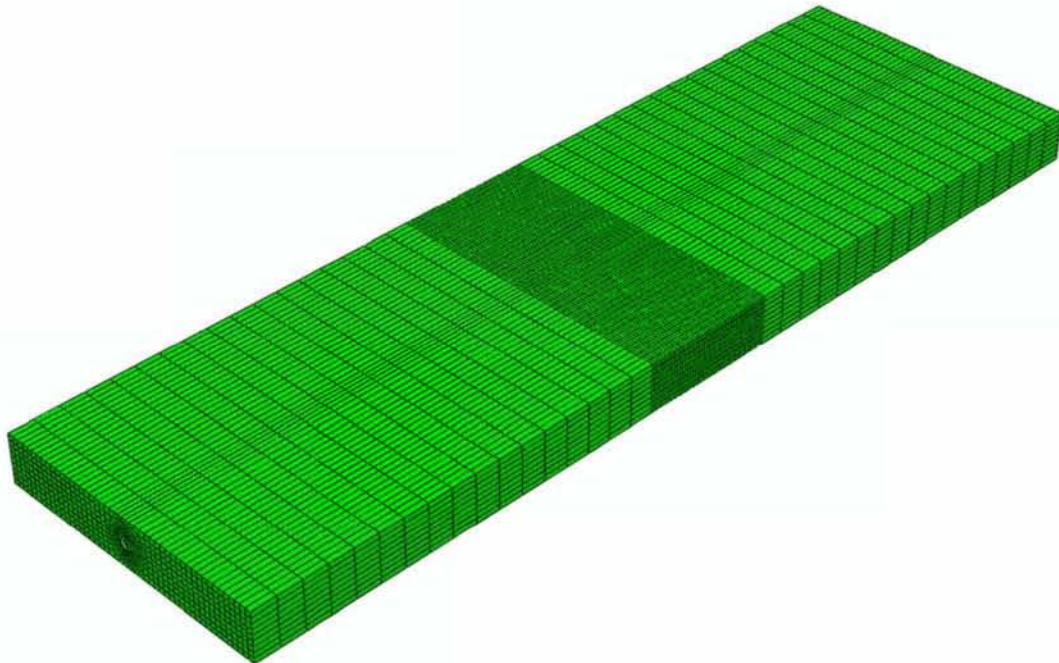
Figure 3.28: Finite element model of the soil-pipeline system having a width equal to 30m and a tectonic strike-slip fault with an angle $\beta = 0°$.
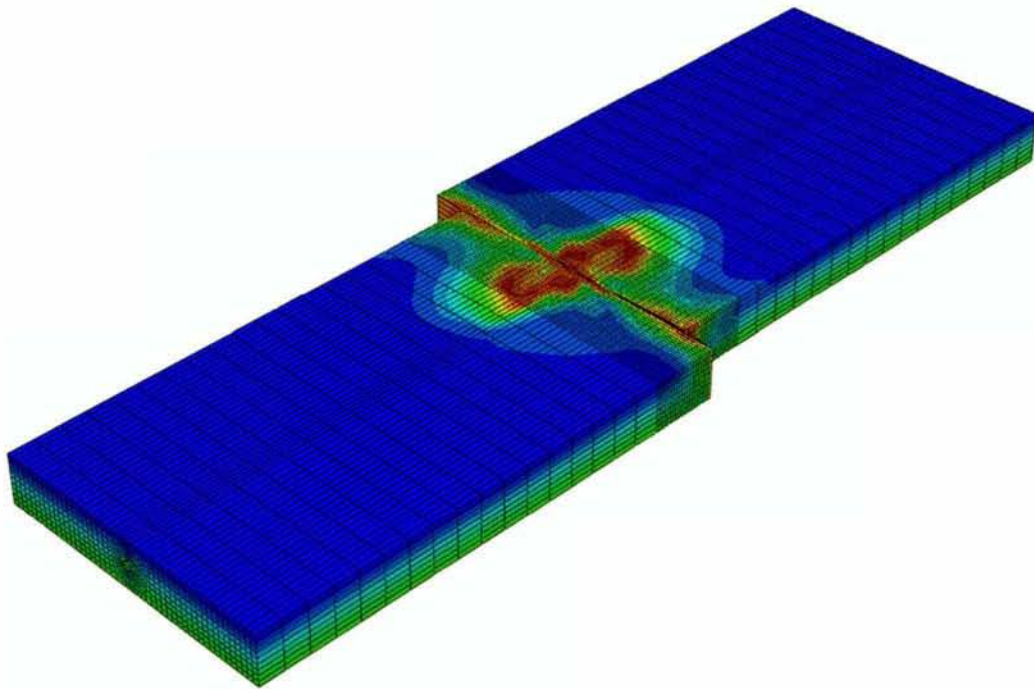
Figure 3.29: Deformation of pipeline-soil system, having a width equal to 30m, subjected to fault displacement at an angle $\beta = 0°$.

Table 3.5. Critical fault displacement for various performance criteria ($\beta = 0°$)

Model (M60-NS)	Critical fault displacement, m		
	Local buckling	Strain 3%	Strain 5%
Width 10m	0.42	1.60	>4.00*
Width 30m	0.44	1.62	>4.00*
Width 50m	0.44	1.67	>4.00*
Width 70m	0.44	1.67	>4.00*

* Not reached within a maximum fault movement of d=4 m

Table 3.6. Critical fault displacement for various performance criteria ($\beta = 25°$)

Model (M60-NS)	Critical fault displacement, m		
	Local buckling	Strain 3%	Strain 5%
Width 10m	none	0.79	1.32
Width 30m	none	0.79	1.41
Width 50m	none	0.80	1.43
Width 70m	none	0.80	1.43

* Not reached within a maximum fault movement of d=4 m

3.9 Effect of the depth of the finite-element soil prism

In order to investigate the effect of soil prism depth, two different numerical models having depths equal to 5m (Figure 3.30) and 25m (Figure 3.32), respectively, are considered. The embedment depth of the pipeline in both models is equal to two pipe diameters below the top surface. The fault movement is applied by imposing the same displacement at the base and the vertical boundaries of the moving block. By doing so, the same critical fault displacement is obtained from two models. Figures 3.31 and 3.33 show the same lateral displacement along the depth. Therefore, the effect of depth may be obscured when the above boundary conditions are used for simulating the fault movement. In that case no fault propagation is taken into consideration. The critical fault displacement is considered to be near the pipeline plane. This explains the fact why the depth of the model was limited to five pipe diameters and was not extended to a larger depth, which would lead to a more demanding model with respect to computation time.

In all previous models, fault movement is realized by a uniform horizontal displacement applied on the nodes of the vertical and base boundaries of the moving block. Alternatively, by using a model which takes into account soil movement propagation from the rock base to the ground surface, the resulting critical fault displacement for pipeline failure (measured at the rock base) is higher. In this case, shown in Figure 3.34, the base and the vertical boundary that is normal to the pipeline are subjected to movement equal to the fault displacement, whereas the other two vertical boundaries are let to deform "freely", but having tied their corresponding opposite nodes (i.e., having the same x and z coordinates). As a result of this multiple-point constraint between the two vertical boundaries nodes, a non-uniform displacement zone develops between the bottom of the prism and the ground surface, leading to a smaller displacement at the pipeline plane. Therefore, for the same mechanical and geometric properties of the soil-pipe system, the model in Figure 3.34 yields greater critical displacement for pipeline failure, compared to the model in Figure 3.33. This kind of simulation, in some cases, may lead to more realistic soil deformation patterns, but in general it may also lead to additional difficulties regarding the interpretation of the pipeline performance criteria, as the latter may be affected by the depth and properties of the soil stratum.
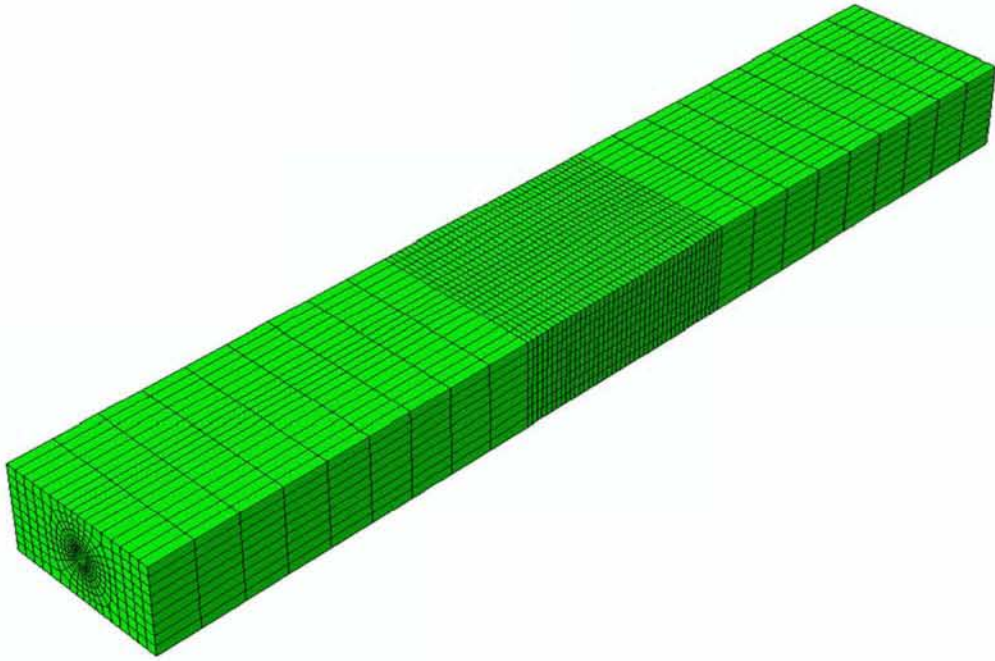
Figure 3.30: Finite element model of the soil prism having a depth of 5 m, with tectonic strike-slip fault at an angle β=0°.
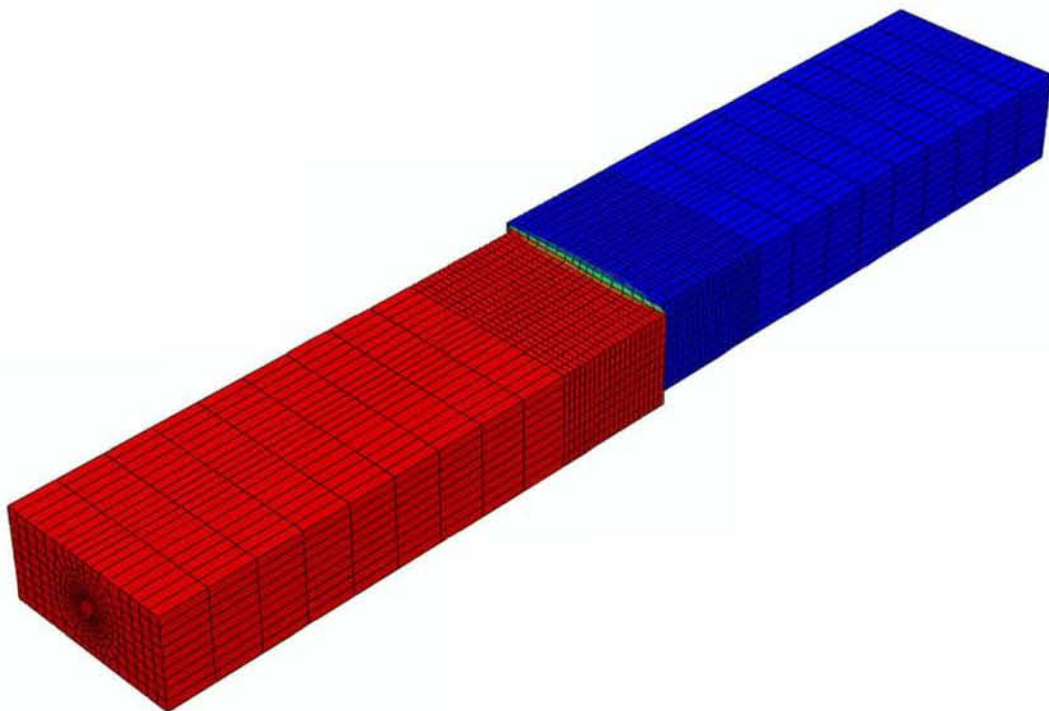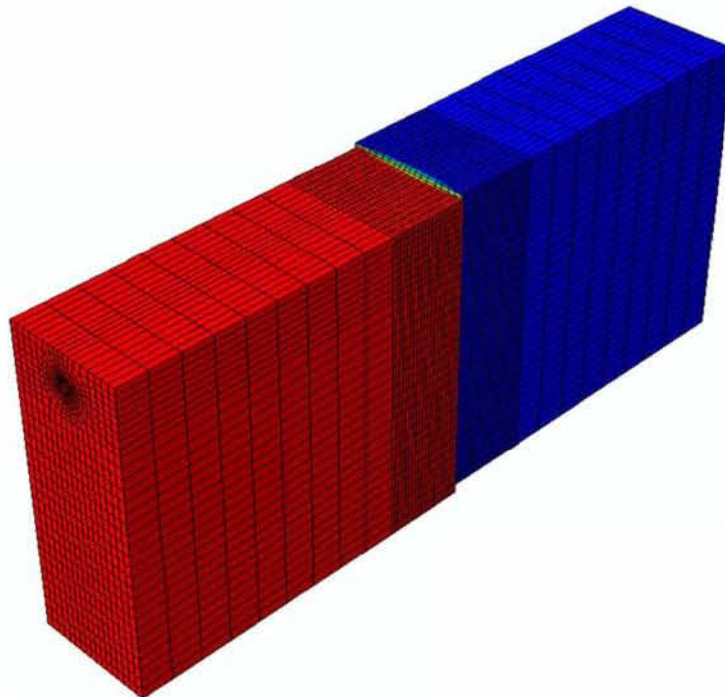

Figure 3.31: Lateral displacement of pipeline-soil system, having a depth of 5 m, after fault displacement (β=0°).
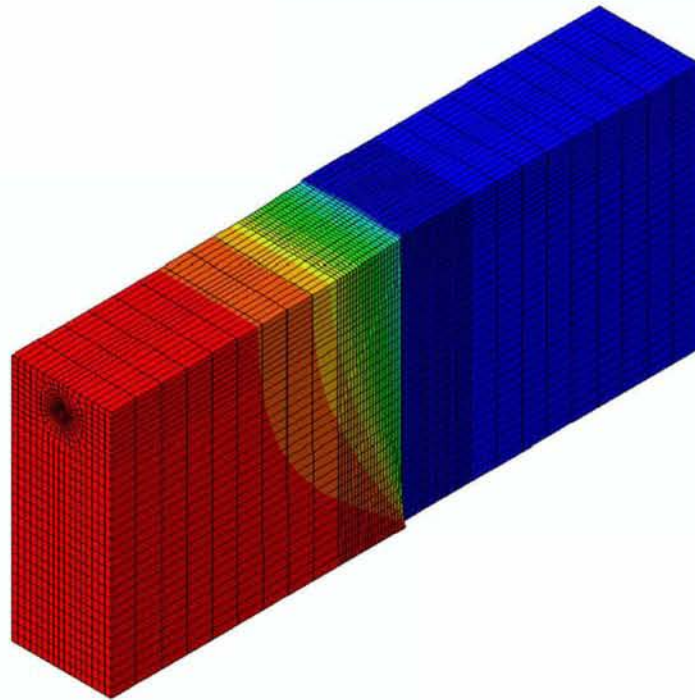
Figure 3.32: Finite element model of the soil prism, having a depth of 25 m, with tectonic strike-slip fault at an angle $\beta=0°$.

Figure 3.33: Lateral displacement of pipeline-soil system, having a depth of 25 m, after fault displacement ($\beta=0°$).

Figure 3.34: Deformation of pipeline soil system after fault displacement using MPC in soil nodes (depth equal to 25m).

4   Buried Pipelines Normal to Fault Plane

4.1   Introduction

The mechanical behavior of buried steel pipelines, crossing an active strike-slip tectonic fault at a right angle is examined in this chapter. Figure 4.1 illustrates the numerical model, in which the fault plane is normal to the pipeline direction, and the displacement of the moving block in the horizontal y direction, causing stress and deformation in the pipeline.
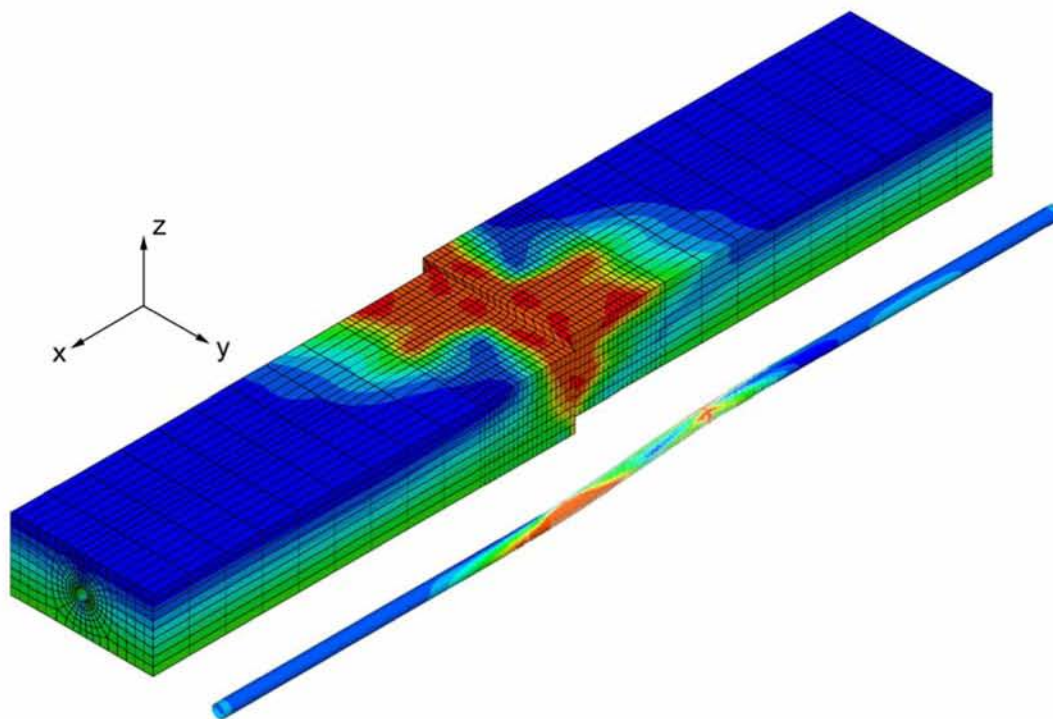
Figure 4.1: Finite element discretization of the soil prism with tectonic strike-slip fault perpendicular to pipeline (angle $\beta = 0°$)

The interacting soil-pipeline system is modeled rigorously through finite elements, which account for large strains and displacements, nonlinear material behavior and special conditions of contact and friction on the soil-pipe interface. Considering steel pipelines of various diameter-to-thickness ratios, and typical steel material for pipeline applications (API 5L grades X65 and X80), this chapter focuses on the effects of various soil and pipeline parameters on the structural response of the pipe, with particular

emphasis on identifying pipeline failure (pipe wall wrinkling/local buckling or rupture). The effects of shear soil strength, soil stiffness, horizontal fault displacement, width of the fault slip zone, are also investigated. Furthermore, the influence of internal pressure on the structural response is examined.

The results from the present investigation are aimed at determining the fault displacement at which the pipeline fails and can be used for pipeline design purposes. The results are presented in a diagram form, which depicts the critical fault displacement, and the corresponding critical strain versus the pipe diameter-to-thickness ratio. The numerical results for the critical strain are also compared with recent provisions of EN 1998-4 and ASCE MOP 119. The results consider a basic finite-element model length equal to sixty meters. Results are also obtained for infinite model length. Comparison between finite and infinite model length shows similar mechanical behavior of the pipeline-soil system.

4.2 Numerical results for finite length

Using the above numerical simulation tools described in Chapter 3, results are obtained for steel pipelines for various values of the diameter-to-thickness ratio, as well as for different soil conditions. In all cases considered in this chapter, the outer pipe diameter of the pipe D is assumed equal to 914.4 mm (36 in), whereas the pipe wall thickness ranges from 6.35 mm (¼ in) to 19.05 mm (¾ in), so that a range of D/t values between 48 and 144 is covered. This range of D/t values is typical for onshore applications.

The surrounding soil has dimensions 60m×10m×5m in directions x, y, z respectively. The seismic fault plane is located at the middle cross-section of the pipeline.

In sections 4.2.1 and 4.2.2, steel pipelines with API 5L [54] X65 steel material and thickness equal to 12.7 mm (0.5 in) are examined under cohesive and non-cohesive soil conditions, respectively, using appropriate values of soil parameters c, φ and E. The influence of the effects of internal pressure, the influence of steel material hardening on the structural response and the failure mode are investigated.

Subsequently, in section 4.2.3, X65 pipelines with different values of the diameter-to-thickness ratio D/t are analyzed, to identify the influence of the diameter to thickness ratio on the structural response. Finally, high-strength steel X80 pipelines under fault imposed deformations are analyzed in section 4.2.4.

4.2.1 Moderately thick X65 steel pipeline in cohesive soils

A moderately thick-walled X65 pipeline is considered first, with diameter and thickness equal to 914.4 mm (36 in) and 12.7 mm (0.5 in) respectively, so that D/t =72. The API 5L X65 steel is a typical material for oil and gas pipeline applications, with a nominal stress-strain curve shown with solid line in Figure 4.3a, obtained from a uniaxial tensile test. The yield stress σ_y and ultimate stress σ_u are equal to 450 MPa (65 ksi) and 560 MPa (81.2 ksi), respectively, with a 30% elongation at the ultimate stress ($\varepsilon_u = 0.3$). Considering a safety (reduction) factor equal to 0.72 [55, 56], the maximum operating pressure max p of this pipeline, given by the following expression can be readily calculated equal to 9 MPa (90 bar).

$$p_{max} = 0.72 \times \left(2\sigma_y \frac{t}{D} \right) \tag{4.1}$$

This expression is plotted versus the D/t value with the dashed blue line in Figure 4.2. The pipeline is assumed to be embedded in a soft-to-firm clay and crossing a fault zone of width w equal to 0.33 m. Its internal pressure, p, is taken initially to be equal to zero, but it is increased subsequently to the maximum value. The soft-to-firm clay, referred to as Clay I, has a cohesion c = 50 kPa, friction angle φ=0°, Young's modulus E = 25 MPa and Poisson's ratio v = 0.5. The clay is assumed to respond under "undrained conditions", which implies zero volumetric strains and a relatively higher Young's modulus.
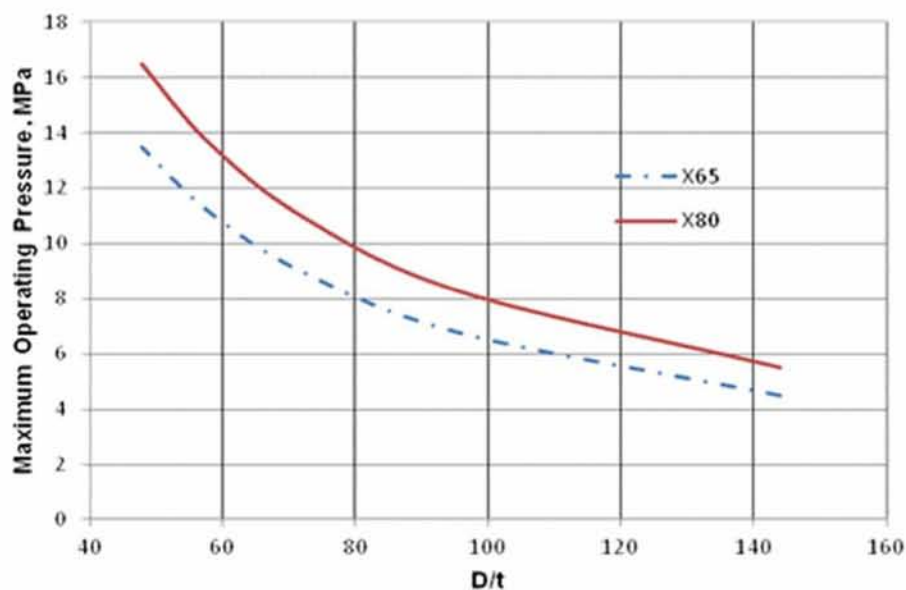
Figure 4.2: Variation of maximum operating pipeline pressure with respect to the diameter-to-thickness ratio D/t.
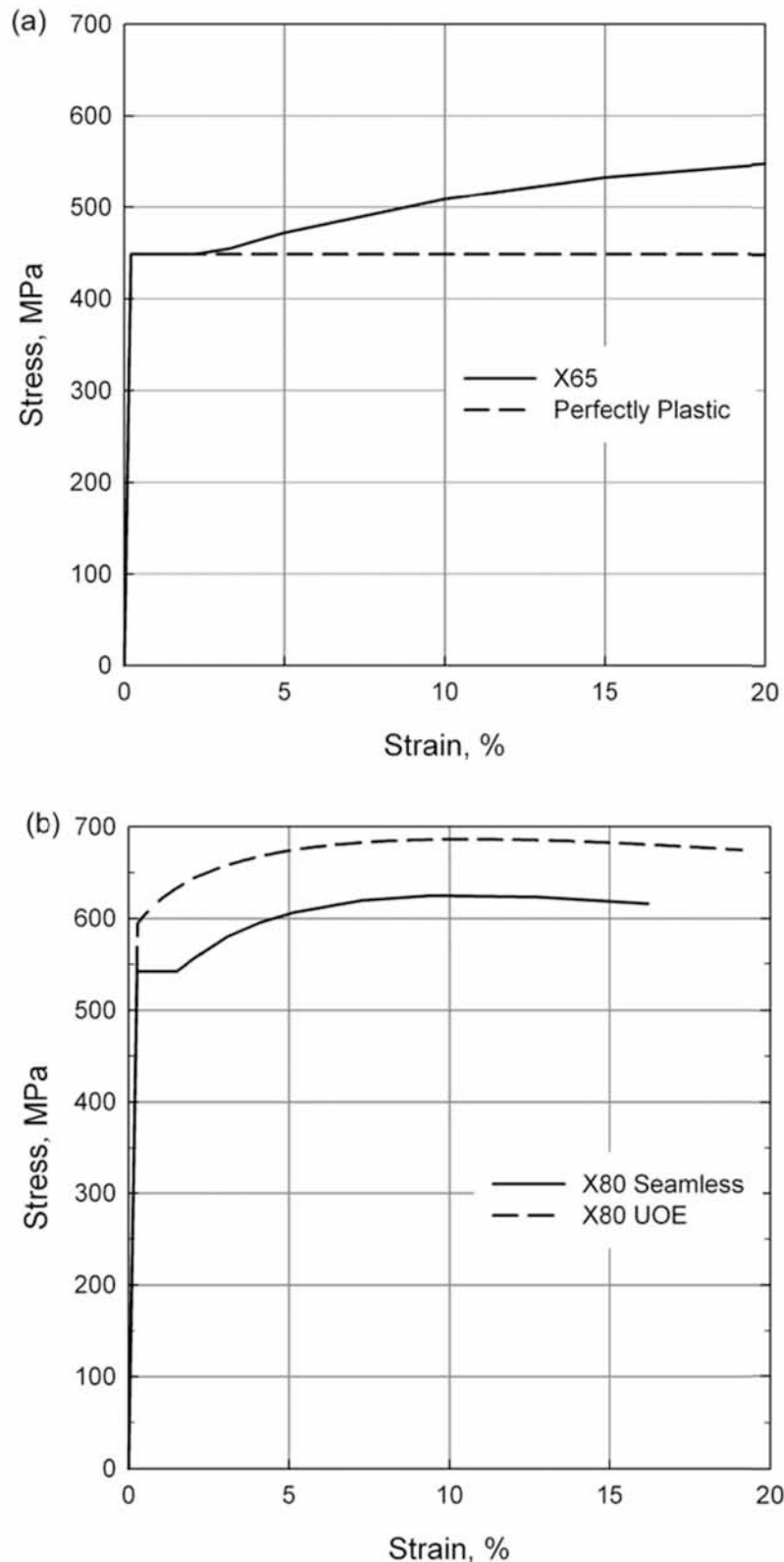
Figure 4.3: Uniaxial stress-strain relation for (a) API 5L X65 steel; (b) API 5L X80 steel.

Figure 4.4a depicts the shape of the deformed pipeline at fault displacements d = 1 m, 2 m, 3 m and 4 m in the area near the fault. Moreover, Figure 4.4b plots depicts the shape of the deformed pipeline and the distribution of the minor principal strain ε_3 (indicating

maximum compressive strains) on its outer surface at fault displacement equal to $d = 1$ m and $d = 4$ m.
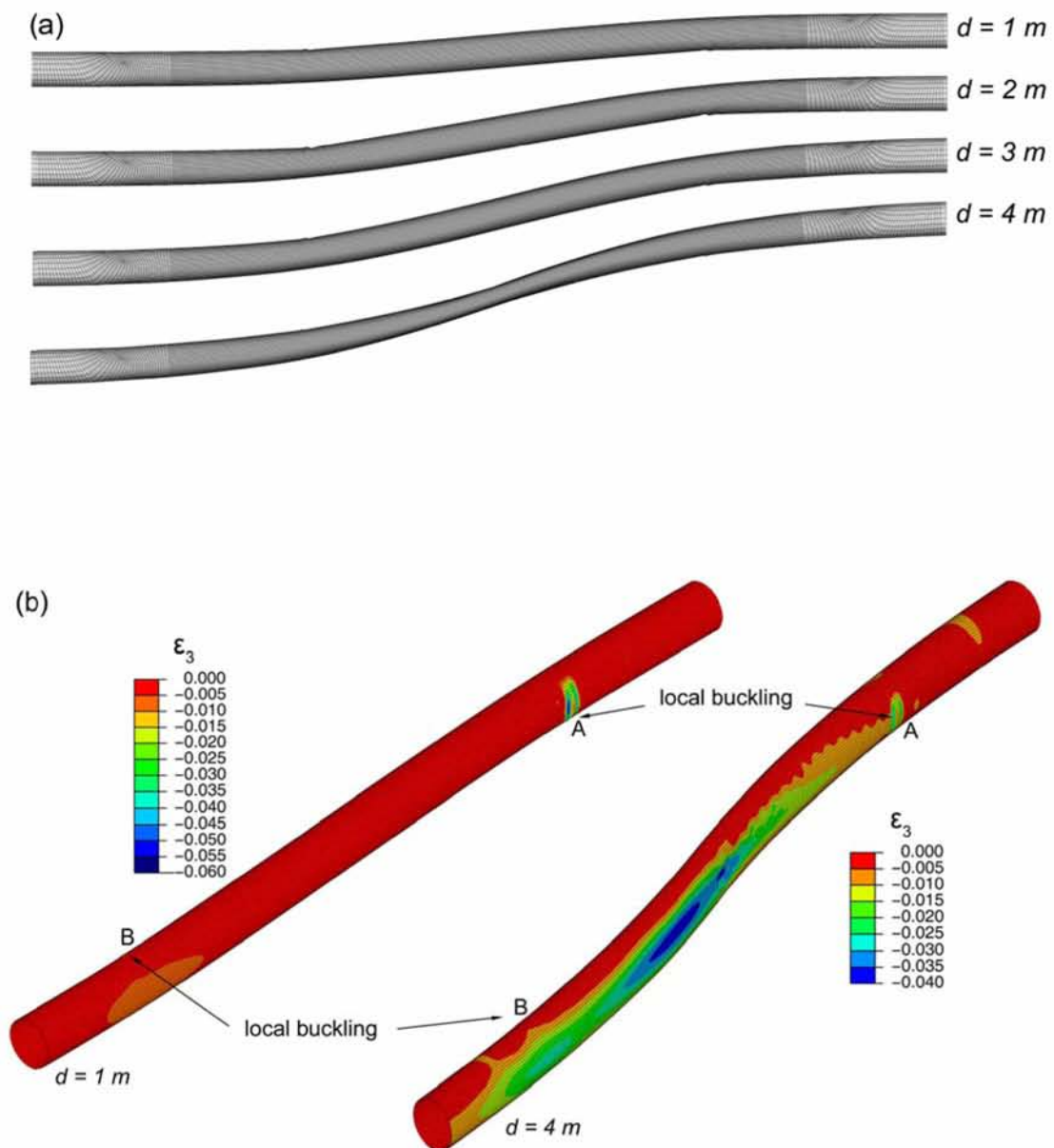
Figure 4.4: (a) Plan view of deformed shape of the pipeline for d = 1m, 2m, 3m, and 4m (b) Distribution of minor principal strain ε_3 for seismic fault displacements equal to 1 m and 4 m. (X65 pipe, D/t= 72, Clay I, w = 0.33 m, p = 0).

The deformed shape of the pipeline at $d = 1$ m shows a localized deformation at point A, referred to as "local buckling" or "kinking", whereas point A is the "critical location" of the pipeline, at a distance of 5.45 m from the fault. Due to the skew-symmetry of the problem, a similar local deformation pattern occurs at point B, on the hidden side of the pipeline. Under increasing fault movement, a substantial development of this localized deformation pattern is observed, associated with the distortion of a significant part of

the pipeline around this area, as shown in Figure 4.4b, for a fault displacement of $d = 4$ m. Furthermore, at the critical location of point A for $d = 1$ m (Figure 4.4b), there are two zones of compressive strains reaching a maximum value of 5.7%.

As the pipeline length increases with continued fault movement, it results to higher tensile and smaller compressive strains in the longitudinal direction. This is shown in Figure 4.4b, where for a fault displacement of $d = 4$ m, the maximum compressive strains in the two aforementioned zones at point A decrease to 3.2%. This overtaking of the tensile strains after some critical value of d is discussed later in this chapter.

Figure 4.5 shows two consecutive deformed shapes of the pipeline at fault displacements d equal to 0.2 m and 1 m, whereas Figure 4.6 plots the same deformed shapes in a plan view. The localized buckling pattern depicted in Figure 4.5 and Figure 4.6 develops on the critical location along the pipeline, where the compressive stresses and strains, and the corresponding bending curvature reach a maximum value.
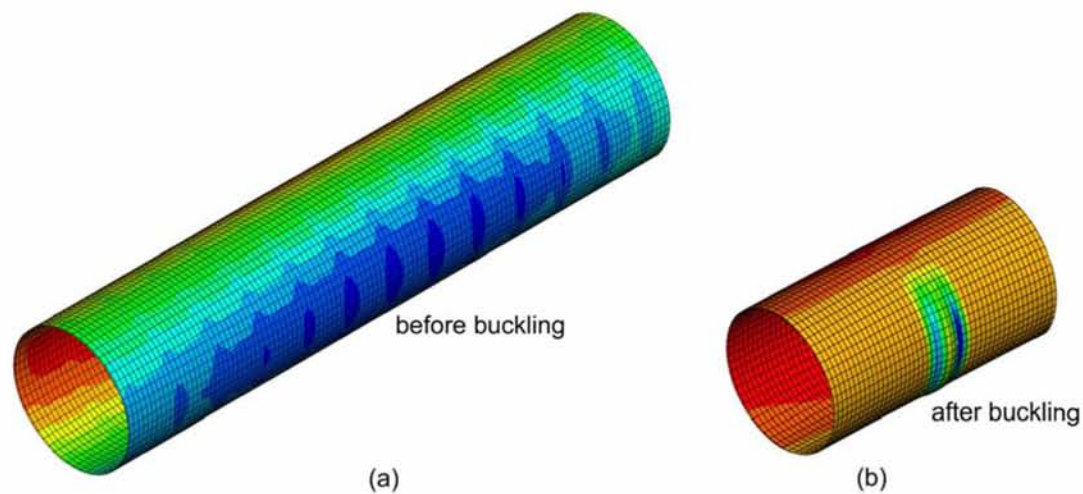
Figure 4.5: Details of the critical pipeline area: (a) transition from a smooth configuration to a wavy pattern, which is quasi-uniform along the pipeline; (b) local buckling formation (X65 pipe, D/t =72, Clay I, w =0.33m, p = 0).
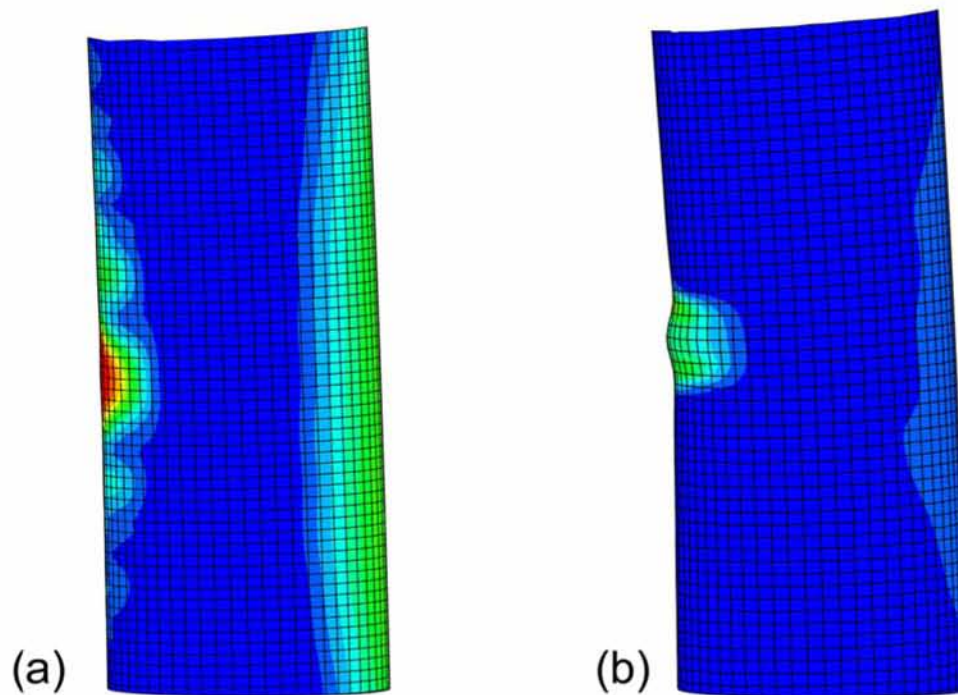
Figure 4.6: Variation of equivalent plastic shear strain at the critical pipeline area: (a) transition from a smooth configuration to a uniform wavy pattern, (b) local buckling formation (X65 pipe, D/t =72, Clay I, w =0.33m, p = 0).

It is interesting to note that the buckled shape of the compressed wall is formed in two stages. First a transition from a "smooth" deformation shape to a "wavy" pattern occurs, in the form of quasi-uniform wrinkling along a certain part of the pipeline about the critical cross-section, as shown clearly in Figure 4.5a. Subsequently, one of the wrinkles becomes dominant and the deformation localizes ("buckle localization"), forming a sharp "kink" or "local buckle", depicted in Figure 4.5b. This mechanism of buckle initiation and localization is in accordance with previous experimental observations in metal cylinders subjected to bending [42, 57].

The variations of longitudinal compressive and tensile strain ε along the two outer (most stressed) generators of the pipe cylinder are shown in Figure 4.7 and Figure 4.8 for different values of the fault displacement and for a small segment of the pipeline near the critical area.
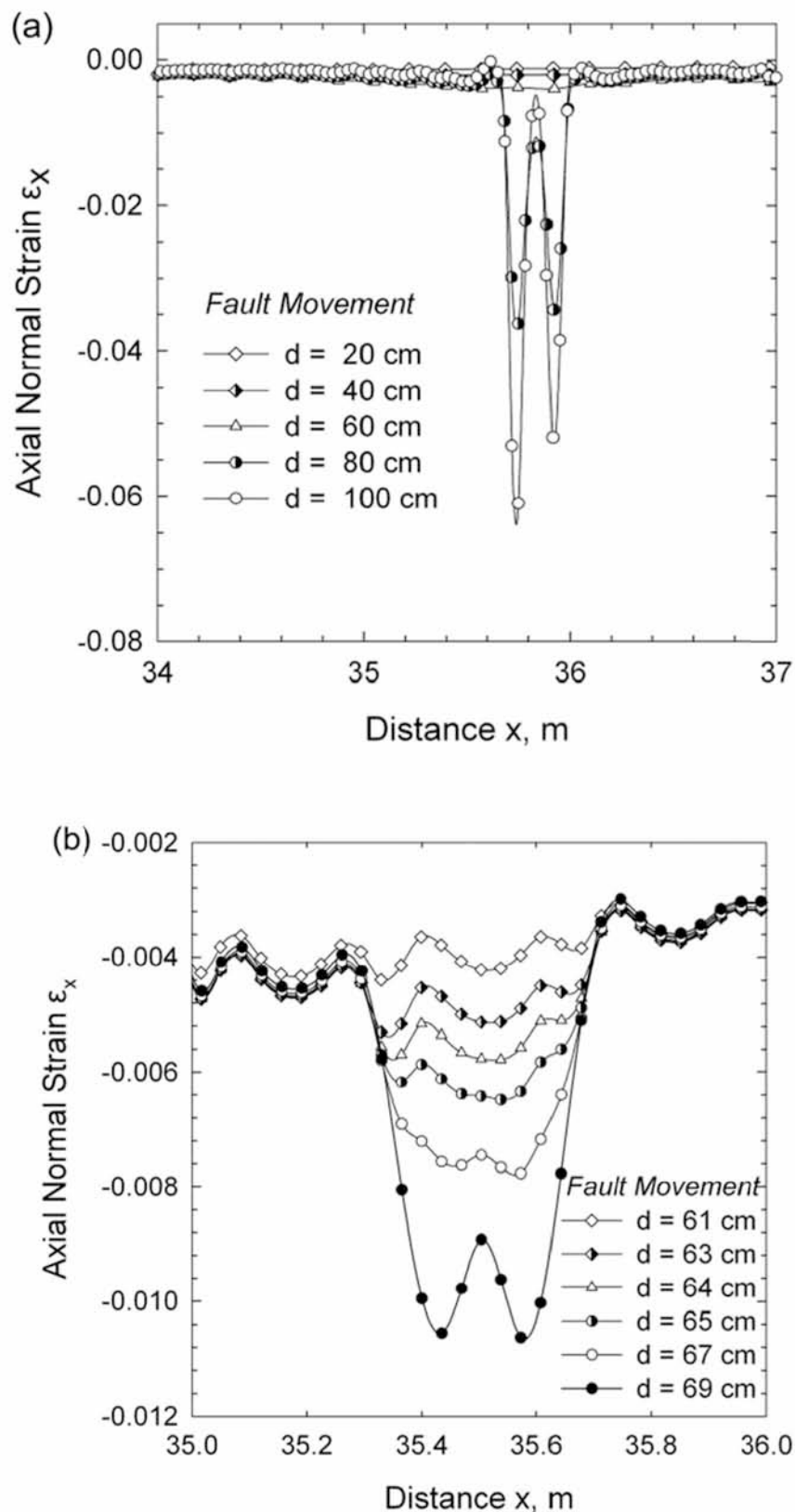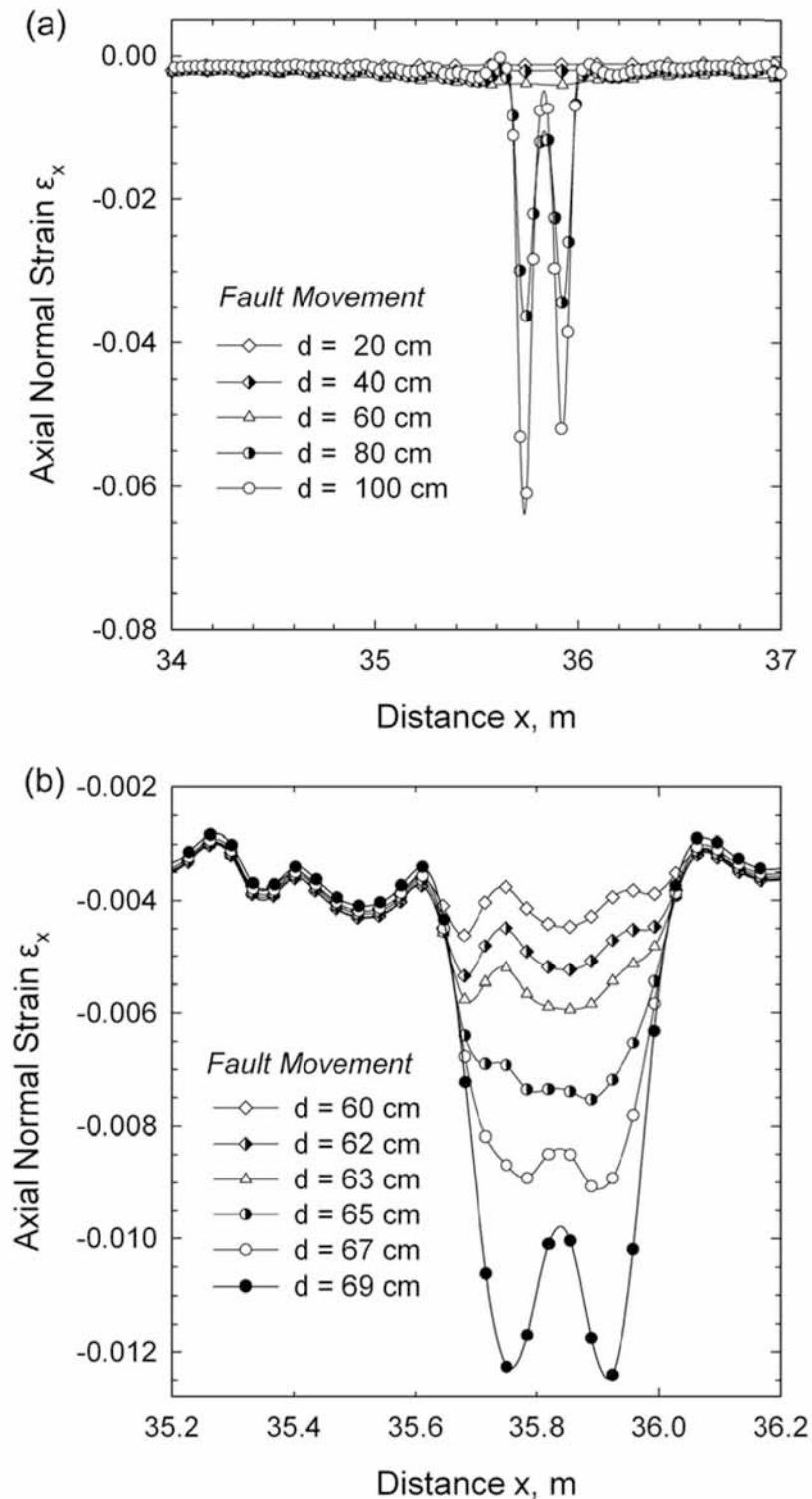
Figure 4.7: Variation of axial strain at the compression side of the buckled area for different values of fault displacement: (a) fault movement from 0.2m to 1.0m and (b) fault movement from 0.61m to 0.69m (X65 pipe, $D/t = 72$, Clay I, $w = 0.33$m, $p = 0$)
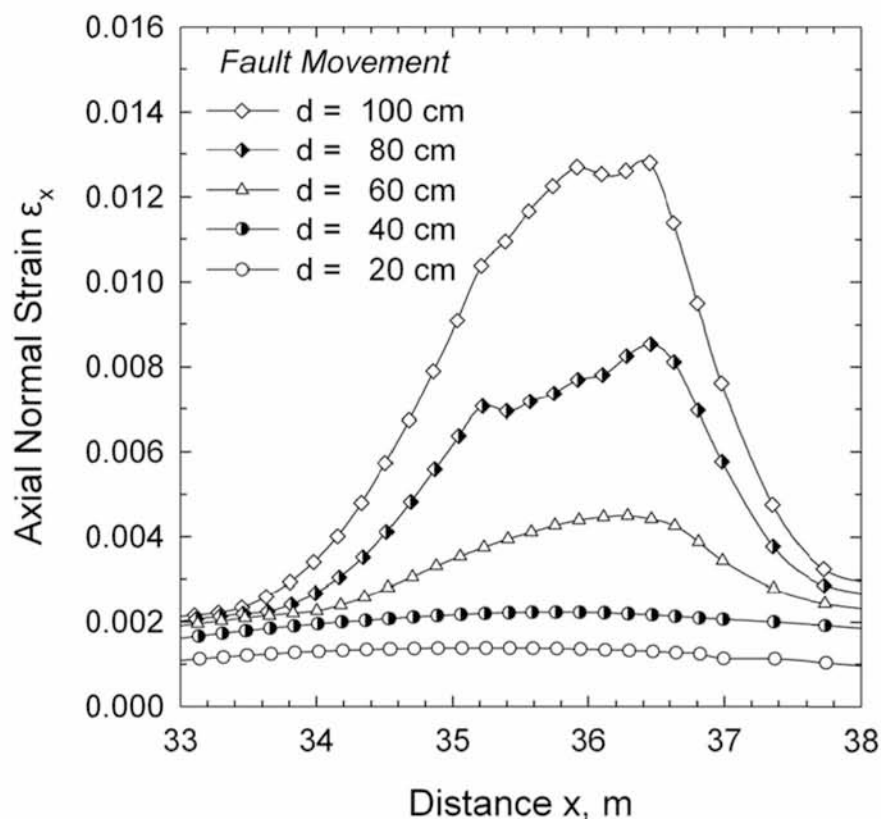
Figure 4.8: Variation of axial strain at the tension side of the buckled area for values of fault displacement from 0.2m to 1.0m (X65 pipe, $D/t = 72$, Clay I, $w = 0.33$m, $p = 0$).

The results for the compressive strain shown in detail in Figure 4.7b, indicate that for a value of fault displacement greater than 0.67 m, significant distortion of the cross-section occurs due to the development of a localized wrinkling pattern (local buckling) on the pipe wall, on the compression side of the deformed pipeline. This stage is considered to be the onset of local buckling.

It should be noted that determining the value of fault displacement at which the onset of localized buckling occurs (d_{cr}), referred to as "critical fault displacement", can be defined in many ways. In the present work, the onset of local buckling is considered at the stage where outward displacement of the pipe wall starts at the area of maximum compression. At that stage, bending strains due to pipe wall wrinkling develop (Figure 4.7), associated with significant tensile strains at the "ridge" of the buckle, so that the longitudinal compressive strains at this location at the outer surface of the pipe wall start decreasing, forming a "short wave" at this location. In the case examined, this stage corresponds to a fault displacement equal to 0.67m, as shown in Figure 4.7b.

At the above stage of local buckling onset, the longitudinal strain at the location of the buckle (ε_{cr}) is measured equal to 7.7×10^{-3}. Furthermore, at this critical buckling

stage, the maximum tensile strain on the opposite side of the pipe ($\varepsilon_{T,max}$) is 5.2×10^{-3}, which is much less than the strain that would cause tensile failure in the form of rupture in a non-seriously-defected pipeline [46, 58].

Figure 4.9: Variation of axial strain at the compression side of the buckled area for different values of fault displacement: (a) fault movement from 0.2m to 1.0m and (b) fault movement from 0.60m to 0.69m (X65 pipe, D/t=72, Clay I, w = 1m, p = 0).

101

Beyond the formation of the local buckle, pipe deformation concentrates around the buckled cross-section, and the localized wrinkling pattern is significantly developed. Further continuation of the imposed deformation results in pipe-wall folding, which is accompanied by significant local strains (compressive and tensile) at the buckled area. Similarly, the maximum tensile strain on the opposite (tensile) side of the pipe is also significantly increased. Those local tensile stresses, on either side of the pipeline cross-section, may lead to local fracture at welds or other locations where minor defects exist, resulting in loss of pipeline containment with possibly catastrophic consequences for the population and the environment.

The effects of the size of fault zone w on the mechanical response of the pipeline have also been examined. Finite element analyses have been conducted for several values of w ranging from 0.33 m to 1.0 m. The numerical results indicate that the width of the fault zone w has a minor effect on the response of the pipeline. This can be readily verified by comparing the results of Figure 4.9 for w = 1m to those depicted in Figure 4.7 for w = 0.33 m.

The effects of internal pressure on pipeline mechanical behavior are investigated by considering internally pressurized pipelines embedded in the same soil conditions (Clay I). The numerical results presented in Figures 4.10, F4.11 and 4.12 correspond to a pressure level of 50 bar, which is equal to 56% of the maximum operating pressure $p_{\max}$ expressed by eq. (4.1), whereas the results in Figures 4.13, 4.14 and 4.15 refer to a pressure level of 25 bar, which is equal to 28% of $p_{\max}$.

Despite the fact that the buckled shapes shown in Figures 4.10 and 4.13 are similar to that in Figure 4.6, the corresponding values of critical fault displacement d_{cr} and compressive strain along the critical generator of the steel pipeline shown in Figures 4.11b and 4.14b are slightly different than the ones shown in Figure 4.7b. Those results indicate that, in the case of buried (confined) pipes, the presence of internal pressure results in a decrease of critical fault displacement. The decrease is attributed to the development of additional stresses and strains in the pipeline wall that cause early yielding and lead to a premature local buckling failure. For the case of $p/p_{\max}$ =0.56, the critical strain ε_{cr} at buckling is equal to 8.3×10^{-3}, which is similar yet slightly higher than the critical strain for zero pressure. The structural response of the same steel pipeline is shown in Figures 4.16 and 4.17 considering steel material of 450 MPa yield stress (same as in X65) but exhibiting an elastic-perfect plastic behavior. The stress-strain curve of this material is plotted with dotted line in Figure 4.3a. The values of soil parameters c, E and φ are equal to 50 kPa, 25 MPa and 0°, respectively (Clay I).
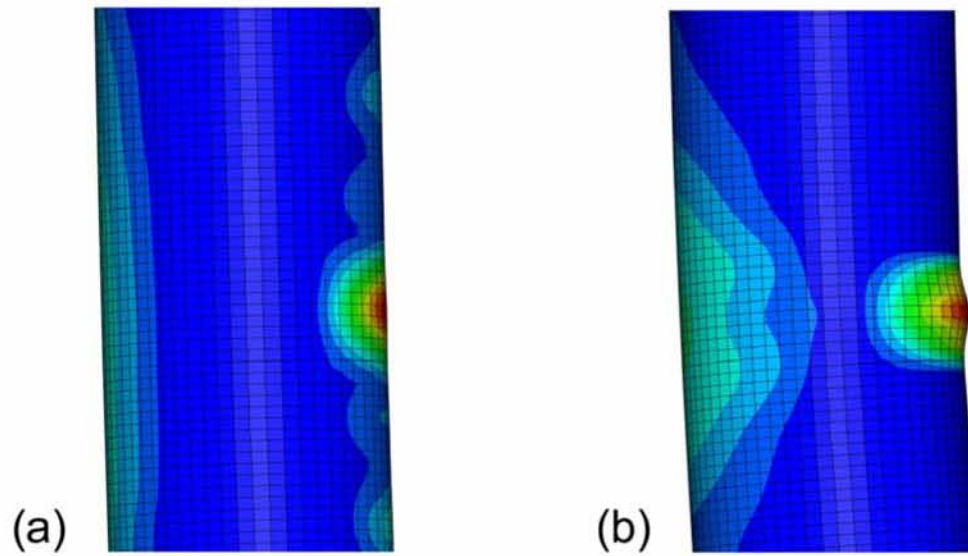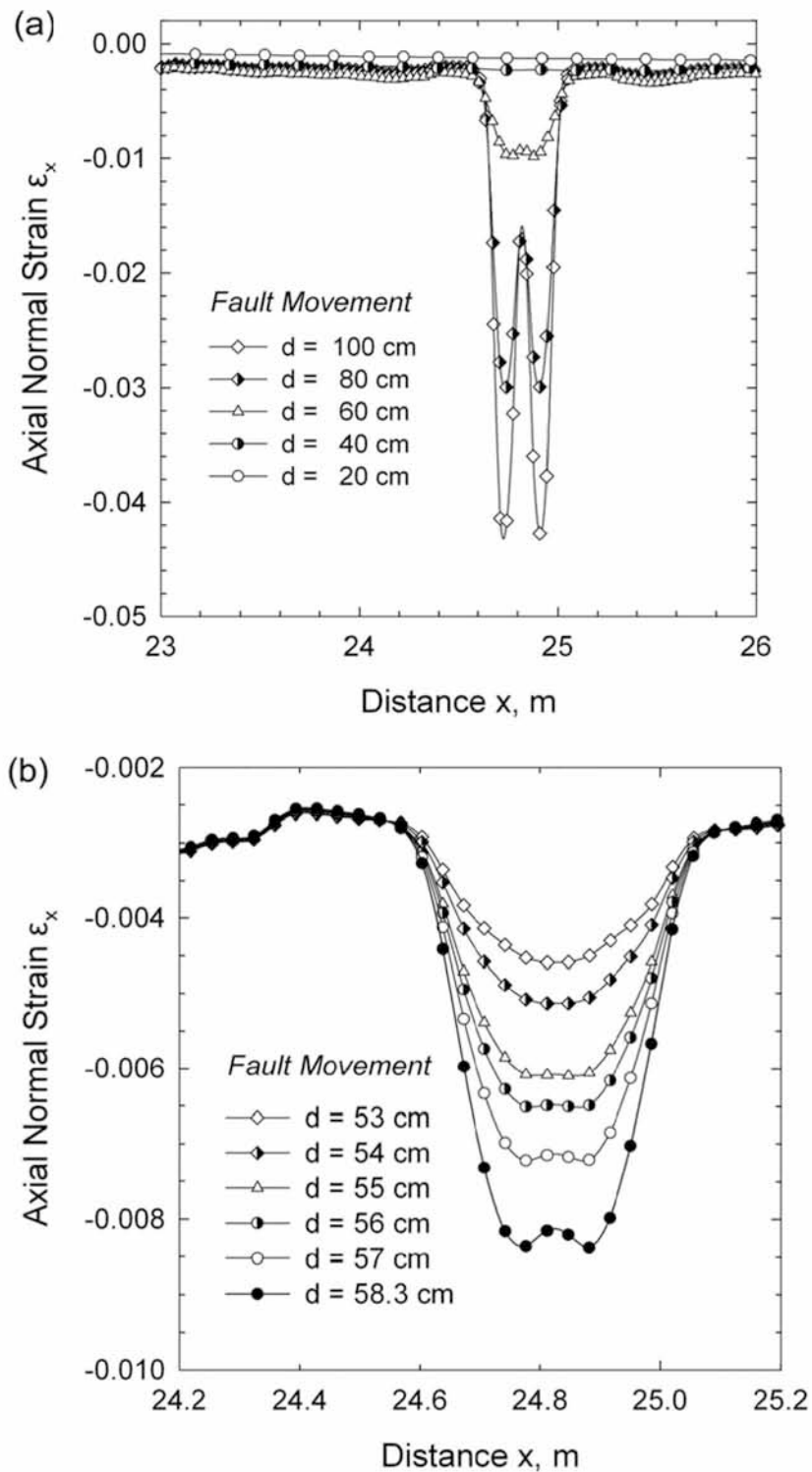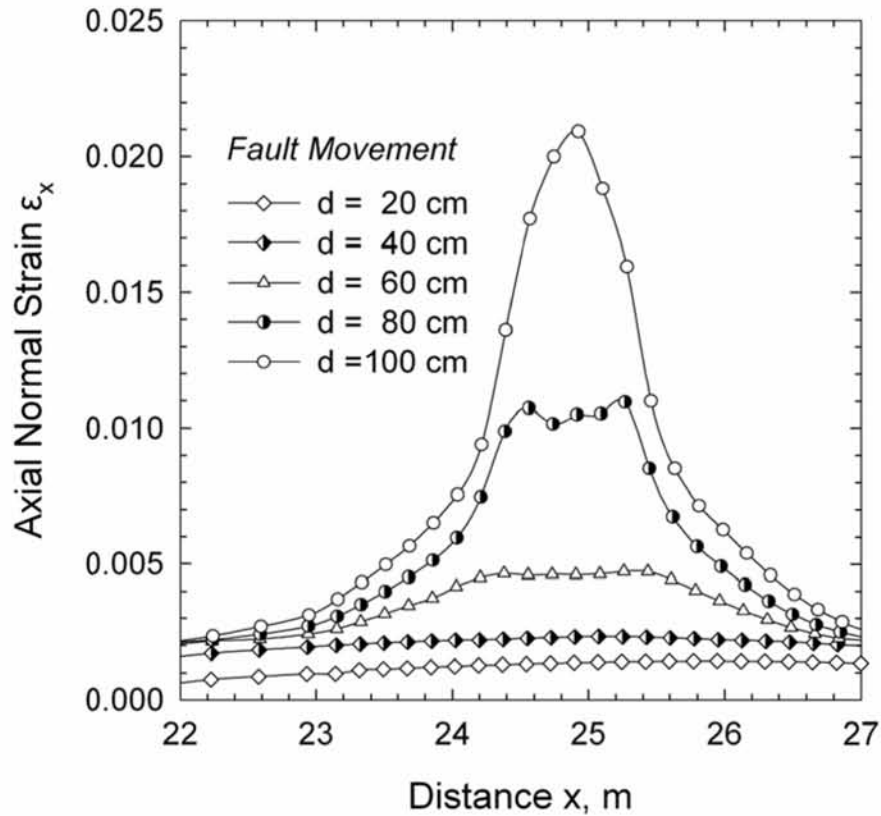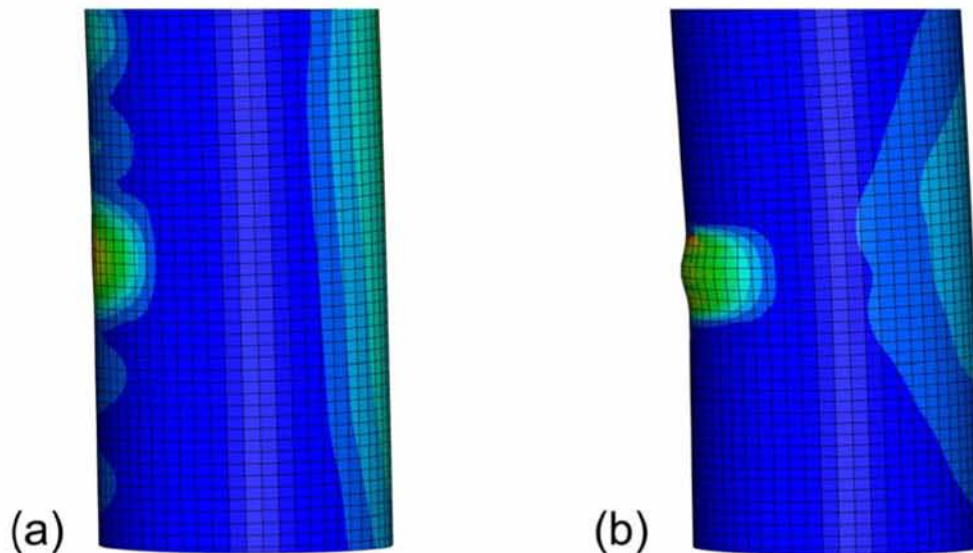
Figure 4.10: Variation of equivalent plastic shear strain at the critical pipeline area: (a) transition from a smooth configuration to a uniform wavy pattern and (b) local buckling formation (X65 pipe, D/t =72, Clay I, w =0.33m, p =0.56 p_{max})
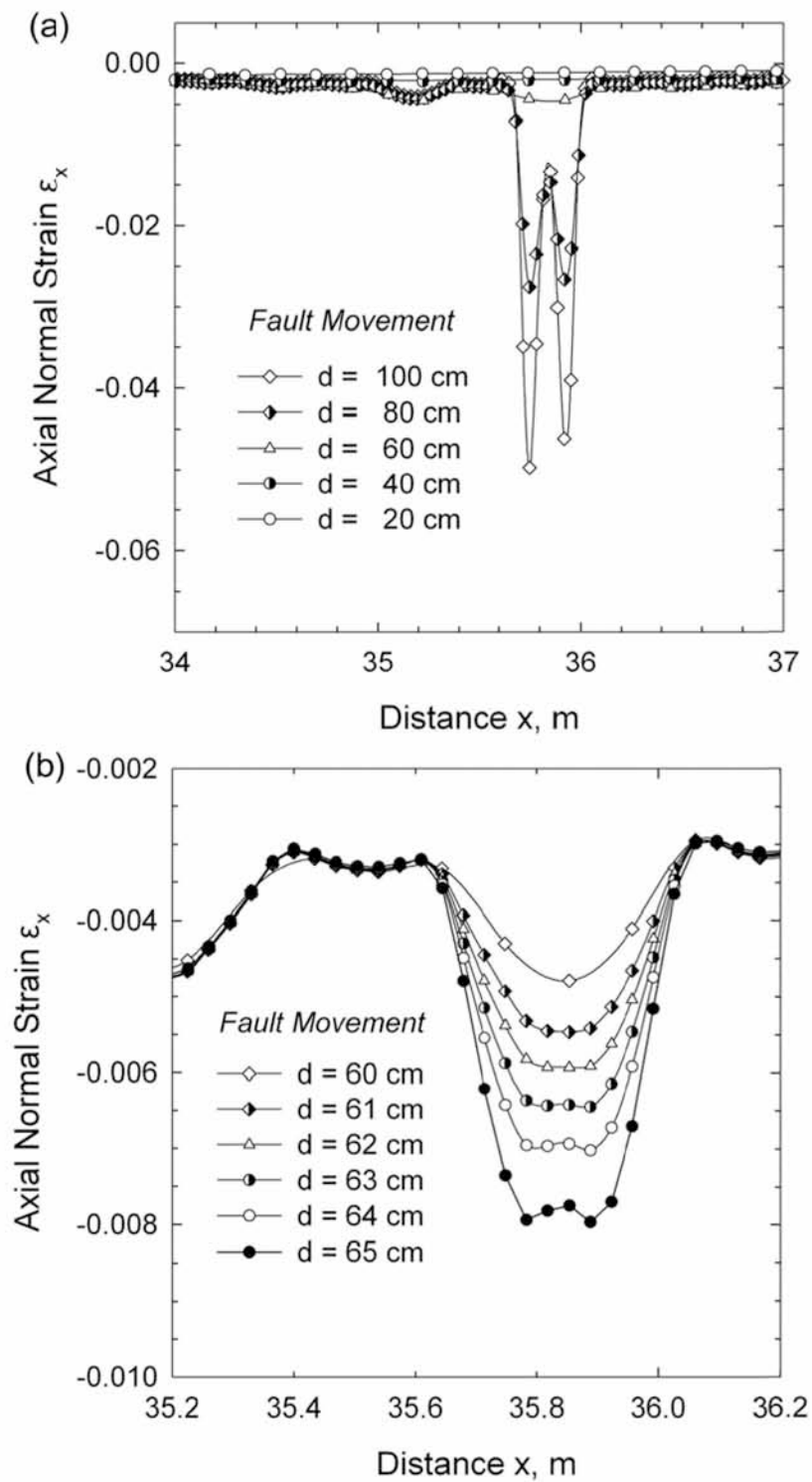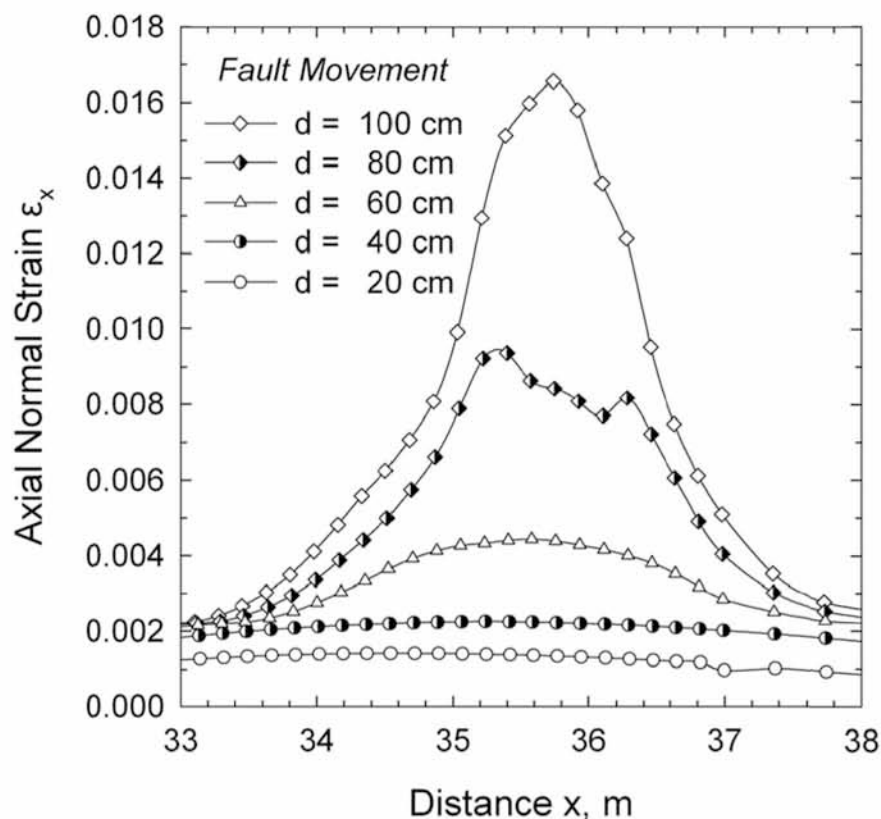
Figure 4.11: Variation of axial strain at the compression side of the buckled area for different values of fault displacement: (a) fault movement from 0.2m to 1.0m and (b) fault movement from 0.53m to 0.58m (X65 pipe, D/t =72, Clay I, w =0.33 m, p =0.56 p_{max})

Figure 4.12: Variation of axial strain at the tension side of the buckled area for different values of fault displacement from 0.2m to 1.0m (X65 pipe, D/t =72, Clay I, w =0.33m, p =0.56 p_{max})

Figure 4.13: Variation of equivalent plastic shear strain at the critical pipeline area: (a) transition from a smooth configuration to a uniform wavy pattern and (b) local buckling formation (X65 pipe, D/t =72, Clay I, w =0.33m, p =0.28 p_{max})

Figure 4.14: Variation of axial strain at the compression side of the buckled area for different values of fault displacement: (a) fault movement from 0.2m to 1.0m and (b) fault movement from 0.60m to 0.65m (X65 pipe, D/t =72, Clay I, w =0.33m, p =0.28 p_{max})

Figure 4.15: Variation of axial strain at the tension side of the buckled area for different values of fault displacement from 0.2m to 1.0m (X65 pipe, D/t =72, Clay I, w =0.33m, p =0.28 p_{max})

The critical fault displacement has been computed equal to 67 cm. Comparison of those results with the results in Figures 4.7 and 4.8 indicates that the hardening of the steel material has a negligible influence on the structural response of the pipeline subjected to strike-slip fault displacement.

The results in Figure 4.18, 4.19 and 4.20 refer to an X65 steel pipeline with D/t = 72, buried in stiffer cohesive soil conditions. The values of soil parameters c, E and φ are equal to 200 kPa, 100 MPa and 0°, respectively, and correspond to a very stiff clay under "undrained conditions", referred to as Clay II. The width of the fault zone is w = 0.33 m.

The numerical results indicate that pipe bending deformation in the very stiff soil occurs within a shorter distance from the fault location, and the critical area is at 3.2 m from the fault. Comparison of the results with those shown in Figures 4.6, 4.7 and 4.8 demonstrates the significant effect of site conditions on the mechanical behavior of the steel pipeline. In other words, for the same fault displacement d, higher bending stresses and strains occur in the case of a stiffer soil than those in the case of a softer soil. The numerical verification of the above observation is offered in Figures 4.19 and 4.20, which depict the variation of axial normal strain along the compression generator.
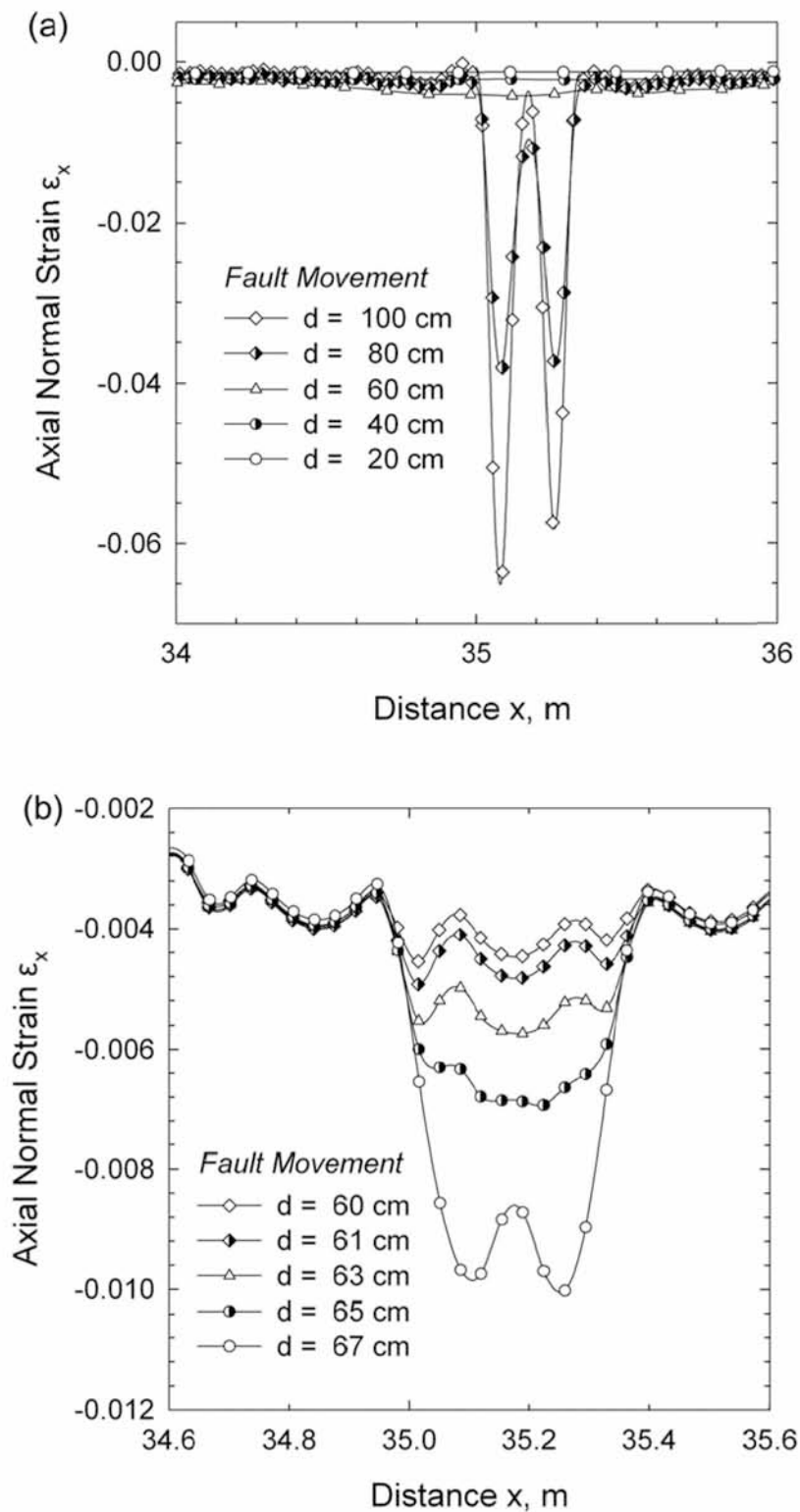
Figure 4.16: Variation of axial strain at the compression side of the buckled area for X65 steel with no hardening: (a) fault movement from 0.2m to 1.0m and (b) fault movement from 0.60m to 0.67m (D/t =72, Clay I, w =0.33m, p =0).
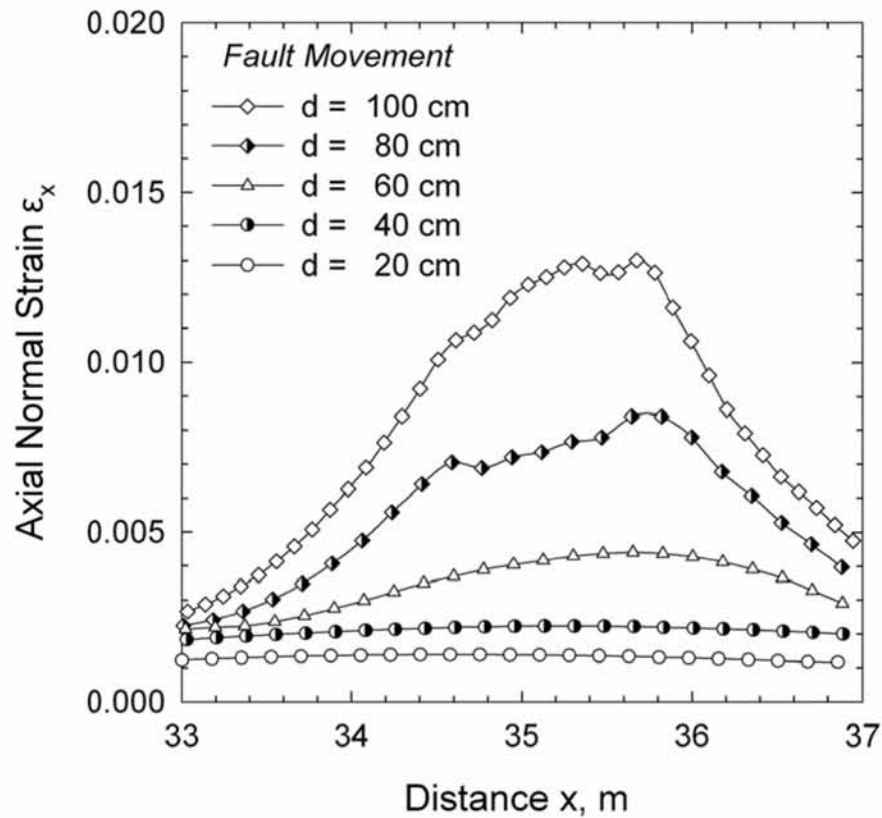
Figure 4.17: Variation of axial strain at the tension side of the buckled area for X65 steel with no hardening and different values of fault displacement from 0.2m to 1.0m (D/t =72, Clay I, w =0.33m, p =0).
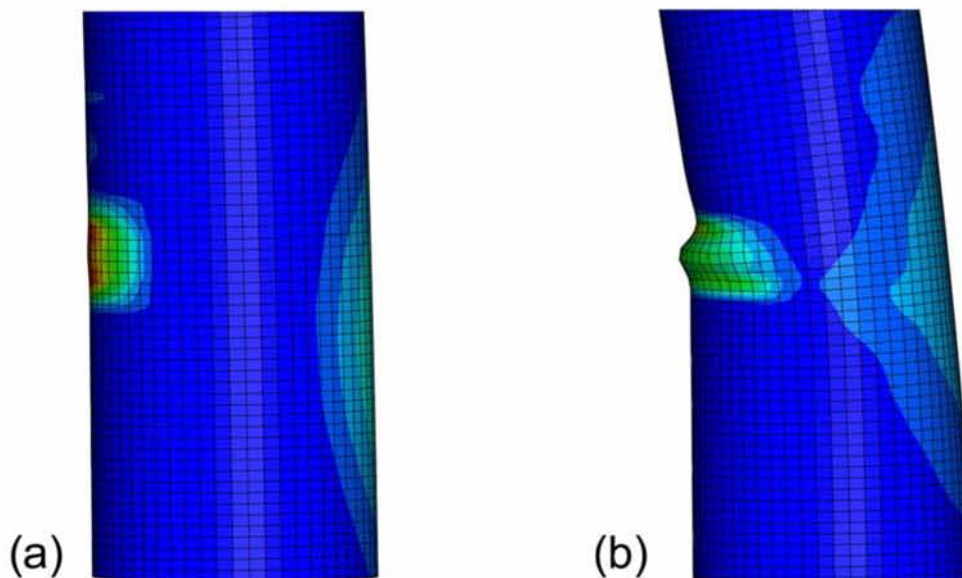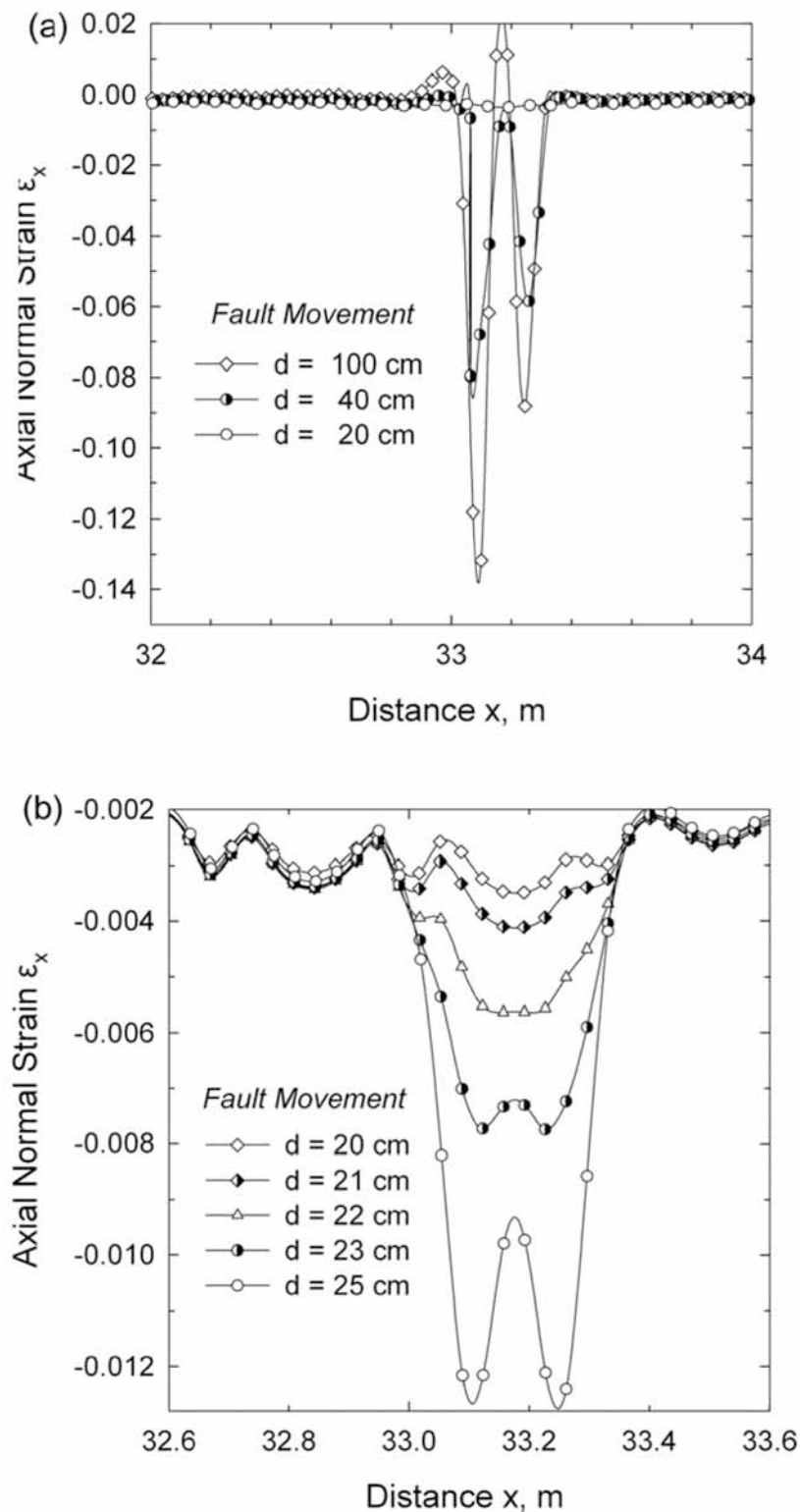

Figure 4.18: Variation of equivalent plastic shear strain at the critical pipeline area: (a) onset of local buckling and (b) post- buckling configuration (X65 pipe, D/t =72, Clay II, w =0.33m, p =0).

Figure 4.19: Variation of axial strain at the compression side of the buckled area for different values of fault displacement: (a) fault movement from 0.2m to 1.0m and (b) fault movement from 0.20m to 0.25m (X65 pipe, D/t =72, Clay II, w =0.33m, p =0).
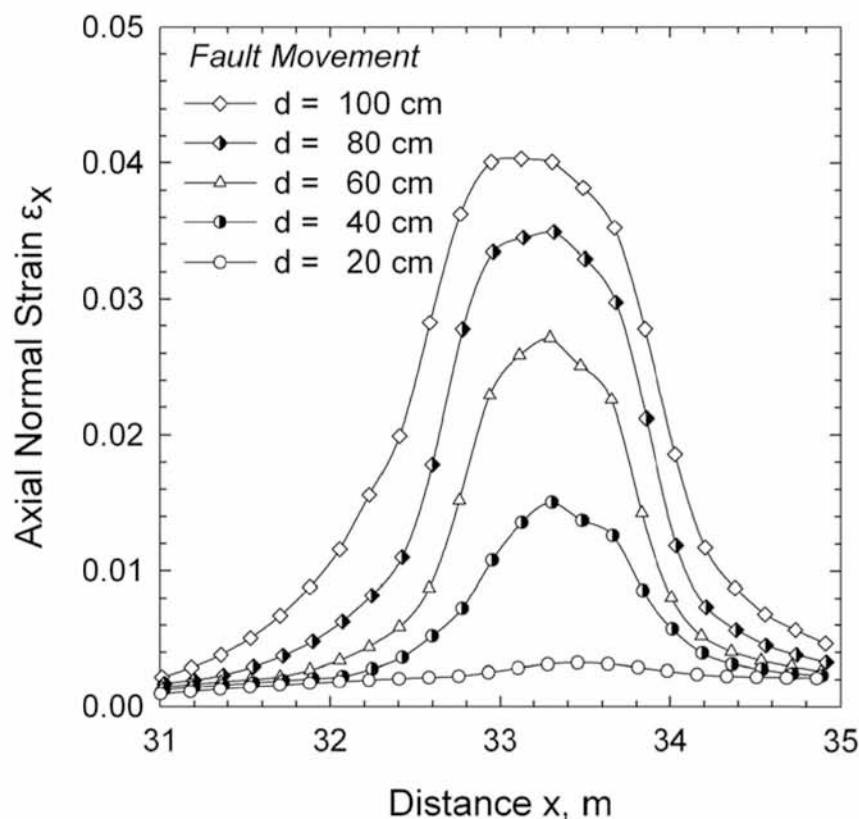
Figure 4.20: Variation of axial strain at the tension side of the buckled area for different values of fault displacement from 0.2m to 1.0m (X65 pipe, D/t =72, Clay II, w =0.33m, p =0).

Local buckling occurs at fault displacement equal to 0.23 m, which is much less than the corresponding critical fault displacement for the case of softer clay (0.67 m). The corresponding maximum compressive strain ε_{cr} that causes local buckling is equal to 7.3×10^{-3}, whereas the maximum tensile strain $\varepsilon_{T,max}$ along the opposite generator at the stage of local buckling onset is equal to 4.8×10^{-3}. The striking difference between soft-to-firm and very stiff soil conditions is attributed to the fact that a steel pipeline in a soft soil, when subjected to a fault displacement, accommodates itself easier within the deformable soil without very high stress concentrations. This results in lower bending stresses and strains, allowing the pipeline to sustain larger ground-imposed displacements.

4.2.2 Moderately thick X65 steel pipeline in non-cohesive soils

The response of an X65 steel pipeline with $D/t = 72$ embedded in non-cohesive soils is examined, by considering representative results for two frictional soils and comparing them to those obtained for the cohesive soils. First, a granular soil is considered with a friction angle $\varphi=30°$, Young's modulus $E=8$ MPa and Poisson's ratio $v =0.3$, corresponding to loose sand and referred to as "Sand I". The relatively small value of the stress-depended Young's modulus E is justified by the shallow embedment depth of the pipeline. A small amount of artificial cohesion equal to $c = 5$ kPa was also included in the analysis to prevent numerical difficulties associated with the behavior of a purely frictional material at very small confining stress, such as in the case of a gap opening at the pipe-soil interface. Figures 4.21 and 4.22 show the variation of the axial strain ε along the compression and tension outer sides, respectively, of the buckled area for Sand I.

The critical distance from the fault, corresponding to the point with maximum bending curvature along the pipe, is 6.1 meters. The results for the compressive strain shown in Figure 4.21 indicate that at a fault displacement equal to 0.87 m, local buckling occurs and, subsequently, significant distortion of the cross section. The shape of the developing buckling is similar to that of Clay I. The longitudinal strain at the location of the buckle (ε_{cr}) is equal to 9.7×10^{-3}. Furthermore, at the critical buckling stage ($d =0.87$ m), the maximum tensile strain on the opposite side of the pipe ($\varepsilon_{T,max}$) is 6.8×10^{-3}, which is much less than the strain that would cause tensile rupture. Beyond the formation of the local buckle, pipe deformation concentrates around the buckled cross-section and the localized wrinkling pattern is further developed. Further continuation of the imposed deformation results in pipe-wall folding, which is accompanied by significant local strains (compressive and tensile) at the buckled area. Moreover, the maximum tensile strain on the opposite (tensile) side of the pipe is also significantly increased.
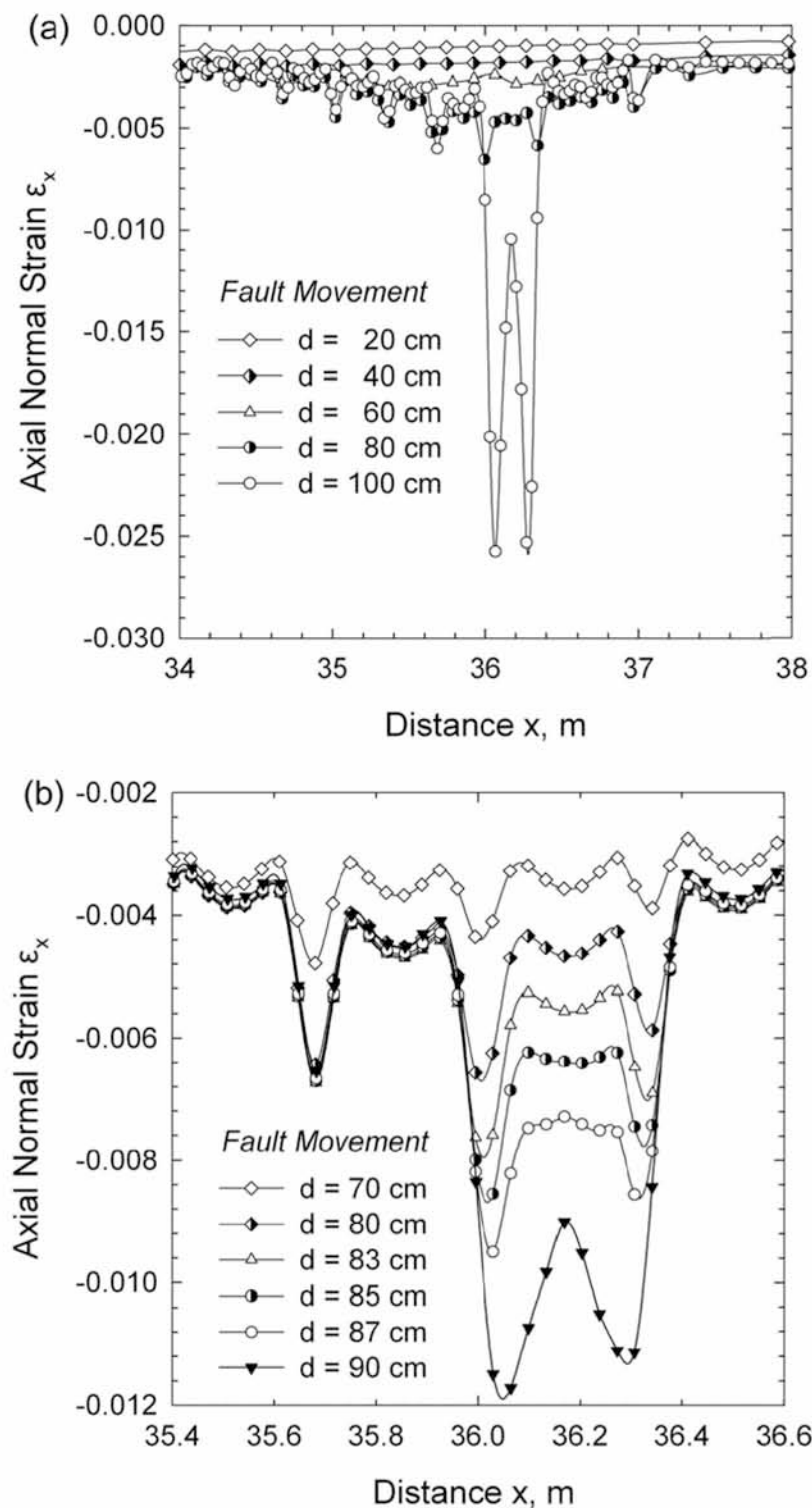
Figure 4.21: Variation of axial strain at the compression side of the buckled area for different values of fault displacement (a) fault movement from 0.2m to 1.0m and (b) fault movement from 0.70m to 0.90m (X65 pipe, D/t =72, Sand I, w =0.33m, p =0).
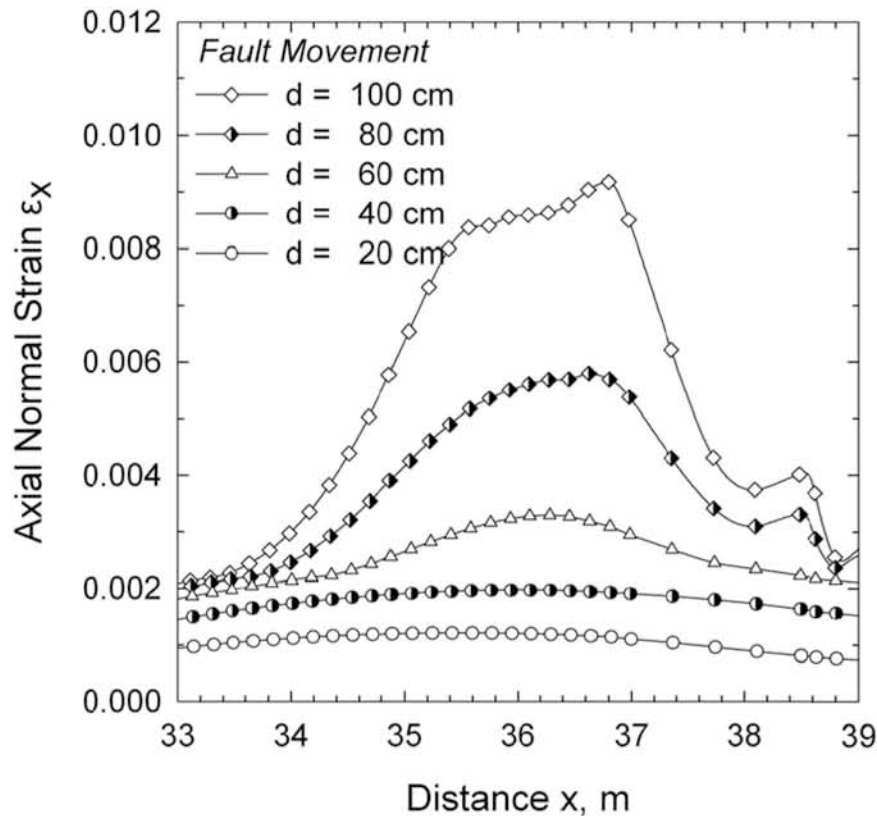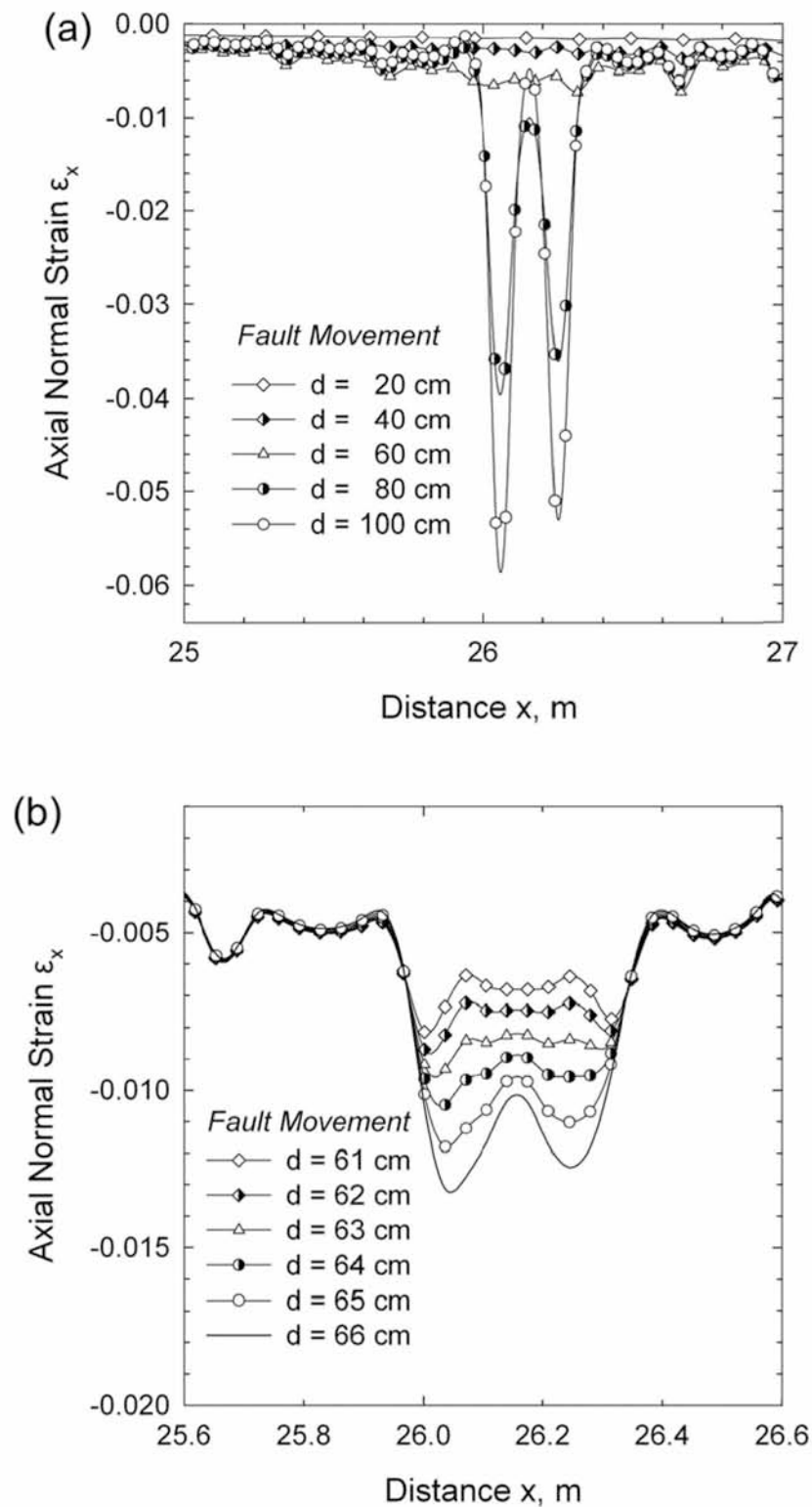
Figure 4.22: Variation of axial strain at the tension side of the buckled area for different values of fault displacement from 0.2m to 1.0m (X65 pipe, D/t =72, Sand I, w =0.33m, p =0).

Similarly, Figures 4.23 and 4.24 present the results for an X65 steel pipeline with D/t =72, embedded in a more dense sand with values of φ and E equal to 40° and 10 MPa, respectively, referred to as "Sand II". The numerical results indicate that pipe bending deformation in Sand II occurs within a shorter distance from the fault location (5.1 m) due to the higher strength and stiffness of this sand. Comparison of those results with the results in Figures 4.21 and 4.22 demonstrates that for the same fault displacement d, higher bending stresses and strains occur in the case of Sand II. Local buckling occurs when the fault displacement becomes equal to 0.65m, which is less than the corresponding critical fault displacement for the case of loose sand (0.87 m). The maximum compressive strain ε_{cr} that causes local buckling is equal to 11.3×10^{-3}, whereas the corresponding maximum tensile strain $\varepsilon_{T,\max}$ along the opposite generator is equal to 6.2×10^{-3}.

Figure 4.23. Variation of axial strain at the compression side of the buckled area for different values of fault displacement: (a) fault movement from 0.2m to 1.0m and (b) fault movement from 0.61m to 0.66m (X65 pipe, D/t =72, Sand II, w =0.33m, p =0).
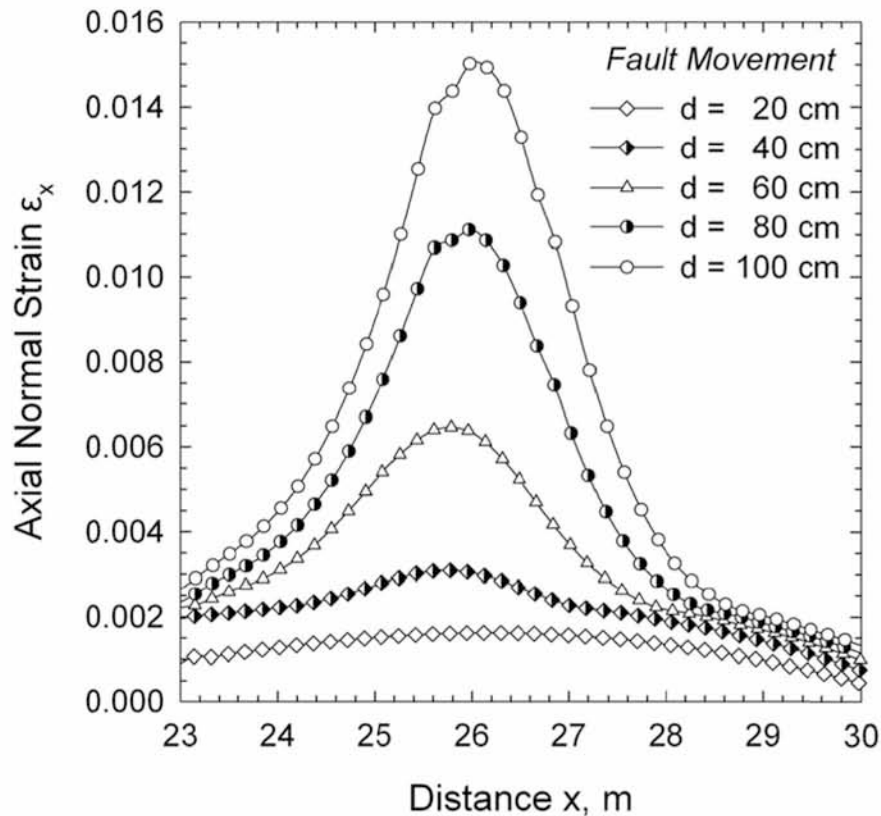
Figure 4.24. Variation of axial strain at the tension side of the buckled area for different values of fault movement from 0.2m to 1.0m (X65 pipe, D/t =72, Sand II, w =0.33m, p =0).

4.2.3 Effects of the diameter-to-thickness ratio and design implications

In order to investigate the effects of the diameter-to-thickness ratio, results are obtained for 36-inch diameter X65 steel pipelines with thickness ranging between ¼-inch and ¾-inch, corresponding to D/t values between 48 and 144. Both cohesive soils (Clay I, II) and non-cohesive soils (Sand I, II) are considered. The numerical results for cohesive soils (Clay I and II) are summarized in Figure 4.25. In particular, Figure 4.25a plots the fault critical displacement, d_{cr}, normalized by the pipe diameter D, in terms of the diameter-to-thickness ratio, D/t. The results show a substantial decrease of d_{cr} with increasing value of the D/t ratio, which means that thin-walled pipelines are more prone to buckling and fail at relatively small values of fault displacement.

Furthermore, very stiff soil conditions result in significantly lower deformation capacity of the pipeline. In Figure 4.25b the corresponding critical compressive strain at the onset of local buckling, ε_{cr}, is plotted against the value of the diameter-to-thickness ratio, D/t. The results indicate that thinner pipes buckle at smaller critical strain, which is in accordance with test data and numerical results from unconfined pipes [42, 57, 59].

In the above results, no critical displacement or critical strain is shown for $D/t=44$ and soft-to-firm soil conditions (Clay I). In this particular case, the numerical results did not indicate local buckling. The pipeline exhibited significant ground-induced deformation without any wrinkling of its wall for fault displacements in excess of 2.5 m. The tensile strains developed in the pipeline due to longitudinal pipeline stretching are responsible for this behavior.

In Figure 4.25b, the numerical results for the critical strain (ε_{cr}) are also compared with the predictions of the new European standard EN 1998-4 [46] for seismic design of buried pipelines, also adopted by the very recent ASCE Manual of Practice 119 for Buried Steel Pipes [47]. The EN 1998-4 standard specifies a maximum allowable strain for compression ($\varepsilon_{C,w}$) equal to the minimum of [0.01, 0.4t/D] and a maximum allowable tensile strain ($\varepsilon_{T,w}$) equal to 0.03. Those provisions predict a decrease of the critical strain with increasing D/t values, which is in accordance with the finite-element results. However, it should be noticed that the allowable compressive strain appears to be conservative for the range of cohesive soil conditions expressed by Clay I and Clay II shown in Figure 4.25b.

Moreover, the numerical results of axial strain at the tension side of the pipe for all the cases considered in Figure 4.25, show that at the onset of local buckling the computed maximum tensile strain $\varepsilon_{T,\max}$ varies from 0.002 to 0.01, which is significantly lower than the EN 1998-4 allowable value of $\varepsilon_{T,w}$ =0.03. This observation verifies that for the range of parameters considered, local buckling rather than tensile rupture is the governing mode of pipeline failure.

The effects of internal pressure are also depicted in Figure 4.25. The numerical results are obtained for a pressure level equal to 56% of the maximum operating pressure, $p_{\max}$, and show that the presence of internal pressure results to a small decrease of critical fault movement, d_{cr}, (Figure 425a). This decrease is attributed to the additional stresses and strains in the pipe wall because of the pressure. Furthermore, the corresponding critical strain in the presence of pressure is similar to the corresponding critical strain for the zero pressure case, as shown in Figure 4.25b. Note that EN 1998-4 provisions [46] specify a value of critical strain independent of the level of internal pressure, and this is verified by the present numerical results.
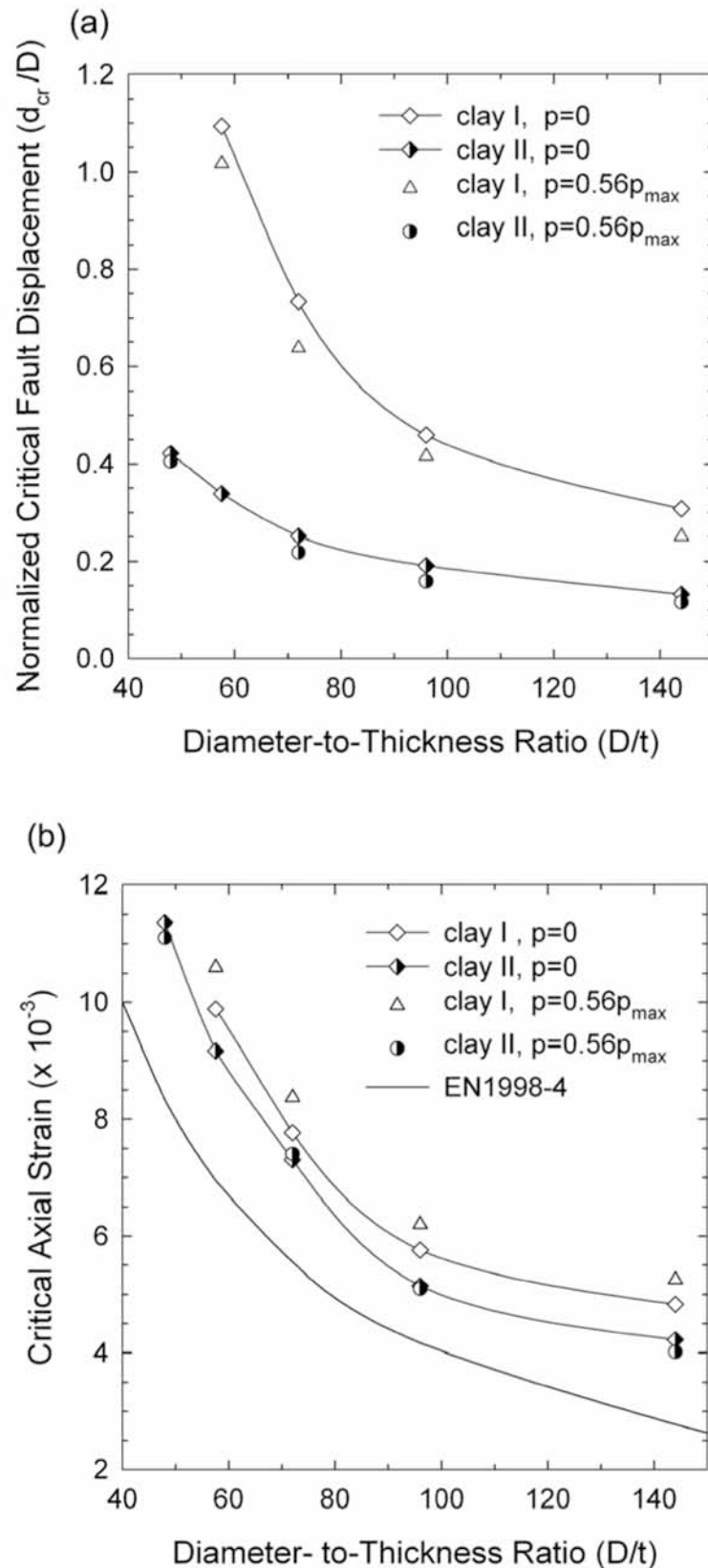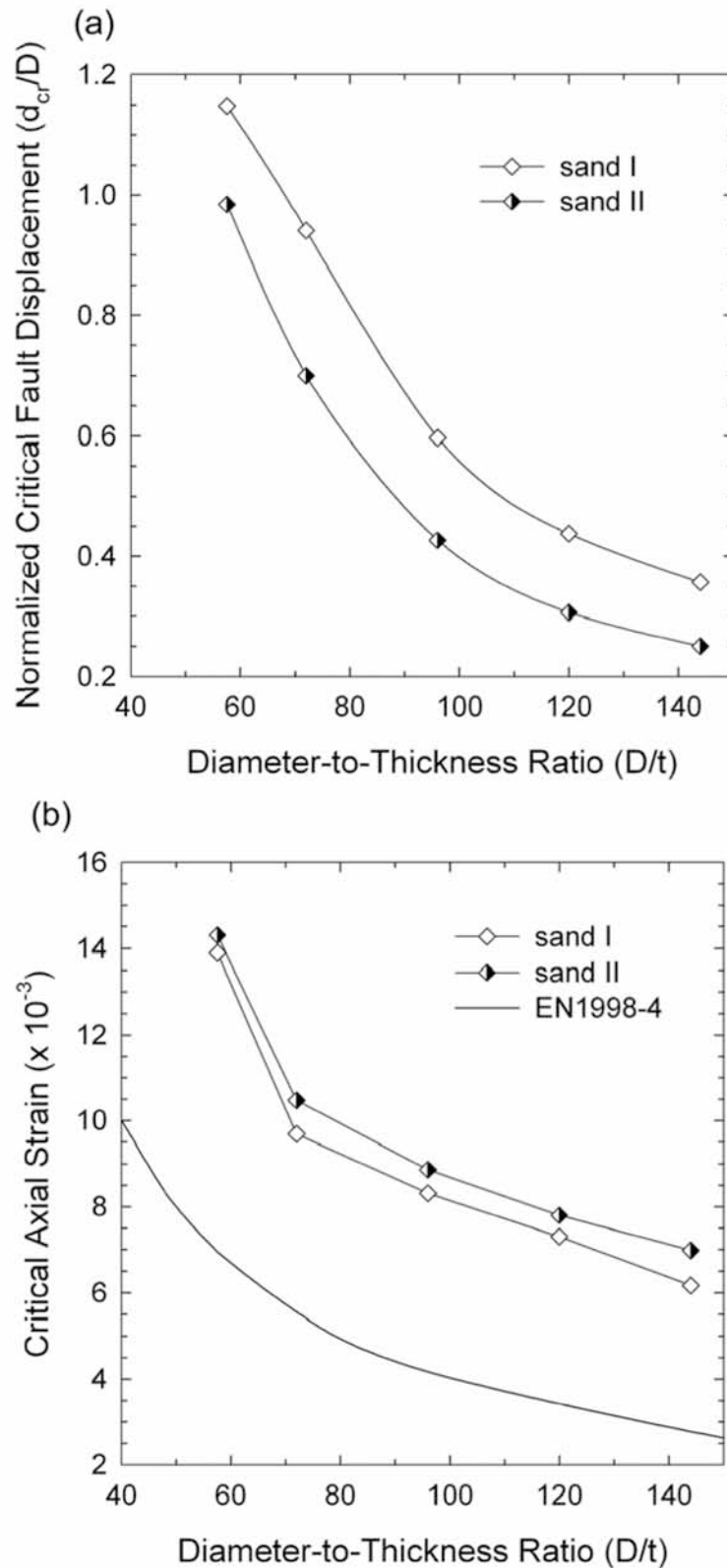
Figure 4.25: (a) Critical fault movement versus the diameter-to-thickness ratio D/t for clay I, II and (b) Critical axial strain versus the diameter-to-thickness ratio D/t for clay I, II – predictions from EN 1998-4 (X65 pipe, w =0.33m, p =0 and p =0.56 p_{max}).

Figure 4.26: (a) Critical fault movement versus the diameter-to-thickness ratio D/t for sand I, II and (b) Critical axial strain versus the diameter-to-thickness ratio D/t for sand I, II – predictions from EN 1998-4 (X65 pipe, w= 0.33m, p = 0).

Finally, the numerical results for the mechanical behavior of X65 pipelines in non-cohesive soils (Sand I and II) are summarized in Figure 4.26, in terms of the normalized fault critical displacement and the critical strain at buckling with respect to the diameter-to-thickness ratio, D/t. The results shown in Figure 4.26a indicate that dense soil conditions (Sand II) result in lower deformation capacity of the pipeline. Furthermore, for both sands, the critical compressive strain, ε_{cr}, shown in Figure 4.26b, is significantly higher than the one predicted by the provisions of EN 1998-4 [46].

4.2.4   Structural behavior of high-strength X80 steel pipelines

The behavior of buried high-strength steel (API X80) pipelines under fault-induced deformation is also analyzed, using the numerical tools described in the previous sections. The nominal uniaxial tensile stress-strain relationship of the X80 material is plotted in Figure 4.3b. The dashed material curve, which has a yield stress of 596 MPa and does not have a plastic plateau, corresponds to a cold expanded (UOE) pipe. The solid material curve with a yield stress of 550 MPa and a plastic plateau up to a strain of 1.48% represents a seamless steel pipe material. Results are obtained for 36-inch-diameter X80 steel pipelines with D/t ratios between 48 and 144. Figure 4.27a plots the value of the fault critical displacement ratio, d_{cr}/D, in terms of the diameter-to-thickness ratio, D/t, for the two types of X80 steel (Figure 4.3b) and for cohesive soil conditions (Clay I and II). As in the case of X65, the value of d_{cr} decreases significantly with increasing value of D/t, indicating that thin-walled pipelines are more vulnerable to buckling and may fail at relatively small values of fault displacement. It should be noted that for the softer Clay I material, no values of d_{cr} are given for D/t = 48 and 72, as no wrinkling of the pipeline wall was observed in this case even for fault displacements exceeding 4 m. This is attributed to the beneficial effect of tensile deformation on the mechanical behavior of those relatively thick pipes. In this case, pipeline extension occurs resulting in significant increase of the tensile strains with simultaneous reduction of the compressive bending strains, preventing in this way the development of local buckling. Naturally, the values of d_{cr} for the high-strength steel X80 pipes in Figure 4.27a are higher than those for the X65 pipes given in Figure 4.25a. Similarly, Figure 4.27b plots the critical axial strain, ε_{cr}, versus the diameter-to-thickness ratio, D/t, for zero internal pressure. Also plotted in the figure is the recommendation by the EN 1998-4 giving more conservative values of ε_{cr}. Comparing the behavior of the two X80 materials, it is evident that both d_{cr} and ε_{cr} are higher for UOE pipe due to both increase of yield strength and higher initial post-yielding tangent modulus. Finally, the numerical results for the maximum axial strain ε_x at the tension side of the pipe at the onset of local

buckling have been found to be significantly lower than the EN 1998-4 [46] allowable value of $\varepsilon_{T,w} = 0.03$ for all values of D/t ratio examined herein.
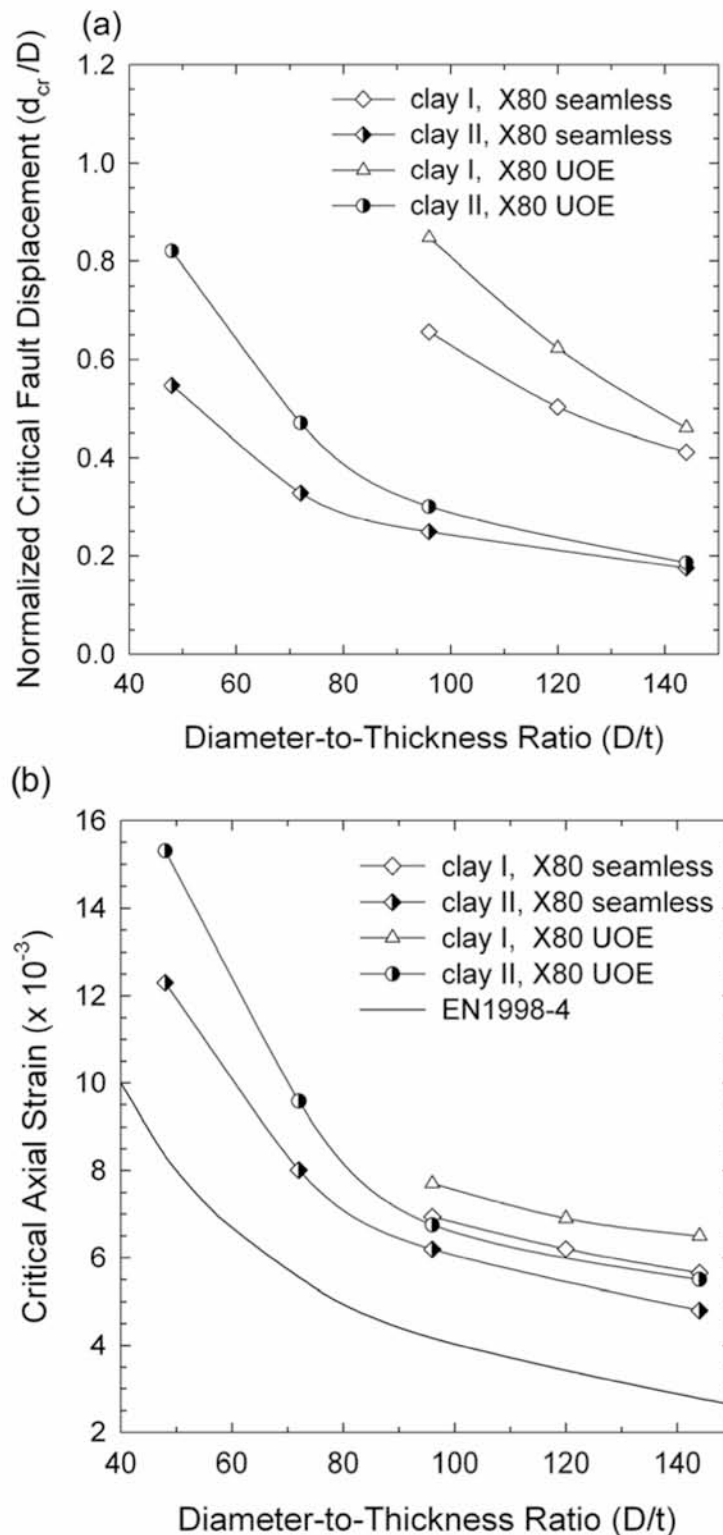

Figure 4.27: (a) Critical fault movement versus the diameter-to-thickness ratio D/t for two types of X80 pipelines (b) Critical axial strain versus the diameter-to-thickness ratio D/t for two types of X80 and predictions from EN 1998-4 (w =0.33m, p = 0).

4.3 Numerical results for pipelines of infinite length

Using model M60-NS, presented in Chapter 3, Figures 4.28a and 4.28b plot the distribution of axial normal strain at the tension and compression sides of the pipeline respectively, for different values of fault displacement d. These results are obtained for a pipe with D/t equal to 96 embedded in Clay I soil conditions. Figure 4.28c shows the evolution of pipeline stress state and deformation just before and immediately after local buckling. Considering the convention of local buckling onset given in [60, 61], local buckling occurs at a fault displacement of about d_{cr} =0.43 m; this is the most critical performance criterion for the present case. The 3% tensile strain is reached at d_{cr} =1.13 m, whereas the critical flattening occurs at about 1.96 m. Note that both of these criteria are reached at the buckled location well beyond the formation of the buckle. The 5% tensile strain performance criterion is not reached within the maximum fault displacement (4 m) considered in the analysis; in fact, the tensile strain reaches a value of about 4.1% in the course of this analysis.
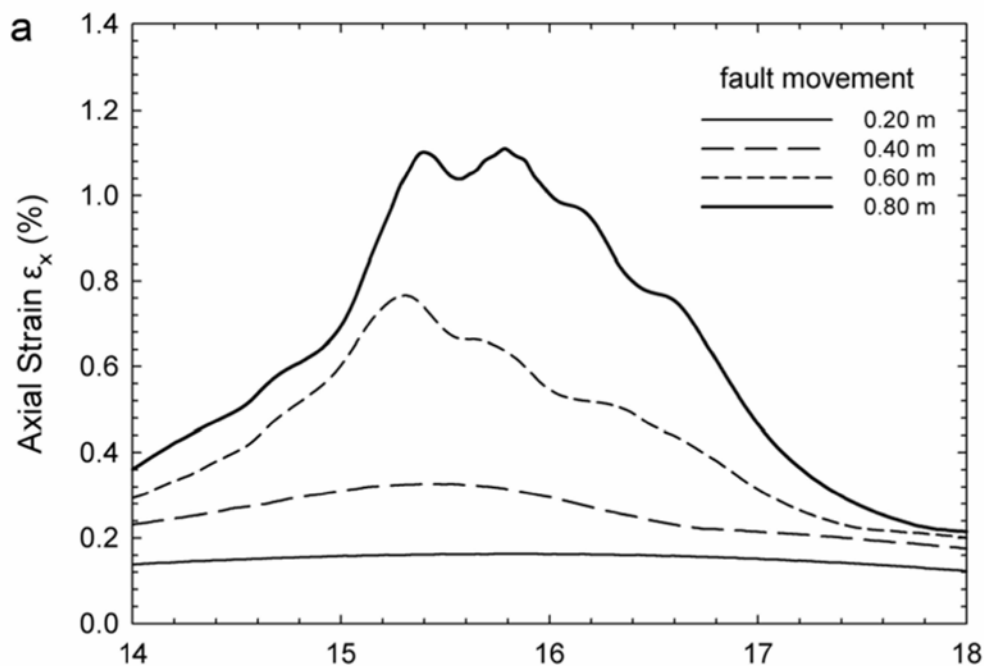
Figure 4.28 (continued): (a) Axial normal strain along the pipeline side under tension (b) axial normal strain along the pipeline side under compression (c) axial normal strain concentration before and after buckling. (Model B60-NS, angle β=0°).
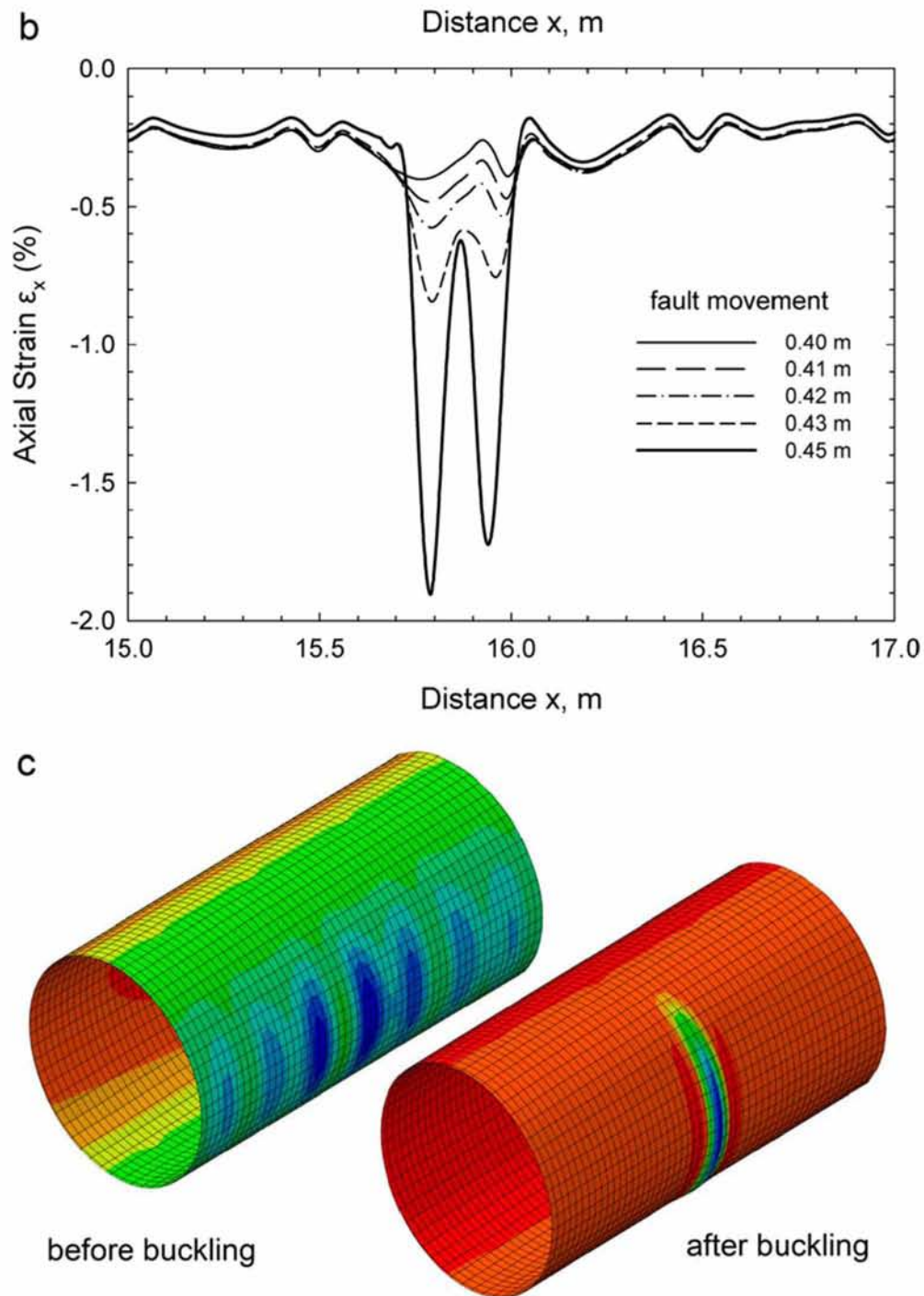
Figure 4.28 (continued): (a) Axial normal strain along the pipeline side under tension (b) axial normal strain along the pipeline side under compression (c) axial normal strain concentration before and after buckling. (Model B60-NS, angle β=0°).

Figures 4.29 to 4.32 plot the normalized critical fault displacements along with D/t ratio for different soil conditions, different steel materials, with or without internal pressure. It is evident that the effect of length plays no significant role for cases in which buckling occurs in small fault displacements, having a D/t greater than 72. For thicker pipes, having a D/t less than 72, divergence of the results is obvious and local buckling can occur for infinite length pipeline (even though for a finite length pipeline it does not occur) as shown in Figure 4.32. These results verify the beneficial effect of axial stretching in the case of a zero crossing angle β.
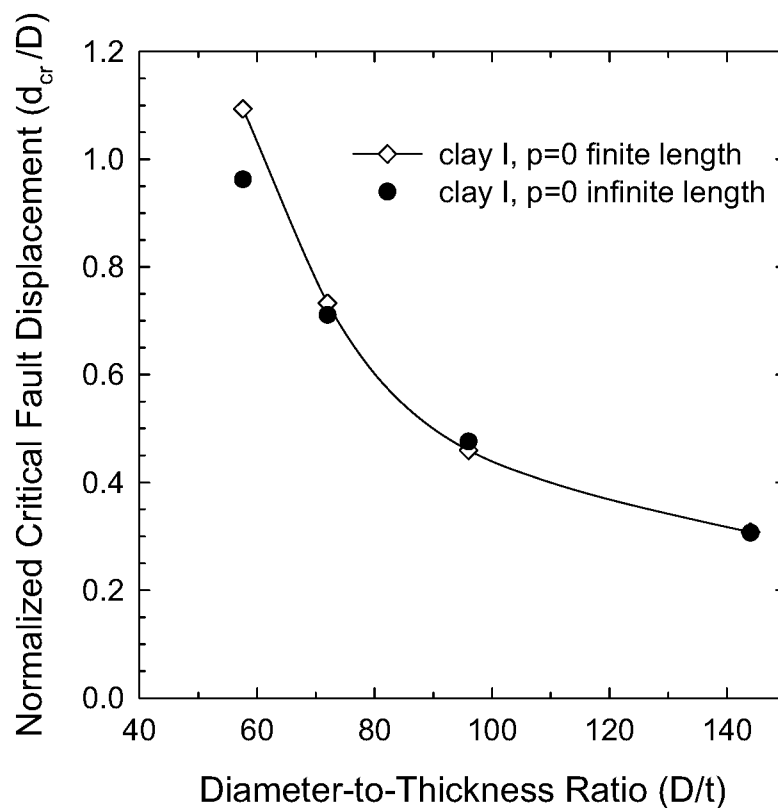
Figure 4.29: Critical fault movement versus the diameter-to-thickness ratio D/t for infinite and finite length of X65 pipelines, Clay I conditions.
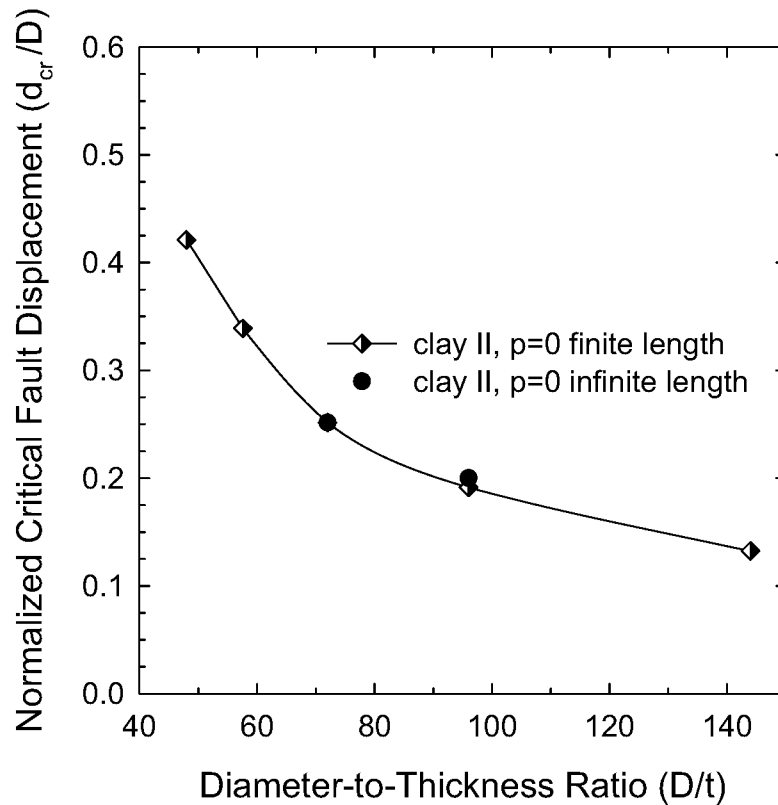
Figure 4.30: Critical fault movement versus the diameter-to-thickness ratio D/t for infinite and finite length of X65 pipelines, Clay II conditions.
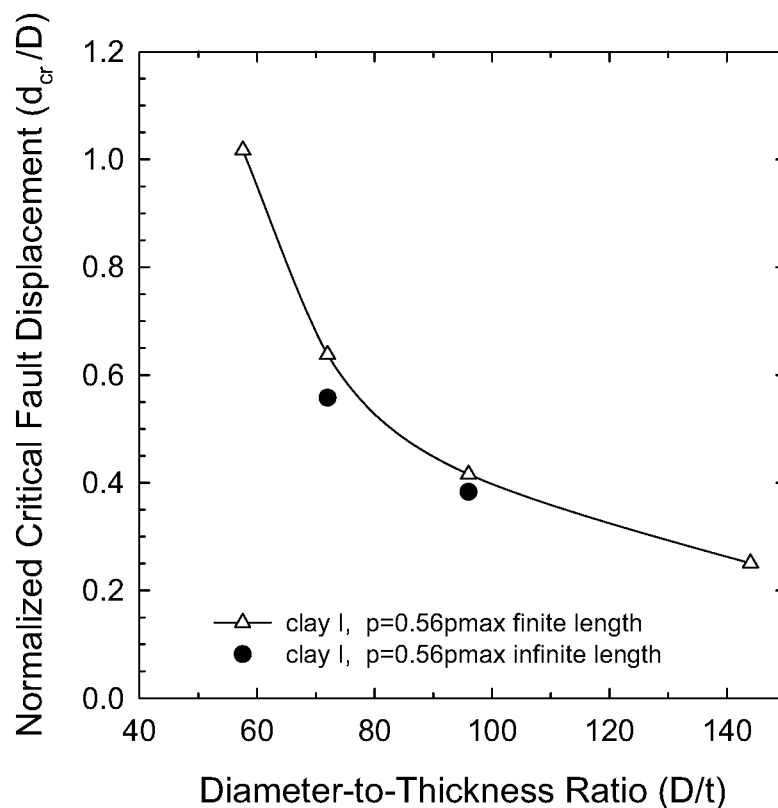
Figure 4.31: Critical fault movement versus the diameter-to-thickness ratio D/t for infinite and finite length of X65 pipelines with internal pressure, Clay I conditions
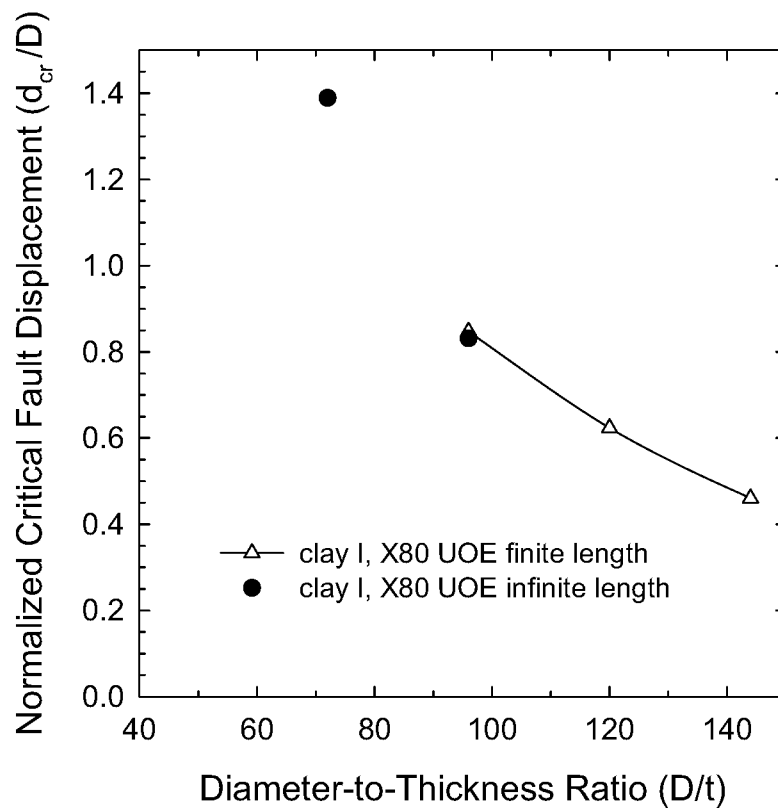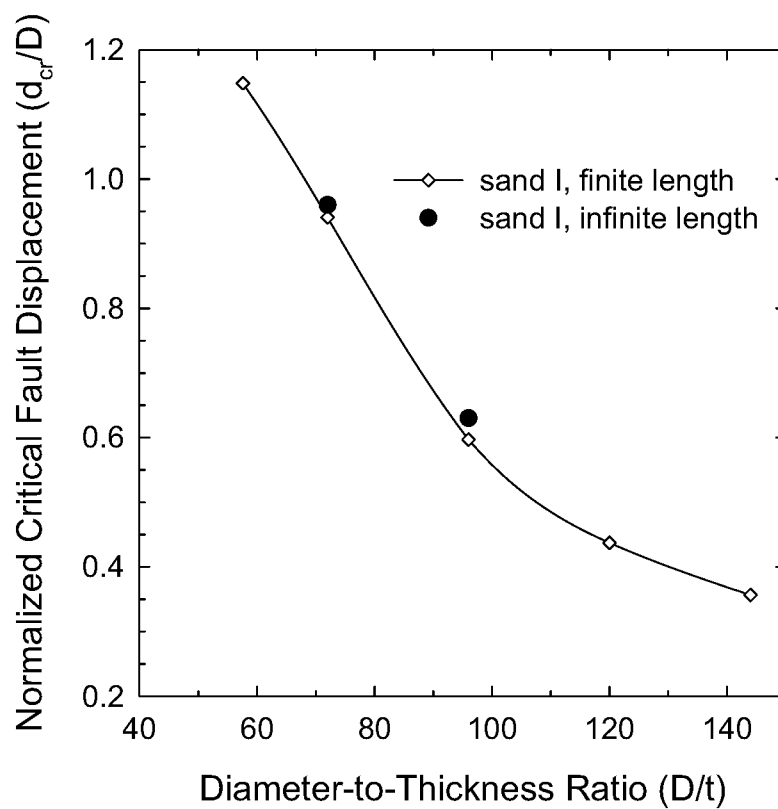
Figure 4.32: Critical fault movement versus the diameter-to-thickness ratio D/t for infinite and finite length of X80 pipelines, Clay I conditions

Figure 4.33: Critical fault movement versus the diameter-to-thickness ratio D/t for infinite and finite length of X65pipelines, Sand I conditions

126

5   Effect of fault crossing angle on pipeline response

5.1   Introduction

The structural response of steel pipelines crossing a strike-slip fault at an oblique angle and subjected to fault movement is examined numerically in this Chapter. The nonlinear material behaviour of the steel pipe and the surrounding soil, the interaction between soil and pipe, as well as the distortion of the pipeline cross-section and large deformation of the soil are modelled in a rigorous manner, so that the pipeline performance criteria are evaluated with a high-level of accuracy. A detailed description of the numerical model was presented in Chapter 3.

Figure 5.1 illustrates the numerical model, indicating the oblique fault plane that divides the soil in two blocks of equal size. As in Chapter 4, the analysis is conducted in two steps: first, gravity loading is applied and subsequently, fault movement is imposed using a displacement-controlled scheme, which increases gradually the fault displacement d. When pressurized pipelines are analysed an intermediate step of internal pressure application is considered.

Section 5.2 presents results for the case of pipelines having a finite length. In this case, the nodes on the vertical boundary planes of the first block (pipe and soil nodes) remain fixed in the horizontal directions. A uniform horizontal displacement due to fault movement is imposed at the external nodes (pipe and soil) of the moving block in a horizontal direction parallel to the fault plane, whereas the motion along the vertical direction is not restrained. All nodes on the base are fixed with respect to vertical displacement to avoid rigid body motion.

Section 5.3 presents results for the case of infinitely long pipelines, in which the force-displacement behaviour at the two pipeline ends is simulated by the equivalent nonlinear spring proposed in Chapter 3. In this case, both the external soil-block nodes and the supports of the nonlinear springs of the moving block are subjected to displacement parallel to the fault plane.
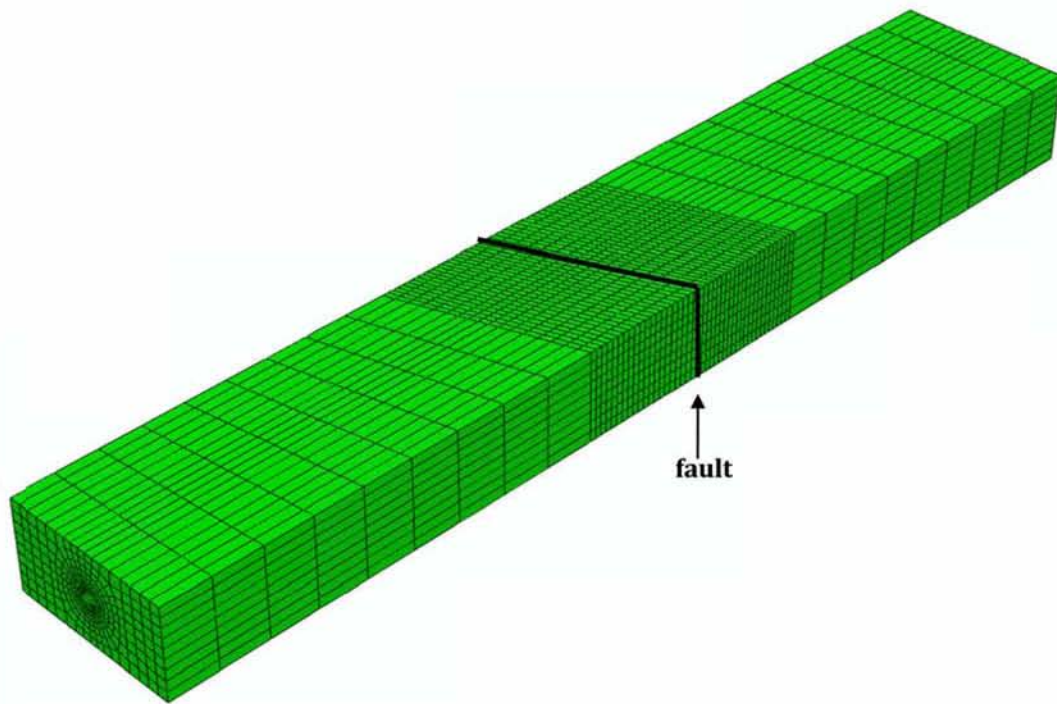
Figure 5.1: Finite element model of the soil prism with tectonic strike-slip fault.
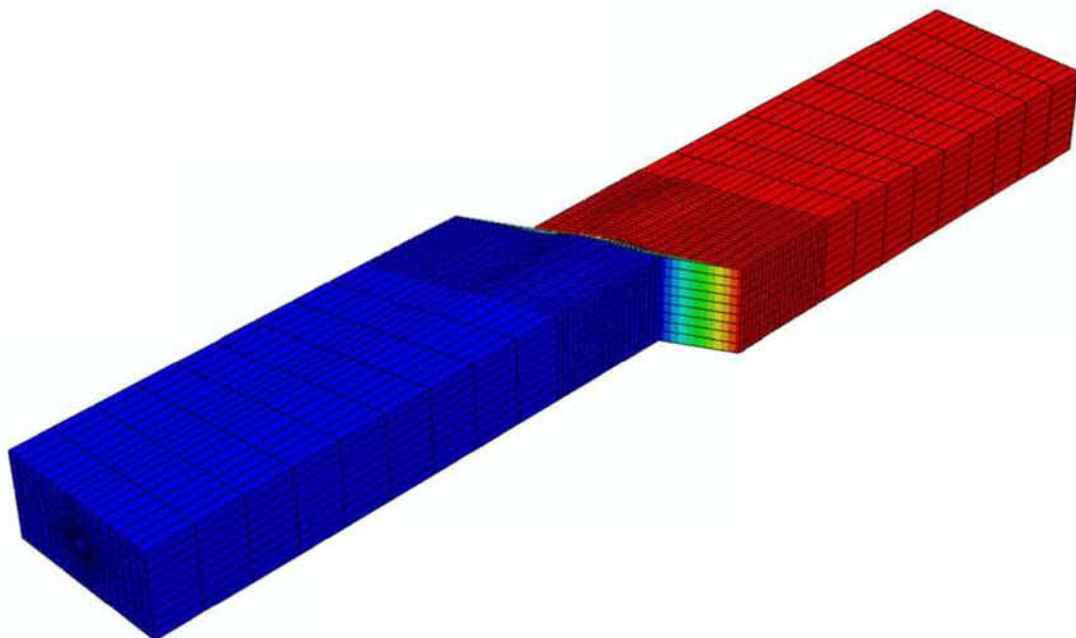

Figure 5.2: Deformation of the pipeline-soil system after application of fault displacement.

Figure 5.2 plots the soil–pipeline system after a seismic fault movement in the horizontal direction. The angle β between the fault direction n and the direction y (see Figure 3.9) is a key parameter of the present study. Positive values of β indicate that the fault movement induces tension to the pipeline, whereas negative values of β induce compression. To overcome numerical complications due to discontinuity at the vicinity of the fault, the fault movement is considered to occur within a narrow zone of width w, as in Chapter 4, a common practice in several recent numerical studies of fault-foundation interaction [62, 63, 64], which is also probably a more realistic representation of the fault displacement mechanism [67].

During the consecutive stages of fault displacement, the performance criteria are evaluated, monitoring the maximum values of longitudinal and hoop strain along the pipeline, the cross-sectional distortion at critical locations and the formation of pipeline wall wrinkling.

In the following sub-sections 5.2.1 and 5.2.2, non-pressurized X65 pipelines are analyzed under cohesive and non-cohesive soil conditions respectively, whereas in sub-section 5.2.3 the effects of internal pressure are investigated. Finally, in sub-section 5.2.4, the structural response of high-strength X80 steel pipelines is examined, including the effects of internal pressure.

5.2 Numerical results for pipelines of finite length

Numerical results are obtained for X65 and X80 steel pipelines for typical values of the diameter-to-thickness ratio, and for different soil conditions. The outer diameter D of the pipe is equal to 914.4 mm (36 in), which is a typical size for oil and gas transmission pipelines. Four values for the pipe wall thickness are considered, namely 6.35 mm ($\frac{1}{4}$ in) 9.53 mm ($\frac{3}{8}$ in), 12.7 mm ($\frac{1}{2}$ in) and 15.88 mm ($\frac{5}{8}$ in), corresponding to D/t values equal to 144, 96, 72 and 57.6 respectively, which cover a wide range of oil and gas pipeline applications. Note that the first value corresponds (D/t =144) to relatively thin-walled pipes, which may also be used for water transmission pipelines.

The soil-pipeline model has dimensions 60 m $\times$ 10 m $\times$ 5 m in directions x, y, z respectively, as the model used in the previous chapter. The seismic fault plane crosses the pipeline axis at different angles, so that the value of angle β (see Figure 3.9) ranges between -10° and 45°, where the minus sign indicates a configuration in which the pipeline is subjected to global compression.

5.2.1 Non-pressurized X65 steel pipelines in cohesive soils

Buried X65 steel pipelines, having a 36-inch-diameter, are examined first, in the absence of internal pressure, considering cohesive soil conditions with appropriate values of soil parameters c, φ and E. The API 5L X65 steel is a typical steel material for oil and gas pipeline applications, with a nominal stress - engineering strain curve shown with a dashed line in Figure 4.3a, obtained from a uniaxial tensile test. The yield stress σ_y is equal to 448.5 MPa (65 ksi) followed by a plastic plateau up to 1.48% strain and, subsequently, by a strain-hardening region with a hardening modulus equal to about $E_s/300$, where E_s is the Young's modulus of steel equal to 210 GPa.

A buried steel pipeline with wall thickness equal to $\frac{3}{8}$-inch, embedded in a soft-to-firm clay soil (Clay I) is considered first. This clay, responding under "undrained conditions", has a cohesion c = 50 kPa, friction angle $\varphi=0^{\circ}$, Young's modulus E = 25 MPa and Poisson's ratio ν = 0.5. Figure 5.3 depicts the shape of the deformed pipeline at fault displacements d = 0.4 m, 1.37 m, 2 m and 2.9 m in the area near the fault, crossing the fault at a right angle (β = 0°). Moreover, it depicts distribution of the longitudinal normal strain ε_x on its outer surface and the distortion of the pipe cross-section at the same four values of fault displacement.

Figure 5.4a plots the distribution of the longitudinal normal strain ε_x on its outer surface for fault displacement values d from 0.4m to 0.45m. For $d=0.43$ m, the pipeline wall exhibits local buckling, in the form of a short-wave wrinkling pattern. It is reminded that the wrinkling pattern is formed gradually with increasing fault displacement. Figure 5.4b illustrates the deformed pipeline in the buckled area and plots the pipeline surface displacements for values of d from 0.4m to 0.45m.

As discussed in the previous chapter, the onset of buckling is defined as the stage in which outward displacement of the pipe wall starts at the area of maximum compression and the corresponding displacement is referred to as "critical fault displacement" (d_{cr}). At that stage, bending strains due to pipe wall wrinkling develop, associated with significant tensile strains at the "ridge" or "crest" of the buckle, so that the longitudinal compressive strains at this location at the outer surface of the pipe wall start decreasing, forming a short wavy pattern at this location.
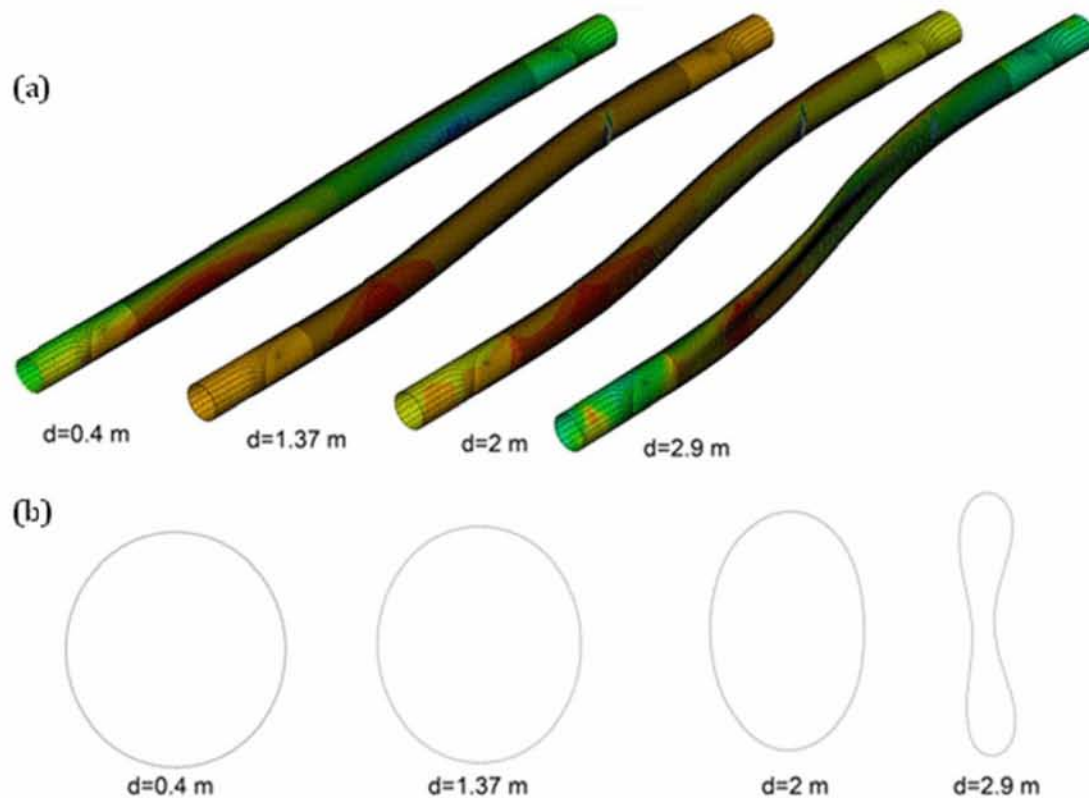
Figure 5.3: (a) Deformed shape and distribution of longitudinal strain along a pipeline crossing a strike-slip fault ($\beta = 0°$) for various values of fault displacement and (b) cross-sectional deformation at a distance of 0.5 m from the fault (X65 steel, $D/t = 96$, Clay I, $p=0$)

At the onset of local buckling, the longitudinal compressive strain at the buckle location (ε_{cr}) is equal to -6.90×10^{-3}, which is considerably higher than the corresponding value of -2.71×10^{-3} predicted by the equation of Gresnigt and Karamanos [50]. Furthermore, the maximum tensile strain on the opposite side of the pipe ($\varepsilon_{T,max}$) is 3.54×10^{-3}, which is substantially lower than the strain that would cause tensile failure in the form of rupture in a non-seriously-defected pipeline.

Under increasing fault displacement the wrinkled pattern develops further, resulting in a significant localization of deformation at the buckled area. However, this wrinkle development occurs up to a fault displacement equal to 1.37m, whereas beyond this value, the depth of the buckle (i.e. the wrinkling wave amplitude) starts decreasing due

to longitudinal stretching of the pipeline, as shown in Figure 5.3b for values of fault displacements d greater than 1.37 m. Furthermore, as the total pipeline length increases with continued fault movement due to longitudinal stretching, it results to higher tensile strains in the longitudinal direction, whereas the corresponding compressive strains become smaller. This is shown in Figure 5.3b, where for a fault displacement of d = 2.9 m, compressive longitudinal strains are significantly lower than those corresponding to a fault displacement of d = 1.4 m. The variations of longitudinal compressive and tensile strain ε_x along the two outer (most stressed) generators of the pipe cylinder are shown in Figures 5.4 and 5.5 for a small segment of the pipeline about the critical area and for different values of the fault displacement.

Beyond the formation of the local buckle and for fault displacement greater than 1.5m, significant distortion of the cross-section in the form of ovalization is observed. The pipeline cross-section with maximum distortion is located at a distance of 0.5 m from the fault, and the corresponding flattening parameter (equation 2.17) reaches the critical value of 0.15 at a fault displacement equal to $d = 1.71$ m. In addition, the maximum tensile longitudinal strain of the pipe is significantly increased, on either side of the pipeline cross-section, which may lead to local fracture at welds or at locations of minor defects. For a fault displacement of d = 1.62 m, the maximum tensile strain is equal to 3%, a critical value as discussed above. At the end of the analysis (fault displacement equal to 4m), the longitudinal tensile strain limit of 5% has not been reached at any location of the pipeline wall.
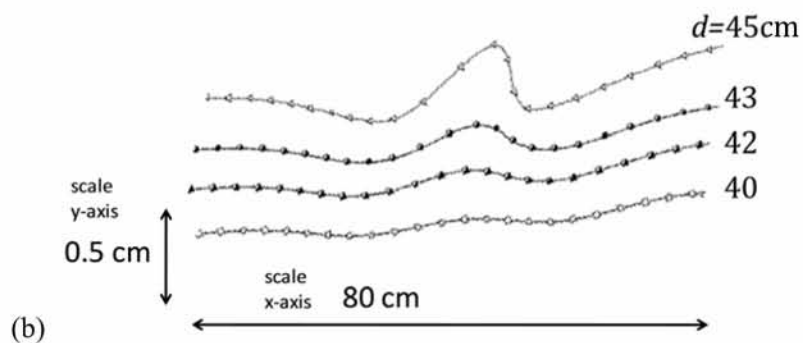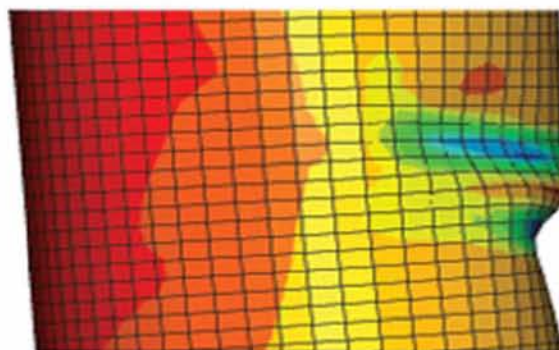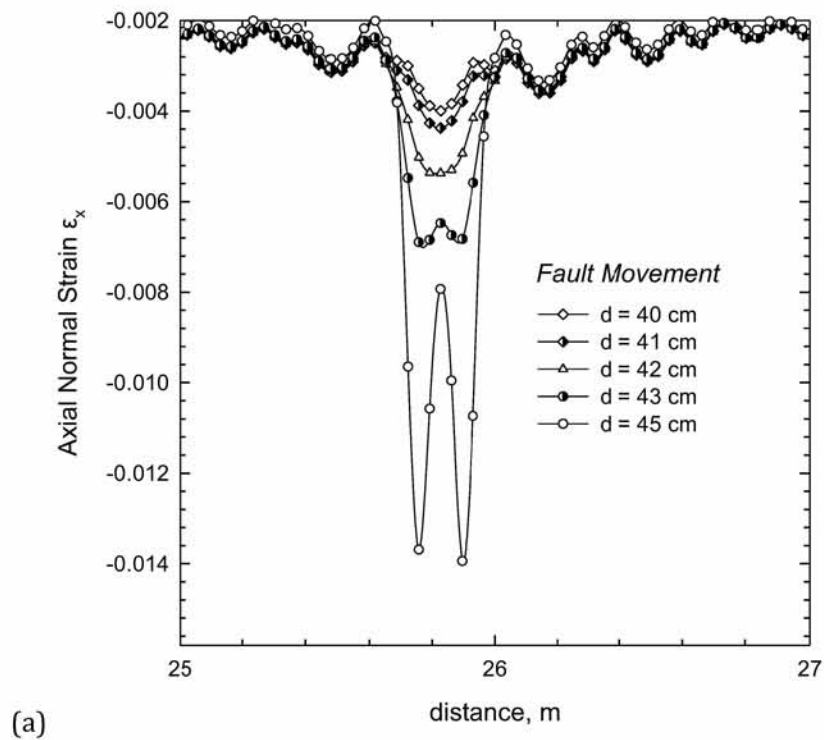
(a)

(b)

Figure 5.4: (a) Variation of axial strain along the critical pipeline generator at the compression side of the buckled area for different values of fault displacement, (b) evolution of wall wrinkling (X65 steel, $D/t = 96$, Clay I, and $\beta = 0°$).
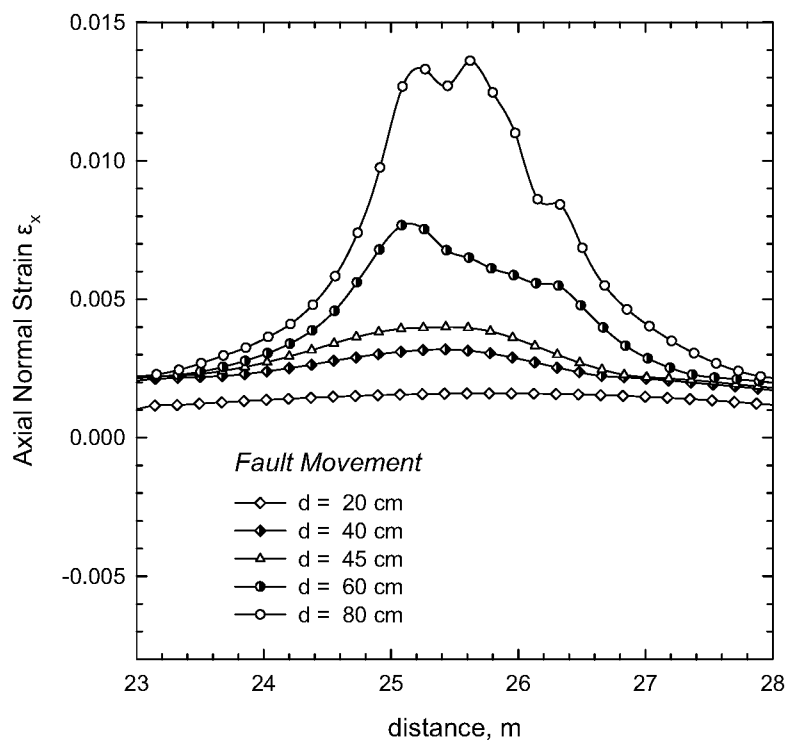
Figure 5.5: Variation of axial strain at the tension side of the buckled area for different values of fault displacement (X65 steel, $D/t = 96$, Clay I, and $\beta = 0°$).

The same X65 steel, 36-inch-diameter ⅜-inch-thick pipeline, embedded in the same soft-to-firm clay (Clay I), is also examined for various crossing angles. Figure 5.6 shows the deformed shapes of the pipeline for a value of β equal to 25°, at various fault displacements. At this angle, local buckling of the pipeline wall does not occur. The deformed shape shows a significant distortion of the pipeline cross-section in the form of ovalization. The amount of ovalization, measured according to the flattening parameter f, reaches a critical value of 0.15 at fault displacement of 0.77 m, at the area where the pipe intersects with the fault. Under increasing fault movement, this ovalization pattern is further developed resulting in a severe distortion of the pipe cross-section (see Figure 5.6), associated with negative hoop curvature of the pipeline wall, sometimes referred to as "inversion", for a fault displacement d = 1.45 m. The critical longitudinal tensile strain limits of 3% and 5% appear at a fault displacements of d = 0.58 m and d = 1.15 m, respectively, one meter away from fault.
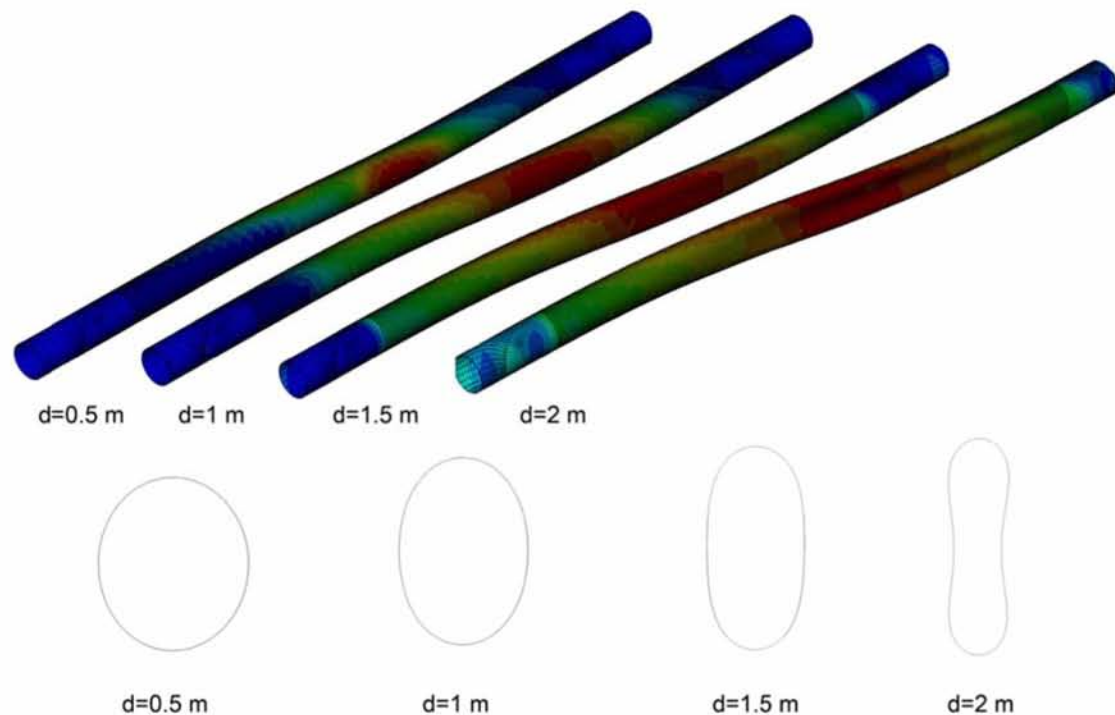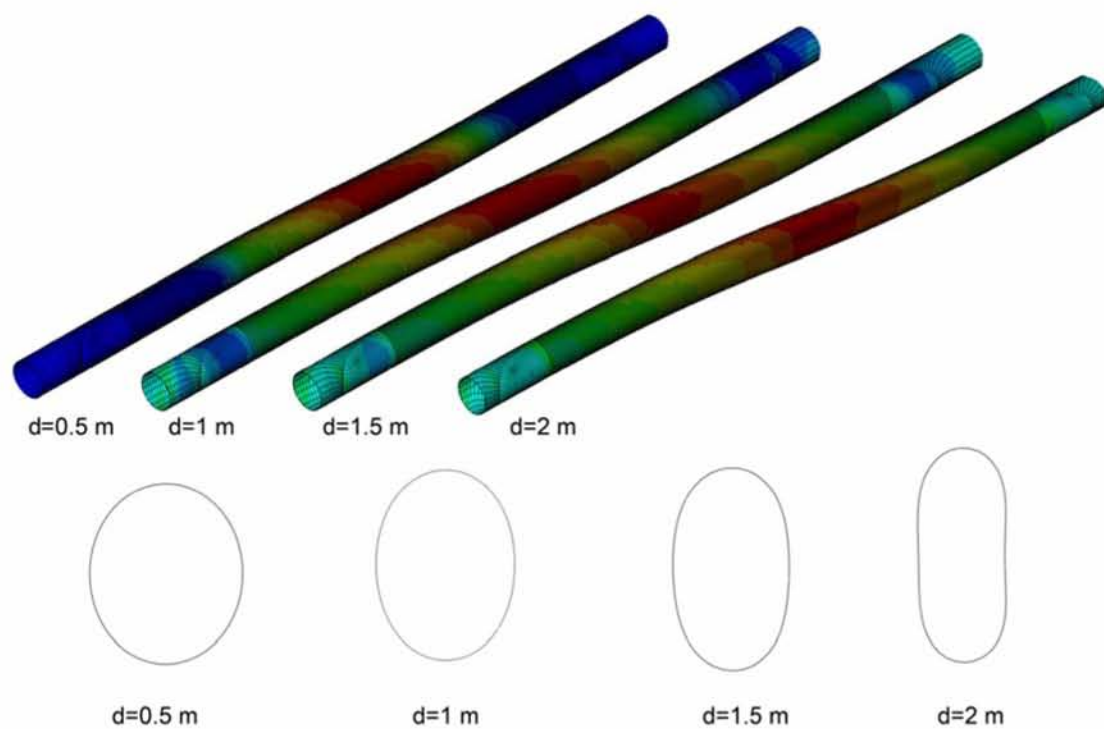
Figure 5.6: (a) Deformed shape and distribution of longitudinal strain along a pipeline crossing a strike-slip fault at $\beta = 25°$ for various values of fault displacement and (b) cross-sectional deformation at a distance of 0.5 m from the fault (X65 steel, $D/t = 96$, Clay I, p=0)

Moreover, the same pipeline embedded in Clay I soil conditions is also analysed for the case of crossing the fault plane at an angle of β equal to 45°. The deformed shapes of the pipeline are shown in Figure 5.7 for fault displacement values equal to 0.5m, 1m, 1.5m, and 2m. Maximum longitudinal tensile strain occurs at the cross-section where the pipeline crosses the fault plane and reaches the critical values of 3% and 5% at a fault displacements d = 0.335 m and 0.885 m, respectively. Furthermore, the cross-sectional flattening parameter f reaches the critical value of 0.15 at fault displacement of 0.74 m, at the area where the pipeline intersects the fault plane. Under increasing fault movement, this flattening pattern develops further as shown in Figure 5.7, resulting into an inversion of the pipeline wall, for a fault displacement of d = 1.80 m.

The response of the pipeline becomes quite different if a negative crossing angle β is considered. In this case, the fault motion is associated with a decrease of length of the pipeline, resulting in the development of significant compressive stresses and strains, leading to local buckling.

Figure 5.8 shows the deformed shape of the above ⅜-inch X65 steel pipeline embedded in Clay I soil conditions, crossing the fault plane at an angle of β equal to -10°. The critical fault displacement at which wrinkling initiates has been computed equal to 0.225 m at a distance of 3.6 m away from the fault. At this point the values of compressive strain at buckle is -5.32×10^{-3}, higher than the value of -2.71×10^{-3} predicted by equation (2.15), whereas the corresponding maximum tensile strain on the opposite side of the pipeline wall is equal to 1.01×10^{-3}. Upon continuation of fault displacement, the buckle pattern is further developed resulting in folding of the pipeline wall and inversion of the buckled cross-section at fault displacement d=0.75m. Tensile strain of 3% occurs at fault displacement d=0.49m and 5% at d=0.67m, and the ovalization performance criterion is reached at d=2.3m, at a distance of 0.5m from the fault.

Figure 5.7: (a) Deformed shape and distribution of longitudinal strain along a pipeline crossing a strike-slip fault at $\beta = 45°$ for various values of fault displacement and (b) cross-sectional deformation at a distance of 0.5 m from the fault (X65 steel, $D/t = 96$, Clay I, $p=0$)
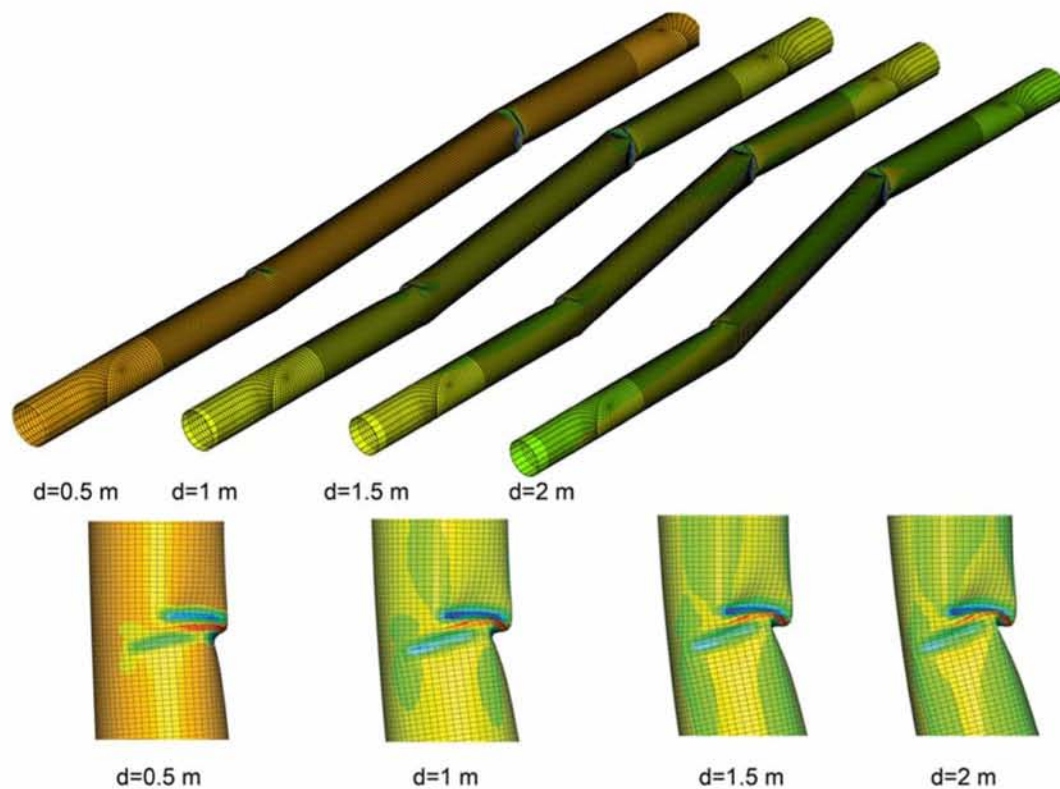
Figure 5.8: (a) Deformed shape and distribution of longitudinal strain along a pipeline crossing a strike-slip fault at $\beta = -10°$ for various values of fault displacement and (b) cross-sectional deformation at a distance of 0.5 m from the fault (X65 steel, $D/t = 96$, Clay I, $p=0$)

Results from an extensive parametric investigation for different values of the angle β are shown in graphical form in Figure 5.9 for X65 steel, $D/t = 96$, Clay I soil condtions and zero internal pressure p. The results are plotted in terms of critical fault displacements versus the crossing angle β for each of the four performance criteria: (a) local buckling, (b) longitudinal strain equal to 3%, (c) longitudinal strain equal to 5% and (d) cross-sectional flattening $f = 0.15$.

The results indicate that for non-positive values of angle β, local buckling is the dominant limit state. For positive values of β, two major limit states, namely the 3% longitudinal tensile strain and the cross section flattening are most important. For values of β up to about 15°, cross sectional flattening is reached first, whereas for greater values of β the 3% tensile strain criterion becomes the dominant limit state. It is further observed that, an increase of the value of β results in a significant decrease of the value of normalized critical fault displacement.
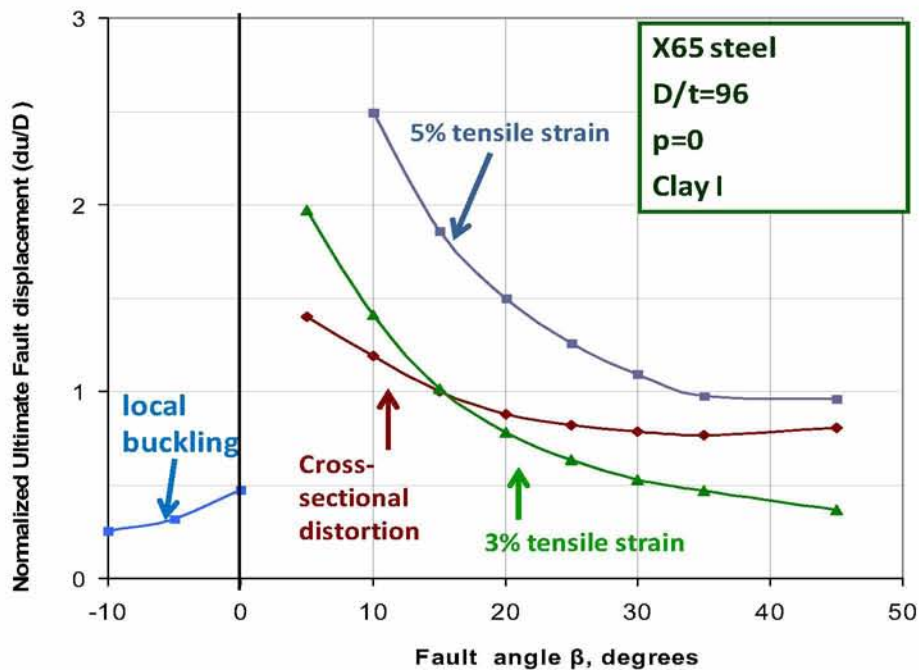
Figure 5.9: Normalized critical fault displacement for various performance limits at different angles of β (X65 steel, Clay I, D/t=96, p =0).

In a similar way, Figures 5.10, 5.11 and 5.12 plot the fault displacement values corresponding to the four performance criteria with respect to the crossing angle β for X65 pipelines with D/t ratios equal to 144, 72 and 57.6, respectively. The results indicate that the behaviour has several similarities with the results in Figure 5.9. Nevertheless, the results show a significant dependence of the critical fault displacement with respect to the D/t ratio. Local buckling is observed at non-positive values of β. In addition, for the thin-walled pipeline (D/t = 144) local buckling may also occur for small positive values of β (β =5º) at a value of fault displacement equal to 0.52m. With increasing fault displacement, the local buckle does not develop further, and its size is reduced due to longitudinal stretching.

For all cases with positive values of β , the flattening limit state and the 3% tensile strain limit state are dominant, as in the case of D/t = 96. The angle β at which the 3% tensile strain limit state becomes critical over the flattening limit state depends on the D/t ratio. For the case of D/t equal to 57.6 the 3% tensile strain is the governing limit state criterion.
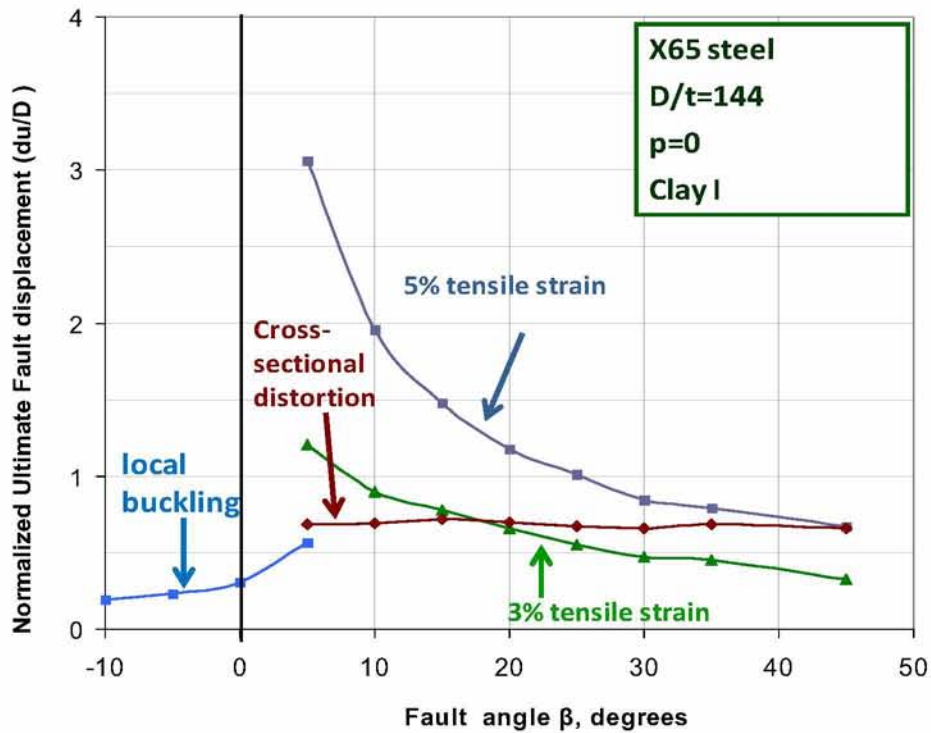
Figure 5.10: Normalized critical fault displacement for various performance limits at different angles of β (X65 steel, Clay I, D/t=144, p =0).
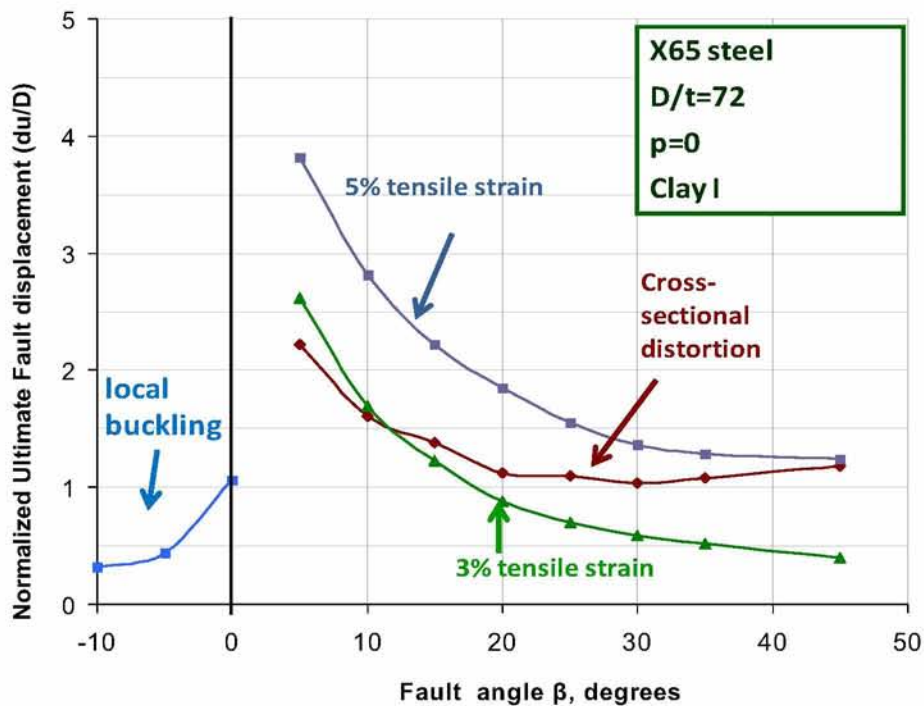

Figure 5.11: Normalized critical fault displacement for various performance limits at different angles of β (X65 steel, Clay I, D/t=72, p=0).
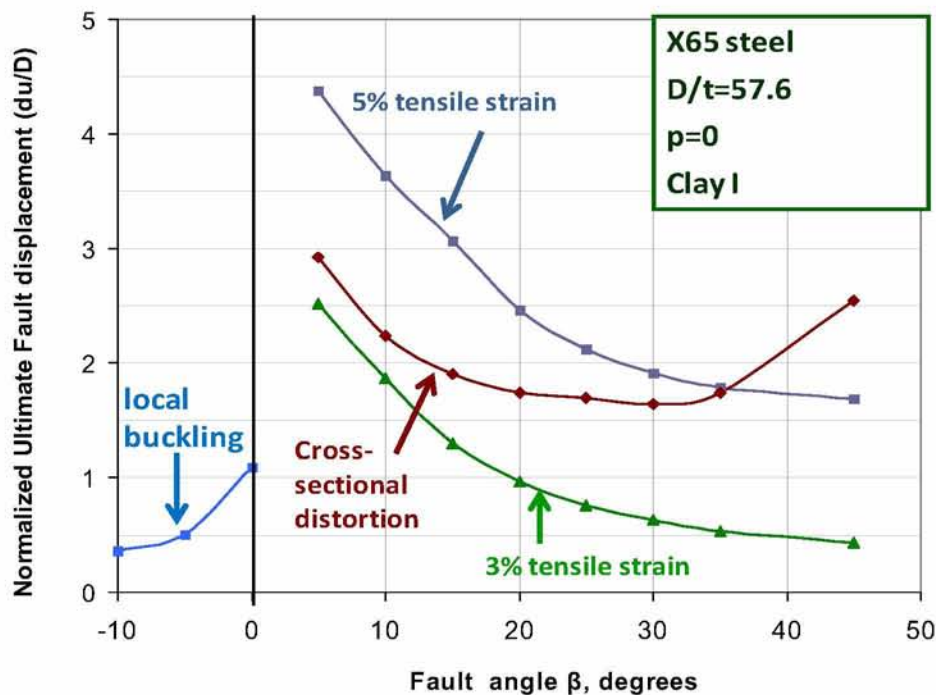
Figure 5.12: Normalized critical fault displacement for various performance limits at different angles of β (X65 steel, Clay I, D/t=57.6, p=0)

The response of the above X65 steel pipeline (D/t = 96), buried in stiffer cohesive soil conditions, is examined, assuming values of soil parameters c, E and φ equal to 200 kPa, 100 MPa and 0°, respectively. This soil represents a very stiff clay under "undrained conditions", referred to as Clay II. The numerical results indicate that the bending deformation of the pipeline in stiff soil occurs within a short distance from the fault location. For the particular case of $\beta = 0°$, the critical cross-section is at a distance of 2.5 m from the fault. Comparison of results in Figure 5.13 with those shown in Figure 5.9 (for Clay I) demonstrates the significant effect of site conditions on the response of the steel pipeline. In the case of a stiff soil, bending deformation affects a smaller length of the pipeline, so that higher bending stresses and strains develop for the same fault displacement d, than those in the case of a soft soil. Thus, the performance limits for the stiff soil are reached at significantly lower value of fault displacement. Furthermore, in stiff soil conditions, Figures 5.14 and 5.15 depict the corresponding results for X65 pipelines with D/t equal to 144 and 72. The results, compared with those in Figures 5.9, 5.10 and 5.11 indicate a significantly lower deformation capacity for stiff soil conditions. Furthermore, the results show that for positive values of angle β the 3% tensile strain is the governing mode of failure.
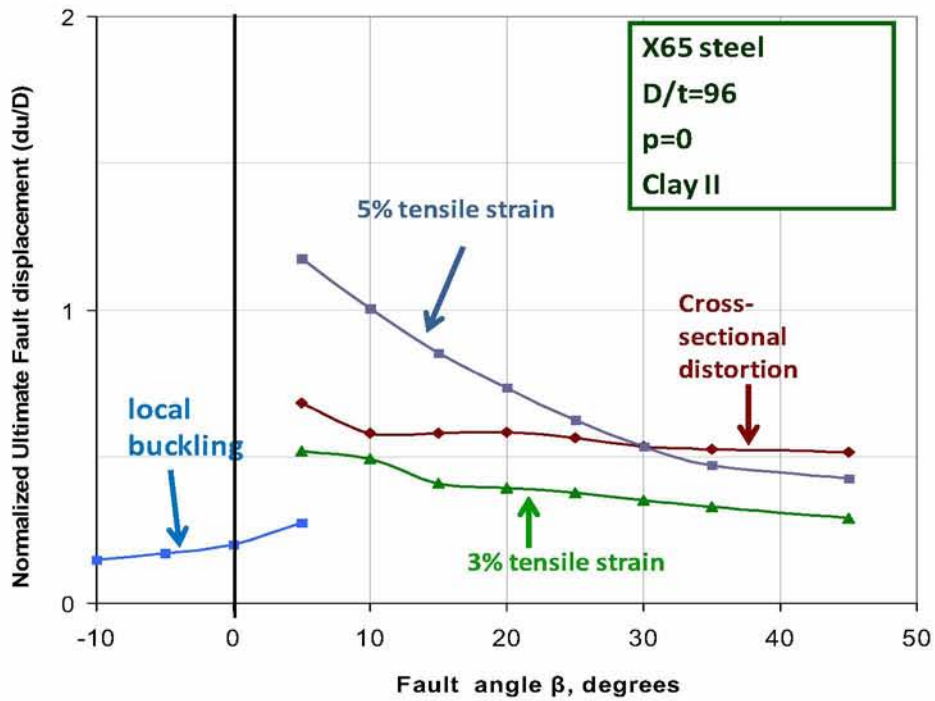
Figure 5.13: Normalized critical fault displacement for various performance limits at different angles of β (X65 steel, Clay II, D/t=96, p=0).
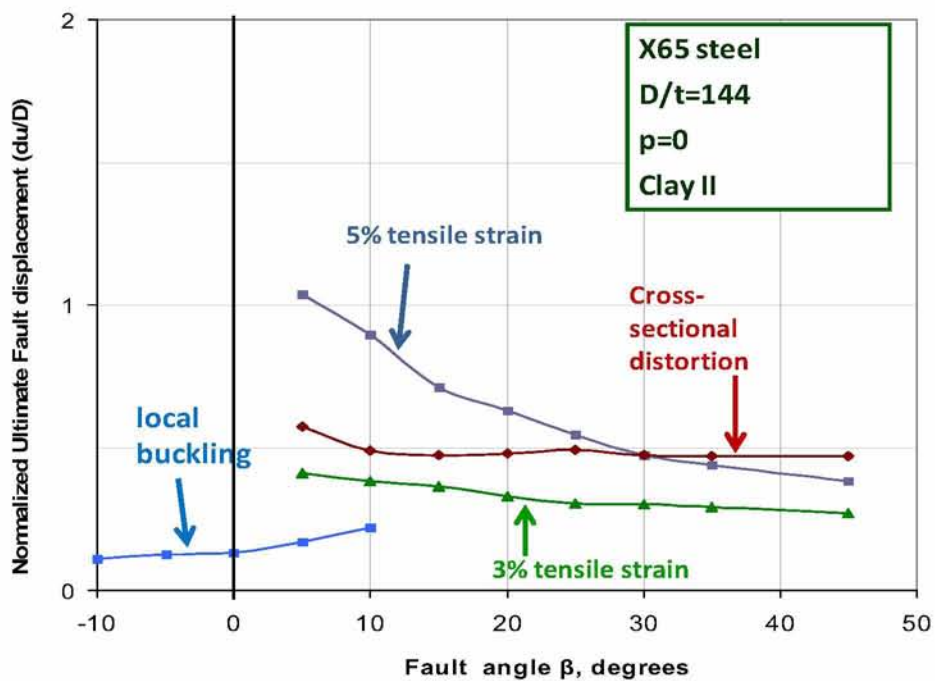

Figure 5.14: Normalized critical fault displacement for various performance limits at different angles of β (X65 steel, Clay II, D/t=144, p=0).
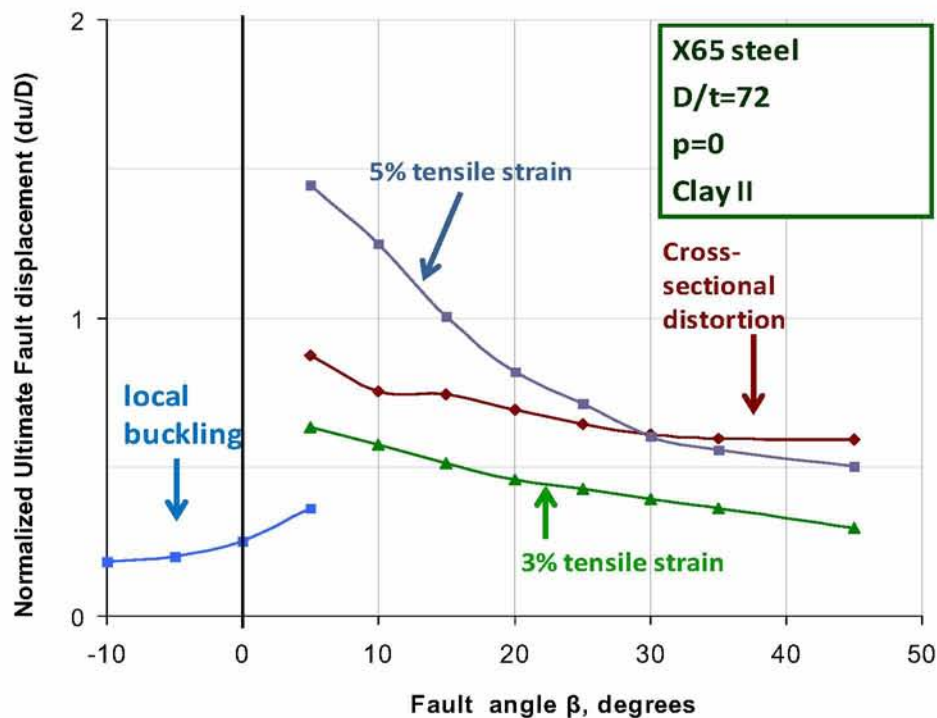
Figure 5.15: Normalized critical fault displacement for various performance limits at different angles of β (X65 steel, Clay II, D/t=72, p=0).

Depending on pipeline thickness, local buckling may also occur at positive values of angle β. More specifically, local buckling occurs for $\beta = 5^{\circ}$ in the case of D/t equal to 72 and 96, whereas for the case of thin-walled pipeline ($D/t = 144$) local buckling occurs even at $\beta = 10^{\circ}$

5.2.2   Non-pressurized X65 steel pipelines in cohesionless soils

In this section, the response of the above X65 steel pipeline ($D/t = 96$) embedded in cohesionless soils is examined and compared to the response obtained for the cohesive soils. A granular soil is considered with a friction angle φ =30°, Young's modulus E =8 MPa and Poisson's ratio v =0.3, corresponding to loose sand and referred to as "Sand". The relatively small value of the stress-depended Young's modulus E is justified by the shallow embedment depth of the pipeline. A small amount of artificial cohesion equal to c = 5 kPa is also assumed to prevent numerical difficulties associated with the behaviour of a purely frictional material at very small confining stress, such as during gap opening at the pipe-soil interface.

For various values of β, the results for the X65 pipeline with D/t =96 are summarized in Figure 5.16. The numerical results indicate that, for non-positive values of the angle β, local buckling is the dominant limit state. For the particular case of zero crossing angle (β =0°), a value of fault displacement equal to 0.59 m is required for local buckling to occur. Beyond this stage, significant distortion of the cross-section occurs due to local buckling on the pipe wall on the compression side of the bent pipeline. The shape of the developing buckling is similar to that of Clay I. The longitudinal compressive strain at the onset of local buckling (ε_{cr}) is equal to -8.4×10^{-3}, higher than the value calculated via equation (2.15). For positive values of angle β up to 20°, the cross-sectional flattening limit state is dominant, whereas for larger values of β the 3% tensile strain is the governing limit state.

The corresponding results for an X65 pipeline with D/t equal to 72 are depicted in Figure 5.17. The behaviour of this thicker buried pipeline has similar trends, but the results indicate that larger fault displacements are required in order to reach the performance criteria.
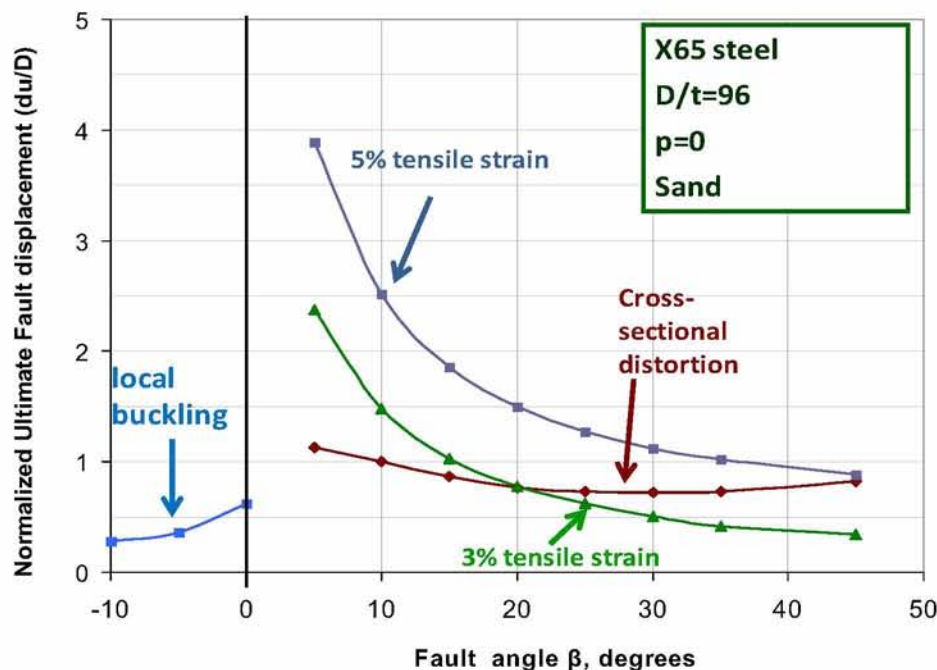

Figure 5.16: Normalized critical fault displacement for various performance limits at different angles of β (X65 steel, Sand, D/t=96, p=0).
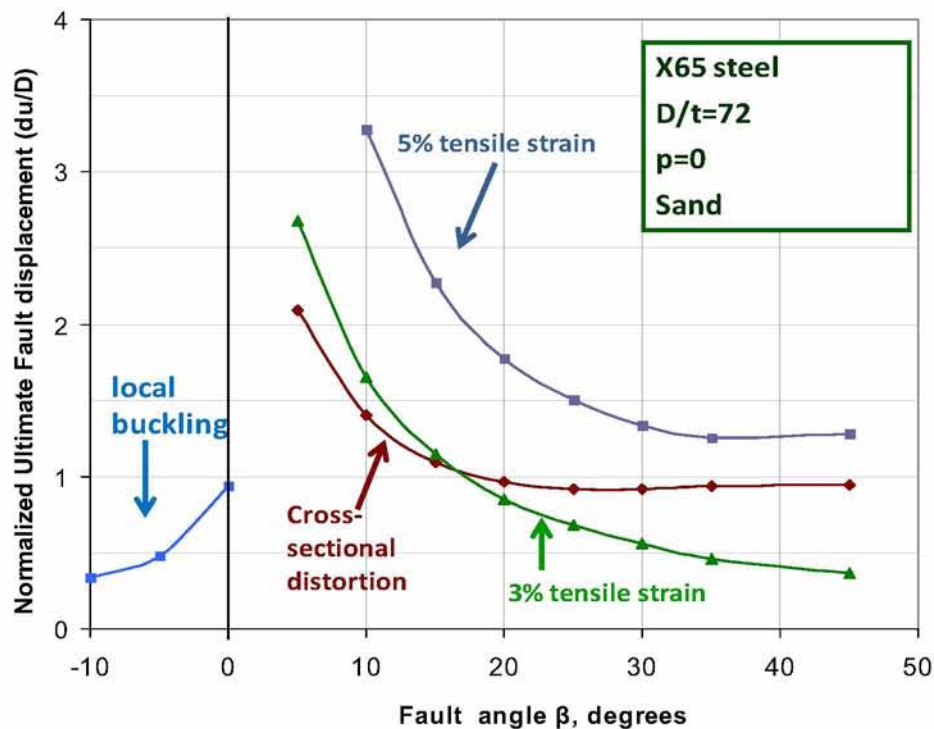
Figure 5.17: Normalized critical fault displacement for various performance limits at different angles of β (X65 steel, Sand, D/t=72, p=0).

5.2.3 Mechanical behavior of pressurized X65 steel pipelines

The effects of internal pressure on pipeline mechanical behaviour are investigated considering internally pressurized X65 pipelines with thickness of ⅜ inch, embedded in soft-to-firm soil conditions (Clay I). The numerical results presented in Figures 5.18 and 5.19 correspond to a pressure level of 38 bar, which is equal to 56% of the maximum operating pressure p_{max} expressed by equation (4.1), whereas the results in Figures 5.20 and 5.21 show the corresponding results for a lower pressure level equal to 26 bar, which is 38% of p_{max}. At those levels of internal pressure, cross sectional distortion of the pipeline is quite small and flattening does not reach the critical value of 0.15, even for large values of the imposed fault displacement. For non-positive values of angle β local buckling occurs. The buckled shapes of the pressurized pipelines, shown in Figure 5.22 are quite different from those of the non-pressurized pipelines shown in Figure 5.4b. Nevertheless, the corresponding values of critical fault displacement d_{cr} (0.41 m and 0.39 m for 38% and 56% of p_{max}, respectively) are somewhat lower than the corresponding value without pressure. This is attributed to the development of

144

additional stresses and strains in the pipeline wall that cause early yielding and premature local buckling formation, an observation also noted in [60].
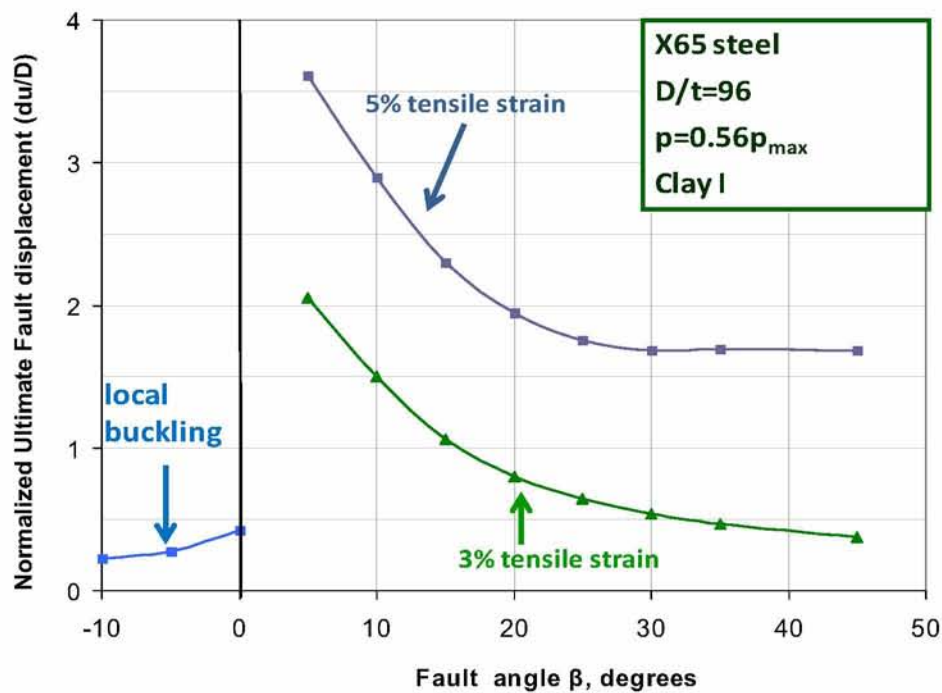

Figure 5.18. Normalized critical fault displacement for various performance limits at different angles of β (X65 steel, Clay I, D/t=96, p= 0.56 p_{max}).
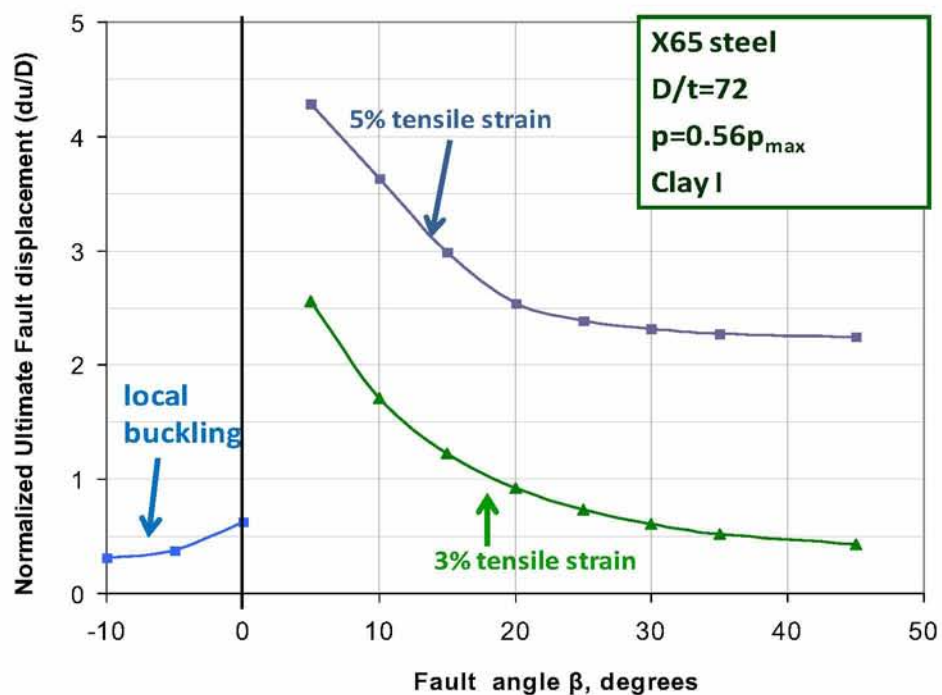

Figure 5.19: Normalized critical fault displacement for various performance limits at different angles of β (X65 steel, Clay I, D/t=72, p= 0.56 p_{max}).
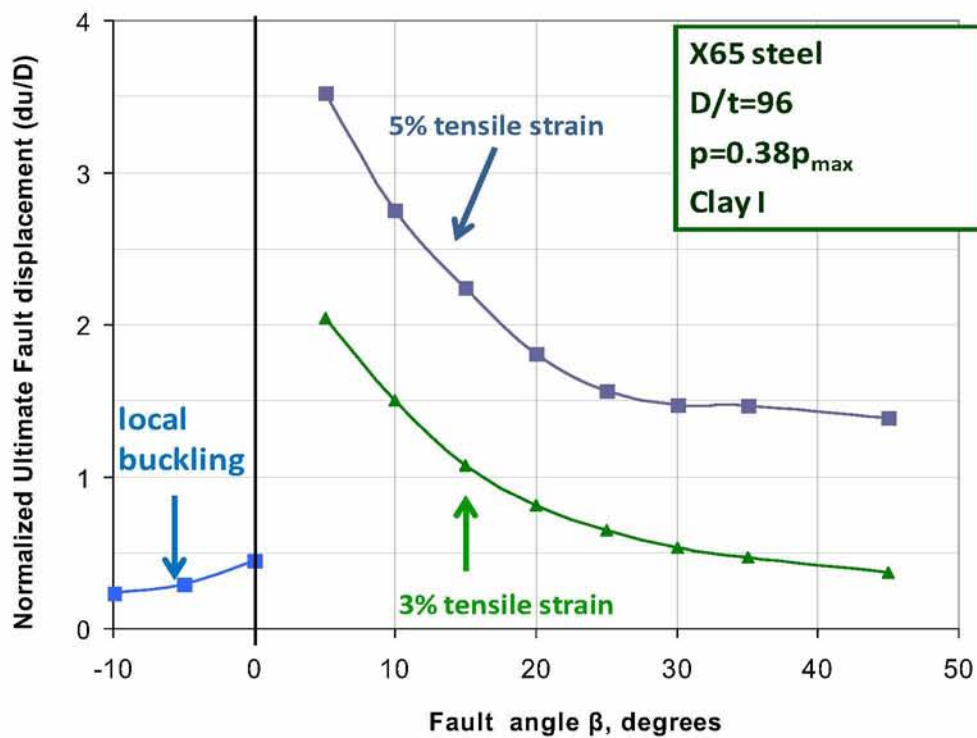
Figure 5.20: Normalized critical fault displacement for various performance limits at different angles of β (X65 steel, Clay I, D/t=96, p= 0.38 p_{max}).
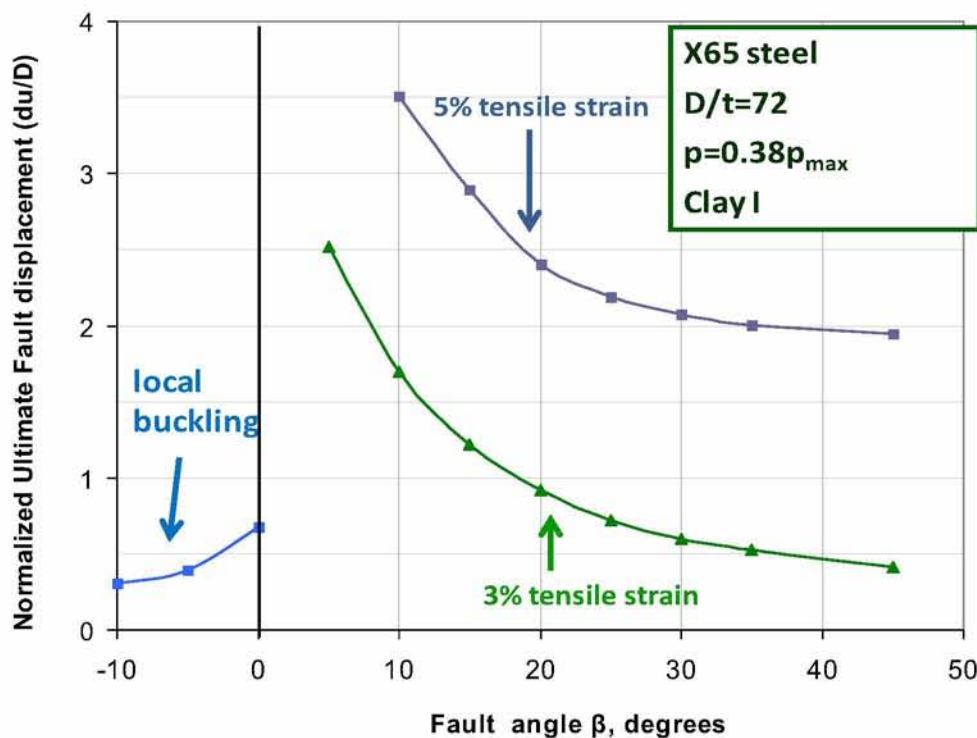

Figure 5.21: Normalized critical fault displacement for various performance limits at different angles of β (X65 steel, Clay I, D/t=72, p= 0.38 p_{max}).
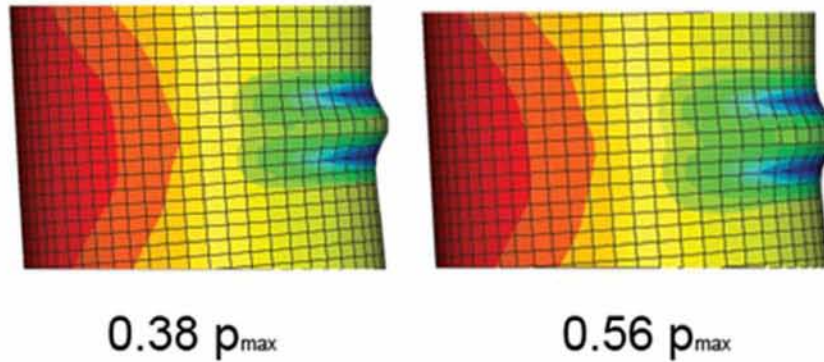
0.38 p_{max} 0.56 p_{max}

Figure 5.22: Buckled shapes of pressurized pipes.

The compressive longitudinal strains along the critical generator of the pressurized steel pipeline at the onset of local buckling are equal to -8.5×10^{-3} and -7.2×10^{-3} for 56% and 38% of p_{max}, which are higher compared to the values given from equation (2.15), equal to -4.9×10^{-3} and -3.77×10^{-3}, respectively. For positive values of angle β, the 3% longitudinal tensile strain criterion is the governing limit state.

The evolution of cross-sectional deformation in pressurized pipelines is shown in Figure 5.23 in terms of the flattening parameter f at the critical cross-section with respect to the applied fault displacement, for various levels of internal pressure.
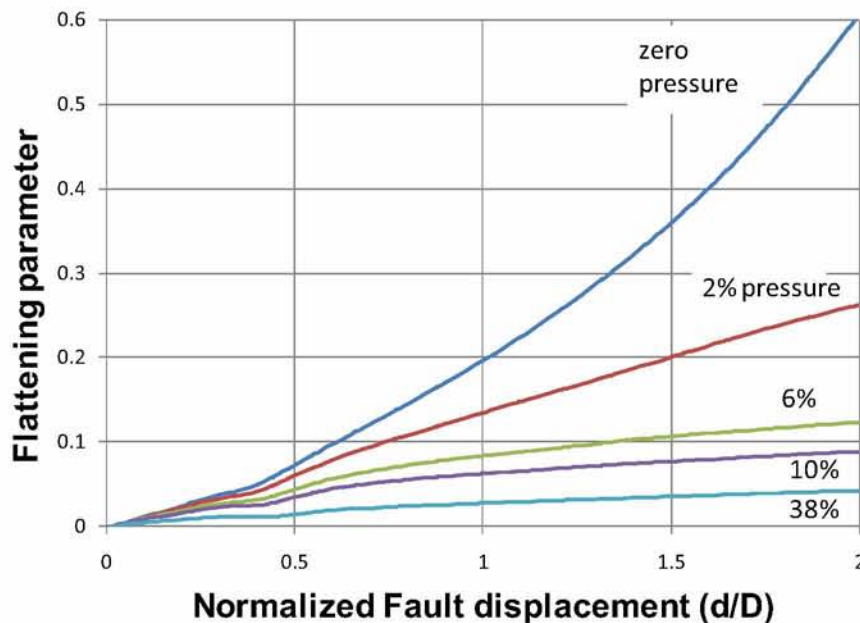

Figure 5.23: Evolution of flattening parameter f versus fault displacement for different values of internal pressure (X65 steel, $D/t = 96$, Clay I, $\beta = 25°$).

d=1 m

pr=0   pr=2%   pr=6%   pr=10%   pr=38%

Figure 5.24: Evolution of cross-sectional deformation in pressurized pipelines for the same fault displacement $d = 1$m (X65 steel, $D/t = 96$, Clay I, $\beta = 25°$).

It is interesting to note that even for low levels of internal pressure, the distortion of the cross-section is significantly reduced. Furthermore, in Figure 5.24, the cross-sectional shape of the pressurized pipelines is depicted for the same value of fault displacement ($d = 1$m), demonstrating the effects of internal pressure on cross-sectional deformation.

Finally, the evolution of hoop, longitudinal and von Mises stresses of the pipeline pressurized at 38% of p_{max} is shown in Figures 5.25, 5.26 and 5.27. The stresses are measured at the cross-section where maximum stresses occur during the application of fault movement, located 0.77 m from the fault. The measurements are obtained at location A, as defined from the sketch indicated in Figures 5.25 to 5.27, at both the inner and the outer surface of the pipeline wall. The starting value of hoop stress is about 125 MPa, which corresponds to a level of internal pressure equal to 38% of p_{max}. For fault displacement values less than 0.25 m, the pipeline remains elastic and, because of cross-sectional flattening, hoop stress at the inner and the outer surface have opposite variations (increase of the stress at the inner surface and decrease of the stress at the outer surface). After a fault displacement of 0.25 m (d/D≥0.3), the pipeline material is no longer elastic. The hoop stresses at both the inner and outer surface tend to stabilize

at the initial value of 125 MPa. Finally, the small increase of longitudinal stress and the von Mises stress with fault displacement is due to hardening.
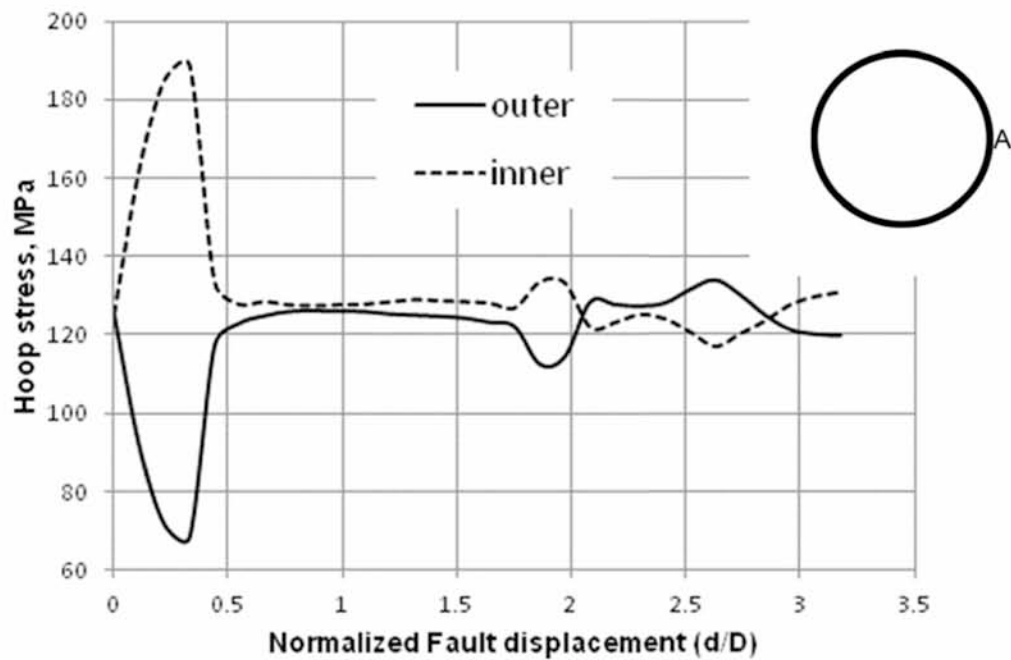

Figure 5.25: Hoop stress versus fault displacement at inner and outer surface cross-section, location A , at 0.77 m from the fault (X65 steel, $D/t = 96$, Clay I, p=0.38 p_{max}, $\beta = 25º$).
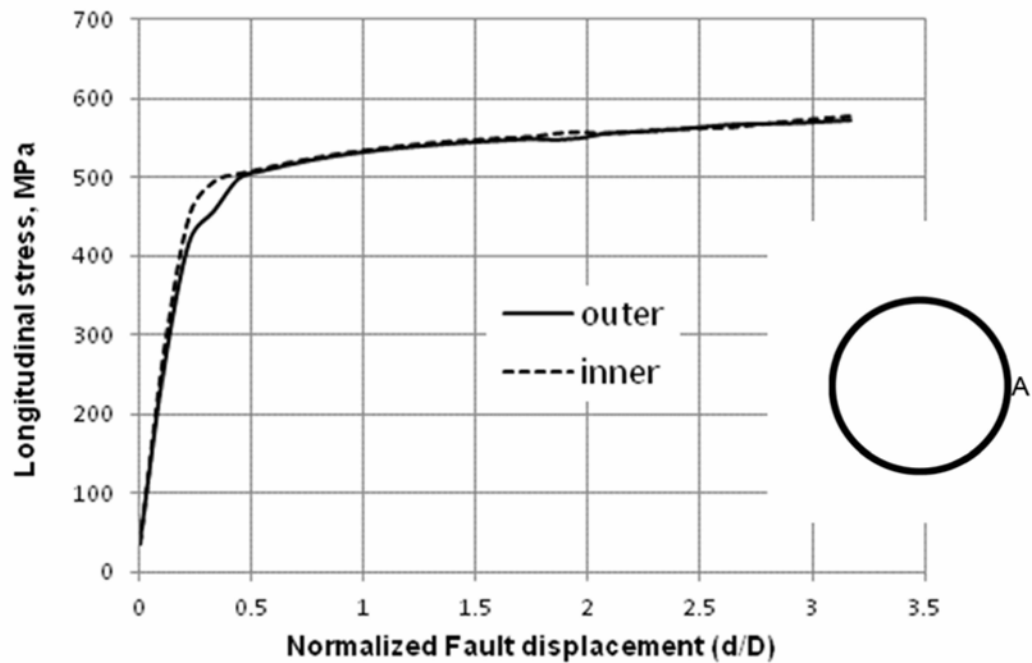
Figure 5.26: Longitudinal stress versus fault displacement at inner and outer surface cross-section, location A , at 0.77 m from the fault (X65 steel, $D/t = 96$, Clay I, p=0.38 p_{max} , $\beta = 25^{o}$).
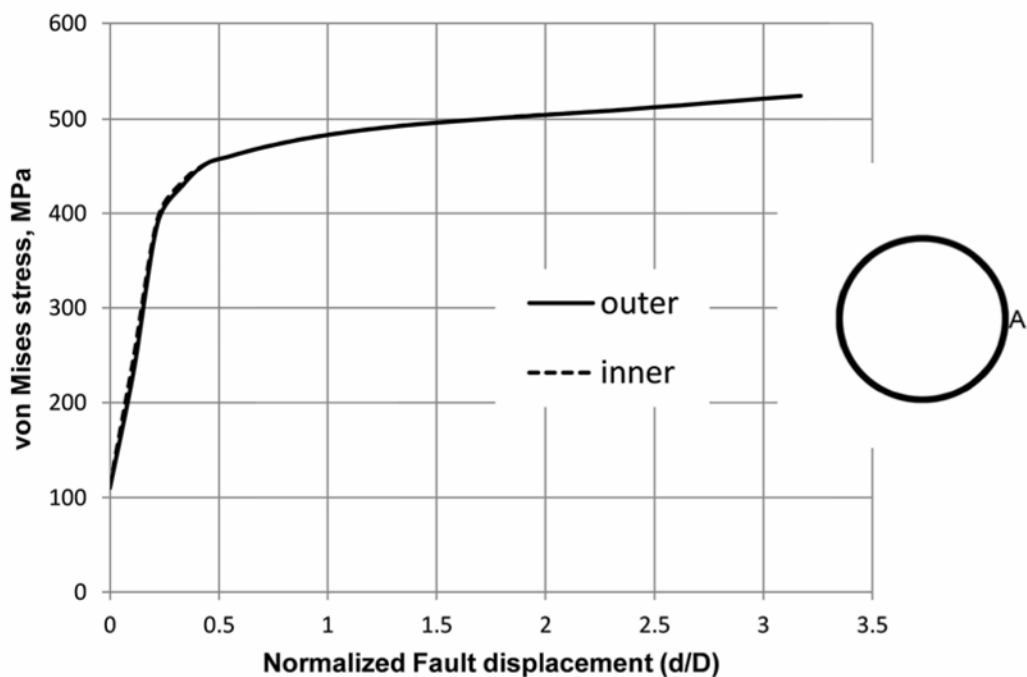

Figure 5.27: von Mises stress versus fault displacement at inner and outer surface cross-section, location A , at 0.77 m from the fault (X65 steel, $D/t = 96$, Clay I, p=0.38 p_{max} , $\beta = 25^{o}$).

5.2.4 Mechanical behavior of X80 steel pipelines

The behaviour of buried high-strength steel X80 pipelines under fault-induced deformation is also analysed, using the numerical tools described in the previous sections. The uniaxial nominal tensile stress–strain relationship of the API 5L X80 material is plotted in Figure 4.3 with a solid curve. The material has a yield stress of 596 MPa without a plastic plateau, corresponding to a cold expanded (UOE) line pipe. The maximum operating pressure p_{max} is given by equation (4.1) and is plotted with the solid line in Figure 4.2 in terms of the D/t value.

Numerical results are obtained for 36-inch-diameter X80 steel pipelines with thickness equal to $\frac{3}{8}$-inch and ½-inch, corresponding to D/t values equal to 96 and 72 respectively, embedded in soft-to-firm cohesive soils (Clay I). The numerical results for zero pressure are summarized in Figures 5.28 and 5.29 and indicate similar trends with those observed and discussed in the above paragraphs for the X65 pipelines. In both cases, local buckling of pipeline wall occurs at non-positive values of β. A comparison of these results with those in Figures 5.9 and 5.10 for the X65 pipelines indicate that buckling occurs at higher values of fault displacements. Nevertheless, for the specific case where $\beta = 0°$ and $D/t = 72$, local buckling does not occur. In this case the compressive buckling critical strain is rather high due to the high grade of steel. Thus, owed to the tensile strains induced by longitudinal stretching, this critical strain is not reached. More details on this behaviour regarding the onset of buckling are offered in Chapter 6, where a simplified model is presented. For positive values of the angle β, the ovalization performance criterion is reached first, for both values of D/t, up to an angle of β equal to about 40°.

The behavior of pressurized x80 steel pipelines is shown in figures 5.30 and 5.31. for non-positive values of β, local buckling occurs at critical fault displacement values that are similar, yet somewhat lower, than those of the non-pressurized x80 pipelines with the same D/t ratio. In addition, for positive values of the angle β, the cross-sectional shape of the pipeline remains quasi-circular, the flattening criterion is never reached, and the 3% longitudinal tensile strain is the governing limit state.
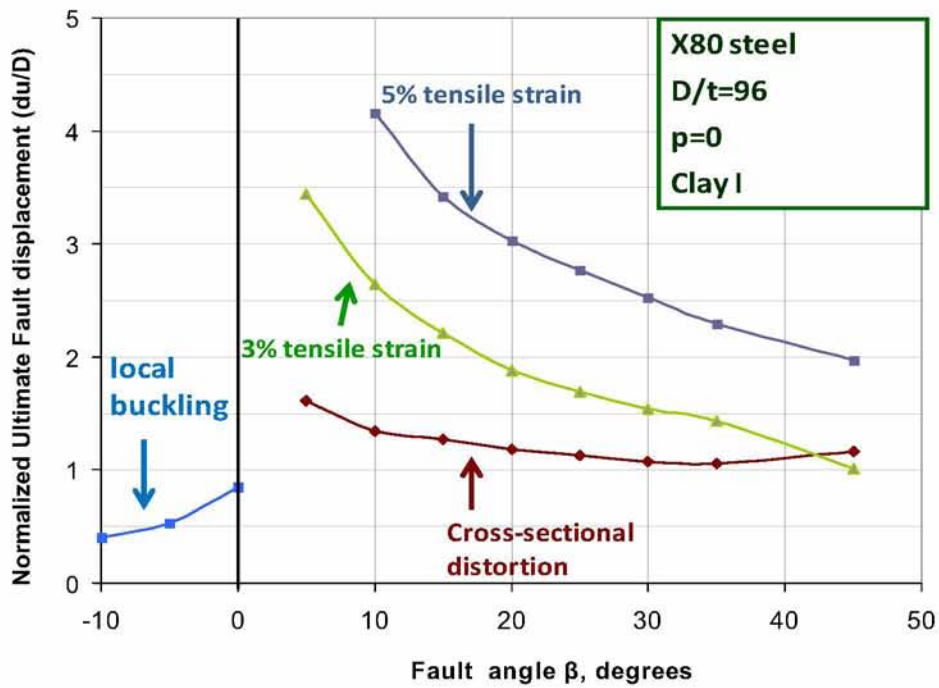
Figure 5.28: Normalized critical fault displacement for various performance limits at different angles of β (X80 steel, D/t=96, Clay I, p=0).

Figure 5.29: Normalized critical fault displacement for various performance limits at different angles of β (X80 steel, D/t=72, Clay I, p=0).

Figure 5.30: Normalized critical fault displacement for various performance limits at different angles of β (X80 steel, D/t=96, Clay I, p=0.46 p_{max}).
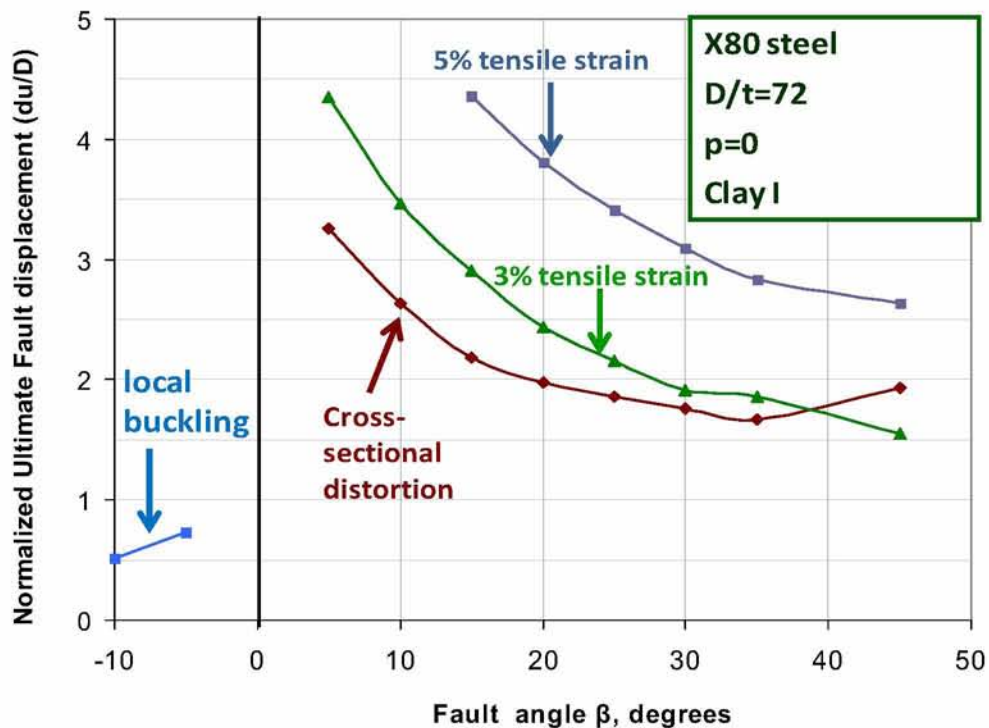

Figure 5.31: Normalized critical fault displacement for various performance limits at different angles of β (X80 steel, D/t=72, Clay I, p=0.46 p_{max}).
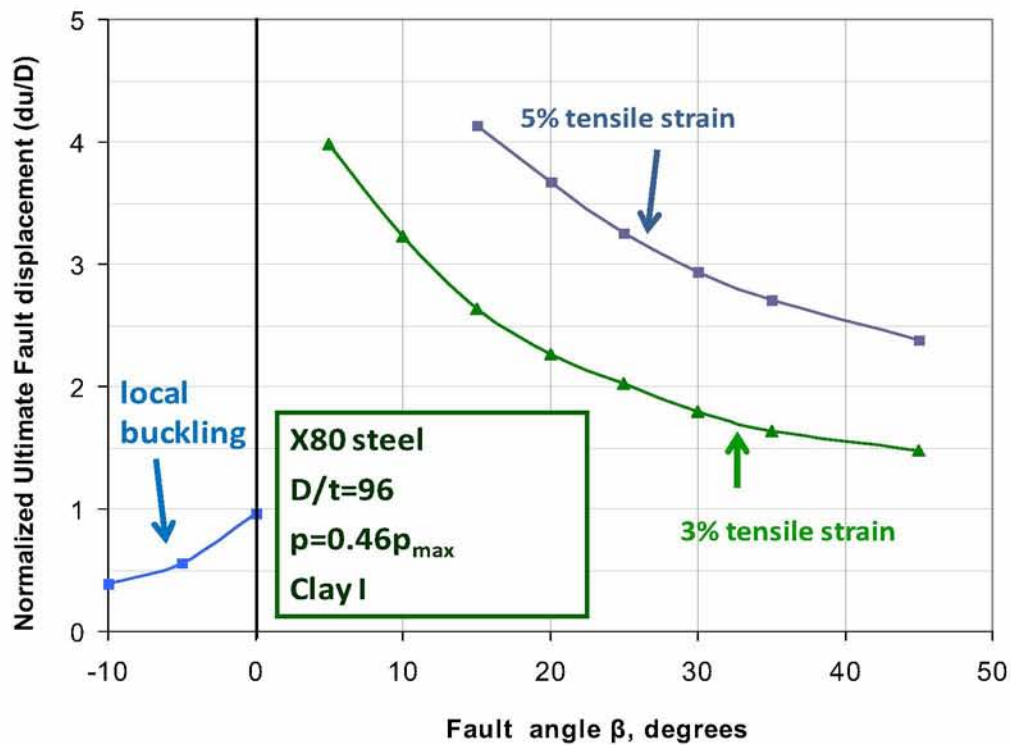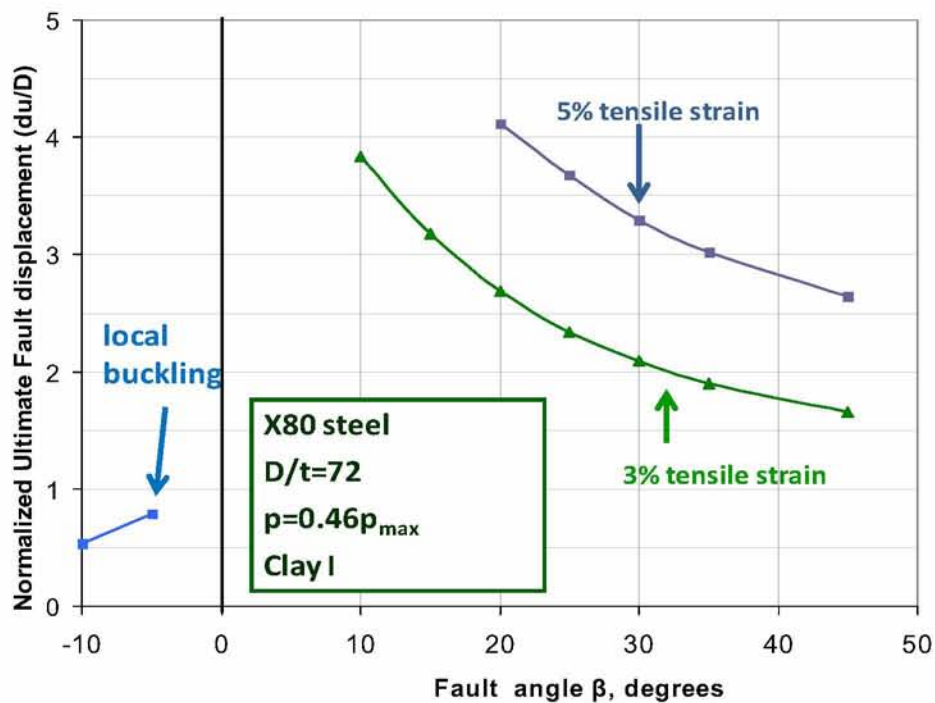
5.3 Numerical results for pipelines of infinite length

In this section, numerical results are obtained for the 36-inch, X65 steel pipeline, that crosses strike-slip faults at different angles, assuming infinite pipeline length, considering a pipe thickness equal to 9.53mm ($\frac{3}{8}$ in) resulting in a D/t ratio equal to 96. The soil-pipeline model has dimensions 60m × 10m × 5m in directions x, y, z respectively, which complies with the size requirements stated in the previous chapter. Finally, the equivalent nonlinear spring attached at the ends of the pipeline accounts for the infinite length, as presented in Chapter 3.

5.3.1 Pipeline performance for fault angle $\beta = 25°$

Based on model M60-NS, Figure 5.32 plots the deformed shape of the pipeline and the distribution of the axial normal strain at fault displacements equal to $d =$1, 1.5, 2 and 2.5 m. In this case, additional pipeline extension equal to $d \sin \beta$ occurs, resulting to significant reduction of the compressive bending strains and, thereby, preventing the development of local buckling.
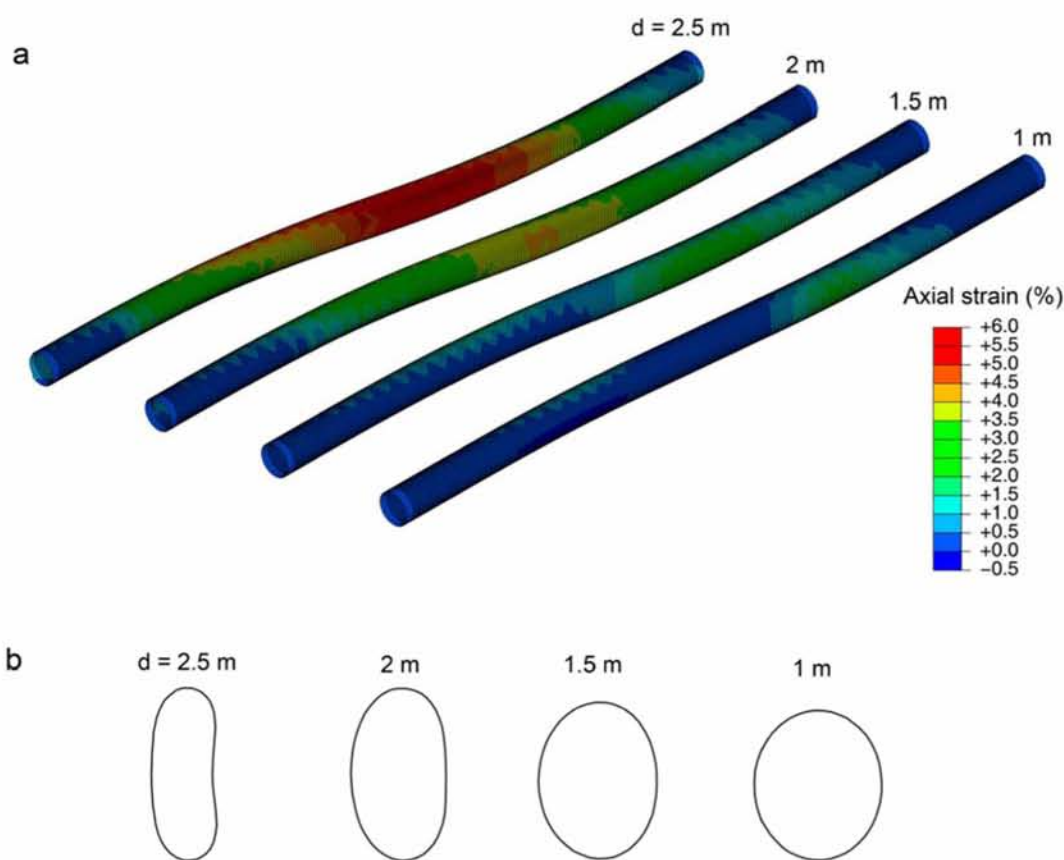

Figure 5.32: Finite element results from model M60-NS and β=25°:(a) Axial normal strain and (b) pipeline section deformation at $d = 1, 1.5, 2$ and 2.5 m.

Figure 5.32b illustrates the ovalization of the pipe cross-section at the fault location ($x = 0$). The critical fault displacement for ovalization given in Table 5.1 is 1.28 m. Hence, the deformed pipeline shapes at $d \geq 1.5$ m, shown in Figure 5.32b, have already exceeded the ovalization performance criterion. Figure 5.33 plots the distribution of displacement in the longitudinal x direction at generators A and B (shown in the figure) of the pipeline in terms of the distance from the fault, for fault displacements d =1, 1.5, 2 and 2.5 m. It is evident that the movement along the generators varies due to bending for x <10 m, but it is practically identical for x >10 m, indicating that, outside the most-strained region near the fault, the pipeline is practically under pure axial tension.
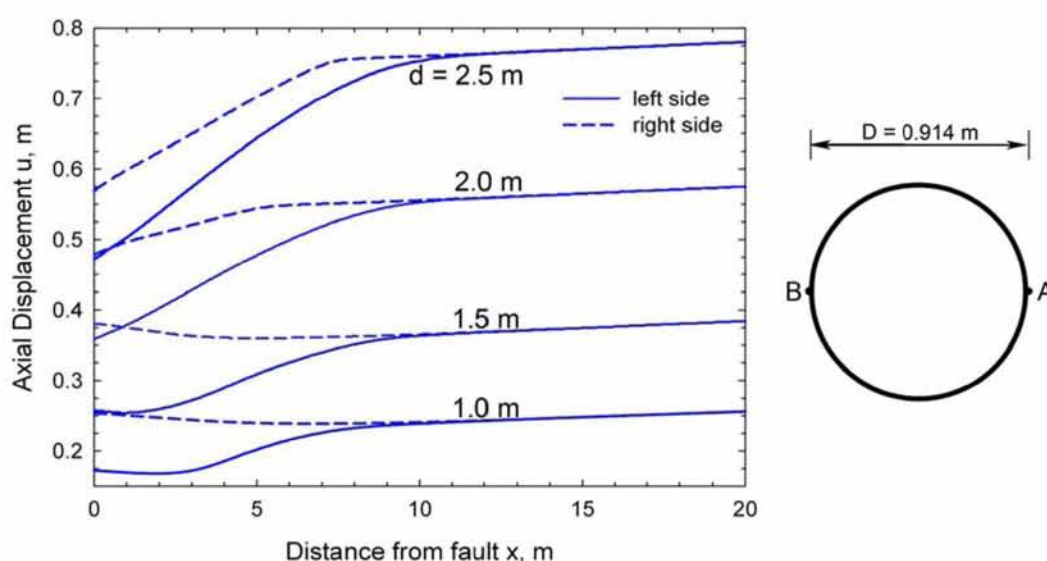

Figure 5.33: Distribution of axial displacement at the outer generators located at the right and left (A and B) sides of the pipeline versus the distance from the fault, using model M60-NS with β=25°.

The axial normal strain at the left and right sides of the pipeline is plotted in Figures. 5.34a and b versus the distance from the fault for d =1, 1.5, 2 and 2.5 m. As shown in the figure, for $d \leq 1.5$m, high values of tensile axial strains develop at one side of the pipeline due to the combined effect of stretching and bending, but for $d \geq 2$ m both sides undergo large tensile strains within a region of about 8 m from the fault location. The effect of bending becomes maximum at a distance of about 3-4 m from the fault and is decreasing with increasing value of d . The 3% and 5% tensile-strain limits are reached at displacements d =1.73 m and 2.17 m, respectively. Finally, Figures 5.35a and b plot the distribution of axial and hoop strains along the perimeter of the pipe at the location of the fault plane (x =0). The tensile axial strain does not vary significantly with θ, but

the hoop strain varies substantially attaining its maximum compressive stresses at the top and the base of the pipeline cross-section, due to cross sectional flattening.

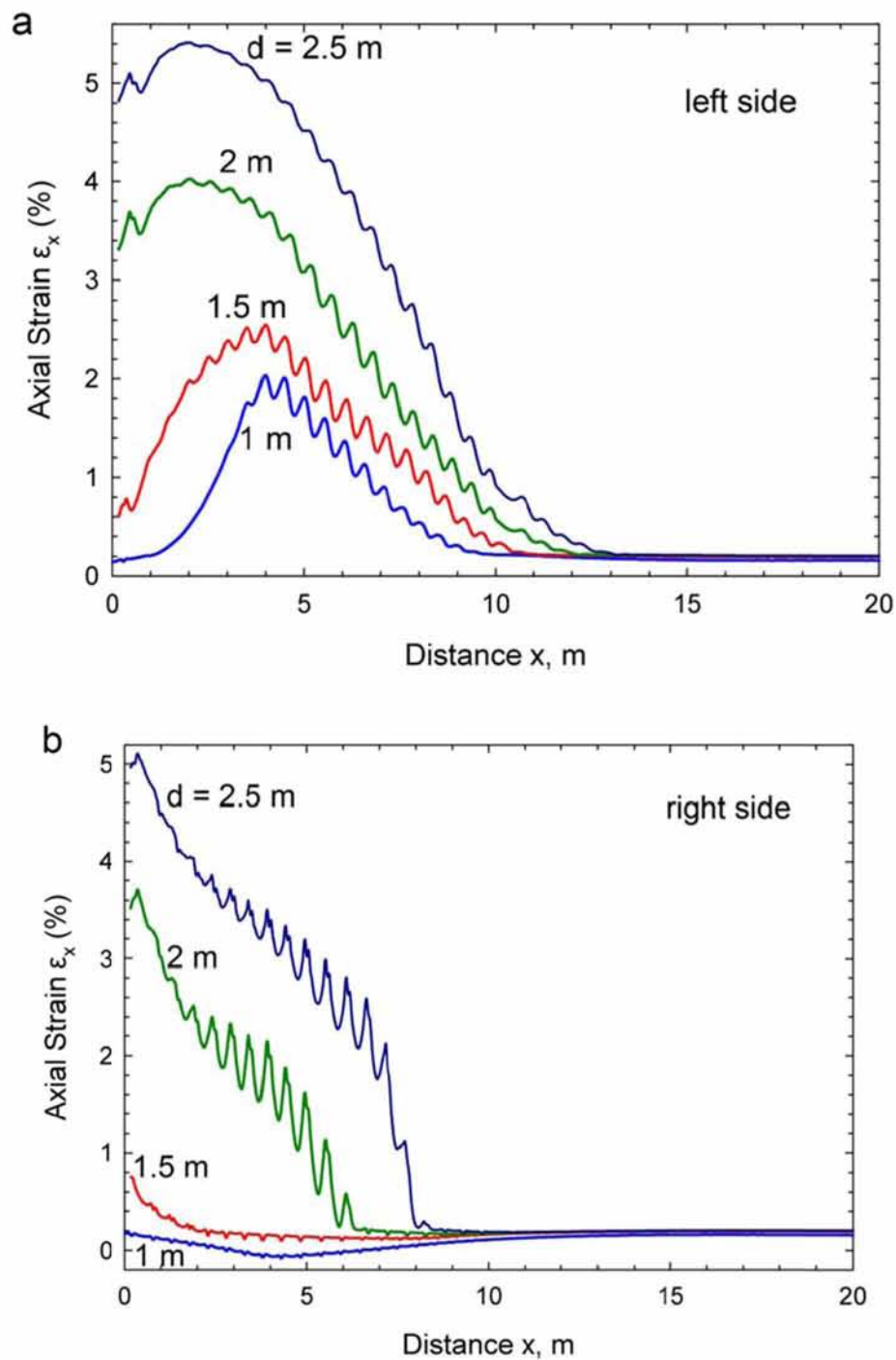**Figure 5.34**: Distribution of axial normal strain versus distance from the fault, using model M60-NS for $\beta=25°$ along generator at the (a) left side and (b) right side of the pipeline.

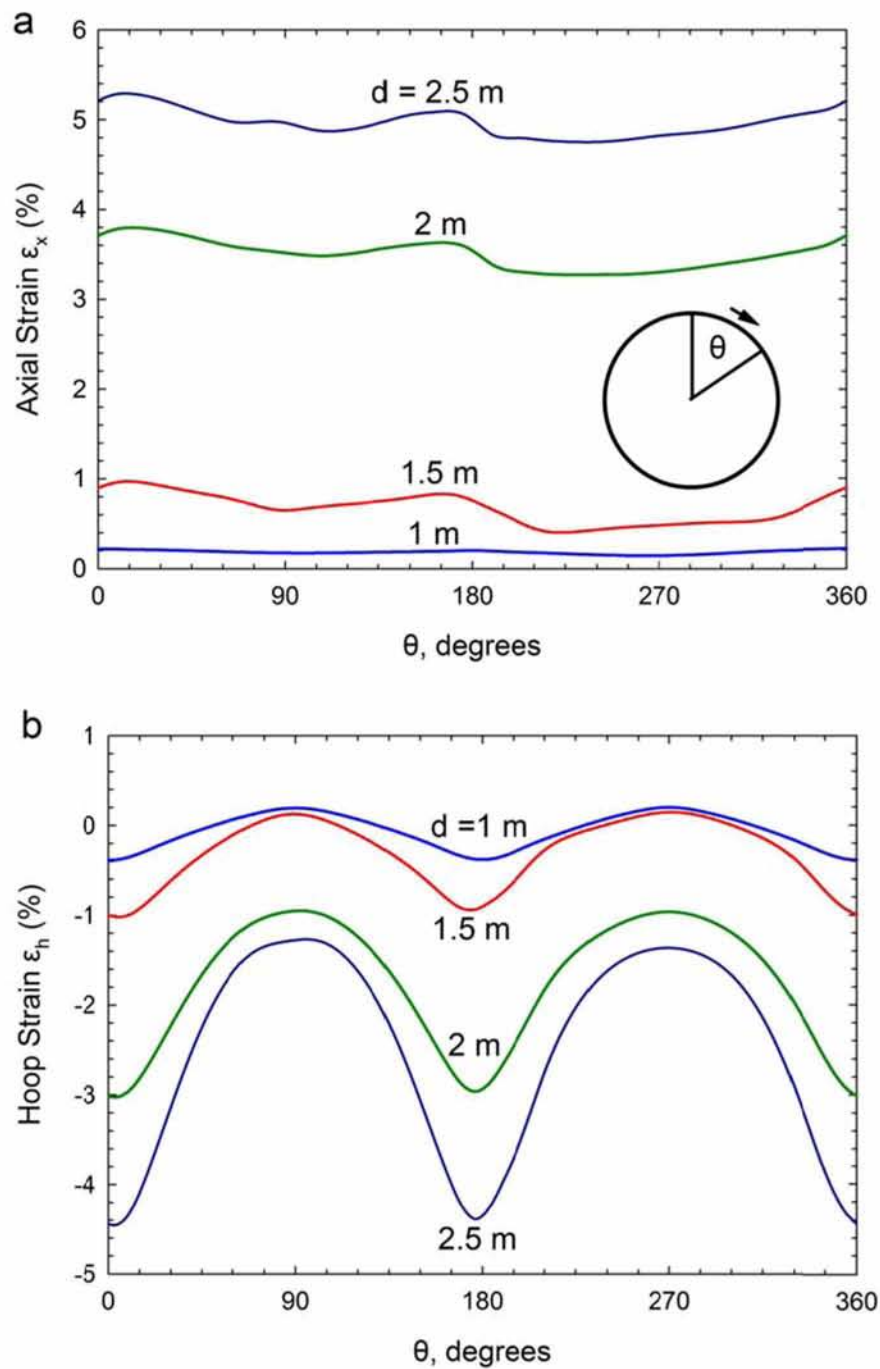**Figure 5.35**: Distribution of (a) axial normal strain and (b) hoop strain around the perimeter of the pipeline section at $x = 0$, using model M60-NS (crossing angle β equal to 25°).

5.3.2 Pipeline performance for fault angle $\beta = 45°$

For a fault angle $\beta = 45°$, the pipeline is subjected to substantial extension during fault movement in the x direction by $d \sin \beta$. In this case, local buckling does not occur, but the other performance criteria are reached at much smaller fault displacement values. Flattening occurs at 1.12m, whereas the 3% and 5% tensile axial strain criteria at 1.08m and 1.40m, respectively.

5.3.3 Effect of crossing angle β

The above numerical results for the X65-steel infinite length pipeline are summarized in graphical form in Figure 5.36, where the fault displacement values corresponding to the performance criteria under consideration, are plotted with respect to the crossing angle β. The results indicate that for non-positive and small positive (less than 5°) values of β, local buckling is the dominant limit state. For greater values of β, cross section flattening becomes the most important limit state. Under increasing angle β, the normalized ultimate displacement for cross-sectional distortion remains the same, whereas 3% and 5% of tensile strain decrease.

These results are also compared with the results in Figure 5.37, derived from a M60 finite element model with fixed pipeline end conditions, for the same soil and geometric properties. Comparison of the two sets of numerical results shows that values of fault displacements corresponding to the adopted performance criteria depend on the boundary conditions. Furthermore the assumption of rigid (fixed) boundary conditions offers conservative estimates of the critical fault displacement. Using the present refined model for infinitely long pipelines, it is found that the cross-section flattening limit becomes dominant for positive values of angle β and local buckling does occur at small positive values of angle β.
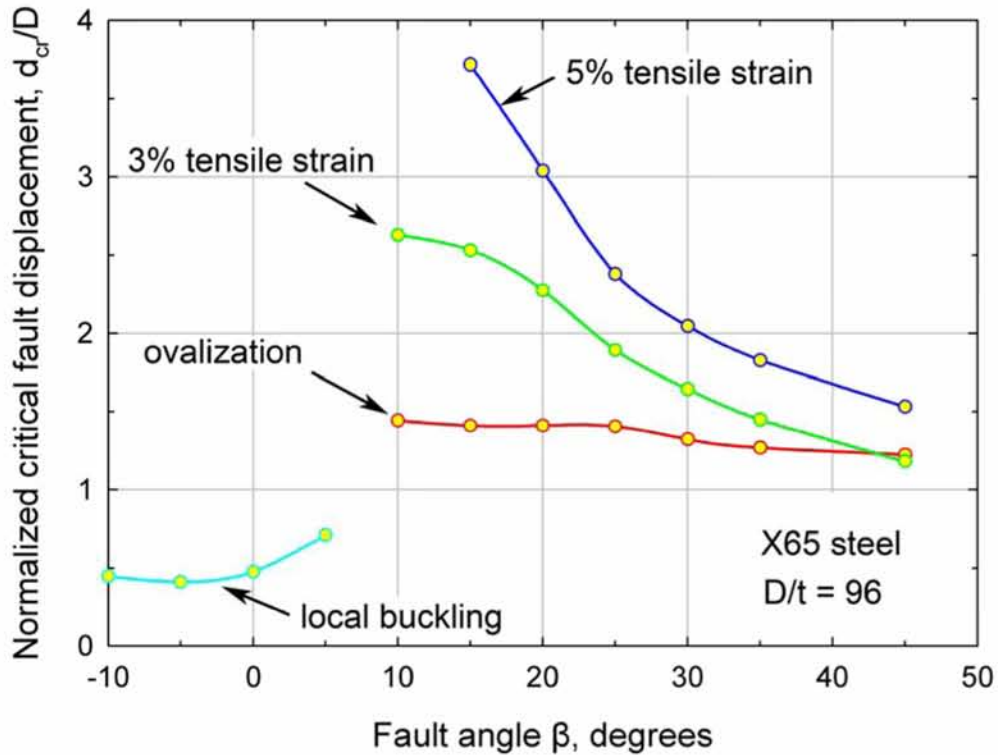
Figure 5.36: Normalized critical fault displacement for various performance limits at different angles of β (M60-NS) for infinite pipeline length.
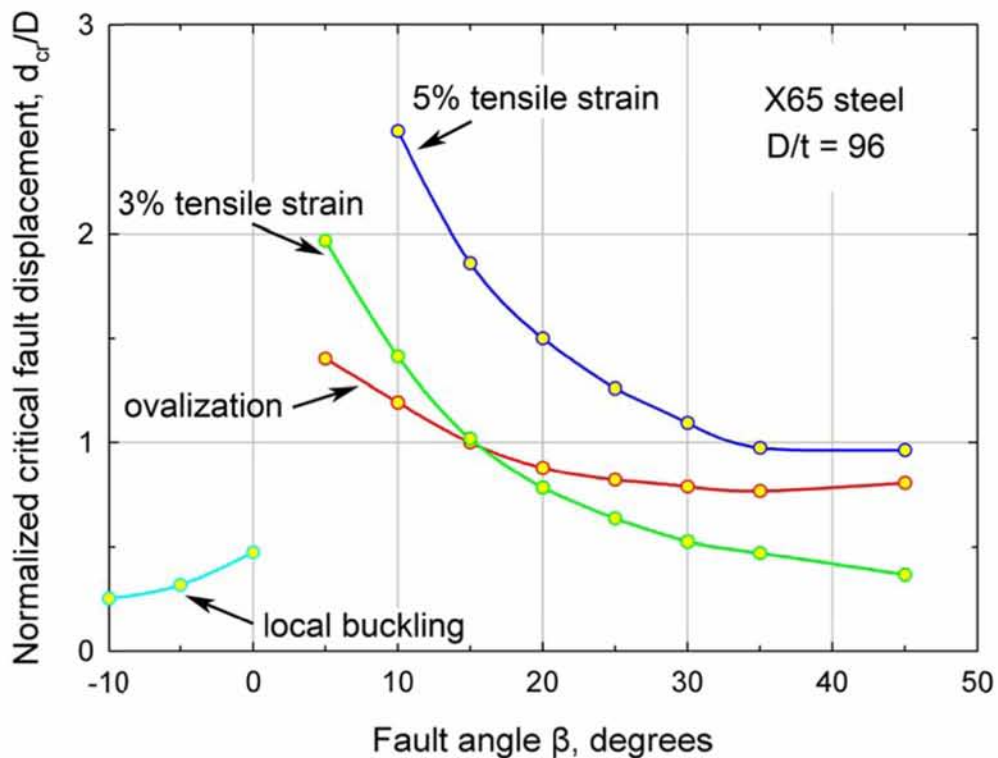

Figure 5.37: Normalized critical fault displacement for various performance limits at different angles of β for fixed ends of the pipeline segment.

5.3.4 Effect of pipeline length

Figure 5.38a plots the distribution of pipeline displacement in the x direction using model M60-NS, for seven different values of the total length L (100, 200, 400, 500, 600, 700 and 2000 m), fault movement equal to $d = 2$m and $\beta = 25^\circ$. The displacement distribution is plotted from the location of the fault ($x = 0$) to the pipeline end ($x = L/2$). The results show that for $L \geq 500$ m, the pipeline response converges to that of an infinitely long pipeline. This is also shown in Table 5.1, which depicts the fault displacement for different performance criteria. It is noted that, for a pipeline length L less than 400 m, the ovalization performance limit is reached at small fault displacements, due to the high tensile stresses imposed by the proximity of the constrained pipeline ends. For values of L greater than 400 m, a critical value of d_{cr} = 1.28 m, is calculated corresponding to flattening limit state. For comparison purposes, the above results have also been obtained using models M60-B (see Section 3.6). The agreement between the two models is excellent.

Moreover, Figure 5.38b plots the distribution of the axial normal strain along generator A of the pipeline, versus the distance x from the fault. As shown in Figure 5.38b, for displacement $d = 2$ m, the largest tensile axial strains are concentrated within a distance of about 10 m from the fault and their maximum values range between 4% and 7%, depending on the value of pipeline length L. Beyond that distance, the axial normal strains remain relatively small (equal to about 0.2% or less, i.e. below the elastic limit of steel material).
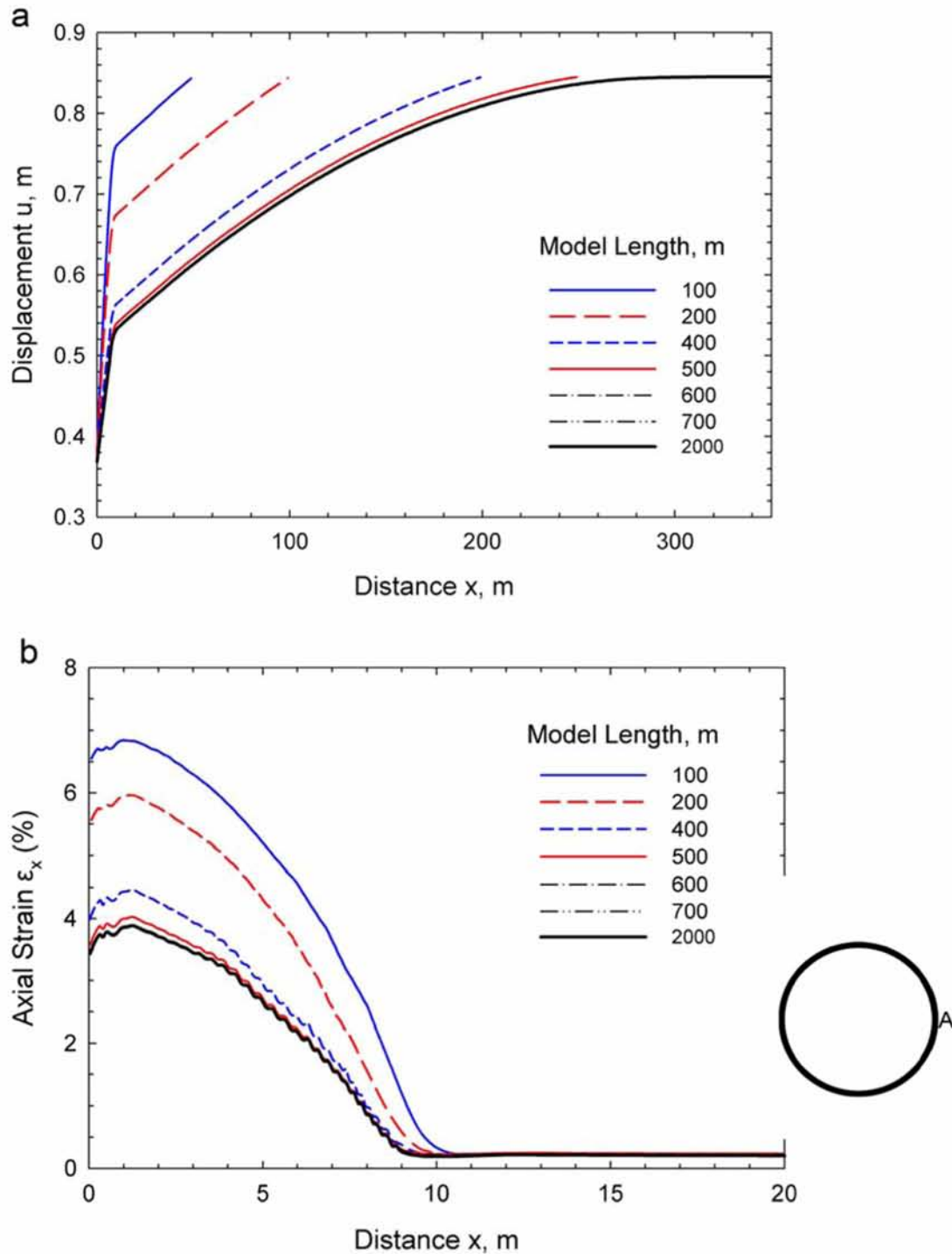
Figure 5.38: Effect of model length using model M60-NS: (a) axial displacement and (b) axial strain along generator A versus distance from the fault. (Fault movement d = 2 m, crossing angle β equal to 25°)

Table 5.1. Effect of total model length for $\beta = 25°$

Model (length L, m)	Critical fault displacement, m			
	Local buckling	Flattening	Strain 3%	Strain 5%
M60-NS, (100)	None	0.85	0.77	1.32
M60-NS, (200)	None	1.07	1.16	1.61
M60-NS, (400)	None	1.28	1.60	2.00
M60-NS, (500)	None	1.28	1.70	2.13
M60-NS, (600)	None	1.28	1.73	2.17
M60-NS, (700)	None	1.28	1.73	2.17
M60-NS, (2000)	None	1.28	1.73	2.17
M60-NS, (∞)	None	1.28	1.73	2.17

Figures 5.39, 5.40 and 5.41 show the effect of pipe wall thickness for various crossing angles when a pipeline model of infinite length is considered, using the equivalent nonlinear springs at its two ends. It is clear from the results that, as the pipe-wall becomes thicker, the dominant criterion switches from cross-section distortion to 3% of tensile axial strain and for D/t equal to 57.6 no intersection of the two limit states is observed regarding positive fault angle β. Also, local buckling is extended to small positive values of crossing angle β (about 5°) for all thicknesses analyzed for an X65 steel embedded to Clay I conditions. For fixed boundary conditions, this was only obvious to pipelines having a D/t equal to 144.

For the very stiff Clay II soil conditions, both limit states of 3% of axial strain and ovalization occur at the same fault displacement for positive fault angles, as shown in Figures 5.42 and 5.43. Local buckling extends to greater positive values of fault angle reaching the value of 15° for both cases.

Higher strength X80 steel pipelines exhibit local buckling up to 5° of fault angle and cross-sectional distortion is the limit state for fault angles greater than 5° for a pipeline with D/t=96 (Figure 5.44). For D/t=72, the limit states of cross-sectional distortion and 3% tensile strain occur at the same fault displacement (Figure 5.45) indicating similar behavior with an X65 steel.

Finally, pressurized pipelines of infinite length do not exhibit cross-sectional distortion and the limit state for positive fault angles is tensile failure. Local buckling occurs even for 10° of fault angle for an X65 steel (see Figures 5.46 and 5.47) and up to 5° of fault angle for an X80 (see Figures 5.48 and 5.49).

Figure 5.39: Normalized critical fault displacement for various performance limits at different angles of *β* for a the pipeline of infinite length (X65, D/t=144, Clay I, *p*=0)

Figure 5.40: Normalized critical fault displacement for various performance limits at different angles of *β* for a the pipeline of infinite length (X65, D/t=72, Clay I, *p*=0)

Figure 5.41: Normalized critical fault displacement for various performance limits at different angles of β for a the pipeline of infinite length (X65, D/t=57.6, Clay I, p=0)

Figure 5.42: Normalized critical fault displacement for various performance limits at different angles of β for a the pipeline of infinite length (X65, D/t=96, Clay II, p=0)
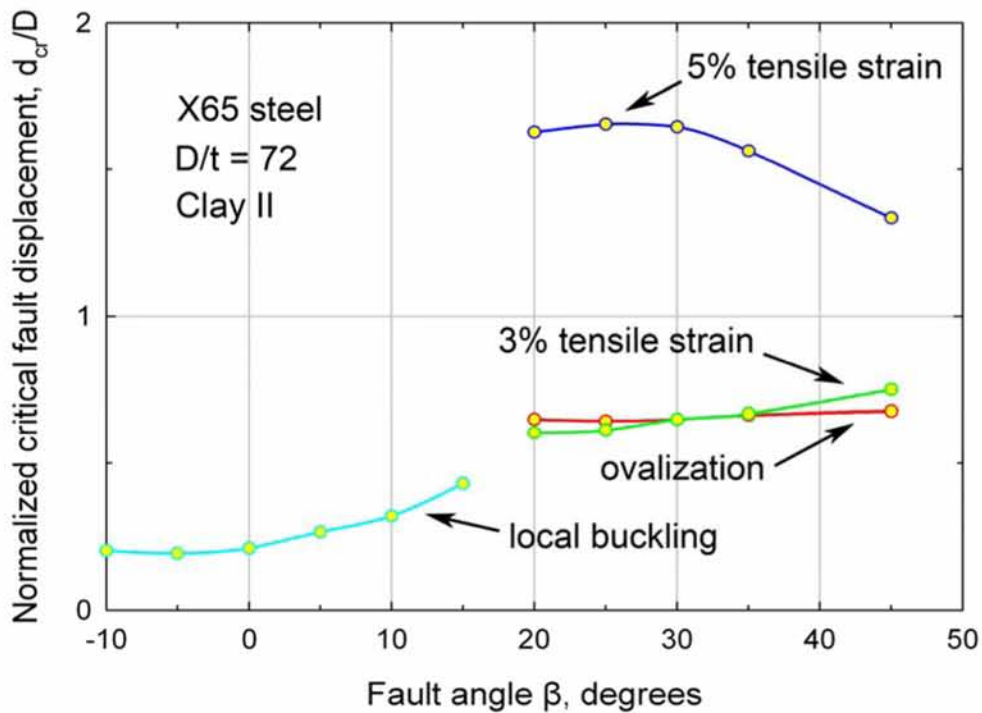
Figure 5.43: Normalized critical fault displacement for various performance limits at different angles of β for a the pipeline of infinite length (X65, D/t=72, Clay II, p=0)
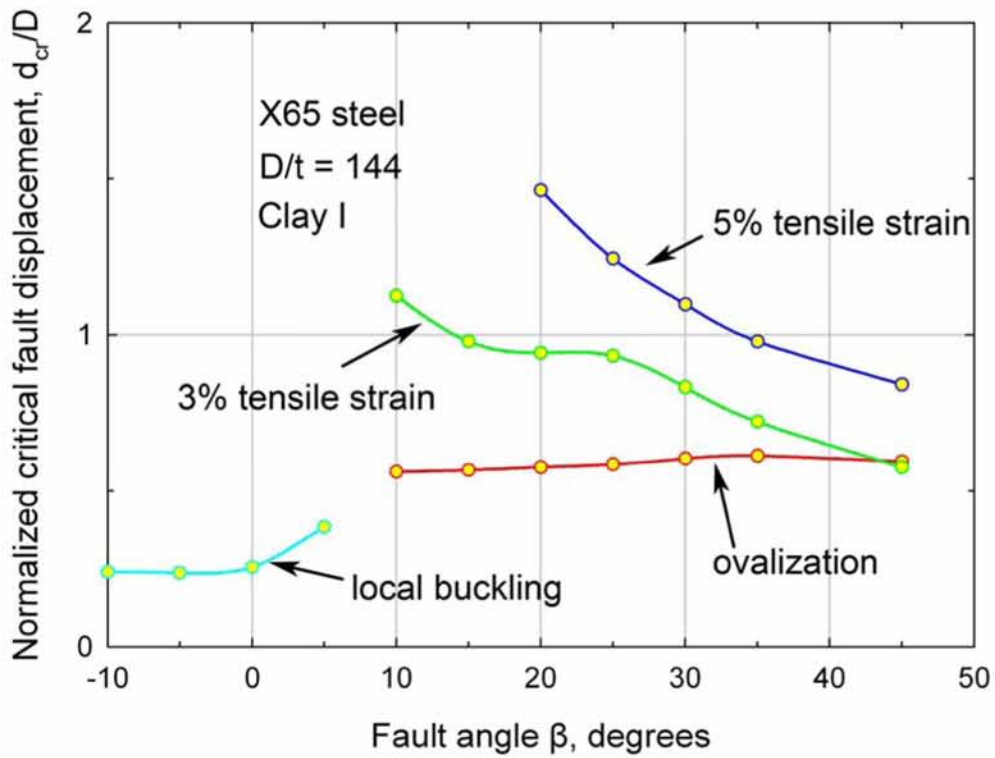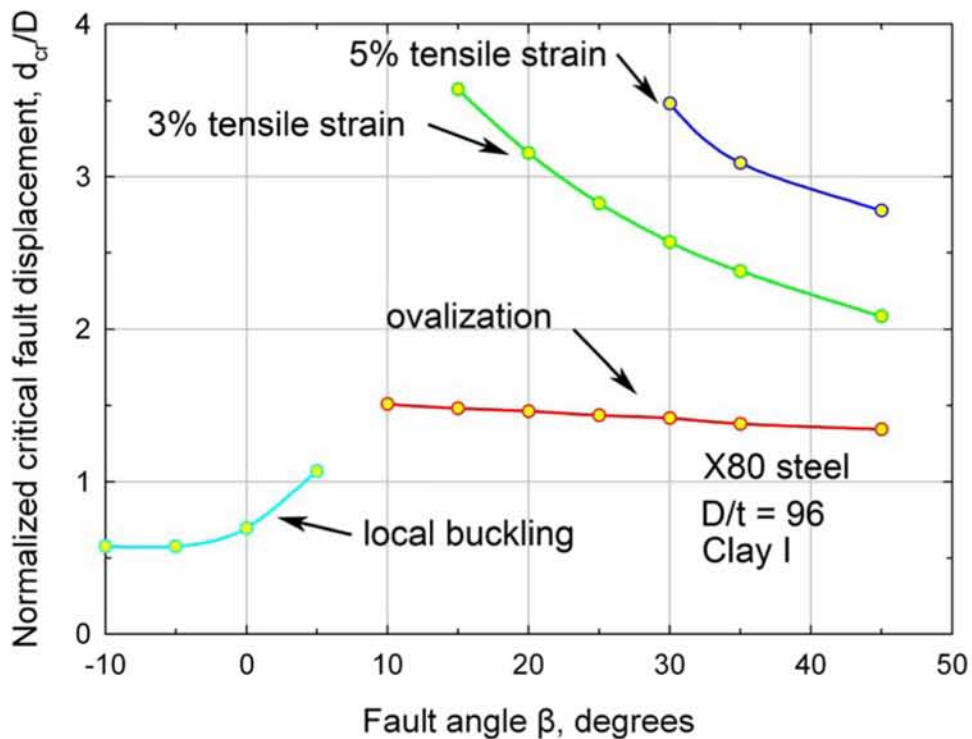

Figure 5.44: Normalized critical fault displacement for various performance limits at different angles of β for a the pipeline of infinite length (X80, D/t=96, Clay I, p=0)
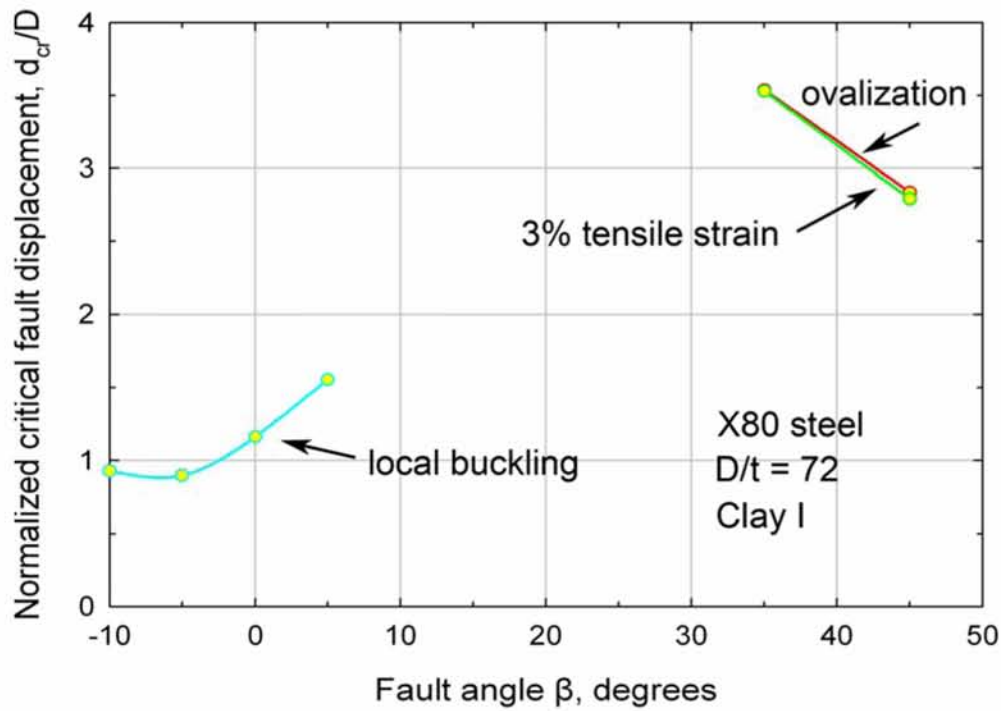
Figure 5.45: Normalized critical fault displacement for various performance limits at different angles of β for a the pipeline of infinite length (X80, D/t=72, Clay I, p=0)
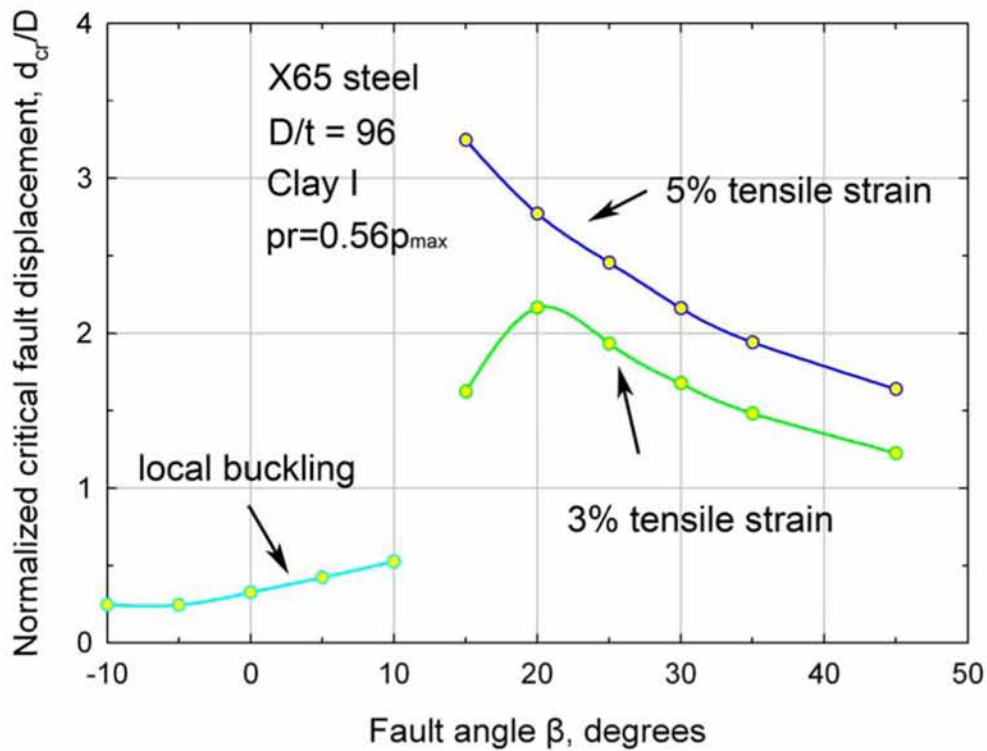
Figure 5.46: Normalized critical fault displacement for various performance limits at different angles of β for a the pipeline of infinite length (X65, D/t=96, Clay I, p=0.56p$_{max}$)
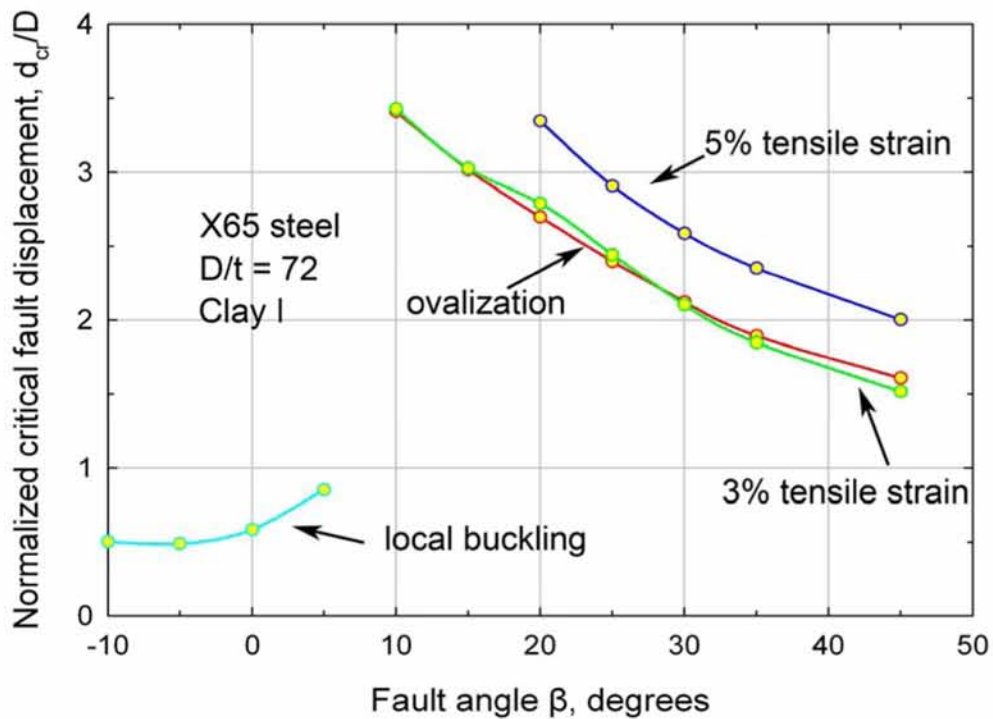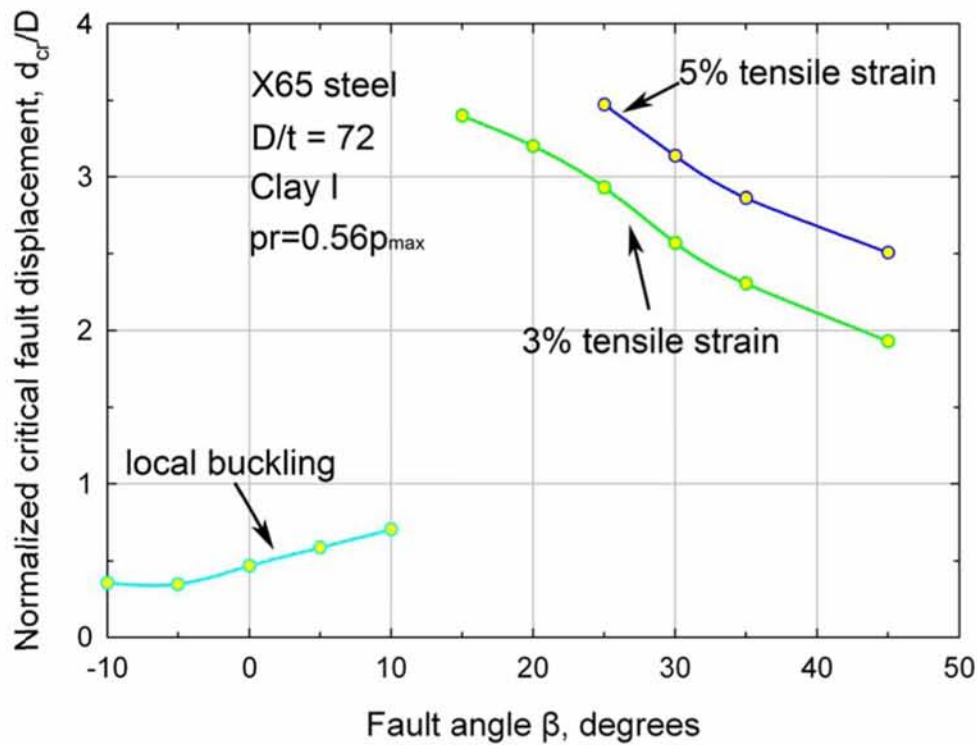
Figure 5.47: Normalized critical fault displacement for various performance limits at different angles of β for a the pipeline of infinite length (X65, D/t=72, Clay I, p=0.56p$_{max}$)
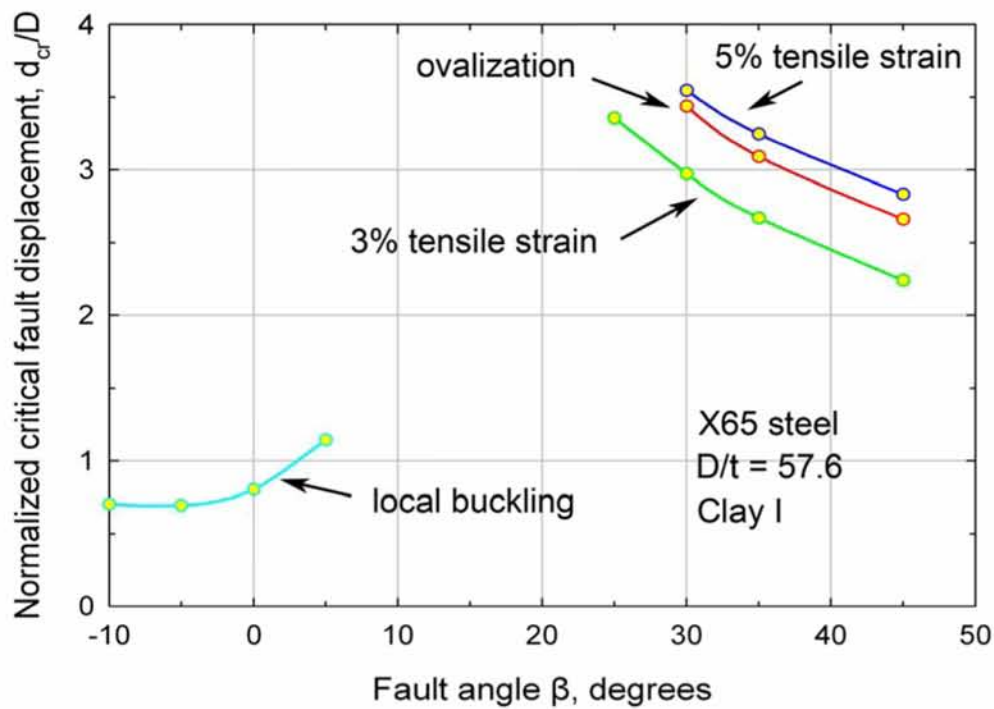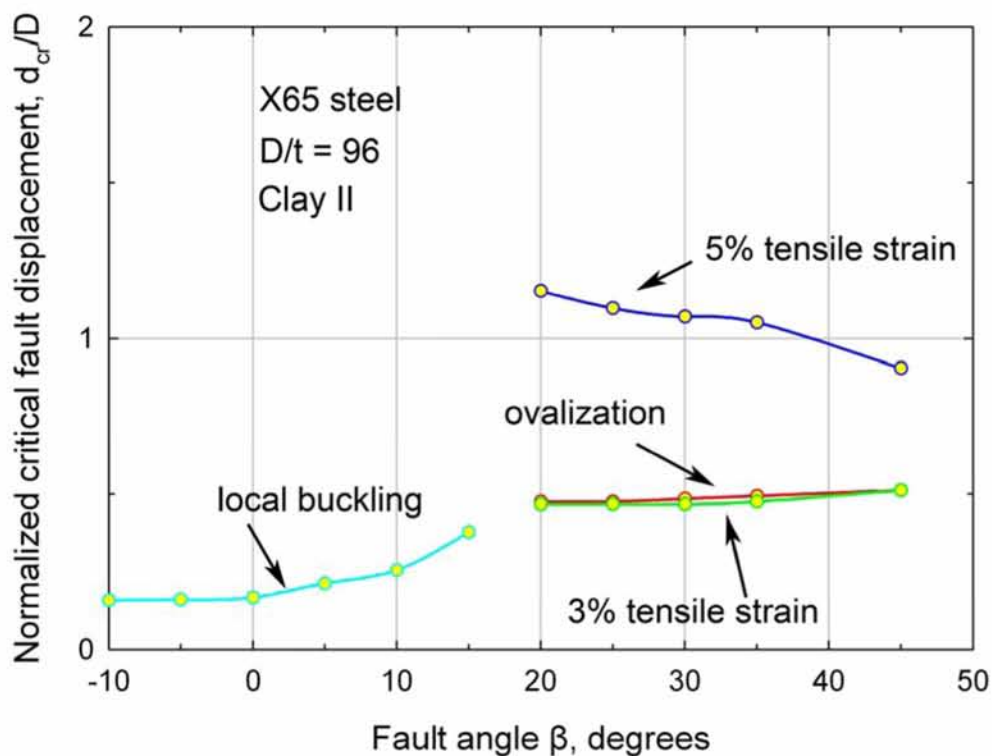

Figure 5.48: Normalized critical fault displacement for various performance limits at different angles of β for a the pipeline of infinite length (X80, D/t=72, Clay I, p=0.46p$_{max}$)
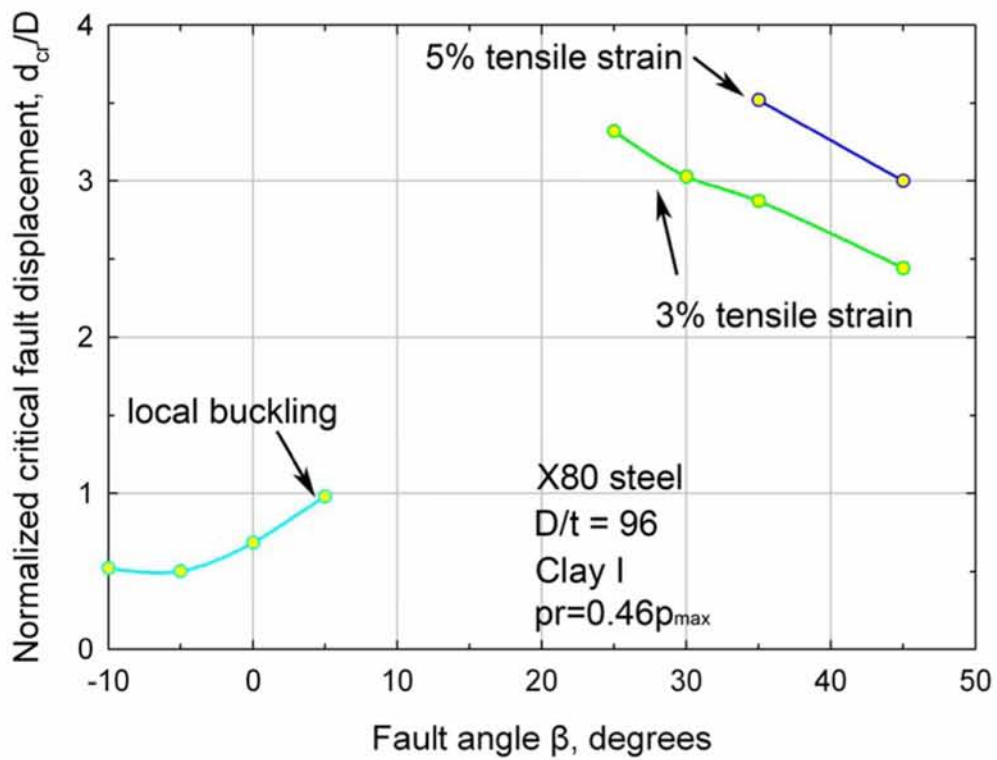
Figure 5.49: Normalized critical fault displacement for various performance limits at different angles of β for a the pipeline of infinite length (X80, D/t=96, Clay I, $p=0.46p_{max}$)
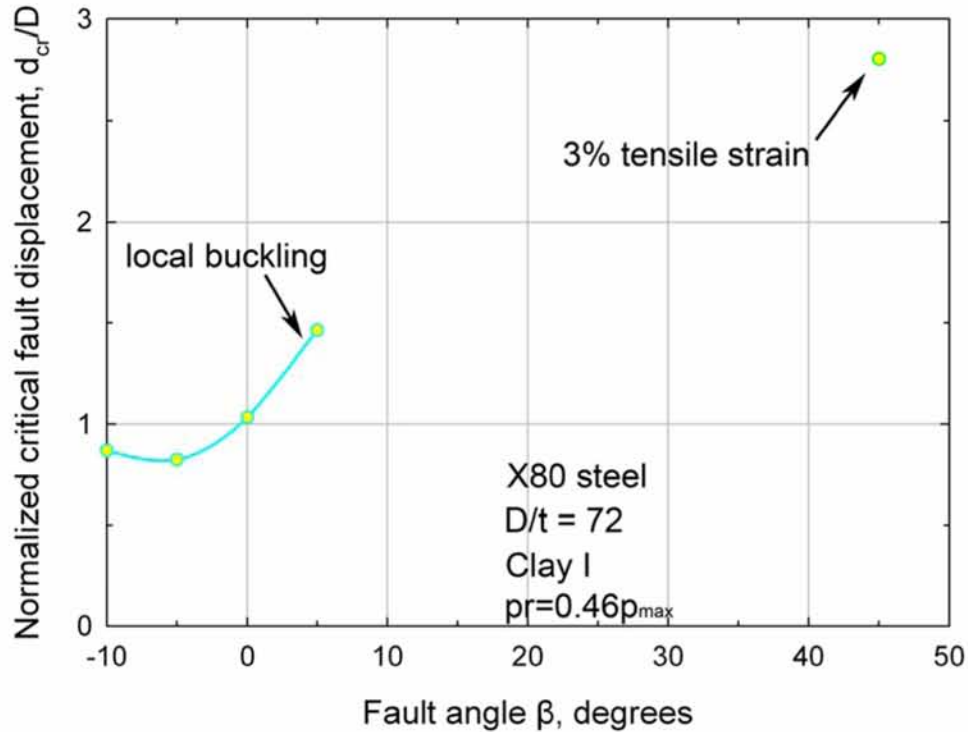
6   Simplified model for local buckling of pipeline wall

6.1   Introduction

The results presented in the previous Chapters of the dissertation demonstrated that, for non-positive or small positive values of the crossing angle β, local buckling of pipeline wall is the governing limit state of the pipeline. Furthermore, it has been shown that the occurrence of local buckling depends on several parameters related to the pipe steel grade, the soil conditions, the value of the crossing angle and the end effects. In the present Chapter a simplified formulation is presented for describing pipeline deformation under strike-slip fault action, in order to estimate under which conditions the compressive strains that develop in the pipeline wall can cause local buckling. The model accounts for the boundary effects of the pipeline segment and illustrates the formation of the local buckling in a simple and efficient way. At the end of this chapter a comparison of the simplified model prediction with finite element results is performed.

6.2   Model description

Upon application of fault displacement the pipeline is assumed to deform in an S-shaped "shearing type" configuration, within a segment of length L_1, as shown in Figure 6.1. The pipeline outside this segment of length L_1, is assumed to be under direct tension only, without bending deformation. It is also assumed that the pipeline shape is smooth, of circular cross-section and free of discontinuities due to local cross-sectional distortions. A shape function for the transverse displacement $u(x)$ of the pipeline is considered in the form:

$$u(x) = \frac{d}{2}\cos\beta\left(1 - \cos\frac{\pi x}{L_1}\right) \tag{6.1}$$

where x=0 and x=L_1 are the two ends of the S-shaped pipe segment. In addition, the axial displacement $v(x)$ of the pipeline within this segment due to longitudinal stretching is assumed to be linearly distributed along the pipeline:

$$v(x) = \frac{d \sin \beta}{L_1} x \qquad (6.2)$$
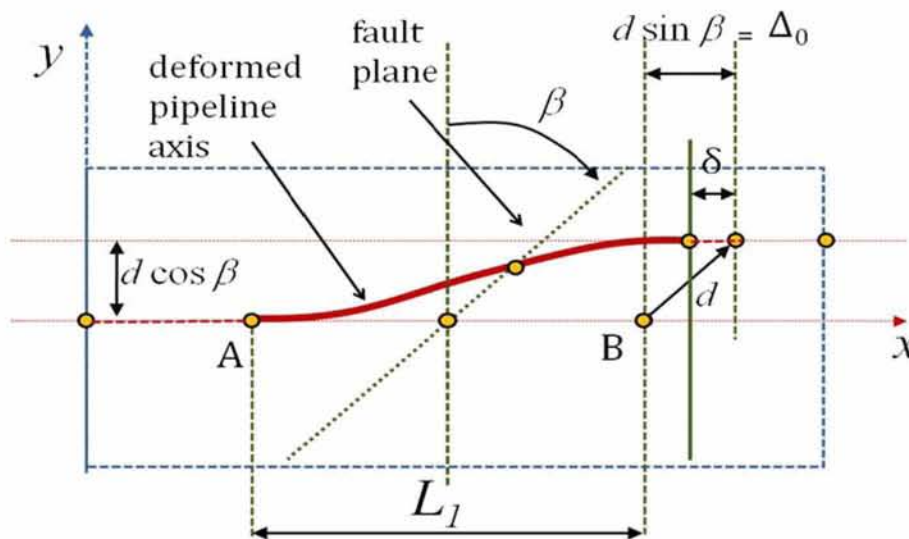
Figure 6.1: Schematic representation of fault-induced deformation of pipeline axis, for the development of a simplified formulation for local buckling.

In the above equations (6.1) and (6.2), d is the fault-imposed displacement. The length L_1 of the S-shaped deformed pipeline segment depends mainly on the soil stiffness and the value of D/t ratio, and will be discussed later.

From equation (6.1), the maximum bending curvature, k, due to the imposed deformation d, can be readily computed as follows

$$k = -\left(\frac{d^2 u}{dx^2}\right)_{\max} = \frac{d\cos\beta}{2}\left(\frac{\pi}{L_1}\right)^2 \cos\frac{\pi x}{L_1}$$ (6.3)

Neglecting cross-sectional distortion, i.e. assuming a circular pipeline cross-section, the corresponding bending strain ε_b is

$$\varepsilon_b = \frac{kD}{2} = \frac{\pi^2}{4}\left(\frac{d\cos\beta}{L_1}\right)\left(\frac{D}{L_1}\right)$$ (6.4)

Furthermore, axial strains due to the increase of pipeline length between cross-sections at $x=0$ and L_1 due to pipeline stretching should be considered. This increase of length consists of two parts; the first part is due to the bending shape and the second part refers to the oblique direction of the fault with respect to the pipeline. Assuming for a moment that the pipe segment under consideration is fixed at the two ends of the segment ($x=0$ and $x=L_1$), the increase of pipeline length is

$$\Delta_0 = \int_0^{L_1} \sqrt{1 + u'^2}\,dx - L_1 + d\sin\beta$$ (6.5)

The first two terms refer to the increase of the length due to bending, whereas the third term is due to oblique direction of the fault and is derived from differentiation of equation (6.2)

Nevertheless, because of pipeline continuity at the two ends, the real conditions at these locations may not be fixed and the corresponding flexibility should be accounted for. More specifically, due to this flexibility, the total elongation Δ of the pipeline is smaller than Δ_0, so that

$$\Delta = \Delta_0 - \delta$$ (6.6)

where δ is a decrease of the total elongation of the pipeline segment due to the flexibility of the two ends. Consideration of compatibility at the two ends results in the following equilibrium expression that relates D_0 and δ :

$$k_1(D_0 - \delta) = \overline{K}_t \frac{\delta}{2} \tag{6.7}$$

where k_1 is the axial stiffness of the S-shaped pipeline segment and $\overline{K}_t$ is the stiffness of the straight part outside the segment of length L_1, which is subjected to axial tension as described in Sections 3.3 and 3.4. Considering a secant modulus $\overline{K}_t$ for the pipe-soil interaction under axial loading, one may write the following,

$$\frac{EA}{L_1}(D_0 - \delta) = \overline{K}_t \frac{\delta}{2} \tag{6.8}$$

or equivalently

$$D_0 = (1 + \frac{\overline{K}_t L_1}{2E_s A})\delta \tag{6.9}$$

The value of $\overline{K}_t$ can be obtained from the analytical models described in sections 3.3 and 3.4.

Introducing the dimensionless parameter $\omega = \dfrac{\overline{K}_t L_1}{2E_s A}$, the following expression is obtained from equation (6.9)

$$D_0 = (1 + \omega)\delta \tag{6.10}$$

The corresponding axial strain (also referred to as "membrane" or "stretching" strain) ε_m can be computed from equations (6.5) and (6.6) as follows:

$$\varepsilon_m = \frac{D}{L_1} = \frac{1}{L_1}\left\{\int_0^{L_1} \sqrt{1 + u'^2}\,dx\right\} - 1 + \frac{d\sin\beta}{L_1} - \frac{\delta}{L_1} \qquad (6.11)$$

which is assumed to be uniformly distributed along the pipeline segment. Using the following series expansion,

$$\sqrt{1 + u'^2} = 1 + \frac{1}{2}u'^2 + \cdots \qquad (6.12)$$

and keeping only the first two terms of the series, the axial membrane strain from equation (6.11) becomes

$$\varepsilon_m = \frac{\Delta}{L_1} = \frac{1}{2L_1}\int_0^{L_1} u'^2\,dx + \frac{d\sin\beta}{L_1} - \frac{\delta}{L_1} \qquad (6.13)$$

Using equations (6.5), (6.10), equation (6.13) becomes

$$\varepsilon_m = \left(\frac{d^2\pi^2\cos^2\beta}{16L_1^2} + \frac{d\sin\beta}{L_1}\right)\left(\frac{\omega}{1+\omega}\right) \qquad (6.14)$$

To compute the axial compressive strain ε_C, the axial (tensile) membrane strain should be subtracted from the compressive bending strain. Combining equations (6.4) and (6.14), one obtains the axial compressive strain at the critical location

$$\varepsilon_C = \varepsilon_b - \varepsilon_m \qquad (6.15)$$

or

$$\varepsilon_C = \underbrace{\frac{\pi^2}{4}\left(\frac{d\cos\beta}{L_1}\right)\left(\frac{D}{L_1}\right)}_{\varepsilon_b} - \left(\underbrace{\frac{d^2\pi^2\cos^2\beta}{16L_1^2}}_{\varepsilon_{m2}} + \underbrace{\frac{d\sin\beta}{L_1}}_{\varepsilon_{m1}}\right)\left(\frac{\omega}{1+\omega}\right) \qquad (6.16)$$

173

At the first stages of deformation, i.e. for small values of d, the membrane strain ε_{m1} due to the oblique orientation of the fault and the bending strain ε_b, both linear in terms of fault displacement d, govern the response. On the other hand, the membrane strain ε_{m2}, which is quadratic on d, becomes more important at large values of d. The value of fault displacement at which the compressive strain ε_C reaches a maximum value is readily obtained by differentiating equation (6.16) with respect to the fault displacement d:

$$\frac{d\varepsilon_C}{dd} = \frac{\pi^2 D}{4L_1^2}\cos\beta - \left[d\,\frac{\pi^2\cos^2\beta}{8L_1^2} + \frac{\sin\beta}{L_1}\left(\frac{\omega}{1+\omega} \right) \right] \tag{6.17}$$

Setting the above derivative equal to zero, one obtains

$$d\,\mathrm{I}\quad d_0 = \frac{2}{\cos\beta}\left[D + \frac{D}{\omega} - \frac{4L_1\tan\beta}{\pi^2} \right] \tag{6.18}$$

The corresponding maximum value of compressive strain ε_C is computed from equation (6.16)

$$\varepsilon_{C,\max} = \frac{\left[\frac{D}{L_1}\pi^2(1+\omega) - 4\omega\tan\beta \right]^2}{4\pi^2\omega(1+\omega)} \tag{6.19}$$

The above expressions are valid for positive values of d_0, implying that

$$\tan\beta < \frac{(\omega+1)}{\omega}\frac{D}{L_1}\frac{\pi^2}{4} \tag{6.20}$$

Beyond the stage defined by equation (6.19), the value of compressive strain ε_C decreases with increasing fault displacement d.

If the maximum axial compressive strain $\varepsilon_{C,\max}$ in equation (6.19) is lower than the critical buckling strain ε_{cr} of the pipeline wall, local buckling of the pipeline wall may not occur. This is expressed by the following inequality,

$$\varepsilon_{C,\max} \leq \varepsilon_{cr} \tag{6.21}$$

In equation (6.21), the critical buckling strain ε_{cr} can be written in the following simplified form [46]:

$$\varepsilon_{cr} = \alpha\left(\frac{t}{D}\right) \tag{6.22}$$

where α is a constant that depends on the pipeline material grade, as well as the amplitude and shape of initial imperfections. Inserting equations (6.19) and (6.22) into equation (6.21), one obtains the following "no buckling" condition in terms of the diameter-to-thickness ratio D/t, the dimensionless parameter α, the diameter-over-length ratio D/L_1 of the S-shaped deformed pipeline and the dimensionless parameter ω:

$$\frac{D}{t} \leq \left(\frac{D}{t}\right)_{\lim} = \frac{\alpha 4\pi^2 \omega(1+\omega)}{\overline{K}\frac{D}{L_1}\pi^2(1+\omega) - 4\omega\tan\beta\left(\frac{\omega}{v}\right)^2} \tag{6.23}$$

Using the above expression shows that, in the case of strike-slip faults in order to avoid local buckling of the pipeline, the diameter-to-thickness ratio D/t should not exceed the limit value $(D/t)_{\lim}$. Equation (6.23) provides an approximation of this limit value and can be employed to derive some useful conclusions; as the value of angle β increases, the limit value $(D/t)_{\lim}$ becomes larger. The decrease of $\overline{K}_t$ results in a smaller $(D/t)_{\lim}$ value because of a decrease of the value of factor ω. Finally, a decrease

of soil stiffness results in an increase on the S-shaped length (decrease of the D/L_1) resulting in greater values of $(D/t)_{\text{lim}}$.

For a steel pipeline having a D/t equal to 96, a diameter equal to 0.9144m and an interface shear strength τ_{max} equal to 15kPa, Figure 6.2 plots the relative displacement $u_0 = \delta/2$ at each end of pipeline versus the fault displacement d for different values of the angle β obtained analytically and numerically. To obtain those plots, the axial strain of equation (6.11) is equated with the value of F_0/EA given in equation (3.23) and the resulting equation is solved in terms of u_0 to provide the analytical prediction. The equation is nonlinear and its solution is performed using mathematical tools. The numerical predictions for the value of relative displacement u_0 are obtained through the finite element model described in Chapter 3. The comparison is good for angle β equal to zero and diverges as the value of angle β becomes larger (Figure 6.2).
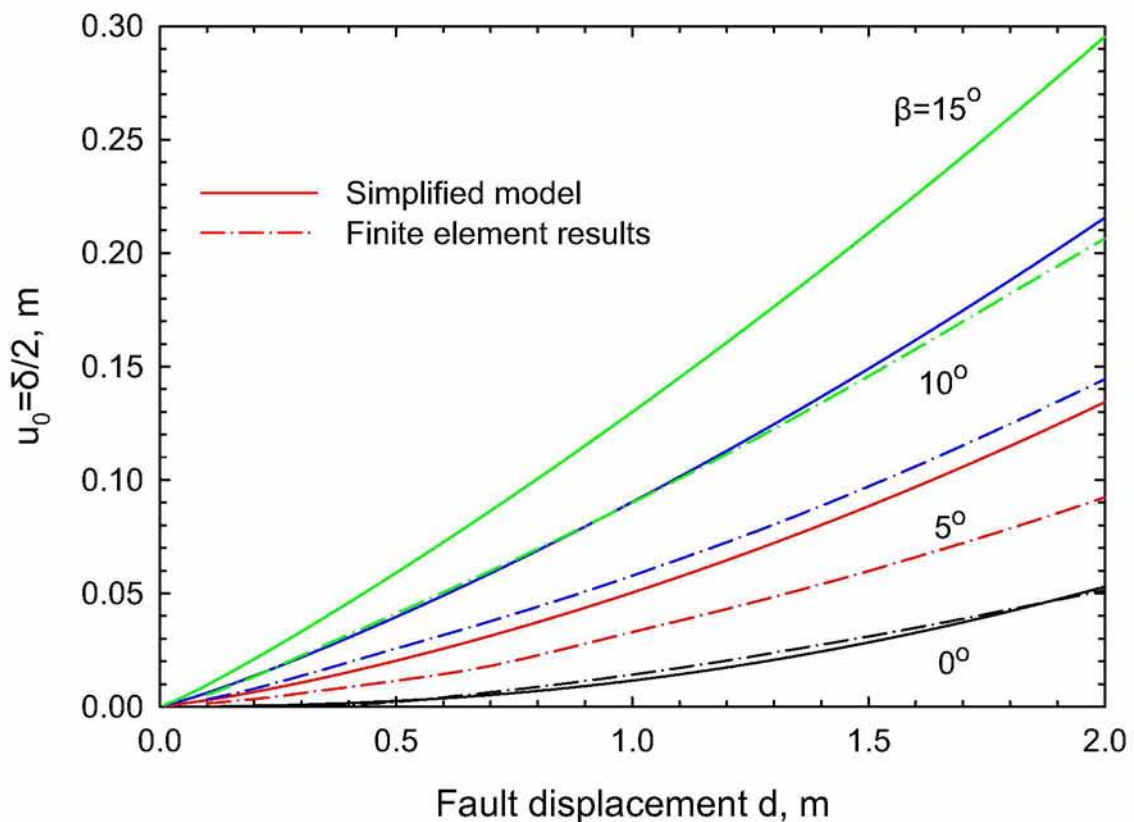
Figure 6.2: Relative displacement $u_0 = \delta/2$ at each end of the pipeline versus fault movement for different values of the angle β
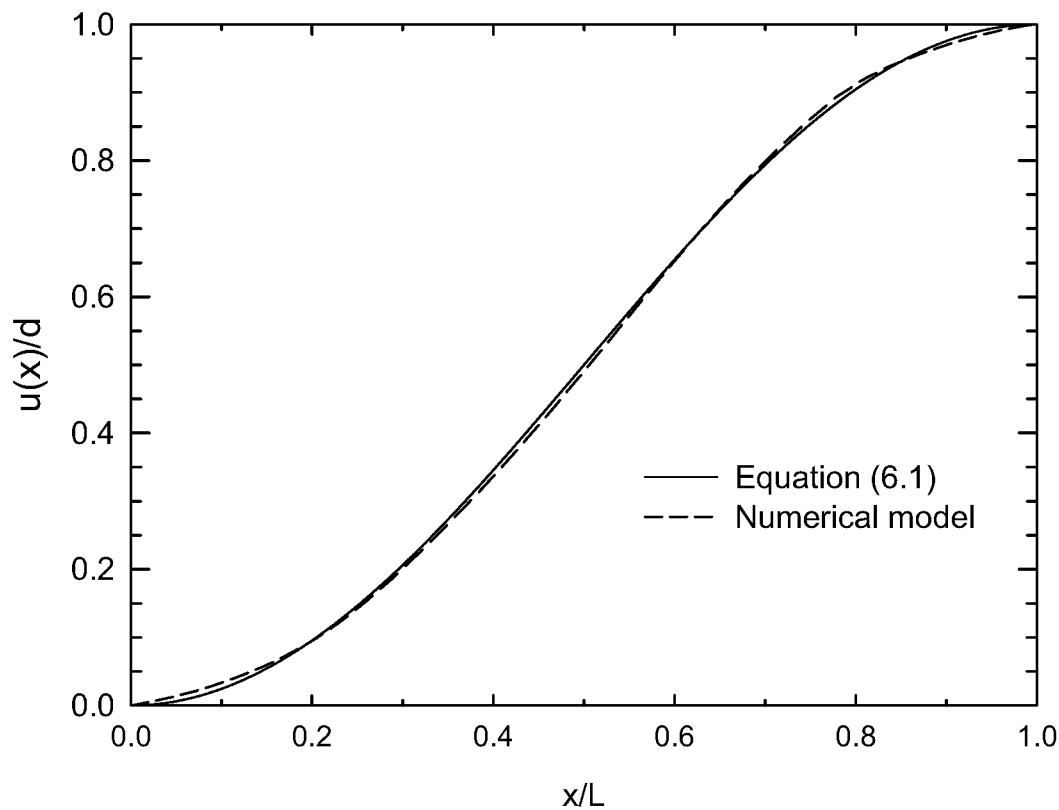
Figure 6.3: Comparison of the pipeline assumed shape at the onset of buckling from equation (6.1) and the finite element analysis (X65 pipe, D/t = 96, Clay I, d = 0.4m, β =0°).

The value L_1/D is an important parameter for the simplified model. It has to be derived from detailed numerical analysis in order to be used as an input parameter in the simplified formula. Based on the results from numerical analyses, Figures 6.4-6.11 present the distribution of lateral and axial displacement of a 36 inch pipeline at certain values of fault movement. The pipeline is of X65 steel with thickness equal to 3/8 inch. Results for two values of the fault angle β equal to 0° and 15° are presented. From these graphs information about the length L_1 may be obtained. As evident from the results, the value of L_1/D depends on the fault displacement d and the crossing angle β.

Figure 6.4: Lateral displacement u_y of pipeline versus pipeline length along generators A, B (angle $\beta=0°$, fault displacement $d = 0.4$ m)

Figure 6.5: Lateral displacement u_y of pipeline versus pipeline length along generators A, B (angle $\beta=0°$, fault displacement $d = 1$ m)

Figure 6.6: Lateral displacement u_y of pipeline versus pipeline length along generators A, B (angle $\beta=0°$, fault displacement $d = 2$ m)
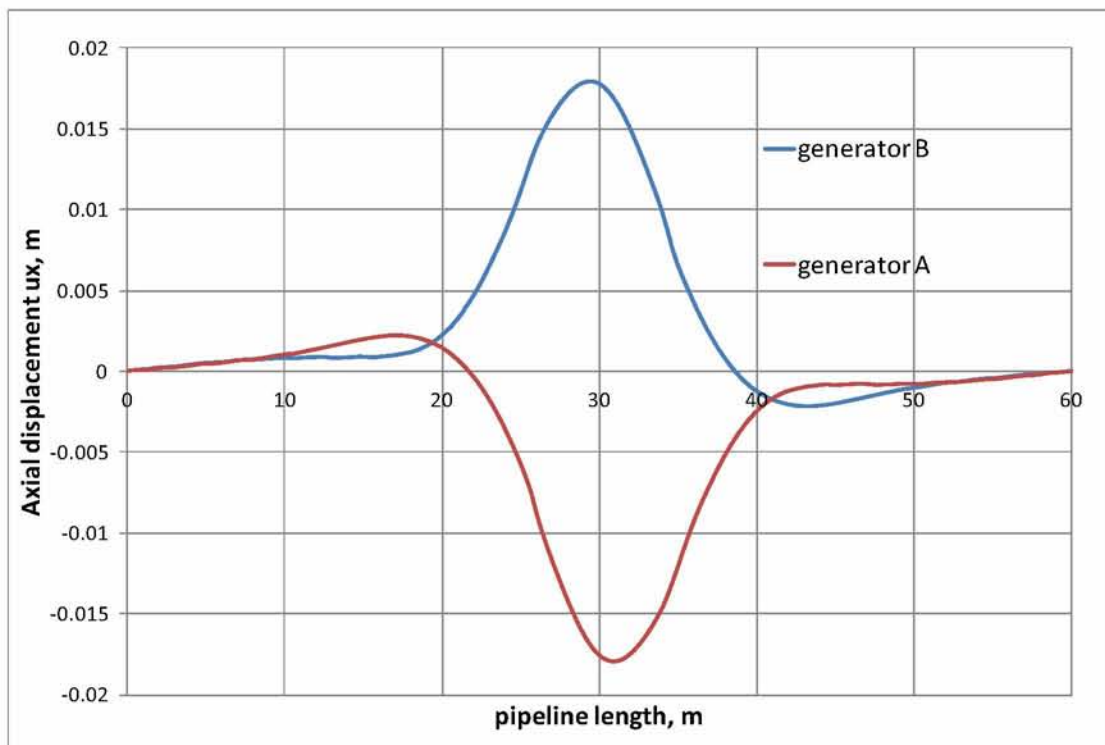
Figure 6.7: Axial displacement u_x of pipeline versus pipeline length along generators A, B (angle $\beta=0°$, fault displacement $d = 0.4$m)
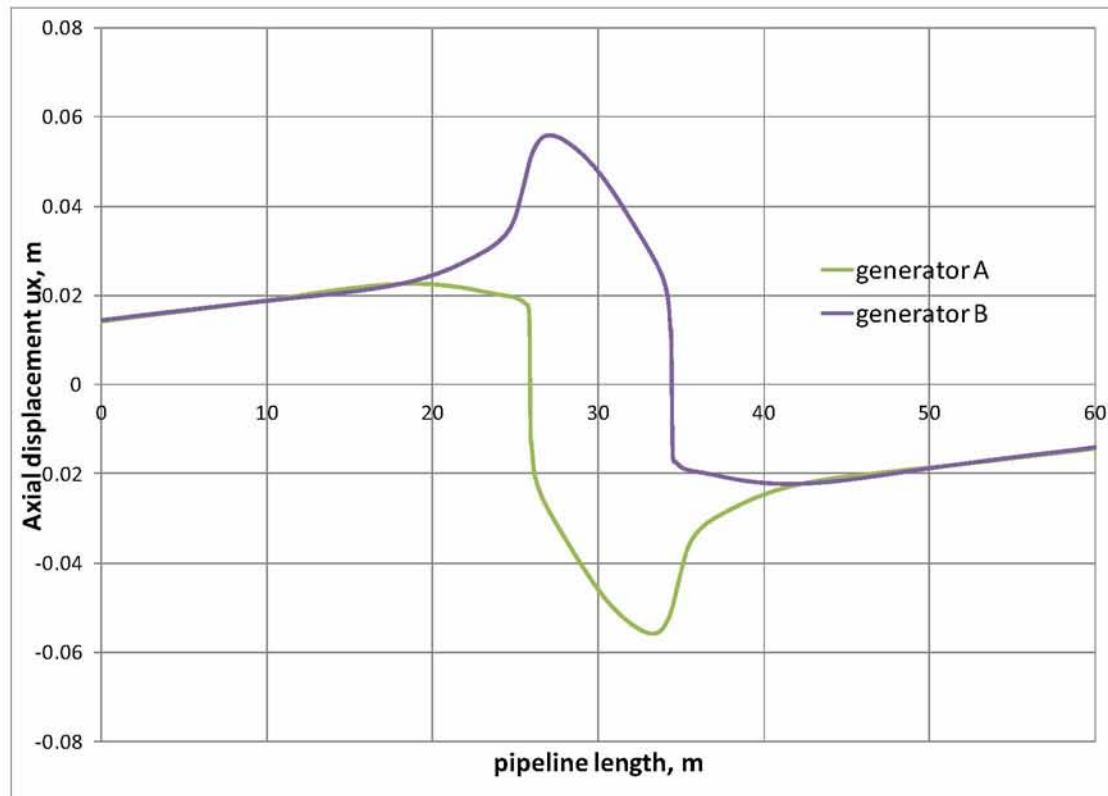
Figure 6.8: Axial displacement u_x versus pipeline length along generators A, B (angle β=0°, fault displacement d = 1 m)
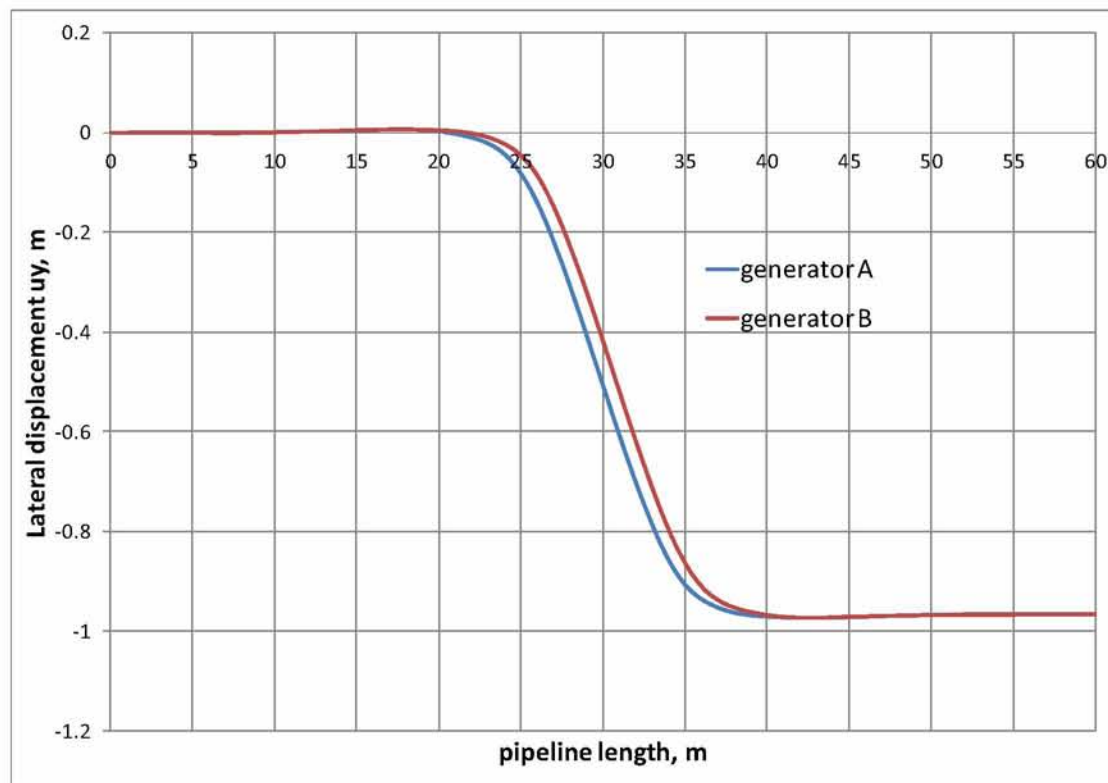
Figure 6.9: Lateral displacement u_y of pipeline versus pipeline length along generators A, B (angle β=15°, fault displacement 1 m)
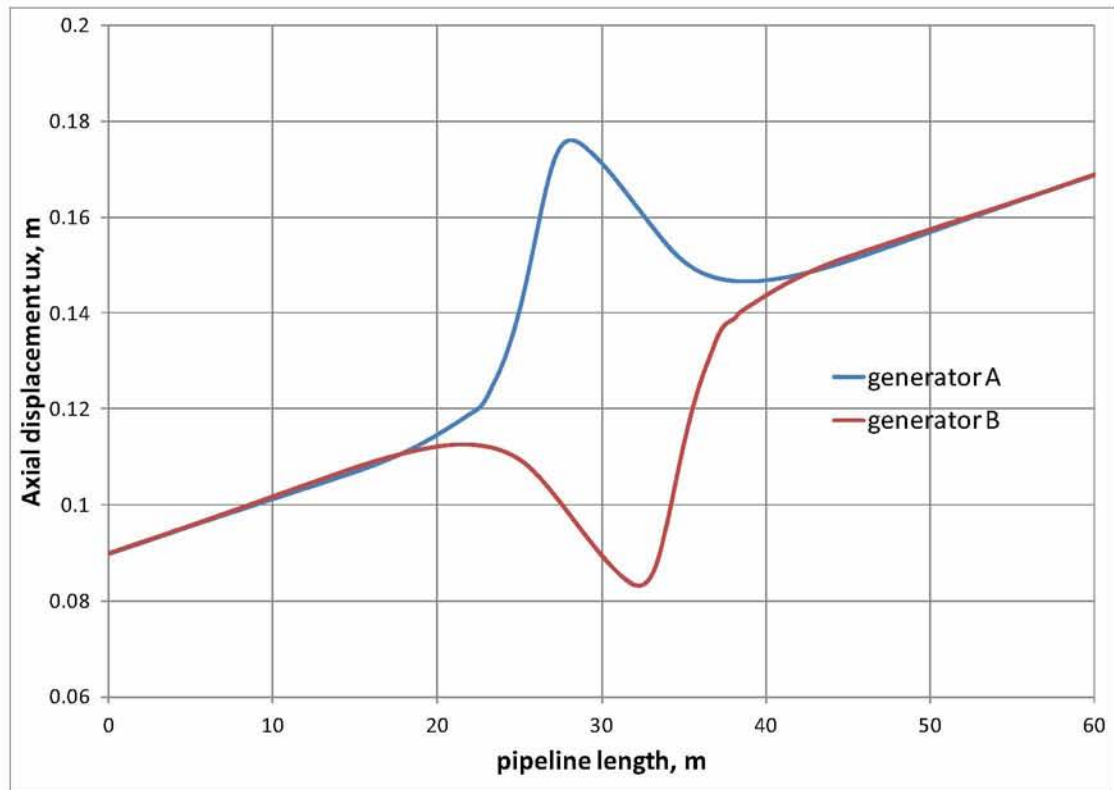
Figure 6.10: Axial displacement u_x of pipeline versus pipeline length along generators A, B (angle β=15°, fault displacement 1m)
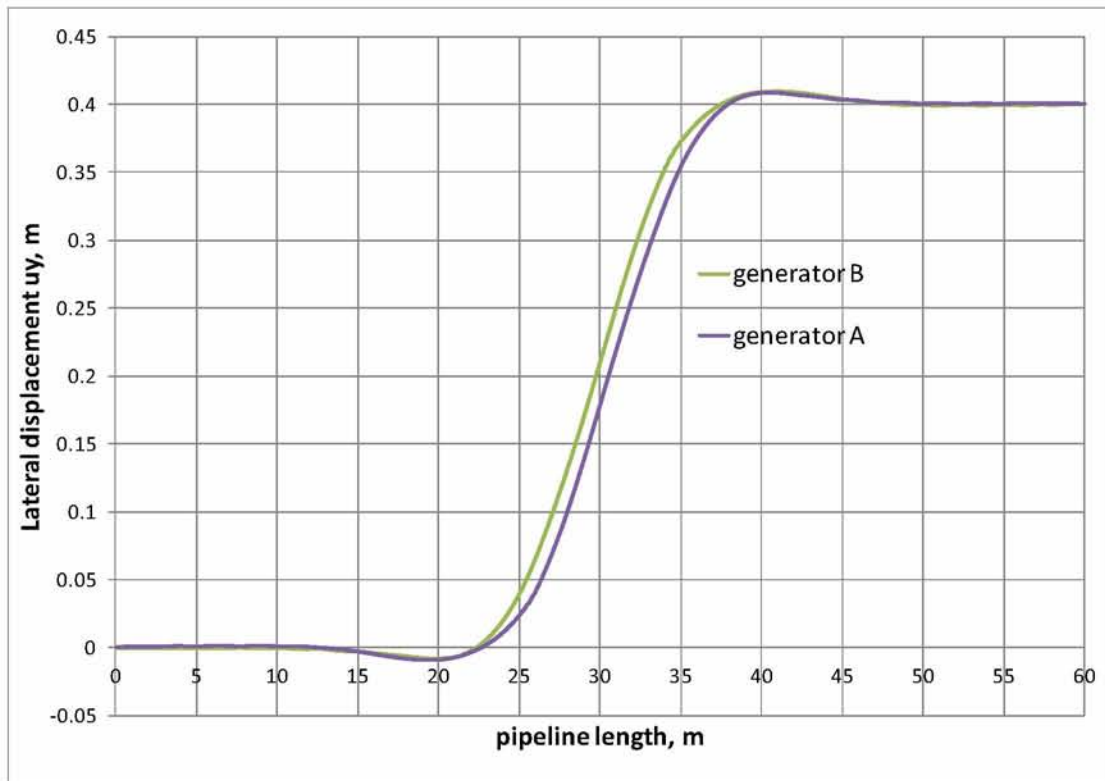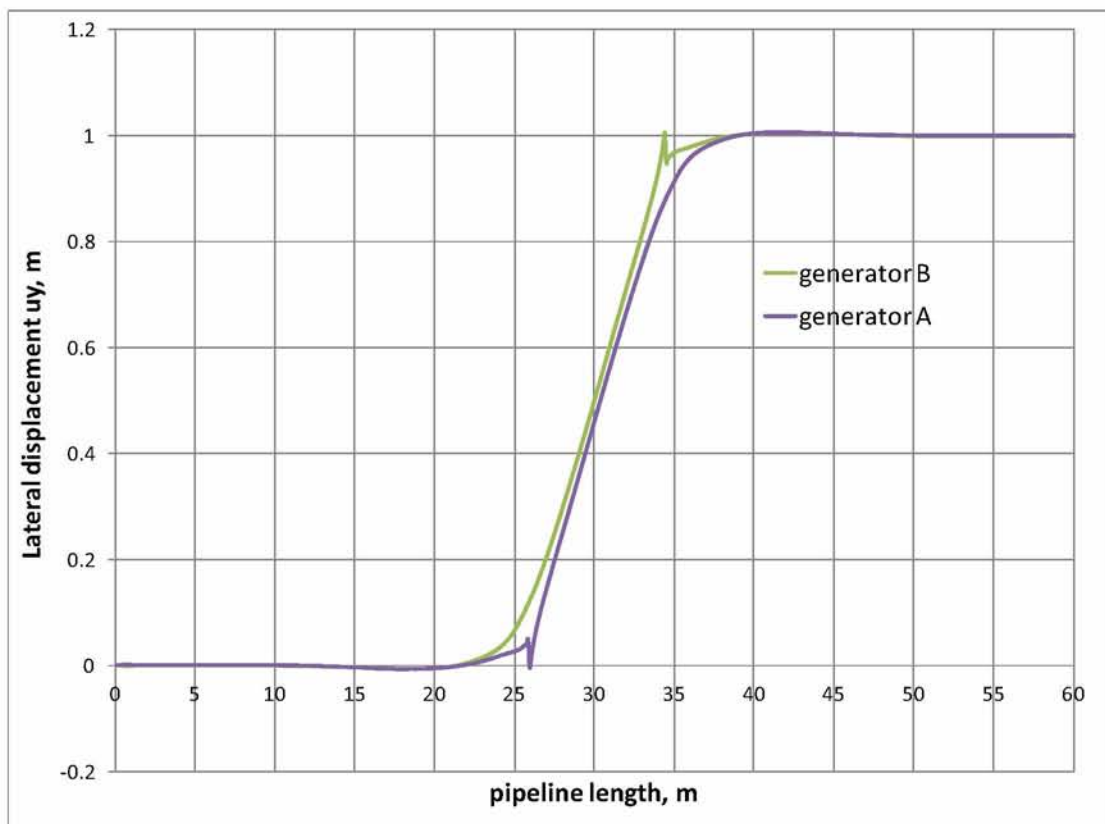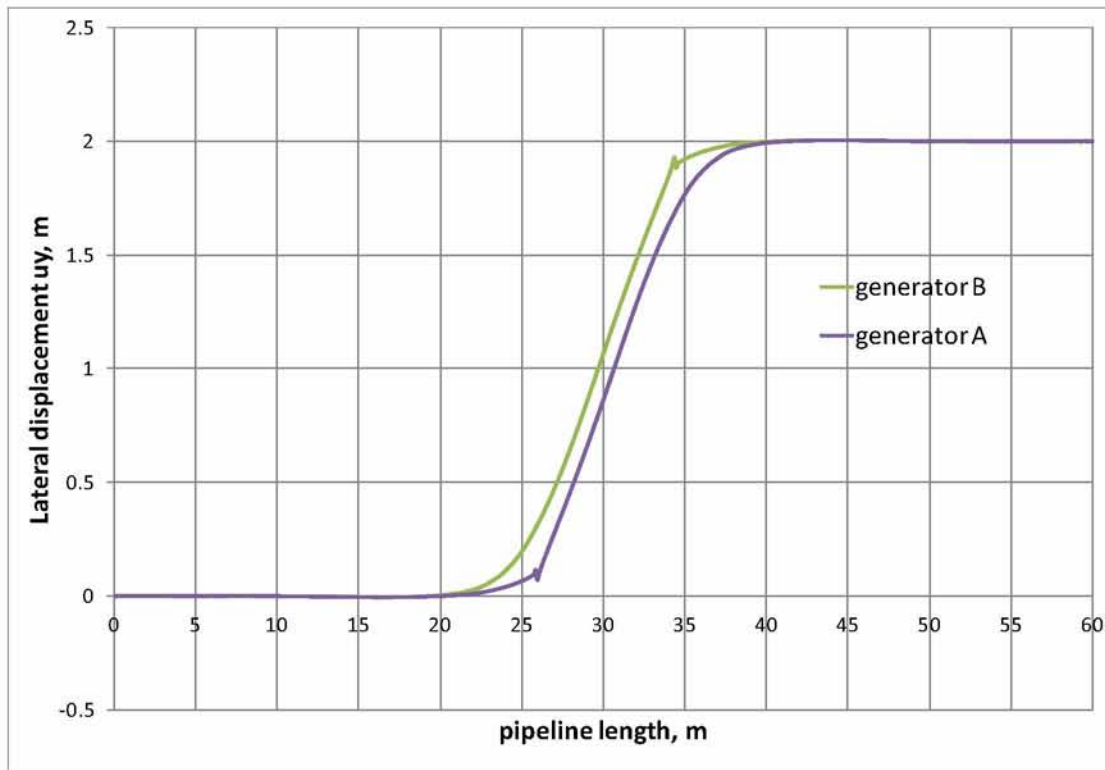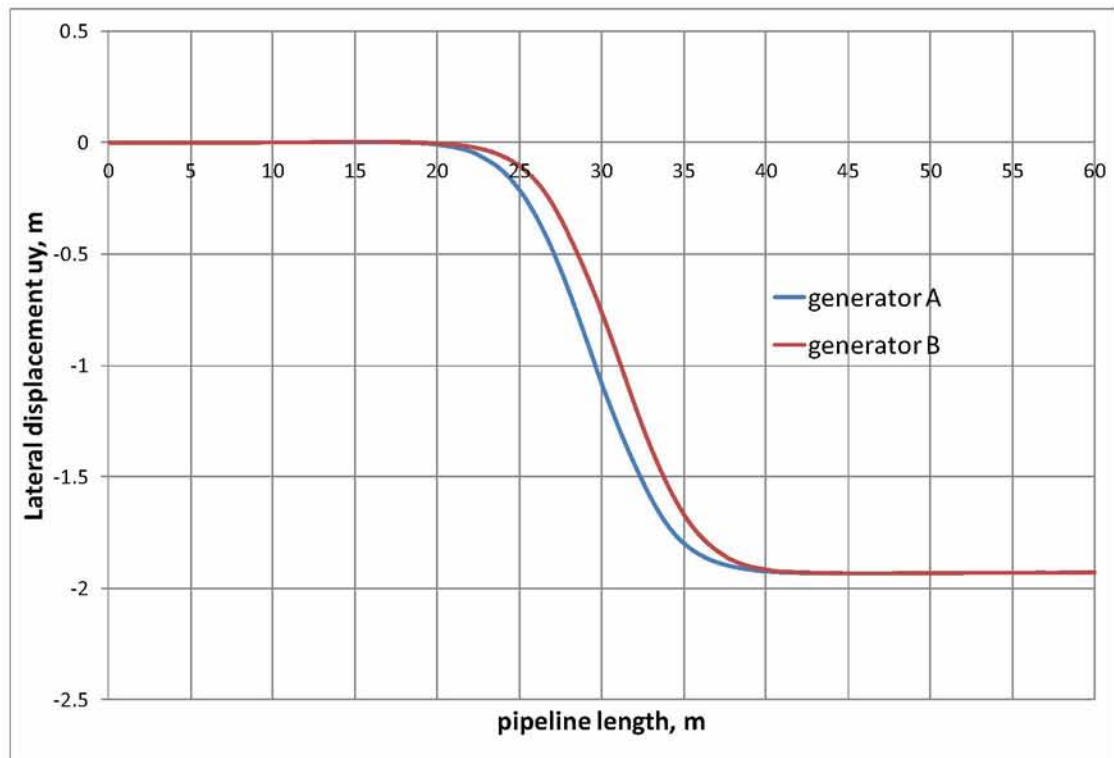

Figure 6.11: Lateral displacement u_y of pipeline versus pipeline length along generators A, B (angle β=15°, fault displacement 2 m)

After determining value L_1/D, the value of $\overline{K}_t$ has to be defined in order to be used in equation (6.23). By obtaining the value u_0 from Figure 6.2 for a given fault displacement, the secant value $\overline{K}_t$ is calculated from Figure 3.21, which plots F_0 versus u_0 for various model lengths.

Applying equation (6.63) for $\beta = 0°$, $L_1/D = 22$ (derived from numerical analysis) and $\overline{K}_t = 240000$ kN/m (obtained from Figure 3.21b for an appropriate value of u_0), a value $(D/t)_{\text{lim}}$ equal to 57 is computed, significantly lower than 96. This verifies that, for $\beta = 0°$, the pipeline considered in the previous section would exhibit local buckling. In addition, for $\beta = 5°$, $L_1/D = 22$ and $\overline{K}_t = 200000$ kN/m, $(D/t)_{\text{lim}}$ is equal to 79, also lower than 96 implying the occurrence of local buckling for infinite pipeline length.

By contrast, for $\beta = 10°$, $L_1/D = 22$ and $\overline{K}_t = 160000$ kN/m, $(D/t)_{\text{lim}}$ becomes equal to 99, suggesting that local buckling may not occur. These conclusions are in agreement with the finite element results shown in Figure 5.36 from Chapter 5.

7   Summary and Conclusions

The performance of underground steel pipelines subjected to permanent strike-slip fault movement have been investigated considering pipeline-soil interaction, using refined models that combine detailed numerical simulations and mathematical solutions, as well as simplified models.

More specifically, a closed-form mathematical solution for the force-displacement relationship of a buried pipeline subjected to tension has been developed for pipelines of finite and infinite lengths. The closed-form solution accounts for the elastic deformation of the soil and pipe, and the development of sliding, when the shear stress at the pipe-soil interface reaches its shear strength. The closed-form solution enables the consideration of equivalent nonlinear springs at the two ends of the pipeline in a refined finite-element formulation, allowing for an efficient, accurate nonlinear analysis of the pipe-soil interaction problem at large strike-slip fault movements.

The numerical investigation of the pipe-soil interaction is based on a large number of refined finite element models for pipeline systems of both infinite and finite lengths and corresponding to various values of angle β between the pipeline axis and the direction normal to the fault plane. Depending on the value of the angle β, the fault movement may subject the pipeline either to overall tension (for positive angles) or compression (for negative angles). Furthermore, an additional series of finite element models of different geometry have been used for the parametric investigation of several special numerical issues such as model size, mesh refinement, fault zone width modelling, or pipeline end-conditions using variable length beam extensions.

The main objective of the present study is the investigation of the effects of key factors, such as the geometric and material characteristics of the pipeline, the properties of surrounding soil, the fault crossing angle, the magnitude of the fault movement, etc., on the performance of the pipeline. Three pipeline performance criteria were considered in all analyses, including: (a) maximum tensile strain leading to rupture of pipeline wall, (b) local buckling associated with pipe wall wrinkling and folding and (c) cross-section flattening resulting in significant cross-sectional distortion. To this end, an extensive parametric investigation utilizing the above refined numerical or combined numerical-analytical models was undertaken. In particular, the effects of various

cohesive and non-cohesive soil conditions (expressed through different values of soil cohesion, friction and stiffness parameters (c, φ, E) on the structural response of the pipeline were examined. The parametric study is extended for various values of D/t ratios of both X65 and X80 steel pipelines, which are representative for oil and gas applications. Furthermore, the effect of various levels of internal pressure is investigated. All analyses are repeated for different values of the fault-pipeline crossing angle β and for different pipeline-end conditions, depending on the available pipeline length.

The numerical results were presented in diagram form for the critical fault displacement d_{cr} and the corresponding critical strain ε_{cr}, versus the pipeline diameter-to thickness ratio D/t and the fault-pipeline crossing angle β. The results were also compared with provisions of recent design standards and recommendations of EN 1998-4 and ASCE MOP 119.

In addition to the above rigorous analysis, a simple analytical model is developed for illustrating pipeline behaviour in terms of buckling, resulting to a simple "no-buckling" condition in a closed-form expression.

The main conclusions derived from this study can be summarized as follows:

1. The proposed closed-form nonlinear force-displacement relationships for buried pipelines of both finite and infinite length subjected to tension, predict pipeline displacements and axial strains which are in excellent agreement with results obtained from more elaborate numerical models, that employ finite elements and distributed soil springs along the pipeline length.

2. Based on the derived closed-form solutions, it has been shown that the main parameters affecting the magnitude of the axial strain in a pull-out test of a pipeline are the displacement, the interface shear strength and the pipeline length, assuming fixed-end conditions. By contrast, soil stiffness does not affect significantly the axial strain developing within the pipeline.

3. The proposed nonlinear force-displacement relationship allows for an efficient, refined numerical simulation of the soil-pipe interaction during large permanent fault movements, through the use of equivalent nonlinear springs in finite-element models that describe the pipe-soil system in a rigorous manner.

4. In the majority of cases of pipelines subjected to strike-slip fault movement that were analyzed using the refined numerical formulation, it was shown that local buckling is the governing mode of failure for negative and small positive values of the crossing angle β for pipelines of both infinite or finite length. Upon development of local buckling during seismic fault movement, the location of maximum flattening and axial strain is at the buckled cross-section.

5. For values of the crossing angle β greater than 15°, local buckling may not occur due to pipeline stretching that reduces the compressive stresses caused by bending. Thus, if practically feasible, aligning the pipeline so that it forms a positive value of β that is just large enough to avoid local buckling, may improve pipeline performance, allowing larger critical fault displacements for the flattening or tensile strain criteria. A value somewhat greater than 15° may be an optimum angle for the cases analyzed.

6. For negative and small positive values of the crossing angle β, soft clays and loose sands accommodate a larger deformation capacity of the pipeline, as opposed to stiff clays and dense sands, which reach the performance criteria at smaller critical fault displacement values.

7. In almost all cases analyzed, the numerical results indicate a strong dependence of the critical performance criteria on the pipeline diameter-to-thickness ratio D/t. For small values of D/t of thick-walled pipelines, local buckling may not occur, especially for pipelines of a finite length, but failure may occur in the form of pipe-wall fracture due to the development of excessive tensile strains.

8. Internal pressure results in a small decrease of deformation capacity and a different buckling shape for pipelines subjected to compression. For pipelines in tension, the presence of internal pressure prevents cross-sectional flattening and the failure criteria are reached at slightly greater values of fault displacement compared to those obtained for zero internal pressure.

9. The ultimate fault displacement reached when the pipeline is in tension is larger compared to that obtained from in compression. As the tension in the pipeline increases with increasing values of the angle β, the critical fault displacement corresponding to the flattening performance criterion and, most importantly, to the 3%- and 5%-tensile strain criteria decrease if finite length is considered. In the case

of infinite length the critical fault displacement can either decrease or remain constant.

10. High-strength X80 steel pipelines have a larger deformation capacity and superior structural behavior with respect to that of X65 pipelines. Furthermore, cold-formed UOE X80 pipes exhibit better behavior in terms of buckling than seamless X80 pipes due to strain hardening of the steel material induced by the manufacturing process and the increase of yield stress.

11. A simplified analytical model for pipeline behavior in terms of buckling resulted to a closed-form "no-buckling" expression which is in agreement with the results from the refined finite-element analyses.

12. The proposed methodology in the present dissertation is applied to simulate the behavior of pipelines crossing strike-slip faults, but can be also applicable to other types of permanent ground-induced actions, such as normal and reverse faults, as well as to buried pipelines subjected to landslides, differential settlement or lateral spreading.

The results of this dissertation offer some useful insight on the performance of underground steel pipelines during fault-induced permanent ground movement and can be used to improve the design of such systems in everyday engineering practice in the framework of a strain-based pipeline design in geohazard areas, in order to mitigate permanent geohazard actions.

References

[1] EGIG. (2011). *Gas Pipeline Incidents.* EGIG 11.R.0402.

[2] Savigny, K., Porter, M., & Leir, M. (2005). *Geohazard Risk Management for the Onshore Pipeline Industry.* Buisiness Briefing: Exploration & Production: The Oil & Gas Review.

[3] Newmark N. M., Hall W. J. (1975), "Pipeline design to resist large fault displacement". *Proceedings of U.S. National Conference on Earthquake Engineering*; 416–425.

[4] Kennedy, R. P., Chow, A. W. and Williamson, R. A. (1977), "Fault movement effects on buried oil pipeline", *ASCE Journal of Transportation Engineering*, Vol. 103, pp. 617-633.

[5] Kennedy R. P., Kincaid R. H. (1983). "Fault crossing design for buried gas oil pipelines". *ASME, PVP conference*; 77:1–9

[6] Wang, L. R. L. and Yeh, Y. A. (1985), "A refined seismic analysis and design of buried pipeline for fault movement", *Earthquake Engineering & Structural Dynamics*, Vol. 13, pp. 75-96.

[7] Vougioukas E. A., Theodossis, C., Carydis P. G. (1979), "Seismic analysis of buried pipelines subjected to vertical fault movement.", *ASCE Journal of Technical Councils*, Vol. 105(TCI), pp. 432– 441.

[8] MaCaffrey MA, O'Rourke TD (1983). Buried pipeline response to reverse faulting during the 1971 San Fernando Earthquake. ASME, *PVP conference* 1983; 77:151–159.

[9] Desmod TP, Power MS, Taylor CL, Lau RW (1995). Behavior of large-diameter pipeline at fault crossings. *ASCE, TCLEE* 1995; (6):296 –303.

[10] Wang L. L. R., Wang L. J. (1995), Parametric study of buried pipelines due to large fault movement. *ASCE, TCLEE* 1995; (6):152–159.

[11] Takada, S., Hassani, N. and Fukuda, K. (2001), "A new proposal for simplified design of buried steel pipes crossing active faults", *Earthquake Engineering and Structural Dynamics*, 2001; Vol. 30: pp.1243–1257.

[12] Lillig D. B., Newbury B. D. and Altstadt S. A. (2009), "The Second ISOPE Strain-Based Design Symposium - A Review.", *International Society of Offshore & Polar Engineering Conference*, Osaka, Japan.

[13] Kokavessis, N. K. and Anagnostidis, G. S. (2006), "Finite Element Modelling of Buried Pipelines Subjected to Seismic Loads: Soil Structure Interaction Using Contact Elements.", *Proceedings, ASME PVP conference*, Vancouver, BC, Canada.

[14] Karamitros, D. K., Bouckovalas, G. D., and Kouretzis, G. P. (2007), "Stress Analysis of Buried Steel Pipelines at Strike-Slip Fault Crossings.", *Soil Dynamics & Earthquake Engineering*, Vol. 27, pp. 200-211

[15] Liu, M., Wang, Y.-Y., and Yu, Z., (2008), "Response of pipelines under fault crossing.", *Proceedings, International Offshore and Polar Engineering Conference*, Vancouver, BC, Canada.

[16] Shitamoto, H., Hamada, M., Okaguchi, S., Takahashi, N., Takeuchi, I., and Fujita, S. (2010), "Evaluation of Compressive Strain Limit of X80 SAW Pipes for Resistance to Ground Movement.", *Proceedings of the Twentieth International Offshore and Polar Engineering Conference,* Beijing, China.

[17] Arifin, R. B., Shafrizal, W. M., Wan, B., Yusof, M., Zhao, P., and Bai, Y. (2010), "Seismic analysis for the subsea pipeline system.", *Proceedings of the ASME 2010 29th International Conference on Ocean, Offshore and Arctic Engineering*, OMAE2010-20671, Shanghai, China.

[18] Odina, L. and Tan, R. (2009), "Seismic Fault Displacement of Buried Pipelines Using Continuum Finite Element Methods.", *Proceedings of the ASME 2009 28th International Conference on Ocean, Offshore and Arctic Engineering*, OMAE2009-79739, Honolulu, Hawaii.

[19] Odina, L. and Conder, R. J. (2010), "Significance of Lüder's Plateau on Pipeline Fault Crossing Assessment", *Proceedings of the ASME 2010 29th International Conference on Ocean, Offshore and Arctic Engineering*, OMAE2010-20715, Shanghai, China.

[20] Gu, X. and Zhang, H. (2009), "Research on Aseismatic Measures of Gas Pipeline Crossing a Fault for Strain-Based Design.", *Proceedings of the ASME 2009 Pressure Vessels and Piping Division Conference*, PVP2009-77987.

[21] Trifonov, O. V. and Cherniy, V. P. (2010), "A semi-analytical approach to a nonlinear stress–strain analysis of buried steel pipelines crossing active faults.", *Soil Dynamics & Earthquake Engineering*, Vol. 30, pp. 1298-1308.

[22] Gill PE, Murray W, Wright MH. (1982), Practical optimization. London, Academic Press;

[23] Himmelblau DM (1972), Applied nonlinear programming. McGraw-Hill

[24] Walters FH, Parker LR, Morgan SL, Deming SN (1991), Sequential simplex optimization, Boca Raton, FL, CRC Press.

[25] Trifonov, O. V. and Cherniy, V. P. (2012), "Elastoplastic stress-strain analysis of buried steel pipelines subjected to fault displacements with account for service loads.", *Soil Dynamics & Earthquake Engineering*, Vol. 33, No. 1, pp. 54-62.

[26] Daiyan, N., Kenny, S., Phillips, R., and Popescu, R. (2010), "Numerical Investigation of Oblique Pipeline/Soil Interaction in Sand", *Proceedings of the 8th International Pipeline Conference*, IPC2010-31644, Calgary, Alberta, Canada.

[27] Fredj A, Dinovitzer A (2012), "Simulation of the response of buried pipelines to slope movement using 3D continuum modeling", *Proceedings of the 9th International Pipeline Conference*, IPC2012, Calgary, Alberta, Canada.

[28] LS-DYNA *"Keywords user's Manual", version 971* (2007), Livermore Software and technology corporation, Livermore, CA.

[29] Karimian, H., and Wijewickreme, D. and Honegger D. (2009) Response of Buried Pipelines Subjected to Relative Axial Soil Movement. Can. Geotech. J. 46: 735-752

[30] Scarpelli,G, Sakellariadi, S and Furlani, G (2003): Evaluation of soil-Pipeline Longitudinal Interaction Forces, Rivisata Italiana Di Geotecnica 4

[31] Bartolini L, Roberto B, Vitali L, (2013) "Strain based design crossing of local features in arctic environment", *Proceedings of the 32nd International Conference on Ocean, Offshore and Arctic Engineering*, OMAE2013, Nantes, France.

[32] Vitali L., Bruschi R., Mørk K., Levold E., Verley R., (1999), "HOTPIPE Project: Capacity of Pipes Subject to Internal Pressure, Axial Force and Bending Moment", Proc. 9th Int. Offshore and Polar Engineering Conference.

[33] Gantes C, Bouckovalas G, (2013), "Seismic verification of the high pressure natural gas pipeline Komotini-Alexandroupolis-Kipi in areas of active fault crossings", Structural Engineering International j.

[34] Ha, D., Abdoun T. H., O'Rourke, M. J., Symans, M. D., O'Rourke, T. D., Palmer, M. C., and Stewart, H. E. (2008), "Buried high-density polyethylene pipelines subjected to normal and strike-slip faulting –   a centrifuge investigation.", *Canadian Geotechnical Journal*, Vol. 45, pp. 1733-1742.

[35] Ha, D., Abdoun T. H., O'Rourke, M. J., Symans, M. D., O'Rourke, T. D., Palmer, M. C., and Stewart, H. E. (2008), "Centrifuge Modelling of Earthquake Effects on Buried High-Density Polyethylene (HDPE) Pipelines Crossing Fault Zones.", *ASCE Journal of Geotechnical and Geoenvironmental Engineering*, Vol. 134, No. 10, pp. 1501-1515.

[36] ASCE. 1984, Guidelines for the seismic design of oil and gas pipeline systems. Committee on Gas and Liquid Fuel Lifelines, Technical Council on Lifeline Earthquake Engineering, American Society of Civil Engineers, Reston, Va.

[37] Abdoun T. H., Ha, D., O'Rourke, M. J., Symans, M. D., O'Rourke, T. D., Palmer, M. C., and Stewart, H. E. (2009), "Factors influencing the behavior of buried pipelines subjected to earthquake faulting.", *Soil Dynamics and Earthquake Engineering*, Vol. 29, pp. 415– 427.

[38] Yoshizaki K, O'Rourke T, Bond T, Mason J, Hamada M, "Large Scale Experiments of Permanent Ground Deformation Effects on Steel Pipelines"

[39] O'Rourke T. D., Stewart H.E., Palmer M.C., Bond T.K., Jezerski J.M., O'Rourke M.J., Symans M.D., Abdoun T., Ha D., (2008), "Evaluation of Ground Rupture Effects on Critical Lifelines", NSF Program Solicitation 03-589, NEESR-SG.

[40] O'Rourke T. D., Palmer M.C., Stewart H.E., Olson N, (2009), "Large-Scale Testing of Fault Rupture Effects" SFPUC Final Report.

[41] PLE4Win, "Short introduction to Ple4, a pipeline stress, strain and stability analysis computer program",Expert design Systems, Rijswijk, The Netherlands.

[42] Gresnigt, A. (1986). *Plastic design of buried steel pipelines in settlement area's.* Delft: Heron - Volume 31 - no. 4.

[43] Wang, X., Kibey, S., Tang, H., Cheng, W., Minnaar, K., Macia, M. L., Kan, W. C., Ford, S. J., Newbury B. (2010), "Strain-based Design – Advances in Prediction Methods of Tensile Strain Capacity, *Twentieth International Offshore and Polar Engineering Conference, ,* ISOPE 2010, Beijing, China.

[44] Canadian Standard Association (2007), *Oil and Gas Pipeline Systems*, CSA-Z662, Mississauga, Ontario, Canada.

[45] Wang, Y. Y., Horsley, D. and Liu, M., (2007), "Strain Based Design of Pipelines.", *16th Joint Technical Meeting,* Australian Pipeline Association, Canberra, Australia.

[46] Comité Européen de Normalisation (2006), *Eurocode 8, Part 4: Silos, tanks and pipelines*, CEN EN1998-4, Brussels, Belgium.

[47] American Society of Civil Engineers (2009). Buried flexible steel pipe; design and structural analysis. In: Whidden WR, editor. ASCE Manual of Practice, MOP. p. 119.

[48] Dama E., Karamanos, S. A., and Gresnigt, A. M. (2007), "Failure of Locally Buckled Pipelines.", *Journal of Pressure Vessel Technology,* ASME, Vol. 129, No. 2, pp. 272-279.

[49] Das, S., Cheng, J. J. R., Murray, D. W., Nazemi, N. (2008), "Effect of Monotonic and Cyclic Bending Deformations onNPS12 Wrinkled Steel Pipeline.", *Journal of Structural Engineering*, ASCE, Vol. 134, No. 12, pp. 1810-1817

[50] Gresnigt, A. M. and Karamanos, S. A. (2009), "Local Buckling Strength and Deformation Capacity of Pipes.", *19th International Offshore and Polar Engineering Conference*, Osaka, Japan, pp. 212-223.

[51] Nederlands Normalisatie-Instituut (2006), *Requirements for Pipeline Systems*, NEN 3650, Part-1: General, and Part-2: Steel Pipelines.

[52] Tomlinson, M.J. (1995), Foundation design and construction, 6th Edition, Longman Scientific and Technical, John Wiley and Sons, Inc., New York.

[53] ABAQUS (2012): *Users' Manual*, Simulia, Providence, RI, USA.

[54] American Petroleum Institute (2007), *Specification for Line Pipe*, 44th Edition, ANSI/API Spec 5L.

[55] American Society of Mechanical Engineers (2006), *Pipeline Transportation Systems for Liquid Hydrocarbons and Other Liquids*, ANSI/ASME B31.4.

[56] American Society of Mechanical Engineers (2007), *Gas Transmission and Distribution Piping Systems*, ANSI/ASME B31.8.

[57] Kyriakides, S., and Ju, G. T., (1992). "Bifurcation and Localization Instabilities in Cylindrical Shells Under Bending I: Experiments", *International Journal of Solids & Structures*, Vol. 29, pp. 1117- 1142.

[58] Igi, S. and Suzuki, N. (2007), "Tensile Strain Limits of X80 High-strain Pipelines.", *Proceedings of the 16th International Offshore and Polar Engineering Conference*, Lisbon, Portugal.

[59] Limam, A., Corona, E., Lee, L.-H. and Kyriakides, S., (2009), "Inelastic wrinkling and collapse of tubes under combined bending and internal pressure.", *International Journal of Mechanical Sciences,* in press, available online.

[60] Vazouras, P., Karamanos, S. A., and Dakoulas, P. (2010), "Finite Element Analysis of Buried Steel Pipelines Under Strike-Slip Fault Displacements", *Soil Dynamics and Earthquake Engineering*, Vol. 30, No. 11, pp. 1361–1376.

[61] Vazouras, P., Karamanos, S. A., and Dakoulas, P. (2012), "Mechanical behavior of buried steel pipes crossing active strike-slip faults", *Soil Dynamics and Earthq. Engineering*, 41:164–180.

[62] Anastasopoulos, I., Callerio, A., Bransby, M. F., Davies, M. C., Nahas, A. El, Faccioli, E., Gazetas, G., Masella, A., Paolucci, R., Pecker, A., Rossigniol, E. (2008), "Numerical analyses of fault foundation interaction.", *Bulletin of Earthquake Engineering*, Springer, 6(4), 645-675.

[63] Gazetas, G., Anastasopoulos, I. and Apostolou, M. (2007), "Shallow and deep foundation under fault rapture or strong seismic shaking.", K. Pitilakis (ed.), *Earthquake Geotechnical Engineering*, Springer, 185-215.

[64] Anastasopoulos I., Gazetas G., Bransby, M. F., Davies, M. C. and Nahas, A. El (2007), "Fault Rupture Propagation through Sand : Finite Element Analysis and Validation through Centrifuge Experiments", Journal of Geotechnical and Geoenvironmental Engineering, ASCE, Vol. 133, No. 8, pp. 943-958.

[65] Bransby, M. F., Davies, M. C. and Nahas, A. El (2008), "Centrifuge modeling of normal fault-foundation interaction.", *Bulletin of Earthquake Engineering*, Springer, 6(4), 585-605.

[66] Trautmann, C.H. and O'Rourke, T.D, (1985), "Lateral Force-Displacement Response of Buried Pipe," Journal of Geotechnical Engineering, ASCE, Vol.111, No.9, pp.1077-1092.

[67] Barbas S, Weir M, (2007) "Strain-based Design Methodology for Seismic and Arctic Regions", *Proceedings of the Sixteenth International Offshore and Polar Engineering Conference Lisbon, Portugal, July 1-6, 2007*

[68] Comité Européen de Normalisation (2009), EN 1594 Gas supply systems – Pipelines for maximum operating pressure over 16 bar – Functional requirements, Brussels, Belgium.

[69] American Water Works Association (2004), Steel Water Pipe: A Guide for Design and Installation

[70] American Lifelines Alliance, (2005), Guidelines for the Design of Buried Steel Pipe

[71] Comité Européen de Normalisation (2000), Water supply – Requirements for systems and components outside buildings, EN805, Brussels, Belgium.

[72] Comité Européen de Normalisation (2012), Metallic industrial piping – Part 3: Design and calculation, EN13480-3, Brussels, Belgium.

[73] Comité Européen de Normalisation (2011), Petroleum and natural gas industries – Pipeline transportation systems, EN14161, Brussels, Belgium.

[74] Comité Européen de Normalisation (2004), Design of steel structures – Eurocode 3, Part 4-3: Pipelines EN1993-4-3, Brussels, Belgium.

[75] Det Norske Veritas, (2012), Offshore Standard OS-F101, Submarine Pipeline Systems DNV-OS-F101, Oslo, Norway

[76] C-CORE (2008), Pipeline Integrity For Ground Movement Hazards, Report prepared for the United States Department of Transportation, C-CORE Report R-07-082-459v2